LATERAL DYNAMICS OF AN AXIALLY TRANSLATING MEDIUM: A THEORETICAL AND EXPERIMENTAL STUDY ON THE EFFECTS OF GUIDING COMPONENTS

A PhD Dissertation Presented

By

Hankang Yang

to

The Department of Mechanical and Industrial Engineering

in partial fulfillment of the requirements
for the degree of

Doctor of Philosophy

in the field of

Mechanics and Design

Northeastern University
Boston, Massachusetts

December 2015

ABSTRACT

By 2020, the average of data stored for each person will reach 5,200 GB. This will put increased demands on cost and reliability of data storage. Compared to its competitors, tape storage technology is more energy efficient and operates at lower cost, with longer media life, hence improved reliability. Nevertheless, there are market and technology pressures to improve all aspects of tape recording. One of the key factors that influence tape storage density is the drive's ability to follow written data tracks. Lateral tape motion (LTM) which can be described as a deviation of the tape from its prescribed, linear path could cause the read/write heads to lose track of the data and lead to lower reliability. LTM is caused by periodic and non-periodic effects. All of the guiding elements, including rollers, stationary guides, read/write head assemblies, and packing reels present rich sources of dynamic effects due to friction, sliding contacts, impulses, and damping effects due to air bearing/entrainment.

The research presented in this thesis is motived by the need to understand the causes of LTM, in order to help increase the volumetric storage density of magnetic tape storage systems. To this end tape is modeled as tensioned, axially moving beam with viscoelasticity. Two major studies were undertaken to investigate the effects of imperfections in roller geometry, and dynamic friction between the tape and a grooved roller. In addition, the effects of periodic impulses, such as those that could develop due to flange contacts, on tape dynamics were investigated. A new model for the coupling between lateral and longitudinal tape vibrations was also presented.

Accuracy of Numerical Solution: All of the models presented in this work were solved numerically, by using the finite element method in spatial and the Newmark's method in temporal dimension. A comprehensive study of the convergence characteristics of the numerical methods was carried out. The numerical and analytical dispersion relations (DR) were compared, in order to measure the accuracy of the fully discretized direct solution method. The waveguide-finite element (WFE)

method was used to find the DR for the finite element solution. Good agreement was found between the numerical and analytical solution. Effects of using finite difference discretization in space were also investigated. For the system under study, it was found that high frequency behavior can be simulated with high accuracy by using the finite element discretization, at a relatively modest computational cost.

Eigenvalue Analysis: In this work we also introduce a way to carryout eigenvalue analysis of gyroscopic systems by using the finite element discretization. It was shown that the results match the classical work. This method was used to find the natural frequencies of the system with internal damping.

Roller Mechanics: A mechanics based model to describe the lateral positioning of a tape over a tilted roller is introduced. It is shown that this condition requires the slope of the neutral axis of the tape and the slope of the centerline of the tilted roller to be the same over the wrapped segment. An experimental setup was used to verify the model. The effects of the roller tilt angle, tape wrap angle, and the lengths of the free-tape spans upstream and downstream of the tilted roller on the steady state lateral tape position were investigated experimentally and by simulations. The experiments show that the circumferential position of the wrap on the upstream side of a tilted roller has the strongest effect on pushing the tape in the lateral direction. The total wrap angle around the roller has a smaller effect. It was also shown that the tape segments upstream and downstream of the tilted roller interact, and the combined effect results in a different overall lateral tape response in steady state.

Lateral Friction over Rollers: Effects of friction forces on the lateral dynamics of a magnetic recording tape, wrapped around a grooved roller were investigated experimentally and theoretically. It was shown that including the effects of 'stick-slip' and velocity dependence of the friction force render the tape's equation of motion non-linear. In the experiments, tape was wrapped around a grooved roller in a customized tape path, and tensioned. The tape running speed along the axial direction was set to zero, thus only the lateral friction effects were studied. The grooved roller was attached to an actuator, which moved across the tape. The test was performed in slow and fast actuation modes. Slow mode was used to identify the static, or

breakaway friction coefficient. In the fast mode, the roller was actuated and a periodic stick and slip phenomenon was observed. The stick-to-slip and slip-to-stick transitions occurred when the tape vibration speed matched the roller actuation speed. The breakaway forces in the slow and fast actuation modes were similar one another. Both experiments and theory show that upon slip, tape vibrates primarily at its natural frequency, and vibrations are attenuated relatively fast due to frictional and internal damping. This work showed that by making a single experimental measurement of friction for a given roller design and tape type, our model can be used to predict the behavior over a wide range of wrap angles and tape tensions.

Flange Impacts: In this work the tape response due to flange hits was investigated by a mathematical model of the tape path. It was shown that flange hits can cause a wide-band frequency response in the tape, and the tape can have a very non-periodic motion. While the head induces vibration during servo tracking, most of the non-rotating guides reduce LTM due to frictional damping. Friction in the system helps reduce some of the complexity of the response.

Coupling between In Plane and Lateral Vibrations: The coupling between lateral and longitudinal deflection component that is due to non-linear longitudinal strain is considered. The equations of motion of the longitudinal and lateral tape motion were derived from first principles. The entire tape path is modeled directly, where the interaction of the tape with the recording head and the guides are represented as concentrated forces, and moments. It was shown that the tension impulse can cause a high frequency high amplitude wave in the longitudinal direction, and also excites lateral motion. The effect of the longitudinal wave can potentially cause local stretching of the bits. The amplitude of the longitudinal and lateral deflections due to tension impulse varies linearly with the impulse strength. It was also shown that the tension fluctuation, which primarily affects the longitudinal tape deflection, can excite resonances in the lateral tape motion. Tape velocity and tension have relatively small effects on the resonant frequencies in the range considered, but deflection amplitudes increase with increasing values of applied tension and transport velocity

as expected. The position of the frictional guides was found to have a significant effect on the damping and natural frequencies.

ACKNOWLEDGMENTS

I am indebted to a great number of people for their assistance and support in the completion of this work, and would like to express my gratitude toward all of them.

First, I think my advisor, Professor Sinan Müftü. His invaluable guidance, mentoring and advice were critical thoughout the course of this research. It has been a great pleasure being a member of the Applied (Bio) Mechanics and Tribology Laboratory.

I would also like to thank the other members of my committee, Professors George G. Adams and Rifat Sipahi for their feedback and valuable advice on my research.

I gratefully acknowledge the technical assistance, support and the inspairing discussions with Drs. Johan B. C. Engelen, Mark A. Lantz, Angeliki Pantazi, Hugo E. Rothuizen, Simeon Furrer and Mr. Walter Häberle of IBM Research Laboratories– Zürich during my work there.

I thank all my colleagues in the Applied (Bio) Mechanics and Tribology Laboratory, Drs. Hsuan-Yu Chou, Baran Yildirim, Qian Sheng, Zhengqi Yang and Mr. Soroush Inrandous, Qiyong Chen for the many useful discussions on various aspects, Ms. Tugce Kasikci for good suggestions on research and Mr. Runyang Zhang for taking the work into next stage.

I think Dr. Hua Zhong, Mr. Clark Jessen, Peter Coburn of Oracle Corporation for their assistance and ideas developed during the technical meetings.

Finally, I would like to thank my family and friends for their support, and my lovely girlfriend Bingxin Li for her patience and encouragement in competition of this dissertation.

This research was supported in part by the Information Storage Industry Consortium, Oracle Corporation, and IBM Research Laboratories – Zürich.

TABLE OF CONTENTS

LIST OF FIGURES

LIST OF TABLES

Chapter 1 Introduction

The motivation and background of the work presented in this thesis is given this chapter. In particular, overview of the state of the art in data storage and the role of magnetic tape recording in this landscape are given in Section 1.1 and 1.2 respectively. Tape drive system technology and the mechanical characteristics of the tape are presented in Section 1.3 and 1.4 respectively. The importance of lateral tape motion (LTM) is described in Section 1.5. The objective and organization of this thesis are presented in Section 1.6 and 1.7.

1.1 Data Storage Overview

The amount of data is vast and growing dramatically, quickly moving from terabyte to petabyte to exabyte and even zettabyte[1] levels. In 2012, over 5 EB (exabytes, 1018 bytes) of new information were stored [1] out of 2,837 EB (2.7 zettabytes) digital universe (that is, all the digital data created, replicated and consumed) and this number is doubled in 2014 [2]. This study also suggests the world's information is doubling every other year. By 2020, the average of data storage for each person will reach 5,200 GB in this world.

[1] 1 TB = 1024 GB
1 PB = 1024 TB
1 EB = 1024 PB
1 ZB = 1024 EB

The demand of data storage is driven by patients' medical history in health care, surveillance camera in security field, large file format in YouTube, human genomic codes in life science and so on. According to INSIC (Information Storage Industry Consortium) roadmap [1] and IDC report for EMC [3], there is a clear growing gap (shown in Figure 1-1) between data generated and data stored and among these unfiled data, 36% has value to be analyzed.

This fast pace of growth comes with challenges for data storage industry. Among these are efficiency, cost, energy consumption, reliability and of course capacity. 'Big data', data mining and machine learning, puts a premium on technologies that promotes data processing efficiency. Predictions of web clicking, custom habits, and spam email demand fast and accurate access to the data stored. The storage device has to meet these requirements in order to boost the performance along with reduction of power consumption and cost, or any combination of these. The vital importance of long-term backup or recovery and archiving technologies is also highlighted by increasing data volumes and regulations. The reliability of data storage should be able to guarantee the possible future inspection or investigation of the data. A reliable digital storage device should also come at a potentially reduced cost.

Presently, the common digital storage technologies are flash memory, hard disk drives (HDD), optical disk and magnetic tape. They all have their own advantages and drawbacks. Within this framework, mechanics of magnetic tape is the main concern in this thesis.

1.2 Tape Storage

Magnetic tape technology turns 60 in 2012, and its popularity in technology circles is as good as ever. Thanks to the new file systems the two biggest complaints that data on tape is hard to find and read do not hold true anymore. IBM firstly implemented Linear Tape File System (LTFS) during 2008/2009 which made magnetic tape data storage system easy to access and modify independent of the file content of the data [4]. With LTFS, tape technology expanded its usefulness to merge with HDD technology as part of a

multi-platform storage architecture, including active archiving (online tape/disk blend), new big data and cloud storage.

In 2007, digital tape shared roughly 11% [5] of the storage market. The outstanding reliability of tape system makes it a perfect storage strategy for backup/restore, disaster recovery, archiving offline/long-term preservation and scientific research/exploration. About 73% of enterprise backup data is stored on tape [1]. Archival data recording on tape was a $2.2B business, in 2012 [6] worldwide, with nearly 30% revenue growth [7].

Compared to its competitors, tape storage system has longer media life, more reliable, more energy efficient and lower long-term cost. Tape has the longest life than any other storage technologies. A tape drive has average life span of 7 to 10 years and a media life span of 30 years [7]. The BER (Bit Error Rate - bits read per hard error) for enterprise tape is rated at 1×10^{19} and 10^{17} for LTO[2] (Linear Tape-Open) tape. This compares to 10^{16} for the most reliable enterprise Fibre Channel disk drive [8]. One of the drawbacks of tape is that currently tape storage solution takes more actual space than HDD. A typical tape drive system, take IBM TS1150 an enterprise product for example, has dimension of 3.8" H × 7.8" W × 18.4" D with a standard cartridge size of 4.25" W × 4.95" L × 1.0" D. In fact the storage capacity to storage volume ratio can be improved by using thinner tape with higher bit density. Nevertheless, overall cost of tape storage is much lower than any other storage scheme (Figure 1-3).

Capacity of tape recording systems has to be improved in order to keep pace with other recording technologies, server demands and growing amounts of data. The INSIC technology roadmap shows (Figure 1-2) that by 2022 digital tape capacity should reach 128 TB per cartridge, data rate per channel at 31.8 MB/sec, total data rate at 2049.6 MB/sec, areal density at 53.22 Gb/in^2 [1]. The current product LTO-6 (Linear Tape Open, an open tape data format) released in December 2012 has native data capacity of 2.5 TB. Some notable achievements toward the 2022 goal announced in 2012 were as follows:

- Oracle announced StorageTek T10000D enterprise with 8.5 TB cartridge in 2013,
- IBM enterprise TS1150 at 10 TB cartridge capacity in 2014,

[2] LTO is the trademark of HP, IBM, and Quantum in the Unites States and other countries.

- Fujifilm in conjunction with IBM recorded 85.9 Gb/in^2 on tape media,
- Sony developed areal recording density for tape of 148 Gb/in^2,
- LTO-9 and LTO-10 are planned to have cartridges with 62.8 and 120 TB, capacity, respectively.

Tape capacity has experienced continued increases ever since the introduction of LTFS. Data areal density is the driven to achieve the capacity goal. The primary impact on tape transport will be felt with increasing track density to nearly 53,000 tracks per inch (TPI), which is equivalent to 0.48 μm track pitch [1]. As in any engineering problem, there are multiple ways to achieve the same goal. The mechanics aspects of this problem are discussed in this proposal. Specifically, the modern tape drive must precisely position recording heads containing multiple read/write elements over the corresponding data tracks on the tape. By 2022, industry report foresees the PES (position error signal) must improve to 15.2 nm from ~100 nm in 2012 [1]. This prediction challenges tape transport with thinner tape, lower tension, and faster tape velocity.

1.3 Magnetic Tape Data Storage System

Modern magnetic tape is most commonly packed in cartridges (a single reel of tape in a plastic enclosure while cassette refers 2 reels enclosure). Depending on recording method there are two tape technologies: linear and scanning. Linear method arranges data in the length direction as parallel tracks and it is widely used in enterprise and open tape path because it allows tape to move faster (Figure 1-5). Opposite to linear method, scanning recording writes short dense tracks in width direction or diagonal manner. This arrangement is implemented in all videotape and some data tape. For data tape, linear arrangement of data is clearly more advantageous especially when quick access becomes a major factor. Scanning tape recording is beyond the scope of this work.

A typical linear tape drive is shown in Figure 1-4. A pen is also placed in this photo as a reference. When a cartridge is inserted to the drive an auto threading mechanism takes the tape from cartridge pack (supply pack), wraps it around several guiding elements (rollers in this case) and head assemblies, and finally attaches to the machine pack (take-up pack). In a data center or library, many cartridges share one tape drive. When

read/write request is made a robotic arm can locate the desired supply pack and place it in to a tape drive.

1.4 Magnetic Tape Media

The magnetic tape used for reading consists of two layers coated on a substrate. The layers are the magnetic layer and the back coat (backside coating and sublayer coating). Figure 1-6 shows arrangement of the different layers of a digital tape. Magnetic layer is in contact with the recording head and the data is stored in this layer. The back coat is on the opposite side of the substrate relative to the magnetic layer. Its function is to prevent static build up and tape wear. Substrate contributes the most to the overall tape thickness and rigidity.

1.5 Lateral Tape Motion

Oracle StorageTek T10000D tape media has 4608 tracks including data tracks and servo tracks on the magnetic layer. As mentioned above, data is stored in a linear manner on the tape. As the tape is translating the read/write heads can read/record the data in parallel tracks. Oracle dual read/write elements have 32 channels and require 144 passes to fully fill the tape. If the tape is "pushed" off of its intended linear path in the lateral direction during the read/write operation, the head assembly could lose the position of a track, resulting in data loss. In order to accommodate for unintended lateral tape motion (LTM) the head assembly can be made to follow a servo-track written on the tape. Presently, head actuation is feasible up to 300-500 Hz. Any LTM with higher frequency can potentially degrade the read/write operation. Figure 1-5 shows the data and servo track layout along the tape (LTO).

1.6 Research Objective

Lateral tape motion (LTM) can be described as a deviation of the tape from its prescribed, linear path as it moves between two reels. LTM could cause the heads to lose track of the data and lead to lower reliability. In order to accommodate for LTM one strategy is to use wider data tracks. But, this leads to lower storage density. In order to keep up with the increasing demands on storage capacity, data reliability, and read/write speed, reduction

of LTM is one of the key factors. The INSIC-2022 roadmap identifies that the standard deviation of the LTM should be below 20 nm by 2022 [1].

The LTM disturbance has periodic and non-periodic sources, which is expected to get worse with smoother, thinner tape as anticipated by the INSIC-2022 roadmap [1]. The periodic disturbance is caused by imperfections in the tape-path components, manufacturing related imperfections in the tape, and the interactions of the tape with the guides, reels and heads. Tape expansion or contraction itself could cause data track shrinking or enlarging. Coupling with LTM, tape stretching has impact on lateral vibration as well. Most common causes of LTM disturbances tend to have relatively low frequencies and high amplitudes; and, the track-following servo system can move the head assembly in this range. The high frequency and relative low amplitude disturbances, which historically stayed inside the track-width, become more important as the LTM margins are reduced to 20 nm levels as foreseen by the technology roadmap.

For guiding or tracking purpose, industry has no other choice than installing guiding elements into tape drive. All the guiding elements, including rollers and stationary guides (e.g. posts), together with read/write head assemblies, and packing reels (machine reel and cartridge reel) present rich sources of dynamic effects due to friction, sliding contacts, impulse, and damping effects due to air bearing/entrainment. More specifically, as tape leaves the cartridge it is subjected to a variety disturbances such as pack wobbling, contact with pack and/or roller flanges, friction on roller/guide surface, roller tilt, tension fluctuation, friction induced vibration from the head and surface friction between different layers of tape at packs. These are certainly unwanted disturbances for the system. The best case scenario due to these negative effects is the LTM, deviating the media from its prescribed path. The worst case scenario could destroy the media or even be detrimental to the entire system.

The primary goal of this study is to analyze how these factors affect the LTM. This work has the following contributions:

i. Investigate the effect of numerical discretization on convergence and accuracy of the linear model [9],

ii. Provide experimental verification to a new roller model,
iii. Conduct friction tests over a grooved roller to determine an effective lateral coefficient of friction and investigate the stick and slip phenomenon observed in the experiments,
iv. Introduce nonlinear model with the ability to couple the longitudinal motion to LTM or vice versa. Implement this model on tension fluctuation, floating layer and guide friction,
v. Based on the existing mathematical models of guides, roller and head, introduce more general modeling method as distributed and generic to improve the simulation and analyze the high frequency LTM due to flange impact.

1.6.1 Other interests

In general, tape can be simulated as axially moving media under tension [10], specifically a tensioned beam [11], string [12], or plate [13]. This includes a class of much broader industries: web transport systems [14], band saw vibration [15], moving cables [16-18], paper recycling production and printing [19]. There are some variations between tape drives and these other operations. Active roller guidance in web handling application is common whereas rollers are passive in tape drive. Head assembly could induce vibration in the tape while web industry does not have such an element with high frequency lateral motion. Nevertheless, the analysis performed for a tape system can be also applied to the above fields with relatively small modifications.

1.7 Thesis Organization

In this work we present a generalized mathematical model of a tape translating between two reels, supported by various guiding elements for predicting LTM. Key to this work is the description of the mechanics of the tape over fixed-guides, rotating-rollers and heads based on Wickert and Brake [9, 20, 21]. The equation of motion is solved numerically. We also couple the longitudinal and lateral tape motions. This coupling results in a nonlinear system, which we also solve numerically.

A comprehensive literature review is provided in Chapter 2. The survey is not only limited to tape modeling, it also covers general models for axially moving media and

various guiding elements. Several unique tape transport phenomena such as air entertainment and tension fluctuation are listed separately. Linear model of LTM is derived and the numerical solution method is presented in Chapters 3.

In Chapter 4, the convergence and accuracy of numeric solution of the linear model is discussed by using wave characterization analysis. A new state space form of eigenvalue solution method for modal shape analysis is also presented. A mathematical model is described that matches the tape slope to the roller slope for a continuous tape supported by multiple rollers in Chapter 5. The model is verified experimentally by using a configurable tape path. The effective lateral coefficient of friction (COF) between magnetic tape and grooved roller is measured in Chapter 6. A model of simulating the friction has good agreement with the measurements. The effect of tape edge contacts with a flanged roller on lateral dynamics is investigated in Chapter 7.

The coupling between lateral and longitudinal dynamics of a translating tape is considered in Chapter 8. This coupled model is tested to investigate the effects of tension fluctuations, number of floating layers in the tape-up pack and location of the frictional guides.

The Chapter 9 and Chapter 10 give a summary of the work and outline of some of potential research topics in the area tape mechanics.

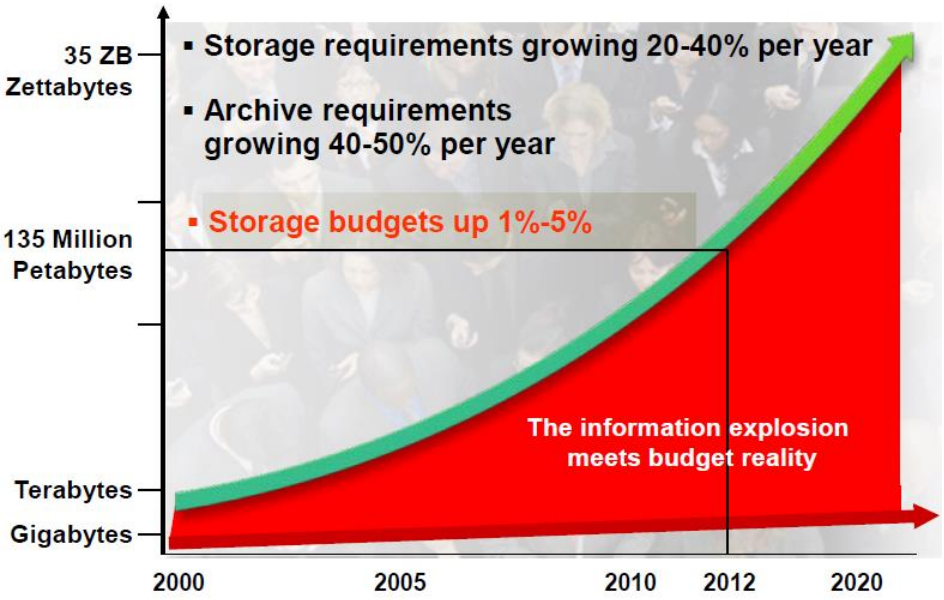

Figure 1-1 Source: Tape Summit 2013

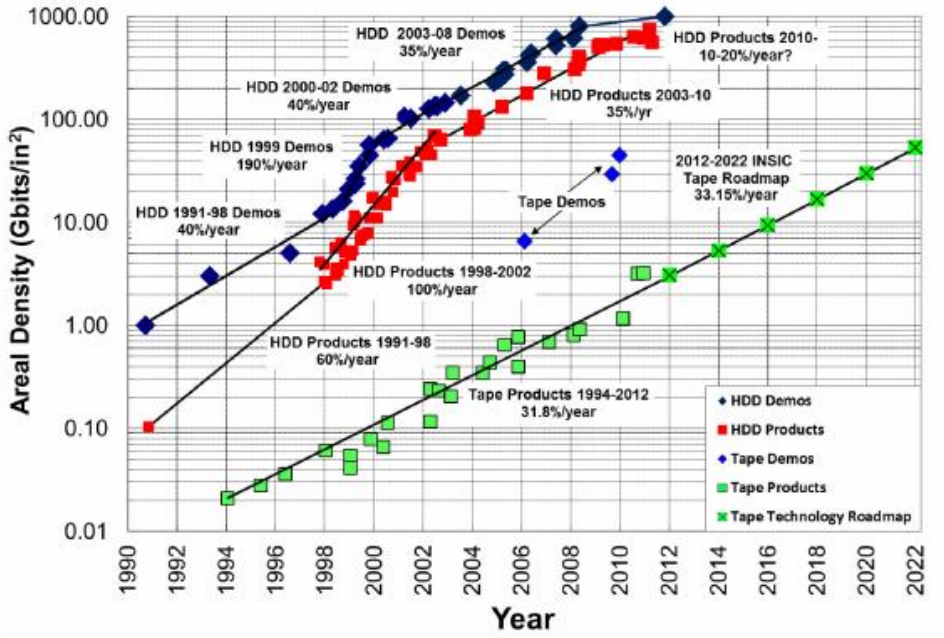

Figure 1-2 Hard Disk Drive, Tape Product and Tape Technology Roadmap Areal Densities [1].

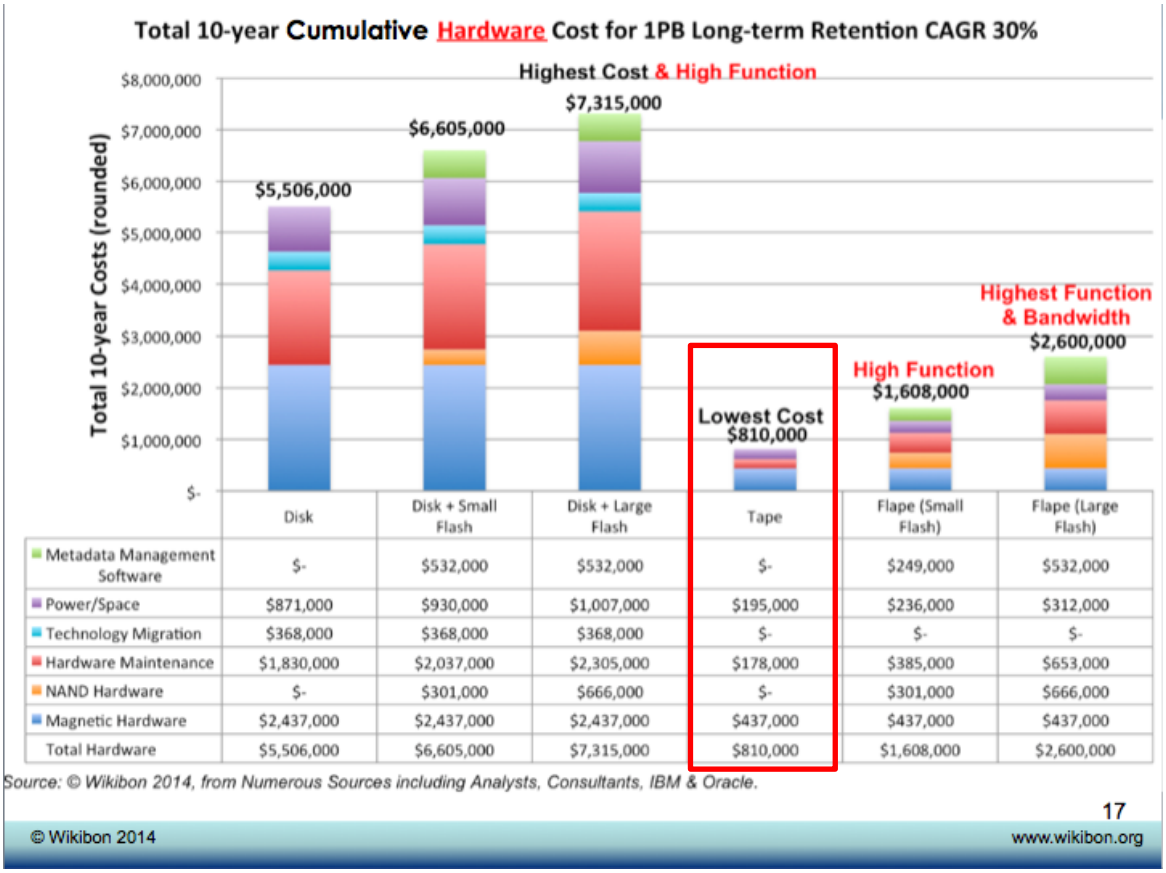

	Disk	Disk + Small Flash	Disk + Large Flash	Tape	Flape (Small Flash)	Flape (Large Flash)
Metadata Management Software	$-	$532,000	$532,000	$-	$249,000	$532,000
Power/Space	$871,000	$930,000	$1,007,000	$195,000	$236,000	$312,000
Technology Migration	$368,000	$368,000	$368,000	$-	$-	$-
Hardware Maintenance	$1,830,000	$2,037,000	$2,305,000	$178,000	$385,000	$653,000
NAND Hardware	$-	$301,000	$666,000	$-	$301,000	$666,000
Magnetic Hardware	$2,437,000	$2,437,000	$2,437,000	$437,000	$437,000	$437,000
Total Hardware	$5,506,000	$6,605,000	$7,315,000	$810,000	$1,608,000	$2,600,000

Figure 1-3 Total 10-year cumulative hardware cost for 1PB long-term retention (Source: Wikibon 2014)

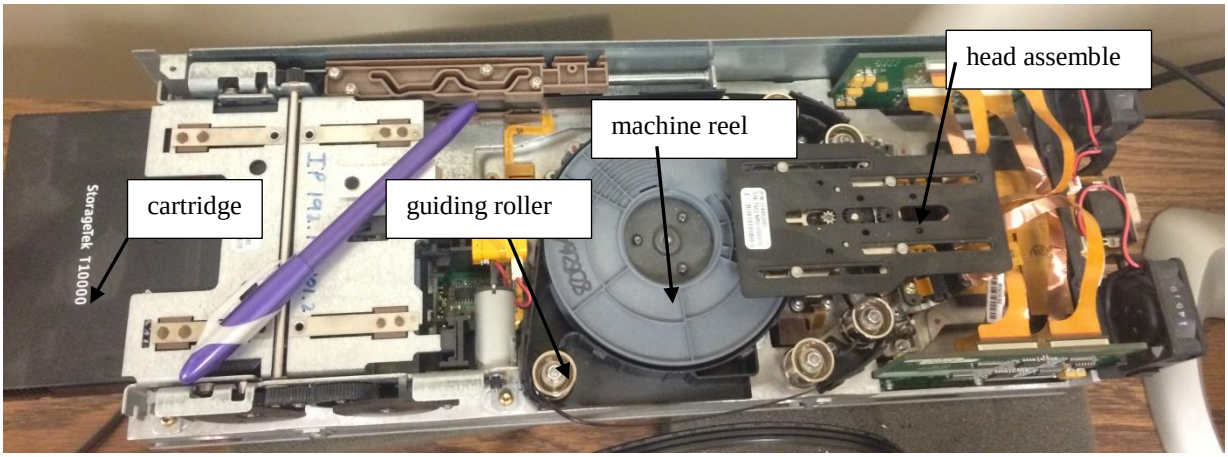

Figure 1-4 Commercial available tape drive (Oracle StorageTek T10000).

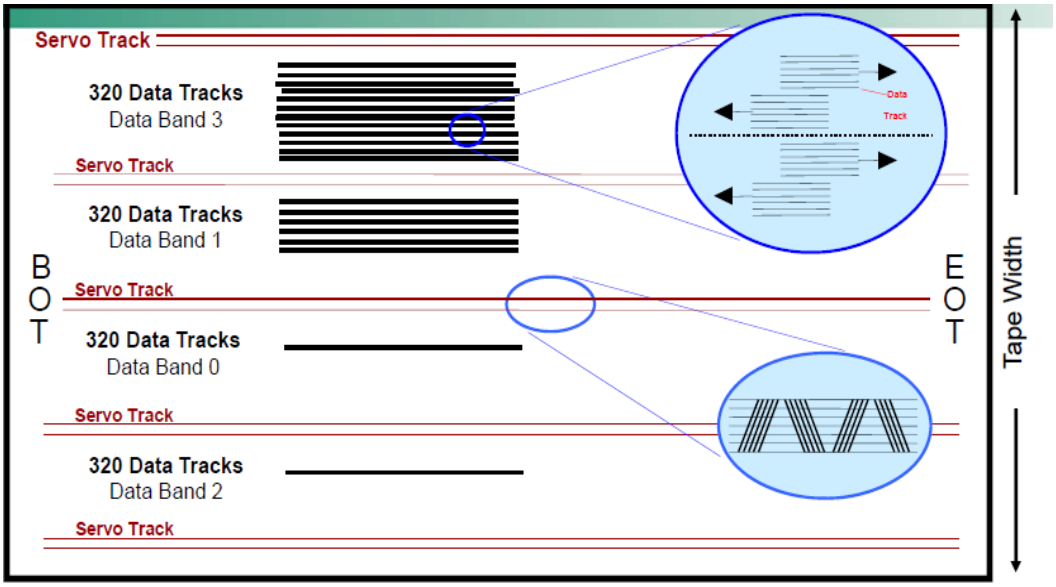

Figure 1-5 LTO tape servo and data track (Source: FUJIFILM, USA)

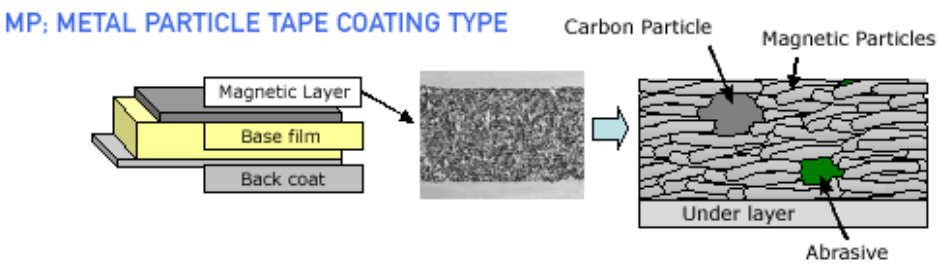

Figure 1-6 Three layers of digital tape (Source: Sony)

Chapter 2 Literature Review

A typical axially translating system can be found in tape drives, web handling systems in a variety of roll-to-roll (R2R) manufacturing systems. Any one of these systems requires various types of guiding elements such as rollers and stationary guides to support the tape/web as it travels between the reels. In addition, tape drive systems in particular use servo controlled read/write head assemblies. These elements which serve the systems in different ways such as guiding, tracking or reading/writing data, also introduce dynamic imperfections into the system, which could be disturbing or even detrimental to tape/web motion along the entire path.

This chapter starts with a review of mechanics of axially moving media for the past two decades in Section 2.1. The effects of various tape-path components on tape mechanics are reviewed in Section 2.2. The effects of tension and speed control on tape dynamics is presented in Section 2.3. The effects of wound-in stresses on the tape packs are briefly discussed in Section 2.4. Finally, the effects of the free length of tape between the components on the dynamics are reviewed in Section 2.5.

2.1 General Modeling

First, some key general concepts related to translating media will be introduced. If the Lagrangian reference frame is used to model axially moving media, the entire media

length including wound roll would have to be described. In order to avoid this, the governing equations are expressed with respect to Eulerian reference fame. In addition this system has the Coriolis or gyroscopic accelerations and it is usually characterized as a *distributed gyroscopic system*. This term arises from gyroscope device which describes the motion due to deflection of moving objects when the motion is described relative to a rotating frame. The velocity is usually defined by material derivative for any tensor field,

$$\frac{Dy}{Dt} \equiv \frac{\partial y}{\partial t} + \boldsymbol{u} \cdot \nabla y \tag{2.1}$$

where, y is the deflection at position x and time t, $\boldsymbol{u}$ is the flow velocity vector and ∇y represents displacement gradient. Its acceleration is then,

$$\frac{D^2 y}{Dt^2} = \frac{\partial^2 y}{\partial t^2} + 2\frac{\partial}{\partial t}\boldsymbol{u} \cdot \nabla y + \boldsymbol{u}^2 \cdot \nabla^2 y \tag{2.2}$$

In the following studies, magnetic tape drive system is simulated as axially moving beam with constant velocity V_x . Therefore Equation (2.2) is simplified as

$$\frac{D^2 y}{Dt^2} = \frac{\partial^2 y}{\partial t^2} + 2V_x \frac{\partial^2 y}{\partial t \partial x} + V_x^2 \frac{\partial^2 y}{\partial x^2} \tag{2.3}$$

where, $\frac{\partial^2 y}{\partial t^2}$, $2V_x \frac{\partial^2 y}{\partial t \partial x}$ and $V_x^2 \frac{\partial^2 y}{\partial x^2}$ represent local, Coriolis and centripetal acceleration respectively, y can be viewed as displacement u, v and w as shown in Figure 3-1. This representation has an analog in fluid dynamics.

Renshaw [10] *et al.* showed that the energy of an axially moving string/beam with constant length is conserved in an Eulerian reference frame for clamped and simple-supported boundary conditions, and the response is bounded under a subcritical translating speed. This ensures the legitimacy of investigation of displacement and slope response instead of energy. In contrast to constant length problem, a string with variable length is only energy bounded. Examples of varying length class can be found in elevator cables, satellite tethers and mining hoists systems. This is beyond the scope of this work.

This review will concentrate on constant length class only. Varying length study can be found in references [16-18, 22].

State-space modal analysis and Green's function methods were used by Wickert and Mote [23] to analysis the stability and dynamic response of axially moving media. This method became a widely used analytical approach to deal with the difficulties from Coriolis acceleration component of a gyroscopic system. Spatial discretization method and discontinuous basis functions [24, 25] were proposed by Jha and Brake to help solve the eigenvalue problem and model the nonlinear constraints, respectively. More recently, numerical methods gained acceptance in the solution of more complex, non-linear problems [9, 26-28].

2.1.1 String model

String model is the most popular studied model to understand the physics of translating media. A translating moving string on elastic foundation model was used to study nonlinear vibration, stability [11], and supercritical behavior of translating media [29]. These works conclude that there is a critical speed at which the first natural frequency becomes zero. Increasing the extent of foundation and the foundation stiffness could result in increasing the natural frequencies, but critical speed value remains the same. Regardless of multiple or infinite critical speed, depending on whether discrete or continuous support, instability happens only after the first one and there is an upper bound critical speed value. Longitudinal friction in string model was studied by Chen *et al.* [30, 31] in constant speed and by Zen and Müftü [32] in accelerating systems, respectively.

Parametric resonance can occur in translating media, when the frequency of the excitation in the longitudinal direction is close to twice that any natural frequencies (principal) or sum of any two natural frequencies (summation). A study of parametric excitation can be found in reference [33] by limit cycle contour analysis. Viscoelasticity in parametric excitation was firstly studied by Zhang *et al.* [34, 35]. Mockensturm *et al.* [12] corrected Zhang's equation of motion and found viscoelasticity significantly alters the excitation amplitude. A recent publication of Chen *et al.* [36] discussed parametric

resonance of accelerating string by the method of multiple scales. In their 2-term truncation solutions, they showed that only increasing the fluctuation amplitude of the axial speed could increase the response amplitude and the instability range. Response and instability range are not sensitive to mean axial speed.

2.1.2 Beam model

Beam model, which includes the effects of bending rigidity, has been shown to be a more reasonable model for a variety of translating media problems [37]. Tension effects on a translating beam were studied in references [12, 15, 16, 23, 38]. Lin [13] in his plate analysis indicated that beam models predict an upper bound for the critical speed, but the error could be significantly large if the non-dimensional ratio of the flexural stiffness to the stiffness derived from the applied longitudinal tension, or the slenderness ratio are large in the beam model. This is because as the width of a plate is increased the beam approximation increasingly worsens. Lateral vibration of interconnected beams by a Winkler foundation was investigated by Gaith and Müftü [39].

Kartik has numerous contributions on the effects of friction on translating beams [40-42]. One of the most important conclusions is that low vibration modes are significantly damped in low transport speeds by lateral friction. The other contributions of his work will be discussed in Section 2.2.

Wickert [43] analyzed the stability and resonances of a nonlinear translating beam by asymptotic and perturbation analysis. He pointed out that nonlinear stiffness becomes important near critical speed where modal stiffness is predominately governed by nonlinear flexure. Foundation stiffness which induced longitudinal friction and its effects of its location were deduced by Chakraborty and Mallik with a nonlinear model [44]. Stiffness not only increases fundamental frequency, but also the critical speed, but the second critical frequency is independent of the stiffness value. Additionally, non-linear effects and natural frequencies strongly depend on foundation stiffness and its location, while they depend weekly on friction. All the other conclusions obtained from string model still hold valid in beam assumptions. Parker and Lin [45] continued Mockensturm *et al.*'s work [33] in multiple parametric excitations by second order approximation for

both string and beam model and investigated secondary instability (driven frequency is the same as natural frequency). They mainly found that primary instability (driven frequency is close to twice a natural frequency) region is wider than the summation (driven frequency is combination of *m*th and *n*th modes of natural frequency) and secondary type instability regions. Furthermore, secondary resonances could be widened substantially if second parametric excitation excites primary instability. Such condition can be observed when fundamental driven frequency excites secondary instability while its first harmonic coincident with primary instability. Chen *et al.* [46] obtained the similar parametric resonances conclusions by modeling the translating media as a Timoshenko beam. Orloske *et al.* [47, 48] extended Chen's interests to a three-dimensional beam model by considering both torsion and buckling besides bending. Furthermore, they showed that buckling dominates the in-plane deflection and twist.

2.1.3 Plate model

Plate model inherently has all the degrees of freedom and provides a comprehensive modeling approach. It also provides the ability to analyze the effects coming through the tape surface. Müftü *et al.* numerically solved the transient equation of motion of a translating shell in the context of a foil bearing [26, 49, 50]. Lin provided a general stability analysis of moving plate [13]. He indicated that critical speed depends positively on stiffness ratio and negatively on slenderness ratio. He also showed that a stable region beyond the critical speed is possible. Parametric excitation of a translating plate by a laterally moving elastic foundation was addressed by Kartik and Wickert [51]. Their analysis explicitly stated that stiffness widens the unstable region and develops multiple primary and combination resonances, while the excitation of torsion mode is strongly affected by low stiffness value. Banichuk *et al.* [52] proved buckled shape of a plate on an elastic foundation is symmetrical by carrying out supercritical stability analysis. Lin and Mote [53, 54] studied the wrinkling of rectangular web by plate theory. They found wrinkling criteria under nonlinear loading is related to flexural stiffness. Their model is able to predict wrinkling line and region. Mockenstum and Mote showed twist angle, tension and aspect ratio increase the chance of wrinkling for a translating twisted plate [55]. They also studied stability of new equilibrium configuration after wrinkling [56].

2.2 Tape Tribology

Topics discussed in previous section benefit the real tape path or web handling problems. Most of the subjects reviewed in this section can be found to have equivalent physical models above. For instance, flange contact is similar to foundation model to a certain extent, tension or velocity fluctuation is a good example of parametric excitation, friction in running direction is equal to the friction in media on foundation model, etc. Lateral friction, depends on relative velocity, can be viewed as analogous to elastic foundation, though it is related to relative velocity rather than displacement. Some of the works addressed in previous section are cited once more based on the fact that applications are built on fundamental studies.

2.2.1 Roller

Roller is one of the most import guiding elements on the web/tape path. Ideally, when a web/tape translates in contact with a roller, the frictional force in the interface will cause the roller to rotate. This attribute provides the roller guidance functionality without causing slip. This behavior is similar to the well-known rolling friction, and depends strongly on the traction between the roller and the web/tape. In addition, under steady state operation conditions the traction in tape-to-roller interface will force the centerline (e.g. neutral axis) of the web/tape to follow the roller surface. This will cause the tape to be shifted away from its intended path, in case the roller is tilted. Mechanics of interaction between a roller and a translating medium has attracted some interest. Moustafa derived the equation of motion of a string over a roller and numerically obtained the displacement distribution [57]. Young implemented string model on an axi-symmetrically shaped roller [58]. Eaton described a translating beam model for the mechanics of a tape wrapped around a post with no slip, and experimentally verified his model [59].

Shelton and Reid (SR) observed that the tape/web would “enter” a spinning roller at ninety-degree-entry angle, if it completely sticks on the roller surface [60-63]. There is a need for a model that considers the effects of rollers on the entire length of tape, considering that tape interacts with multiple rollers as it travels between the two reels.

Models of multi-roller tape spans based on the Shelton and Reid's description have been developed [62, 64, 65]. These models stitch together a collection of straight beam segments with the velocity matching condition at the roller positions, but eventually fail to capture the system level effects that the rollers impart on the tape/web. This is because the velocity matching condition does not allow effects such as slip to pass through the roller. Subsequently, Yang and Müftü developed a numerical model interpolating the Shelton and Reid (SR) boundary conditions in a multi-roller system [27].

The formulation introduced by Brake and Wickert [66], in which the effects of various guiding elements are introduced onto the tape as concentrated forces and moments, is suitable for achieving the goal of properly modeling roller-to-tape interactions. However, no guidance has been given to date on how to introduce this interaction on a continuous (non-seamed) tape-path. Pieces of how to model this interaction have been introduced by Eaton [59], Ono [19, 67], Raeymakers *et al*. [28, 68] and Brake and Wickert [9]. In particular, Eaton [59] and Brake and Wickert [9] have made good progress toward incorporating frictional, but "non-rotating" guides (posts) on the tape path. Lee, McClelland, and Imaino found a very good agreement between their theoretical Timoshenko beam assumption and experimental results [69]. A web-to-roller interaction model in Lagrangian reference frame using plate assumption was established by Yu, Zhao and Ren [70]. Taylor's experimental data demonstrated that the correlation between axial run-out and lateral tape motion (LTM) of grooved roller is higher than smooth roller [71]. A new measure method and coherence analysis were used to assess stick-slip in tape-roller interface by Jape *et al.* [72]. This technique is able to produce a tension-velocity spectrum contour diagram and identify the region where the tape is most likely to slip or stick.

2.2.2 Stationary guide

Unlike a rolling guide, a stationary guide increases tape tension due to sliding friction along the running direction. The term 'stationary' only means that the guide is not spinning, however, slewing, pivoting or other non-rotating motions could be allowed. This term also often refers to a 'post' in tape industry. The effects of an imperfectly

oriented stationary guide on the tape are not as well defined as those described by the SR conditions.

2.2.2.1 Frictional surface

A very comprehensive review paper of theory and experiments was presented by Raeymaekers and Talke [73]. Ono described the tape deflection over guide surface by a string model [19, 67]. Raeymaekers and Talke presented a beam model to simulate LTM over a cylindrical guide. They found that the guide radius and wrap angle predominantly influences LTM rather than tape tension, velocity or thickness [68], and the contributions of coefficient of friction are analog to that of damping respectively [28]. Effects of guide tilt on tape deflections, were simulated by Brake and Wickert [9] by using an effective concentrated force including the friction effects. They improved Eaton's model [59] by introducing an equivalent bending moment and found a good agreement with experimental data. A model, where the forces acting on the tape due to animperfectly oriented guide were modeled as a distributed force acting on a translating beam, was developed by Brake and Wickert [20]. This model enabled studies of the effects of friction on tape's deviation from an idealized prescribed path. A plate model over cylindrical guide surface was developed and solved numerically to simulate the effects of self-acting air lubrication by Müftü and Benson [50].

2.2.2.2 Head motion

In magnetic tape recording applications the read/write head can be actuated in the lateral direction with respect to the direction of tape transport, for track following and track-scaling purposes. The friction induced vibration (FrIV) due tohead motion has been analytically examined in the interests of vibration transmission from head to tape [20, 21]. Yang and Müftü studied FrIV by using a stick-slip algorithm [74]. Jose *et al.* studied the head position error signal (PES) by using LTM as an input to a parametric filter with error-based system identification [75]. A new design of dual stage actuator head with capability of high-bandwidth track following was introduced by Raeymaekers *et al.* [76]. Pivoting motion of frictional surface was analyzed by Kartik *et al.* [41] as an alternative solution to head positioning to accommodate for slope misalignment. Parametric

instability of tape mechanics due to head motion was investigated by Kartik and Wickert [51].

2.2.3 Edge contact/wear

Flanges are used on stationary guides and rollers to improve guiding performance by setting hard limits to LTM. On the other hand, the trade-off due to using a flanged guide could be tape edge wear or even buckling. Edge contact was studied experimentally by Taylor and Talke [77] and theoretically by Yang and Müftü [78] and Brake [21]. These studies showed the same conclusion that edge friction helps regularize tape vibration produced by contact. Tape wear problem was found to be responsible for increasing LTM and causing impulse events by Wang and Talke [79]. A prediction method of edge wear and its improvement were also developed [80, 81]. Lakshmikumaran and Wickert [82] deduced that web wrinkling is governed by a relatively high mode by studying edge guided web behavior. During manufacturing tape is slit into small (12.69 mm wide) segments by circular "knives." Any imperfection in the rotation of the knives is reflected on the tape width. The resulting width variation is known as *tape weave imperfection*. This imperfection could be a source of random and periodic excitations when the medium moves in contact with a flanged guide. This topic was investigated by Kartik and Wickert as function of foundation stiffness, tape speed and guide geometric parameters [51, 83].

2.2.4 Air bearing/entrainment

The interaction of a flexible magnetic recording tape and air when the tape is transported over a rigid surface, gives rise to a foil bearing [26]. Study of this problem refers to formulation of a self-acting air bearing in the tape to guide interface. This effect could cause the media to lose contact with the surface of the guiding elements, while generating a super-ambient pressure in the interface. Thus, hydrodynamic lubrication needs to be considered in modeling. Flying height of tape was found to be sensitive to translating speed and tension analytically, and experimentally until operating parameters reached a certain threshold by Müftü *et al.* [49] and Ducotey *et al.* [84] respectively. Wickert [85] analyzed stability of tape when air bearing developed on a stationary guide. A modified Euler formula which integrated tape speed, hydrodynamic lubrication, surface characteristic and guide dimensions was developed and solved by Raeymaeckers, Etsion

and Talke [86]. Air bearing is usually an unwanted effect for rollers as it reduces traction. Several efforts have been made to avoid the formation of the air bearing. Laser surface texturing was proposed to improve the guide tribology performance [87] by Raeymaekers *et al*. A novel air-breathing type of guide was introduced and validated through experiments to enhance tape-to-guide contacts by Nagao and Chang [88]. Air entrainment is also encountered at the take-up reel during winding. Keshavan and Wickert [89] experimentally studied the cumulative and outmost thickness of air layer as well as the rate of air leaking from the sides of the tape-pack, at steady state. They developed a mathematical model that can predict the upper and lower bounds of measurements. Later, they analyzed the discharge rate of entrained air and introduced the mathematical model that describes the boundaries [90]. The reason why only bounding models can be developed instead of exact prediction is mainly due to the uncertainty of surface roughness [91, 92]. Another difficulty of modeling is due to viscoelastic behavior of tape, causing stress relaxation over time [93].

2.3 Tension/Speed Control

There are three principles of tension control while winding. First of all, large torque is applied at the hub in order to build a solid foundation. Secondly, media can be wound softly at the end of wrap. Finally, the torque changes smoothly from end to end. This change is call *taper*. Under ideal conditions, tension and speed of the tape in a tape drive always remain constant and linear taper is commonly applied. However, variation of tension or speed can arise from start/stop of the system, winding/unwinding of the pack, or acceleration/deceleration during operation. Furthermore, one of the many consequences of air bearing or entrainment is tension change. These realistic issues challenge the linear taper control method. Control community developed tension and velocity control algorithms by simulating the entire tape path as a single degree of freedom system [94-99], or lumped system [100-105].

Measurement of tape tension can be required to diagnose potential problems on the tape path. Imaino [106] designed a non-contact tape tension measurement using a laser Doppler technique to detect photoacoustically generated antisymmetric Lamb waves.

Raeymaekers *et al.* [107] invented an optical, non-contact tension sensor and found the strong correlation between tape tension and LTM.

2.4 Winding

Mechanics of a wound reel itself is an important subject. Winding is a process that turns a straight material into a coil. Tape and web handling industries use, most of the time, the simplest winding scheme, center wind, to wind their media. In this method, the wound roll usually is driven by a speed controlled motor. The tension applied to media controls the tightness of a wound roll. Tension tapering (discussed above) is known to affect misalignment between layers, folding and wrinkling at the wound roll. Altman proposed a formula for computing the radial and hoop stresses for wound roll shape [108]. Based on experiments, 'Pfeiffer model' [109] resolved the growth of compressive strain. 'Hakiel model' [110] incorporated the nonlinear material properties. Benson developed a nonlinear model to predict large deformations caused by large interlayer contact pressures [111]. A relation between interlayer pressure and hoop stress at the core boundary was proposed by Yagoda [112]. Lee and Wickert simulated the stress field in wound rolls by finite element analysis [113]. Slippage in wound roll was modeled and measured by Changwoo *et al*. [114].

2.5 Media Span

In traditional web handling industry, researchers separated the entire web path into several free-spans and modeled each span as a translating, tensioned beam. For each span the boundary conditions are obtained from downstream and upstream rollers individually. A state space control algorithm is then applied to modify the rollers and consequently correct the web path. SR boundary conditions [60-63] were originally introduced in web handling industry, and state that friction moment on the roller would correct the web to follow the ninety-degree rule for small steering angles. Benson developed a Timoshenko beam model of SR boundary conditions [115]. Sievers used the SR boundary conditions in a multiple rollers system and discussed the related control algorithms [116, 117]. SR conditions were further modified by Young, Shelton, and Fang for a moderate (circumferential slippage) and large steering (lateral slippage) angle of static and dynamic

analysis [62, 64]. Subsequently, modeling and related control algorithm of multi-roller system was discussed by Young [118]. Solutions to free-span deflections were modified according to different roller imperfections by Seshadri and Pagilla [119]. Han, Xiong and Shi [120] narrowed their study to a two-roller system with angular misalignment.

A simple roller model assumes no tension change over the roller. However, due to eccentricity or out-of-round shape, tension oscillation is observed in real experiments. Carlo, Pagilla and Reid [101] developed a lumped model to describe tension oscillation in roller-web interaction system and verified experimentally by considering the non-ideal roller causing changing of length of web span. In modern processing lines, frequently accelerating or decelerating the running web is a common manufacture requirement. It certainly causes speed variation as well as tension fluctuation. How this tension/speed variation changes the resonant frequency of the entire system was discussed by Pagilla and Diao [121]. Wrinkling is also an important topic in web handling. A typical wrinkling is formed as ‘L’ shape and the classic bulking can be applied to the lower portion which is independent of speed [122]. The speed dependent portion and critical twist angle prior to wrinkling were discussed by Good and Straughan [123]. A closed form of critical machine direction (CMD) stress of web twist was found. Furthermore authors’ analytical solution showed reasonable prediction compared to their measurements.

Chapter 3 Equation of Lateral Tape Dynamics: Linear Case

The tape mechanics is described with respect to a *tape-based coordinate* system (x, z) that coincides with the neutral axis of the idealized tape as shown in Figure 3-1(a). The origin of the tape-coordinate system is located at the tape tangency point on the supply reel. Figure 3-1(b) shows the tape in a configuration that is unwrapped onto a plane. This figure will be used as tape path baseline for the following discussion in next sections and chapters.

Figure 3-1(c) shows schematic depictions of a typical tape path and the definitions of the deflection components u, v, w with respect to a fixed Cartesian coordinate system (x, y, z), where x-, y- and z- axes represent the longitudinal, lateral and out-of plane directions. The tape is assumed to be translating in the longitudinal direction with transport velocity V_x. Each one of the deflection components is a function of (x, t). The strain free configuration of the tape follows an idealized path between the two reels with perfectly aligned components. Tape mechanics is analyzed in an unwrapped, straight configuration, and the effects of the various guides and the reels are imposed with appropriate external forces and boundary conditions, respectively [97]. In this chapter we only focus on lateral tape motion and the interaction among lateral, longitudinal and out-of-plane is assumed to be negligible.

The equation of motion of axially moving beam is derived in Section 3.1. Section 3.2 describes how the governing equation is discretized by the finite element method. The solution method is outlined in Section 3.3.

3.1 Theory

The equation of motion is obtained by using the Hamilton's principle which minimizes the following functional,

$$\delta\int_{t_1}^{t_2}\left(K-U+W\right)dt=0 \tag{3.1}$$

where δK, δU and δW represent the variations in kinetic energy, strain energy, and external work on the system, defined in the usual sense of the variational calculus, respectively [124]. The details of the derivation are omitted here for the sake of brevity. However, it should be mentioned that the viscoelastic nature of the polymeric tape material is considered. The constitutive behavior for a translating viscoelastic beam is given as follows [12] from Kelvin-Voigt model,

$$\sigma_{xx}=\eta\frac{D\varepsilon_{xx}}{Dt} \tag{3.2}$$

where η is the loss modulus of the tape, and σ_{xx} and ε_{xx} are the longitudinal stress and strain, respectively. The motion is observed in an Eulerian reference frame, therefore the material time derivative,

$$\frac{D(\bullet)}{Dt}=\frac{\partial(\bullet)}{\partial t}+V_x\frac{\partial(\bullet)}{\partial x} \tag{3.3}$$

is used in rate calculations. The kinetic energy (K) of the system due to LTM is expressed as follows,

$$K=\int_{t_1}^{t_2}\int_0^L\frac{\rho}{2}\left(\frac{Dw}{Dt}\right)^2dxdt \tag{3.4}$$

where, ρ is the mass density of the tape, t is time and L is the length of media. The strain energy of the translating beam is given as follows,

$$U = \int_{t_1}^{t_2} \int_0^L \left[\frac{1}{2} T \left(\frac{\partial w}{\partial x} \right)^2 + \frac{1}{2} EI \left(\frac{\partial^2 w}{\partial x^2} \right)^2 + \frac{1}{2} \eta I \left(\frac{\partial^3 w}{\partial x^2 \partial t} + V_x \frac{\partial^3 w}{\partial x^3} \right) \left(\frac{\partial^2 w}{\partial x^2} \right)^2 \right] dx dt \qquad (3.5)$$

where T represents the tension, E is the Yong's modulus, I is the second moment of inertia, V_x is media translating speed. Moreover, first, second and third terms represent the contributions due to tension, beam bending and viscoelasticity in bending, respectively.

Equation of motion of a translating tape is then found by using Equation (3.1) as follows,

$$\rho A \frac{D^2 w}{Dt^2} + \frac{\partial^2}{\partial x^2} \left[EI \frac{\partial^2 w}{\partial x^2} + \eta I \frac{D}{Dt} \left(\frac{\partial^2 w}{\partial x^2} \right) \right] - \frac{\partial}{\partial x} \left(T \frac{\partial w}{\partial x} \right) = f(x,t) \qquad (3.6)$$

The first three terms in Equation (3.6) represent effects of inertial forces, internal shear force and bending moment resultants, and the restoring force due to tape tension, respectively. The general function $f(x,t)$ on the right-hand-side (RHS) represents any form of external forces, or loads produced by guiding elements during tape travel. Examples of such forces are due to roller interactions, flange contact forces, surface stiffness of guiding element, impulse or friction on head surface. Details of $f(x,t)$ will be explained in the following chapters. The following sections will fill the RHS by the different guiding types. Equation (3.6) was derived by using the Kirchhoff-Love hypothesis, which eventually leads to the Euler-Bernoulli (EB) beam theory. Noting the width-to-length ratio for the tape, we also considered using the Timoshenko beam (TB) theory. Comparison of steady state tape deflection as predicted by the EB and TB models, given in Appendix A, shows a modest (~3%) difference in the mid-point tape deflection. The error becomes large near the fixed boundaries, but not near the simply supported boundaries. In this work we use the EB theory due to its ease of implementation. As shown in the subsequent chapters, good match between experiments is obtained with this approach.

As mentioned before tape is formed of three layers. Its equivalent mass per unit length, Poisson's ratio, and bending stiffness are expressed as follows [9],

$$\rho' = b\sum_{j=1}^{3}\rho_j h_j \tag{3.7}$$

$$\nu = \frac{\sum_{j=1}^{3}\nu_j h_j}{\sum_{j=1}^{3} h_j} \tag{3.8}$$

$$EI = \frac{b^3}{12\left(1-\nu^2\right)}\sum_{j=1}^{3} E_j h_j \tag{3.9}$$

In order to model the tape dynamics between two reels we only need two boundary conditions at the supply and take-up reels located at $x = 0$ and L. Brake describes the boundary conditions in case the supply pack axis is not perfectly aligned. In this case the position and slope of the tape coming off of the supply reel are given as follows [9],

$$\text{at } x = 0: \quad w = d_0 + R_0\psi_{0s} \quad \text{and} \quad \frac{\partial w}{\partial x} = \psi_{0s} \tag{3.10}$$

where d_0 is the linear offset of the axis, ψ_0 is the tilt of the reel axis described similar to the roller imperfection (Chapter 5), and R_0 is the radius of the web coming off the reel. On the take-up reel side, at $x = L$, the web velocity and slope match the take-up reel's velocity and slope as follows,

$$\text{at } x = L: \quad \frac{Dw}{Dt} = V_x\psi_L \quad \text{and} \quad \frac{D}{Dt}\left(\frac{\partial w}{\partial x}\right) = V_x\dot{\psi}_L \tag{3.11}$$

where ψ_L represents the misalignment angle of the take-up reel. This equation represents the Shelton and Reid (SR) [61, 63] boundary condition. The initial condition for the tape is specified as follows,

$$\text{at } t = 0: \qquad w(x,0) = 0 \text{ for } 0 \le x \le L \tag{3.12}$$

3.2 Spatial Discretization

The equation of motion is solved numerically; lateral deflection is interpolated by piecewise continuous third-order Hermite polynomials [125].

Deflection w is defined over an element as follows,

$$w(x,t) = \boldsymbol{N}\boldsymbol{d} = \begin{bmatrix} N_1 & N_2 & N_3 & N_4 \end{bmatrix} \begin{Bmatrix} w_1 \\ \theta_1 \\ w_2 \\ \theta_2 \end{Bmatrix} \tag{3.13}$$

where, $\boldsymbol{N}$ is the shape function matrix, $\boldsymbol{d}$ is the degree of freedom vector for an element, w_i and θ_i (i = 1, 2) are the displacement and slope of the tape deflection on the boundaries of an element. The sign convention for degrees of freedom $\boldsymbol{d}$ is defined to be positive along the positive coordinate direction for displacements and counter-clockwise direction for slopes. The shape functions are as follows,

$$\begin{aligned} N_1 &= 1 - \frac{3x^2}{L^2} + \frac{2x^3}{L^3} \quad (a) \\ N_2 &= x - \frac{2x^2}{L^2} + \frac{x^3}{L^3} \quad (b) \\ N_3 &= \frac{3x^2}{L^2} - \frac{2x^3}{L^3} \quad (c) \\ N_4 &= -\frac{x^2}{L^2} + \frac{x^3}{L^3} \quad (d) \end{aligned} \tag{3.14}$$

The details of the derivation, which leads to the following matrix representation of the equation of motion, are outlined in any standard FE textbook (e.g. [125]),

$$\boldsymbol{m}\ddot{\boldsymbol{d}} + \boldsymbol{g}\dot{\boldsymbol{d}} + \boldsymbol{k}\boldsymbol{d} = \boldsymbol{f} \tag{3.15}$$

where $\boldsymbol{m}$, $\boldsymbol{g}$, and $\boldsymbol{k}$ are the element mass, gyroscopic damping, and structural stiffness matrices, respectively, $\boldsymbol{d}$, $\dot{\boldsymbol{d}}$, $\ddot{\boldsymbol{d}}$ and $\boldsymbol{f}$ represent the element displacement, velocity, acceleration and external forces vectors, respectively. The element matrices can be evaluated as follows,

$$\boldsymbol{m} = \rho A \int_0^L \boldsymbol{N}^T \boldsymbol{N} dx$$

$$\boldsymbol{g} = 2\rho A V_x \int_0^L \boldsymbol{N}^T \frac{d}{dx}\boldsymbol{N}\, dx + \eta I \int_0^L \frac{d^2}{dx^2}\boldsymbol{N}^T \frac{d^2}{dx^2}\boldsymbol{N}\, dx \tag{3.16}$$

$$\boldsymbol{k} = \left(T - \rho V_x^2\right)\int_0^L \frac{d}{dx}\boldsymbol{N}^T \frac{d}{dx}\boldsymbol{N} dx + EI \int_0^L \frac{d^2}{dx^2}\boldsymbol{N}^T \frac{d^2}{dx^2}\boldsymbol{N}\, dx + \eta I \int_0^L \frac{d^2}{dx^2}\boldsymbol{N}^T \frac{d^2}{dx^2}\boldsymbol{N}\, dx$$

The form of element load vector $\boldsymbol{f}$ depends on of the nature of the external force (which depends on different guiding elements) and will be discussed case by case in the following chapters. The global equation of motion is obtained by summing the forces acting on the nodes in the usual way [125]. The global equation of motion is represented as follows,

$$\boldsymbol{M}\ddot{\boldsymbol{D}} + \boldsymbol{G}\dot{\boldsymbol{D}} + \boldsymbol{K}\boldsymbol{D} = \boldsymbol{F} \tag{3.17}$$

where $\boldsymbol{M}$, $\boldsymbol{G}$, and $\boldsymbol{K}$ are the global mass, gyroscopic damping, and structural stiffness matrices, respectively, $\boldsymbol{D}$, $\dot{\boldsymbol{D}}$, $\ddot{\boldsymbol{D}}$ and $\boldsymbol{F}$ represent the global displacement, velocity, acceleration and external forces vectors, respectively. In order to use the more commonly used convention lower case letter ($\boldsymbol{d}$) will be used to represent the global degrees of freedom vectors from this point forward.

The boundary values of the translating beam in Equation (3.10) and (3.11) can be specified as,

$$\begin{aligned} d_1 &= w(0,t) && \text{(a)} \\ d_2 &= \frac{\partial w}{\partial x}(0,t) && \text{(b)} \\ d_{2M+1} &= w(L,t) && \text{(c)} \\ d_{2M+2} &= \frac{\partial w}{\partial x}(L,t) && \text{(d)} \end{aligned} \tag{3.18}$$

where, M represents the total number of elements. The boundary conditions are applied to Equation (3.17) by using the penalty method to stiffness matrix ($\boldsymbol{K}$) and force vector ($\boldsymbol{F}$) as follows,

$$K_{ii} = K_{ii} + k \quad \text{(a)}$$
$$F_{ii} = F_{ii} + kd_i \quad \text{(b)} \tag{3.19}$$

where, k is a penalty parameter and set to be 4 order of magnitude larger than displacement, i is one of 1,2, 2M+1, and 2M+2, not index notation.

3.3 Numerical Time Integration

Once the continuous partial differential equation (PDE) is reduced to a set of ordinary differential equations (ODE) numerical time integration method can be implemented. The initial values of this problem are as follows,

$$\boldsymbol{d}(0) = \boldsymbol{d}_0 \tag{3.20}$$

$$\dot{\boldsymbol{d}}(0) = \boldsymbol{v}_0 \tag{3.21}$$

A widely used direct time integration method for solving Equation (3.15) is Newmark's method. This method is expressed as [126],

$$\boldsymbol{M}\ddot{\boldsymbol{d}}^{n+1} + \boldsymbol{G}\dot{\boldsymbol{d}}^{n+1} + \boldsymbol{K}\boldsymbol{d}^{n+1} = \boldsymbol{F}^{n+1} \tag{3.22}$$

$$\boldsymbol{d}^{n+1} = \boldsymbol{d}^n + \Delta t\dot{\boldsymbol{d}}^n + \frac{\Delta t^2}{2}\left[(1-2\beta)\ddot{\boldsymbol{d}}^n + 2\beta\ddot{\boldsymbol{d}}^{n+1}\right] \tag{3.23}$$

$$\dot{\boldsymbol{d}}^{n+1} = \dot{\boldsymbol{d}}^n + \Delta t\left[(1-\gamma)\ddot{\boldsymbol{d}}^n + \gamma\ddot{\boldsymbol{d}}^{n+1}\right] \tag{3.24}$$

where, β and γ are the parameters that determine the stability and accuracy of the algorithm [126]. There are several different possible implementations. In this investigation we use the predictor-corrector and implicit method. The predictor vectors are defined as follows,

$$\tilde{\boldsymbol{d}}^{n+1} = \boldsymbol{d}^n + \Delta t\dot{\boldsymbol{d}}^n + \frac{\Delta t^2}{2}(1-2\beta)\ddot{\boldsymbol{d}}^n \tag{3.25}$$

$$\tilde{\dot{\boldsymbol{d}}}^{n+1} = \dot{\boldsymbol{d}}^n + \Delta t(1-\gamma)\ddot{\boldsymbol{d}}^n \tag{3.26}$$

Equations (3.23) and (3.24) can then be written as corrector vectors, as follows,

$$\boldsymbol{d}^{n+1} = \tilde{\boldsymbol{d}}^{n+1} + \Delta t^2 \beta \ddot{\boldsymbol{d}}^{n+1} \tag{3.27}$$

$$\dot{\boldsymbol{d}}^{n+1} = \tilde{\dot{\boldsymbol{d}}}^{n+1} + \Delta t \gamma \ddot{\boldsymbol{d}}^{n+1} \tag{3.28}$$

To begin the time integration, $\ddot{\boldsymbol{d}}_0$ can be obtained by,

$$\boldsymbol{M}\ddot{\boldsymbol{d}}_0 = \boldsymbol{F}_0 - \boldsymbol{G}\dot{\boldsymbol{d}}_0 - \boldsymbol{K}\boldsymbol{d}_0 \tag{3.29}$$

and the following recursion relation determines $\ddot{\boldsymbol{d}}_{n+1}$

$$\left(\boldsymbol{M} + \gamma \Delta t \boldsymbol{G} + \beta \Delta t^2 \boldsymbol{K}\right) \ddot{\boldsymbol{d}}^{n+1} = \boldsymbol{F}^{n+1} - \boldsymbol{G}\tilde{\dot{\boldsymbol{d}}}^{n+1} - \boldsymbol{K}\tilde{\boldsymbol{d}}^{n+1} \tag{3.30}$$

The flowchart (Figure 3-2) describes the pseudocode of implicit Newmark's method. β = 0.25 and γ = 0.5 are used to obtain stability second order accurate $O(\Delta t^2)$ integration scheme [125].

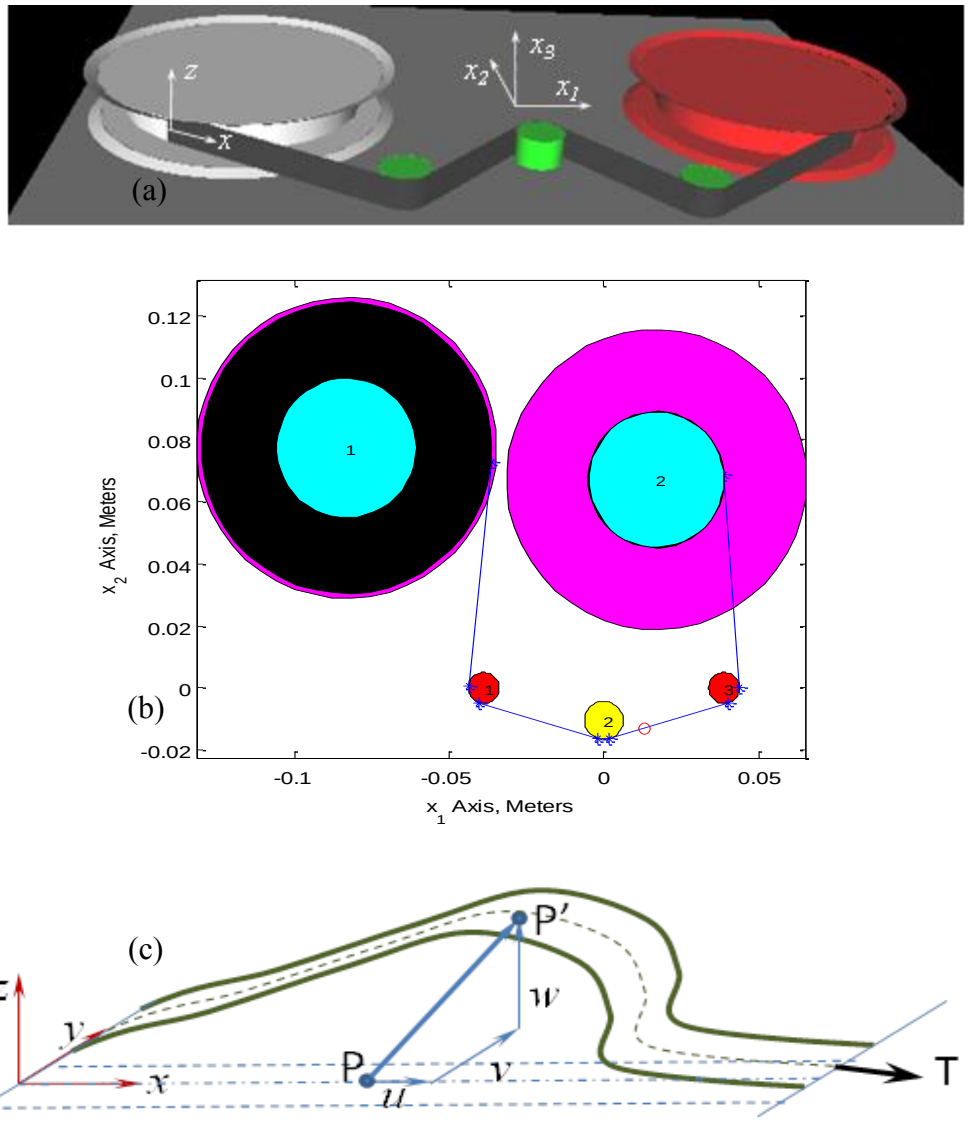

Figure 3-1 (a) Schematic depiction of the tape coordinate system (x, z) and the drive base coordinate system (x_1, x_2, x_3), (b) Schematic diagram of the tape path with supply (1) and take-up reels, two cylindrical guides (1,3) and a cylindrical head (2) depicted in drive base coordinates (x_1, x_2), (c) Schematic diagram of the longitudinal, lateral and out-of-plane tape deflections.

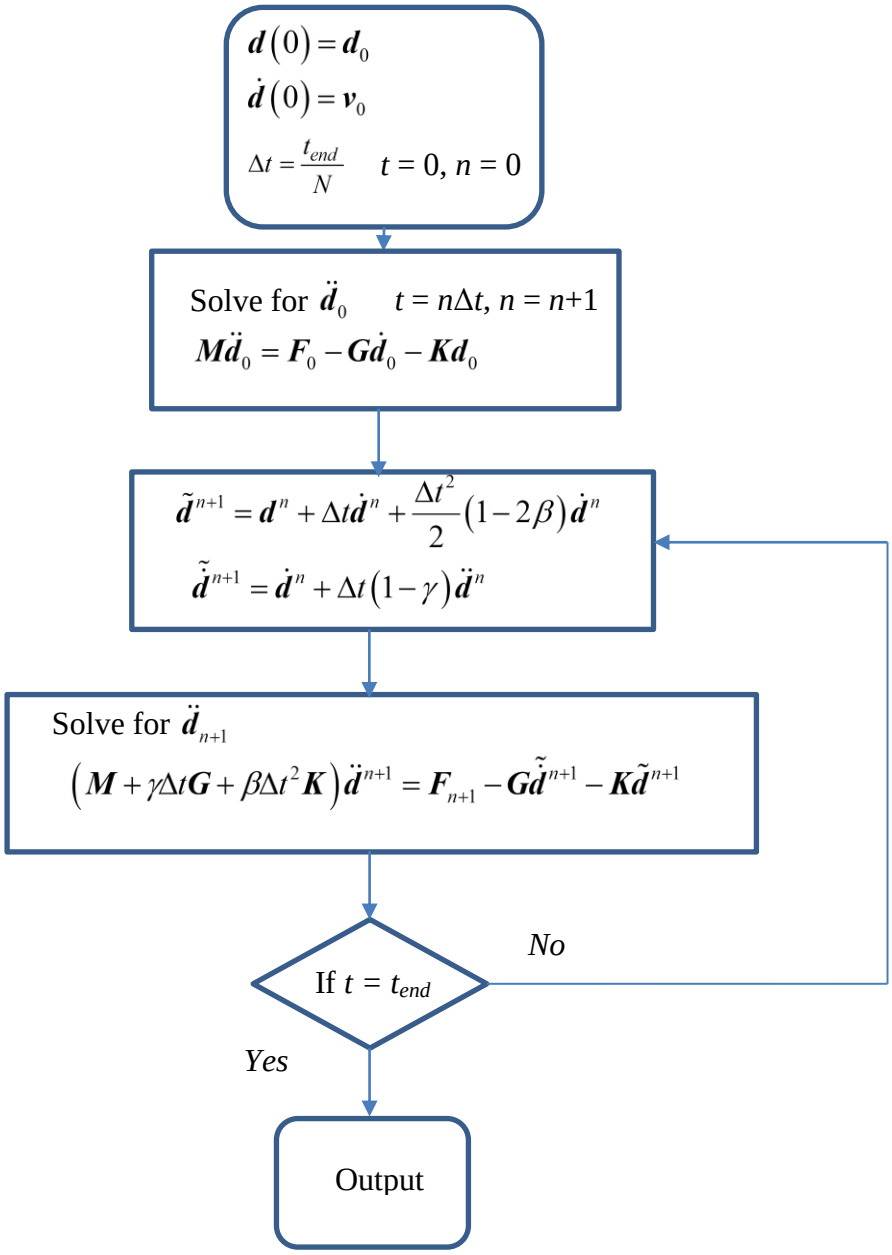

Figure 3-2 Flowchart of Newmark's time integration

Chapter 4 Investigation of the Accuracy of Numerical solution of an Axially Translating, Viscoelastic beam

In this chapter, we investigate the effects of spatial and temporal discretization on the accuracy of the numerical solution of the equation of motion of a translating beam. The equation of motion is solved by using numerical time integration and the finite element (FE) method. The effects of spatial and temporal discretization on the accuracy of high frequency predictions have not been well addressed. We address this problem by modal analysis and wave propagation analysis.

The motivation for this study is given in Section 4.1. Equation of motion is nondimensionalized in Section 4.2. Analysis of wave propagation in a translating viscoelastic beam is given in Section 4.3 by using analytical, finite difference (FD) and waveguide finite element (WFE) approaches. Modal analysis of a beam translating between two supports is demonstrated for spatially and temporally discretized cases in Section 4.4. The conclusions are presented in Section 4.5.

4.1 Introduction

Eigenvalue analysis has been commonly used to identify the natural frequencies of translating media. Meirovitch [127, 128] used the state space representation to find the eigenvalues of gyroscopic systems. Wickert and Mote [23] implemented this approach to moving string/beam systems. This representation enabled researchers to investigate many other axially moving models [13, 17, 34, 35]. Tonoli, Zenerino and Amati [129] used the finite element method to obtain the state space representation of a continuous belt system.

Wave propagation characteristics of a structure are of high interest at higher frequencies. They reveal the characteristics of propagation of a disturbance or transmission of energy. The analytical expression of dispersion relation between frequency (ω) and wavenumbers (k), group velocity, phase velocity, *etc.*, are available for simple structures (rods, beams, plate, etc.,) [130]. Spectral-finite element (SFE) method [131, 132] provides an approach to tackle more complicated problems. Lee and Oh [133], Chakraborty and Mallik [134, 135], Banerjee and Gunawardana [136] applied the SFE to axially moving systems. However, SFE requires development of new elements on a case by case basis [137]. Duhamel, Mace and Brennan [138] proposed the waveguide-finite element (WFE) method to analyze periodic structures. This method uses the existing finite element formulation rather than developing new ones and has been extended to analysis of rod [139], beam [137], plate [140] and cylindrical panel systems [141]. Analysis of non-tensioned translating beams was carried out by using the WFE method for fixed length [142] and varying length [143] beams.

However, eigenvalue analysis, SFE method, or WFE only discretize the space domain, and the time domain remains continuous, despite the fact that the time-step analysis is as important as the spatial discretization in solving dynamic problems. Here, we present eigenvalue and wave characterization analyses of fully discretized translating beam solution. In the present study, the equation of motion of a tensioned, viscoelastic beam is discretized in spatial domain by FEM [125] and in time domain by Newmark's method [144]. The accuracy of both time step and spatial discretization on natural frequency analysis is then studied by using canonical, first order form that is defined by one symmetric and one skew-symmetric matrix differential operator [23]. The discretized

form is solved by WFE method [137] and FD for the wave motion. Each study is validated by the corresponding analytical solutions. The accuracy of the wave motion is established by comparing the dispersion relations of the continuous and discretized systems.

4.2 Governing Equation and Non-dimensionalization

Homogeneous form of the equation of motion of an axially moving, tensioned, viscoelastic beam given by Equation (3.6) can be expressed as follows,

$$\rho\left(\frac{\partial^2 w}{\partial t^2}+2V_x\frac{\partial^2 w}{\partial x\partial t}+V_x^2\frac{\partial^2 w}{\partial x^2}\right)+EI\frac{\partial^4 w}{\partial x^4}-T\frac{\partial^2 w}{\partial x^2}+\eta I\frac{\partial^5 w}{\partial x^4\partial t}+\eta IV_x\frac{\partial^5 w}{\partial x^5}=0 \tag{4.1}$$

where, ρ is the linear density, T represents the tension, E is the Yong's modulus, I is the second moment of area, η is the loss modulus, V_x is media translating speed, w is the transverse deflection, x is the coordinate along the beam, t is time. The Equation (4.1) can be cast in dimensionless form by using,

$$\begin{gathered} X=x/L \quad W=w/L \quad \tau=t/t_c \\ t_c=\sqrt{\left(\rho L^4\right)/\left(EI\right)} \\ \bar{V}=V_x t_c/L \quad \bar{T}=\sqrt{\left(Tt_c^{\,2}\right)/\left(\rho L^2\right)} \quad \bar{\eta}=\left(\eta I t_c\right)/\left(\rho L^4\right) \end{gathered} \tag{4.2}$$

where L is the length of the beam. Nondimensional form of the governing equation becomes,

$$\frac{\partial^2 W}{\partial \tau^2}+2\bar{V}\frac{\partial^2 W}{\partial X\partial \tau}+\left(\bar{V}^2-\bar{T}^2\right)\frac{\partial^2 W}{\partial X^2}+\frac{\partial^4 W}{\partial X^4}+\bar{\eta}\frac{\partial^5 W}{\partial X^4\partial \tau}+\bar{V}\bar{\eta}\frac{\partial^5 W}{\partial X^5}=0 \tag{4.3}$$

Thus, it is seen that the system dynamics will depend on the nondimensional velocity $\bar{V}$, tension $\bar{T}$ and loss modulus $\bar{\eta}$. Note that Equation (4.3) is reduced to the form given by Wickert and Mote [23] for a loss free material ($\bar{\eta}=0$).

4.3 Wave Motion Analysis

We analyze the wave motion due to the basic guidance provided by the CFL (Courant-Friedrich-Lewy) condition in numerical analysis [125]. For hyperbolic problems, this provides a bound for time step size as follows,

$$\Delta t < c\Delta x \tag{4.4}$$

where, c is the wave speed and Δx is a characteristic length of spatial discretization. This bound on Δt, in fact states that a numerical wave should not propagate more than the length between two spatial nodes in a given time step. However, von Neuman stability analysis (also known as Fourier stability analysis) shows that a simple CFL condition cannot be established for dispersive systems [145]. Nevertheless, the convergence of characteristics of the numerical solution can be established by using the dispersion relation. To this end, first we study the dispersion relation for the continuous system. The wavenumber (K), phase ($\bar{V}_p$) and group ($\bar{V}_g$) velocities are identified as functions of wave frequency (Ω) and non-dimensional transport speed ($\bar{V}$), tension ($\bar{T}$) and loss modulus ($\bar{\eta}$). We consider two spatial discretization schemes, namely the finite element and finite difference methods. Temporal discretization is done by the well know Newmark's method. Dispersion relation for the FE discretization is found by using the wave-guide finite element (WFE) method. A semi-analytical expression is used to find the dispersion relation of the FD discretization. The numerical solution obtained by WFE and FD are compared to analytical solution.

4.3.1 Analytical version of the dispersion relation

In dispersive media propagating, evanescent, and attenuating waves can be identified as three distinct wave types. From this point of view, a general wave of the form [131],

$$W\left(X,\tau\right) = Ae^{i(\Omega\tau - kX)} \tag{4.5}$$

can be used as the solution of Equation (4.3), where Ω and K represent the dimensionless oscillation frequency and wavenumber, A represents the wave amplitude and $i = \sqrt{-1}$. While A is a real number, both the Ω and K can be complex variables. The dispersion

relation, which represents a relationship between frequency and wavenumber, is obtained from Equations (4.3) and (4.5) as follows,

$$-i\bar{V}\bar{\eta}K^5+\left(1+i\bar{\eta}\Omega\right)K^4-\left(\bar{V}^2-\bar{T}^2\right)K^2+2\bar{V}\Omega K-\Omega^2=0 \tag{4.6}$$

Solution of wave number K as function of frequency Ω can be obtained by solving the quintic Equation (4.6) numerically. Wavenumber K can be a complex variables as $K=K'+i\mu$. K' and μ are real, and represent the propagation and evanescence (phase change) effect. $\mu=0$ implies absence of damping while $K'=0$ indicates rapid damping. The wave is attenuating if K is complex valued. By definition, any disturbance generated at an arbitrary position would decay as it travels in the material. This implies that solution K of Equation (4.6) has to satisfy $e^{i(-KX)}\to 0$ as $X\to\infty$. The wave and group velocity can then be found as follows [130],

$$\bar{V}_p=\frac{\Omega}{K} \text{ and } \bar{V}_g=\frac{d\Omega}{dK} \tag{4.7}$$

The wave motion in the translating, tensioned beam is said to be dispersive, as both phase and group velocities are functions of the wave number and they are not equal to each other. The wave numbers are ordered as $|K_1|\geq|K_2|\geq|K_3|\geq|K_4|$.

4.3.2 Analysis of wave motion using FEM

Duhamel and Brennan [137] introduced the wave-guide finite element (WFE) method for analyzing wave propagation in solids in the context of FEM. Manconi and Garziera [142] applied this method to a translating elastic untensioned beam. WFE uses only spatial discretization, but time remains continuous. The effect of time integration method on the accuracy of wave motion is worthy of investigation. In this section we briefly introduce the finite element discretization scheme in both spatial and time domain and then apply them to the waveguide concept for characterizing the move motion.

4.3.2.1 Spatial discretization

The semi-discrete form of Equation (4.3) can be obtained by using Galerkin's approach on small segments of a beam (as described in Section 3.1). Deflection W is interpolated by piecewise continuous third-order, Hermite polynomials [125] over a small segment (element) of length ΔX as $W(X,\tau) = \boldsymbol{N}\boldsymbol{d}$, where, $\boldsymbol{N} = \begin{bmatrix} N_1 & N_2 & N_3 & N_4 \end{bmatrix}$ is the basis (shape) function matrix, $\boldsymbol{d} = \begin{Bmatrix} W_1 & \theta_1 & W_2 & \theta_2 \end{Bmatrix}^T$ is the degree of freedom vector for a single element, W_i and θ_i (i = 1, 2) are the displacement and slope of the tape deflection on the boundaries of the element (Figure 4-1b). Spatial domain, $X \in [0,1]$, is discretized into M intervals of equal length ΔX, such that position of the j^{th} node is found as follows, $X_j = (j-1)\Delta X$, where $j \in [1, M+1]$. The shape functions are as follows,

$$\boldsymbol{N} = \begin{bmatrix} N_1 & N_2 & N_3 & N_4 \end{bmatrix} \tag{4.8}$$

with

$$N_1 = 1 - 3\left(\frac{\chi}{\Delta X}\right)^2 + 2\left(\frac{\chi}{\Delta X}\right)^3, \; N_2 = \left(\frac{\chi}{\Delta X}\right) - 2\left(\frac{\chi}{\Delta X}\right)^2 + \left(\frac{\chi}{\Delta X}\right)^2$$
$$N_3 = 3\left(\frac{\chi}{\Delta X}\right)^2 - 2\left(\frac{\chi}{\Delta X}\right)^3, \; N_4 = -\left(\frac{\chi}{\Delta X}\right)^2 + \left(\frac{\chi}{\Delta X}\right)^3$$

where, $\Delta X = 1/M$, is the dimensionless element length, $\chi \in [0, \Delta X]$ is the dimensionless coordinate along one element. The matrix form of the equation of motion for a single element becomes [21],

$$\boldsymbol{m}\ddot{\boldsymbol{d}} + \left(2\bar{V}\boldsymbol{s} + \bar{\eta}\boldsymbol{k}_{EI}\right)\dot{\boldsymbol{d}} + \left(\left(\bar{T}^2 - \bar{V}^2\right)\boldsymbol{k}_T + \boldsymbol{k}_{EI} + \bar{V}\bar{\eta}\boldsymbol{h}\right)\boldsymbol{d} = 0 \tag{4.9}$$

where $\dot{(\,)} = \partial(\,)/\partial t$ and $\ddot{(\,)} = \partial^2(\,)/\partial t^2$. The Coriolis acceleration $\boldsymbol{S}$ and viscoelastic damping $\boldsymbol{h}$ are skew-symmetric due to the gyroscopic operator. $\boldsymbol{m}$, $\boldsymbol{k}_{EI}$ and $\boldsymbol{k}_T$ are matrices of mass, bending flexure and tension respectively. These are defined as follows,

$$\boldsymbol{m} = \int_0^{\Delta X} \boldsymbol{N}^T \boldsymbol{N} dX \quad \text{(a)}$$

$$\boldsymbol{s} = \int_0^{\Delta X} \boldsymbol{N}^T \frac{d}{dx} \boldsymbol{N}\, dX \quad \text{(b)}$$

$$\boldsymbol{k}_{EI} = \int_0^{\Delta X} \frac{d}{dx^2} \boldsymbol{N}^T \frac{d}{dx^2} \boldsymbol{N}\, dX \quad \text{(c)} \quad (4.10)$$

$$\boldsymbol{k}_T = \int_0^{\Delta X} \frac{d}{dx} \boldsymbol{N}^T \frac{d}{dx} \boldsymbol{N} dX \quad \text{(d)}$$

$$\boldsymbol{h} = \int_0^{\Delta X} \frac{d}{dx^2} \boldsymbol{N}^T \frac{d}{dx^3} \boldsymbol{N}\, dX \quad \text{(e)}$$

Equation (4.9), which is the semi-discretized form of the equation of motion which can also be generalized to whole tape as follows by using the usual assembly procedure,

$$\boldsymbol{M}\ddot{\boldsymbol{D}} + \boldsymbol{G}\dot{\boldsymbol{D}} + \boldsymbol{K}\boldsymbol{D} = 0 \quad (4.11)$$

where

$$\boldsymbol{M} = \boldsymbol{M} \quad \text{(a)}$$

$$\boldsymbol{G} = 2\bar{V}\boldsymbol{S} + \bar{\eta}\boldsymbol{K}_{EI} \quad \text{(b)} \quad (4.12)$$

$$\boldsymbol{K} = \left(\bar{T}^2 - \bar{V}^2\right)\boldsymbol{K}_T + \boldsymbol{K}_{EI} + \bar{V}\bar{\eta}\boldsymbol{H} \quad \text{(c)}$$

and $\boldsymbol{D}$ is the global nodal displacement vector of dimensions $2(M+1)$. Each matrix in Equation (4.12) is of dimension $(2(M+1)\times 2(M+1))$ as there are two degrees of freedom at each node.

4.3.2.2 Time discretization

Similarly, time domain, $\tau \in \left[0, \tau_f\right]$, is discretized into N intervals of equal length $\Delta\tau (= \tau_f / N)$, such that time at n^{th} time step can be computed as $\tau^n = (n-1)\Delta\tau$, where $n \in \left[1, N+1\right]$. A displacement form of Newmark's method can be obtained as applied to the solution of Equation (4.11) by eliminating the velocity and acceleration from the governing equations as described in reference [144],

$$\begin{aligned}
&\boldsymbol{M}\left(\boldsymbol{D}^{n+1}-2\boldsymbol{D}^{n}+\boldsymbol{D}^{n-1}\right)+\boldsymbol{G}\left(\gamma\Delta\tau\boldsymbol{D}^{n+1}+\left(1-2\gamma\right)\Delta\tau\boldsymbol{D}^{n}+\left(\gamma-1\right)\Delta\tau\boldsymbol{D}^{n-1}\right)+\\
&\boldsymbol{K}\left(\beta\Delta\tau^{2}\boldsymbol{D}^{n+1}+\left(\frac{1}{2}+\gamma-2\beta\right)\Delta\tau^{2}\boldsymbol{D}^{n}+\left(\frac{1}{2}-\gamma+\beta\right)\Delta\tau^{2}\boldsymbol{D}^{n-1}\right)\\
&=\Delta\tau^{2}\beta\boldsymbol{R}^{n+1}+\left(\frac{1}{2}+\gamma-2\beta\right)\Delta\tau^{2}\boldsymbol{R}^{n}+\left(\frac{1}{2}-\gamma+\beta\right)\Delta\tau^{2}\boldsymbol{R}^{n-1}
\end{aligned}\tag{4.13}$$

where, $\Delta\tau$ is time step, n is the current time step, γ, β are numerical parameters that control characteristics of the algorithm such as accuracy, numerical stability and the amount of algorithmic damping which are set to be $\gamma=1/2$ and $\beta=1/4$ for unconditional stability, $\boldsymbol{R}$ is the external force vector which is not used in this work. The homogeneous form becomes,

$$\begin{aligned}
&\boldsymbol{M}\left(\boldsymbol{D}^{n+1}-2\boldsymbol{D}^{n}+\boldsymbol{D}^{n-1}\right)+\boldsymbol{G}\left(\gamma\Delta\tau\boldsymbol{D}^{n+1}+\left(1-2\gamma\right)\Delta\tau\boldsymbol{D}^{n}+\left(\gamma-1\right)\Delta\tau\boldsymbol{D}^{n-1}\right)+\\
&\boldsymbol{K}\left(\beta\Delta\tau^{2}\boldsymbol{D}^{n+1}+\left(\frac{1}{2}+\gamma-2\beta\right)\Delta\tau^{2}\boldsymbol{D}^{n}+\left(\frac{1}{2}-\gamma+\beta\right)\Delta\tau^{2}\boldsymbol{D}^{n-1}\right)=0
\end{aligned}\tag{4.14}$$

The solution for the fully discretized version of the equation of motion (Equation (4.3)) is obtained by assuming that the solution at time step n is of the form,

$$\boldsymbol{D}^{n}=\hat{A}\hat{\boldsymbol{w}}\left(X\right)e^{i(\Omega n\Delta\tau)}\tag{4.15}$$

where $\hat{}$ indicates that the variables are used in the numerical approach, the relation $\tau=n\Delta\tau$ is also used. $\hat{\boldsymbol{w}}\left(X\right)$ is spatially dependent Fourier coefficients [131] in vector representation. System level dynamic stiffness relationship is obtained from Equation (4.14) and (4.15) as follows,

$$\boldsymbol{\Upsilon}\hat{\boldsymbol{w}}=\boldsymbol{0}\tag{4.16}$$

where $\boldsymbol{\Upsilon}$ the dynamic stiffness matrix in both SFE and WFE methods [131, 137] as follows,

$$\Upsilon = \left[\left(\boldsymbol{M} + \gamma \Delta\tau \boldsymbol{G} + \beta \Delta\tau^2 \boldsymbol{K} \right) e^{i\Omega\Delta\tau} + \left(-2\boldsymbol{M} + (1-2\gamma)\Delta\tau \boldsymbol{G} + \left(\frac{1}{2} + \gamma - 2\beta \right) \Delta\tau^2 \boldsymbol{K} \right) + \left(\boldsymbol{M} + (\gamma - 1)\Delta\tau \boldsymbol{G} + \left(\frac{1}{2} - \gamma + \beta \right) \Delta\tau^2 \boldsymbol{K} \right) e^{-i\Omega\Delta\tau} \right] \tag{4.17}$$

4.3.2.3 Waveguide finite element method

In WFE wave propagation along a solid is analyzed by defining an appropriate transfer matrix between two adjacent elements. Consider a tensioned ($\bar{T}$) translating ($\bar{V}$) beam with internal damping ($\bar{\eta}$) to be discretized as shown in Figure 4-1(a). Two adjacent elements are *s* and *s*+1 with nodes (*j*-1, *j*) and (*j*, *j*+1) respectively (Figure 4-1c). The general degrees of freedom and load vectors for element *s* and *s*+1 are,

$$\begin{Bmatrix} \hat{\boldsymbol{w}}_{j-1}^{s} \\ \hat{\boldsymbol{w}}_{j}^{s} \end{Bmatrix}, \begin{Bmatrix} \hat{\boldsymbol{w}}_{j}^{s+1} \\ \hat{\boldsymbol{w}}_{j+1}^{s+1} \end{Bmatrix}, \begin{Bmatrix} \hat{\boldsymbol{f}}_{j-1}^{s} \\ \hat{\boldsymbol{f}}_{j}^{s} \end{Bmatrix} \text{ and } \begin{Bmatrix} \hat{\boldsymbol{f}}_{j}^{s+1} \\ \hat{\boldsymbol{f}}_{j+1}^{s+1} \end{Bmatrix} \tag{4.18}$$

respectively. Note that at a given node *p*, $\hat{\boldsymbol{w}}_p = \begin{Bmatrix} \hat{W}_p & \hat{\theta}_p \end{Bmatrix}$ and $\hat{\boldsymbol{f}}_p = \begin{Bmatrix} \hat{F}_p & \hat{M}_p \end{Bmatrix}$, where $\hat{W}_p$, $\hat{\theta}_p$, $\hat{F}_p$, and $\hat{M}_p$ are spatially dependent Fourier coefficients of nodal displacement, slope, force and moment respectively. With these definitions Equation (4.16) can be expressed for a given element (*s*+1) as follows,

$$\begin{bmatrix} \Upsilon_{LL} & \Upsilon_{LR} \\ \Upsilon_{RL} & \Upsilon_{RR} \end{bmatrix} \begin{Bmatrix} \hat{\boldsymbol{w}}_{j} \\ \hat{\boldsymbol{w}}_{j+1} \end{Bmatrix} = \begin{Bmatrix} \boldsymbol{f}_{j} \\ \boldsymbol{f}_{j+1} \end{Bmatrix} \tag{4.19}$$

where, the Υ_{LL}, Υ_{LR}, Υ_{RL}, and Υ_{RR} denote the appropriate 2×2 sub matrices of Υ defined in Equation (4.17). Knowing the continuity of displacements and equilibrium of forces on the element boundary *j*,

$$\hat{\boldsymbol{w}}_{j}^{s+1} = \hat{\boldsymbol{w}}_{j+1}^{s}, \ \hat{\boldsymbol{f}}_{j}^{s+1} = -\hat{\boldsymbol{f}}_{j+1}^{s} \tag{4.20}$$

a transfer matrix $\boldsymbol{T}$ which relates the nodal displacements and forces in cross-sections *s* and (*s* + 1) can be defined as follows,

$$\begin{Bmatrix} \hat{\boldsymbol{w}}_j^{s+1} \\ \hat{\boldsymbol{f}}_j^{s+1} \end{Bmatrix} = \boldsymbol{T} \begin{Bmatrix} \hat{\boldsymbol{w}}_{j-1}^{s} \\ \hat{\boldsymbol{f}}_{j-1}^{s} \end{Bmatrix} \tag{4.21}$$

From Equation (4.20) and (4.21), it follows that,

$$\boldsymbol{T} = \begin{bmatrix} -\boldsymbol{\Upsilon}_{LR}^{-1}\boldsymbol{\Upsilon}_{LL} & \boldsymbol{\Upsilon}_{LR}^{-1} \\ -\boldsymbol{\Upsilon}_{RL} + \boldsymbol{\Upsilon}_{RR}\boldsymbol{\Upsilon}_{LR}^{-1}\boldsymbol{\Upsilon}_{LL} & -\boldsymbol{\Upsilon}_{RR}\boldsymbol{\Upsilon}_{LR}^{-1} \end{bmatrix} \tag{4.22}$$

Henceforth the transfer matrix $\boldsymbol{T}$ only depends on the dynamic stiffness matrix in Equation (4.16). When a free wave propagates along the waveguide, the displacements and forces are transmitted successively through the segments as follows,

$$\begin{Bmatrix} \hat{\boldsymbol{w}}_j^{s+1} \\ \hat{\boldsymbol{f}}_j^{s+1} \end{Bmatrix} = \lambda \begin{Bmatrix} \hat{\boldsymbol{w}}_{j-1}^{s} \\ \hat{\boldsymbol{f}}_{j-1}^{s} \end{Bmatrix} \tag{4.23}$$

where λ $(0 \le \lambda \le 1)$ is an amplification factor. Considering the Equation (4.21)-(4.23), the free wave motion can be described as an eigenvalue problem as follows,

$$\left(\boldsymbol{T} - \lambda \boldsymbol{I}\right) \begin{Bmatrix} \hat{\boldsymbol{w}}_{j-1}^{s} \\ \boldsymbol{f}_{j-1}^{s} \end{Bmatrix} = 0 \tag{4.24}$$

where, $\boldsymbol{I}$ is the identity matrix. The solution to Equation (4.24) is sought in the form,

$$\lambda_j = e^{-i\hat{K}_j \Delta X} \tag{4.25}$$

where, wavenumber $\hat{K}_j$ can be complex valued argument as $\hat{K}_j = \hat{K}'_j + i\hat{\mu}_j$. This gives the dispersion relation.

4.3.3 Analysis of wave motion using FDM

The wave Equation (4.3) can also be discretized by the finite difference (FD) method in spatial domain. Discretized version of the displacement $W(X, \tau)$ is expressed as W_j^n at time step-n and spatial node-j. The equation of motion (Equation (4.3)) can be expressed in the following operator format,

$$\mathcal{M}\ddot{W} + \mathcal{G}\left(\dot{W}\right) + \mathcal{K}\left(W\right) = 0 \tag{4.26}$$

where the following are the operators are based on Equation (4.3),

$$\begin{aligned}
&\mathcal{M} = 1 && \text{(a)}\\
&\mathcal{G}(\ ) = 2\bar{V}\frac{\partial(\ )}{\partial X} + \bar{\eta}\frac{\partial^4(\ )}{\partial X^4} && \text{(b)}\\
&\mathcal{K}(\ ) = \left(\bar{V}^2 - \bar{T}^2\right)\frac{\partial^2(\ )}{\partial X^2} + \frac{\partial^4(\ )}{\partial X^4} + \bar{V}\bar{\eta}\frac{\partial^5(\ )}{\partial X^5} && \text{(c)}
\end{aligned} \tag{4.27}$$

Equation of motion can be discretized around the spatial node- *j* as follows,

$$\mathcal{M}\ddot{W}_j + \mathcal{G}\left(\dot{W}_j\right) + \mathcal{K}\left(W_j\right) = 0 \tag{4.28}$$

where the operators are approximated by the following central finite difference formulas,

$$\begin{aligned}
&\frac{\partial W_j}{\partial X} = \frac{W_{j+1} - W_{j-1}}{2\Delta X} + \mathrm{O}\left(\Delta X^2\right) && \text{(a)}\\
&\frac{\partial^2 W_j}{\partial X^2} = \frac{W_{j+1} - 2W_j + W_{j-1}}{\Delta X^2} + \mathrm{O}\left(\Delta X^2\right) && \text{(b)}\\
&\frac{\partial^4 W_j}{\partial X^4} = \frac{W_{j+2} - 4W_{j+1} + 6W_j - 4W_{j-1} + W_{j-2}}{\Delta X^4} + \mathrm{O}\left(\Delta X^2\right) && \text{(c)}\\
&\frac{\partial^5 W_j}{\partial X^5} = \frac{W_{j+3} - 4W_{j+2} + 5W_{j+1} - 5W_{j-1} + 4W_{j-2} - W_{j-3}}{2\Delta X^5} + \mathrm{O}\left(\Delta X^2\right) && \text{(d)}
\end{aligned} \tag{4.29}$$

Displacement form of the Newmark's method gives the fully discretized equation of motion in the following symbolic form,

$$\begin{aligned}
&\mathcal{M}\left(W_j^{n+1} - 2W_j^n + W_j^{n-1}\right) + \Delta\tau\,\mathcal{G}\left(\gamma W_j^{n+1} + (1-2\gamma)W_j^n + (\gamma-1)W_j^{n-1}\right)\\
&\quad + \Delta\tau^2\mathcal{K}\left(\beta W_j^{n+1} + \left(\tfrac{1}{2} + \gamma - 2\beta\right)W_j^n + \left(\tfrac{1}{2} - \gamma + \beta\right)W_j^{n-1}\right) = 0
\end{aligned} \tag{4.30}$$

The dispersion relation for the fully discretized version of the equation of motion is obtained by approximating Equation (4.5) as follows,

$$W_j^n \sim \hat{A}e^{i\left(\Omega n\,\Delta\tau - \hat{K}j\Delta X\right)} \tag{4.31}$$

By using Equations (4.27), (4.31), (4.29) and (4.30), we find the characteristic equation from which the dispersion relation can be obtained as follows,

$$\begin{aligned}
&\left(e^{-i\Omega\Delta\tau}-2+e^{i\Omega\Delta\tau}\right)+\\
&\left[\gamma e^{i\Omega\Delta\tau}+(1-2\gamma)+(\gamma-1)e^{-i\Omega\Delta\tau}\right]\left[2\bar{V}\frac{\Delta\tau}{2\Delta X}\left(e^{-i\hat{K}\Delta x}-e^{i\hat{K}\Delta x}\right)+\right.\\
&\left.\bar{\eta}\frac{\Delta\tau}{\Delta X^4}\left(e^{-2i\hat{K}\Delta X}-4e^{-i\hat{K}\Delta X}+6-4e^{i\hat{K}\Delta X}+e^{2i\hat{K}\Delta X}\right)\right]+\\
&\left[\beta e^{i\Omega\Delta\tau}+\left(\frac{1}{2}+\gamma-2\beta\right)+\left(\frac{1}{2}-\gamma+\beta\right)e^{-i\Omega\Delta\tau}\right]\left[\left(\bar{V}^2-\bar{T}^2\right)\frac{\Delta\tau^2}{\Delta X^2}\left(e^{-i\hat{K}\Delta X}-2+e^{i\hat{K}\Delta X}\right)+\right.\\
&\frac{\Delta\tau^2}{\Delta X^4}\left(e^{-2i\hat{K}\Delta X}-4e^{-i\hat{K}\Delta X}+6-4e^{i\hat{K}\Delta X}+e^{2i\hat{K}\Delta X}\right)+\\
&\left.\bar{V}\bar{\eta}\frac{\Delta\tau^2}{2\Delta X^5}\left(e^{-3i\hat{K}\Delta X}-4e^{-2i\hat{K}\Delta X}+5e^{-i\hat{K}\Delta X}-5e^{i\hat{K}\Delta X}+4e^{2i\hat{K}\Delta X}-e^{3i\hat{K}\Delta X}\right)\right]=0
\end{aligned} \tag{4.32}$$

The dispersion relation between frequency (Ω) and wavenumber ($\hat{K}$) is obtained from Equation (4.32).

4.3.4 Numerical accuracy of WFE and FD methods

Table 4-1 lists typical values and the corresponding dimensionless parameters for magnetic recording tape, web handling and band saw applications. Values in this table are equal in the upcoming analysis.

The wavenumber $\hat{K}_1$ obtained by the WFE and FD approach are compared to the analytical solutions in Figure 4-2 for different number of elements and Figure 4-3 for different time step sizes. As shown in both figures, WFE and FD have good match with theory. Overall the finer the mesh the better is the prediction in Figure 4-2. The WFE method holds smaller error than the FD method. However, the error at low frequencies in the WFE method increases as increasing the number of elements. This is a known numerical issue discussed by Mace [146]. However, at higher frequencies the error of WFE drops dramatically. Nevertheless, the drop in error at high frequencies is not monotonic. This type of error increase is a known issue in FEM and it is related to aliasing effects. The finer mesh (*N = 100*) has the minimum error at the high frequency.

FD method behaves in the same manner but has larger error than WFE. Figure 4-3 demonstrates the effect of time step for a fixed mesh size (*N =100*). The critical frequencies of WFE are clearly shown in WFE error plot in this case. The error of FD is not very sensitive to step times at high frequency.

In order to demonstrate the wave propagation in a tensioned, viscoelastic travelling beam, simulations are carried out by using direct time integration with the FEM as descripted in Chapter 3.

In this example, the two ends of the beam are assigned as free boundaries. An impulse is applied at $t = 0$ as follows,

$$w\left(\frac{L}{2},0\right) = A_0 e^{\left(B_0\left(X-\frac{L}{2}\right)^2\right)}\delta(t) \tag{4.33}$$

where A_0 is the amplitude, B_0 is the width of the impulse and $\delta(t)$ is the Kronecker delta. The initial tape deflection is zero. The parameters used in this simulation are $\bar{T} = 0.4070$, $\bar{V} = 7$, $\bar{\eta} = 2.12\times10^{-5}$, $A_0 = 10^{-4}$ and $B_0 = 10^4$ with 300 elements and $\Delta\tau = 2\times10^{-5}$. Note that a high value is chosen for the transport velocity $\bar{V}$ in order to accentuate its influence on wave propagation. On the other hand a low value of loss modulus $\bar{\eta}$ is chosen to present light damping.

Figure 4-4 shows the effects of $\bar{V}$ and $\bar{\eta}$. In case where these variables are zero the initial impulse separates into a left-propagating and a right-propagating, symmetric waves. The shorter wave lengths have higher speeds and travel ahead of the group. In case the beam has a transport velocity $\bar{V} = 7$ in the positive X direction of transport has larger amplitude. Adding a small amount of internal damping has a significant effect on damping the fast travelling short wavelengths.

4.4 Modal Analysis/ Eigenfunction Expansion

In all approximate solutions of dynamical systems including classical Galerkin, Rayleigh-Ritz, finite difference and finite element methods a finite number of eigenvectors are

involved in the solution. This results in deterioration of the frequencies predicted by the method. This is especially true for higher frequencies. Therefore, the goal of the second part of this study is to assess the effects of the FE discretization on the eigenvalue (and vector) predictions. To this end we employ two approaches. In the first case the equation of motion is spatially discretized and the classical eigenvalue problem is defined in state space. In the second case the equation of motion is fully discretized, and the eigenvalues are obtained by using the state space approach.

4.4.1 Semi-discrete form of eigenfuction expansion

Natural frequencies of the semi-discrete equation of motion, (4.11), can be obtained by eigenfunction expansion [125]. To this end Equation (4.11) is rewritten in state space form [23, 128],

$$\boldsymbol{A}\dot{\boldsymbol{U}} + \boldsymbol{B}\boldsymbol{U} = \boldsymbol{0} \tag{4.34}$$

The state vector $\boldsymbol{U}$ and matrices $\boldsymbol{A}$ and $\boldsymbol{B}$ are defined as follows,

$$\boldsymbol{U}(X,\tau) = \begin{Bmatrix} \dot{\boldsymbol{D}} \\ \boldsymbol{D} \end{Bmatrix} \quad \boldsymbol{A} = \begin{bmatrix} \boldsymbol{M} & \boldsymbol{0} \\ \boldsymbol{0} & \boldsymbol{K} \end{bmatrix} \quad \boldsymbol{B} = \begin{bmatrix} \boldsymbol{G} & \boldsymbol{K} \\ -\boldsymbol{K} & \boldsymbol{0} \end{bmatrix} \tag{4.35}$$

where $\boldsymbol{M}$, $\boldsymbol{G}$ and $\boldsymbol{K}$ matrices are given by Equation (4.12). The sizes of vector $\boldsymbol{U}$ and matrices $\boldsymbol{A}$, $\boldsymbol{B}$ are of dimension $4(M+1)$ and $4(M+1)\times 4(M+1)$. Meirovitch [127, 128] applied state-space form to discrete gyroscopic systems. D'Eleuterio and Hughes [147, 148] extended this method to gyroscopic continua with a distributed angular momentum. String and beam model with translating speed problems were studied by Wickert and Mote [23]. Tonoli, Zenerino and Amati [129] investigated the natural frequencies of travelling beam by FEM in state-space representation. The general solution of Equation (4.34) is of the form [23],

$$\boldsymbol{U}(X,\tau) = \sum \boldsymbol{\phi}_j(X) e^{\Omega\tau} \tag{4.36}$$

where, $\boldsymbol{\phi}_j$ is the mode shape vector, Ω_j is the dimensionless oscillation frequency, and Equation (4.36) leads to the eigenvalue problem,

$$\left(\Omega_j \boldsymbol{A} + \boldsymbol{B}\right)\boldsymbol{\phi}_j = \mathbf{0} \tag{4.37}$$

Note that both Ω_j and $\boldsymbol{\phi}_j$ can be complex valued. There are 2(*M+1*) pairs of complex conjugate eigenvalues Ω_j and eigenvectors $\boldsymbol{\phi}_j$. The eigenvalues can be expressed as, $\Omega_j = \zeta_j + i\omega_j$, where ζ_j and ω_j are real numbers representing damping and oscillation components of the vibration.

Figure 4-5 shows the numerical solution of the eigenvalues of a tensioned translating beam obtained by solving Equation (4.37) with 50 elements. For this case the boundaries are simple supported $\bar{T} = 10$ and $\bar{\eta} = 0$ representing the problem analyzed originally by Wickert and Mote [23]. The critical speed at which the first natural frequency vanishes is predicted by this approach $\bar{V}_c$ = 10.49. This is very close to 10.48 value reported in reference [23]. The same bifurcation behavior is observed at higher frequencies after the critical speed.

4.4.2 Fully-discrete form of eigenfuction expansion

The approach presented above deals only with the semi-discrete version of the equation of motion. However, the effect of time integration on the frequency domain in context of translating continua has not been studied. After boundary conditions are applied, Equation (4.16) can be solved for natural frequencies of the fully discretized system. First the dynamic stiffness matrix $\boldsymbol{\Upsilon}$ is separated into the following components that influence the motion at different time steps,

$$\boldsymbol{\Upsilon}_{\tau+\Delta\tau} = \left(\boldsymbol{M} + \gamma\Delta\tau\boldsymbol{G} + \beta\Delta\tau^2\boldsymbol{K}\right) \tag{a}$$

$$\boldsymbol{\Upsilon}_{\tau} = \left(-2\boldsymbol{M} + \left(1-2\gamma\right)\Delta\tau\boldsymbol{G} + \left(\frac{1}{2}+\gamma-2\beta\right)\Delta\tau^2\boldsymbol{K}\right) \tag{b}$$

$$\boldsymbol{\Upsilon}_{\tau-\Delta\tau} = \left(\boldsymbol{M} + \left(\gamma-1\right)\Delta\tau\boldsymbol{G} + \left(\frac{1}{2}-\gamma+\beta\right)\Delta\tau^2\boldsymbol{K}\right) \tag{c}$$

Then Equation (4.16) can be rewritten in a more compact form as follows,

$$\left(\boldsymbol{\Upsilon}_{\tau+\Delta\tau} e^{i\Omega\Delta\tau} + \boldsymbol{\Upsilon}_{\tau} + \boldsymbol{\Upsilon}_{\tau-\Delta\tau} \frac{1}{e^{i\Omega\Delta\tau}} \right) \hat{\boldsymbol{w}} = \boldsymbol{0} \tag{4.39}$$

Equation (4.39) is another eigenvalue problem but it would cause ill-conditioning in numerical computation if solved directly. Zhong and William [149] investigated a similar problem to look for wave constants for repetitive structure and they expressed the equation in state-space representation,

$$\begin{bmatrix} \boldsymbol{\Upsilon}_{\tau-\Delta\tau} & -\boldsymbol{\Upsilon}_{\tau} \\ 0 & -\boldsymbol{\Upsilon}_{\tau-\Delta\tau} \end{bmatrix} \begin{Bmatrix} \hat{\boldsymbol{w}} \\ \tilde{\boldsymbol{w}} \end{Bmatrix} = e^{i\Omega\Delta\tau} \begin{bmatrix} 0 & \boldsymbol{\Upsilon}_{\tau+\Delta\tau} \\ -\boldsymbol{\Upsilon}_{\tau-\Delta\tau} & 0 \end{bmatrix} \begin{Bmatrix} \hat{\boldsymbol{w}} \\ \tilde{\boldsymbol{w}} \end{Bmatrix} \tag{4.40}$$

where $\tilde{\boldsymbol{w}} = e^{i\Omega\Delta\tau} \hat{\boldsymbol{w}}$. Unlike Equation (4.37), the submatrices in Equation (4.40) are all skew-symmetric. The natural frequencies can be obtained as the eigenvalues of Equation (4.40).

The first ten natural frequencies of magnetic tape are calculated by using the approach defined by Equation (4.37) and Equation (4.40) by using the values in Table 4-1 without internal damping. A convergence study is presented in Table 4-2 for N = 20, 50, 100, 150. Results produced by semi- and full-discretization methods are close to each other. They both demonstrate the asymptotic behavior of the numerical method. The eigenvalues are pure imaginary [128]. The plus and minus signs are due to the accuracy of the numerical solver. Both methods appear to converge to the second digit up to 9th critical frequency for $N \geq 50$.

Table 4-3 and Table 4-4 list the first ten natural frequencies of viscoelastic tape for different mesh scheme and time-steps. The positive real parts of the eigenvalues (natural frequencies) indicate energy dissipation. The higher modes (greater than the 2nd) are overdamped due to the internal damping. Equation (4.40) has better convergence characteristics than Equation (4.37) in terms of different mesh scheme shown in Table 4-3. Full-discretization method converges with a very coarse time step, $\Delta\tau$ = 1×10^{-4} as shown in Table 4-4.

The effects of damping on the first three mode shapes are shown in Figure 4-6. The mode shapes were found by using the approaches described by Equations (4.37) and (4.40).

Because the translating velocity is small compared to the tension applied, the first 3 modes without internal damping have the real components of ϕ close to zero as shown in Figure 4-6a. On the other hand, The third mode shape in Figure 4-6b is heavily distorted due to the internal damping. The nonzero imaginary component represents the phase shift of the mode from its undistorted shape. This figure also shows that the solutions to Equation (4.40) are comparable to the semi-discretization results.

The first ten natural frequencies for the LTM and out-of-plane tape vibrations are investigated in dimensional space with the parameters of the magnetic tape system, given in Table 4-1. The investigated effects include the length of the tape, as indicated by *roller-to-roller* (4 cm) and *reel-to-reel* (24 cm) spans. The boundaries are simulated as simple support. Both semi- discretization (4.37) and full-discretization (4.40) methods are used in analysis, and the results are listed in Table 4-6 – 4-13 for parameters in Table 4-1. In order to organize these results, the results are presented for the short and long tape segments separately, as follows.

Short tape length:

The first ten critical frequencies of the LTM for the 4 cm tape span are presented in Table 4-6 and Table 4-7. These table show that using $\Delta t = 10^{-7}$ s and $N = 150$ gives reasonably converged results for both the classical modal analysis and temporally discretized analysis techniques presented by Equations (4.37) and (4.40), respectively. For LTM vibrations of this short tape span, the natural frequencies are dominated by the real component, indicating that the LTM of third mode and higher are overdamped.

The first ten critical frequencies of the out-of-plane tape vibrations for the 4 cm span length are presented in Table 4-8 and Table 4-9. In general, the convergence characteristics of the temporally discretized eigenvalue extraction technique are better than the modal analysis method, which converges to slightly lower values at high frequencies. Nevertheless, $\Delta t = 10^{-7}$ s and $N = 50$ gives reasonably converged results for both. It is interesting to note that the out-of-plane vibrations are not overdamped and are dominated by the oscillation frequency.

Long tape length:

The first ten critical frequencies of the LTM for the 24 cm span length are presented in Table 4-10 and Table 4-11. It is seen that for this longer span, while the damping is high the vibration frequencies are not overdamped. For both eigenvalue extraction methods N = 50 gives well converged results, and for the fully discretized method the results appear converged at $\Delta t = 10^{-7}$ s. The natural frequency of (LTM) vibration of the longer tape span is 224.3 Hz. This value is considerably smaller than the natural frequency (LTM) of the shorter span, which can be found in Table 4-6 or Table 4-7 as 6413.2 Hz.

Finally, the first ten critical frequencies of the out-of-plane vibrations for the 24 cm span are presented in Table 4-12 and Table 4-13. These tables show that damping effect is minimal. The fully discretized eigenvalue extraction technique converges for $\Delta t = 10^{-7}$ s and N = 50. Interestingly, the modal analysis technique is showing signs of convergence difficulties. Comparing the natural frequencies of the out-of-plane vibrations for the short and long spans, we see ω_1 = 817.99 Hz for the short span, whereas, ω_1 = 136.3 Hz for the long span as reported in Table 4-9 and Table 4-13, respectively.

In summary, we see that both eigenvalue extraction techniques work quit well in the nondimensional space. In dimensional analysis, we see that the classical modal analysis based method could have some convergence difficulties, but overall both techniques give very good results. Convergence of the solutions up tot 10^{th} eigenvalue can be obtained by using at least 50 elements. In dimensional analysis, we also note that the tape stiffness as elucidated by tape length plays a significant role in internal damping. Shorter tape span shows significantly higher damping than the longer tape span. Finally, the out-of-plane tape vibration frequencies were found to be in the 800 − 8,000 Hz range for the short tape span and 136 − 1,360 Hz range for the longer tape span. These values are in the range of interest for the LTM analysis. Therefor analysis of the coupling between LTM and out-of-plane tape vibrations would be recommended for future studies.

4.5 Summary and Conclusions

In this chapter the effects of the numerical solution of the equation of motion of a translating tensioned, viscoelastic beam are analyzed. This work has two components. The first one demonstrated the effects of spatial and temporal discretization on the wave

propagation characteristics in this beam. The second study introduces and compares two methods to extract eigenvalues of the translating beam system. In both cases the equation of motion is nondimensionalized and it is shown that the system dynamics is governed by the nondimensional tension, velocity and loss modulus. Later in the chapter the eigenvalue analysis is provided for the case of tape system in the dimensional space.

The wave propagation characteristics of the translating beam are probed by using FE and FD discretization in the space and Newmarks's method in time domains. The WFE method was used to obtain the dispersion relation for the FE method. Comparison of the dispersion relations of the numerically obtained solutions to the analytical dispersion relation showed that, very reasonable match can be obtained by using as few as 20 elements. By reducing the time step or increasing the element numbers the accuracy of these two methods can be improved. The error is less thatn 1% even at the high frequency. Nevertheless, the analysis with WFE method is in general more accurate than FD method, which may have implications on the accuracy of the over solution.

Both eigenvalue extraction techniques work quite well in the nondimensional space. In dimensional analysis, we see that the classical modal analysis based method could have some convergence difficulties, but overall both techniques give very good results. Convergence of the solutions up to 10^{th} eigenvalue can be obtained by using at least 50 elements. In dimensional analysis, we also note that the tape stiffness, as elucidated by tape length, plays a significant role in internal damping. Shorter tape span shows significantly higher damping, that the longer tape span. Finally, the out-of-plane tape vibration frequencies were found to be in the $800 - 8{,}000$ Hz range for the short tape span and $136 - 1{,}360$ Hz range for the longer tape span. These values are in the range of interest for the LTM analysis. Therefor analysis of the coupling between LTM and out-of-plane tape vibrations would be recommended for future studies.

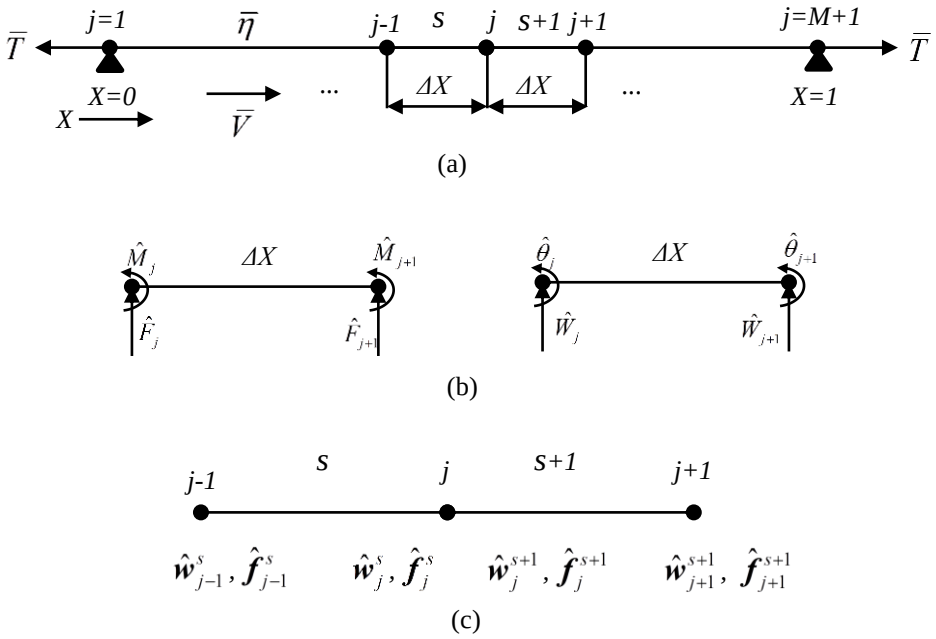

Figure 4-1 Schematic plot of a wave guide structure

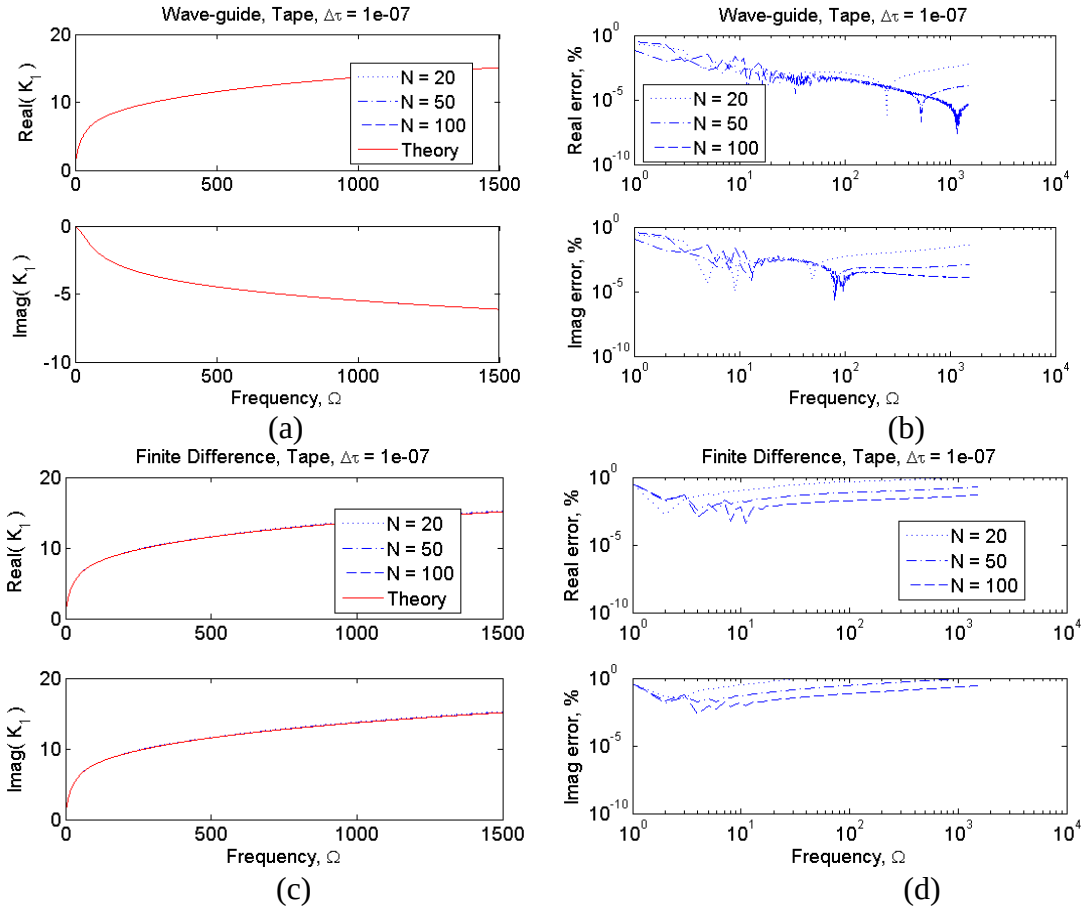

Figure 4-2 Mesh scheme accuracy study for dispersion curve of the real component of k_1 for WFE (a) and FD (b), and error plots for WFE (b) and FD (d)

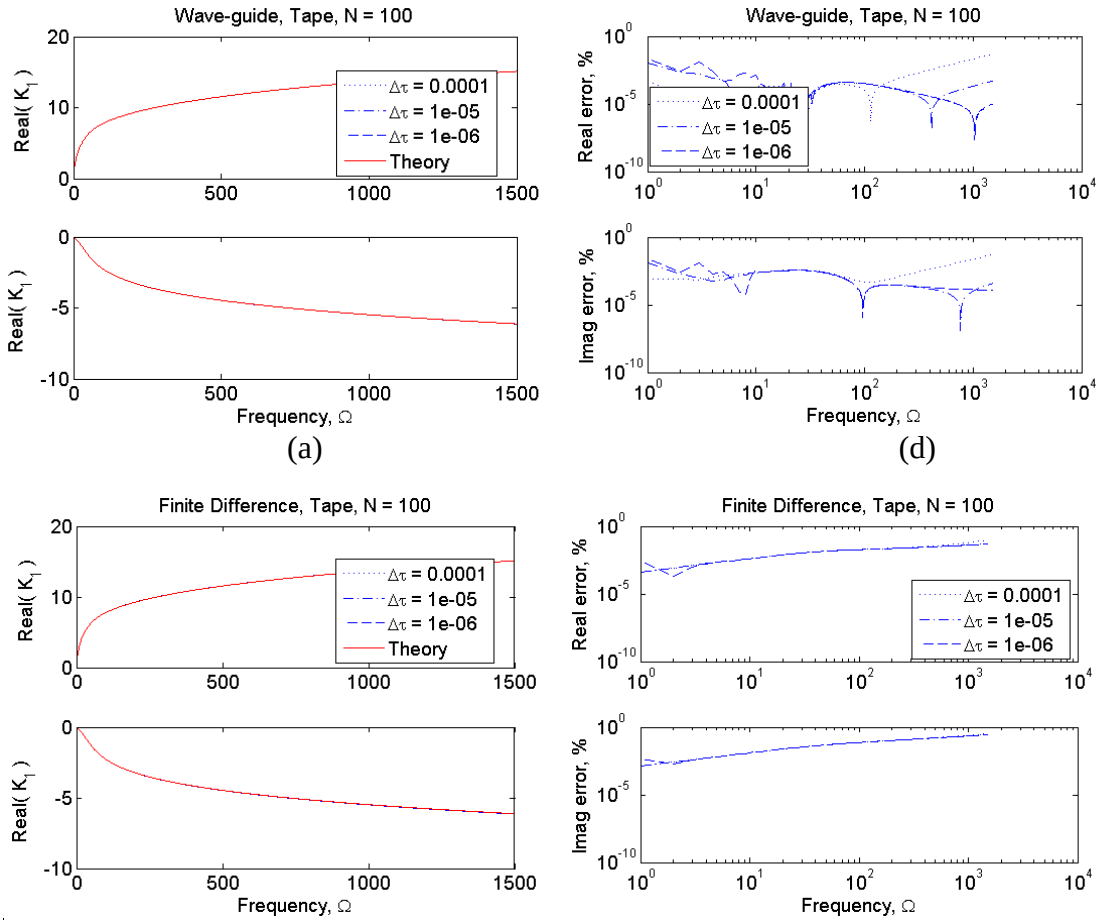

Figure 4-3 Time step accuracy study for dispersion curve of the real component of k_1 for WFE (a) and FD (b), and error plots for WFE (b) and FD (d)

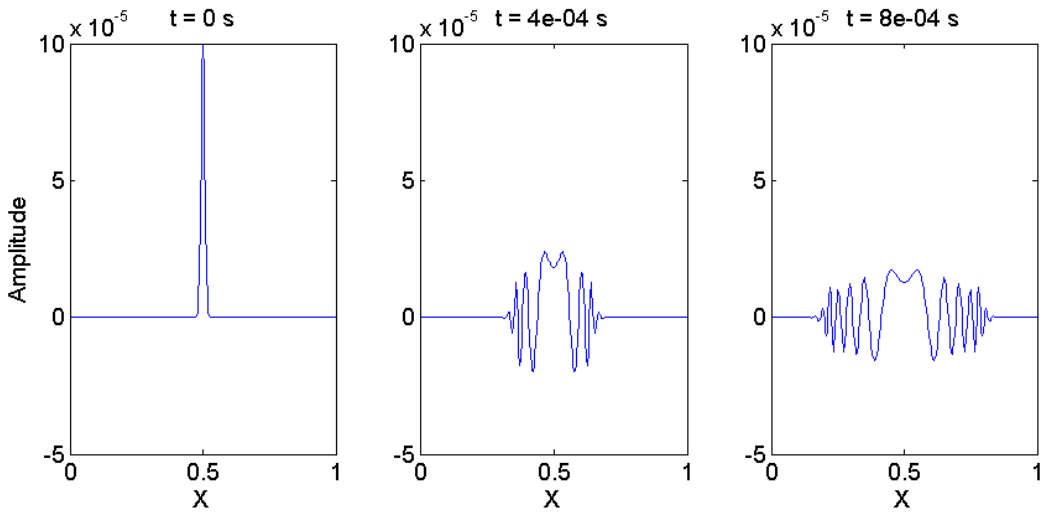

(a) $\bar{T} = 0.4070$, $\bar{V} = 0$, $\bar{\eta} = 0$

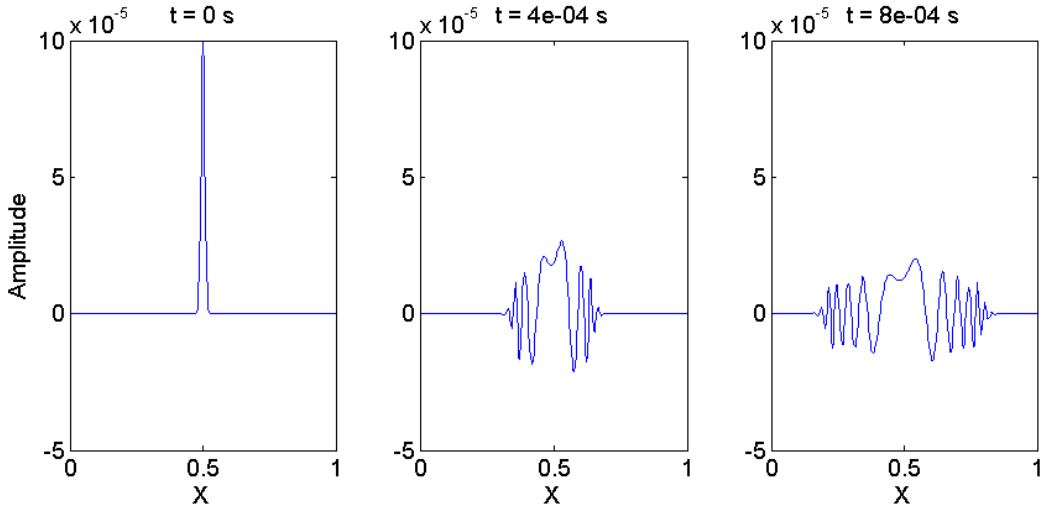

(b) $\bar{T} = 0.4070$, $\bar{V} = 7.0$, $\bar{\eta} = 0$

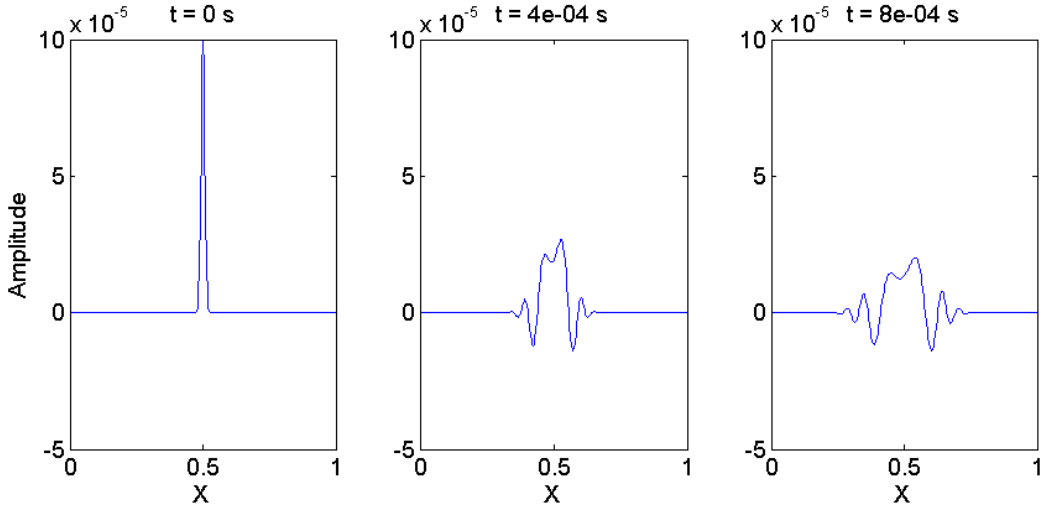

(c) $\bar{T} = 0.4070$, $\bar{V} = 7.0$, $\bar{\eta} = 2.12\times10^{-5}$

Figure 4-4 wave propagation example

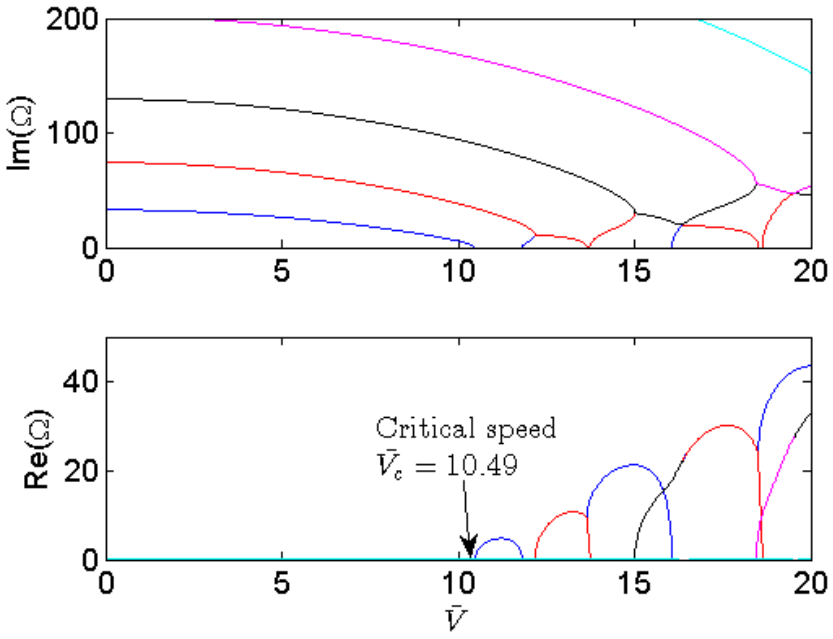

Figure 4-5 Frequency spectrum (first five) of a simple supported translating elastic beam with $\bar{T} = 10$, $\bar{\eta} = 0$.

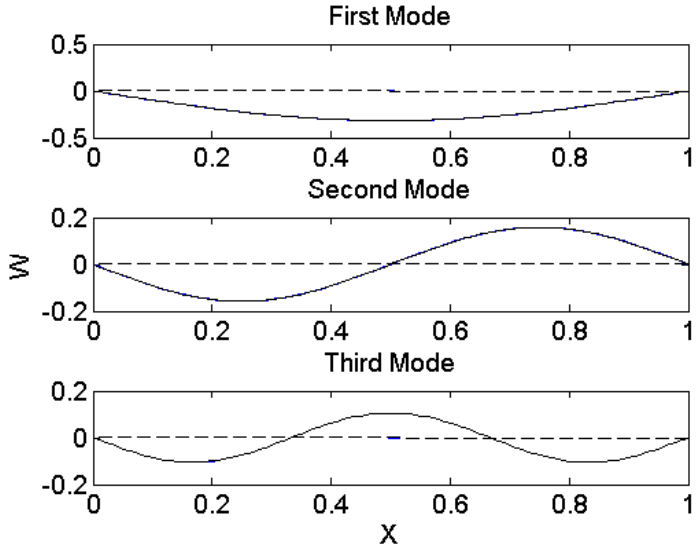

(a)

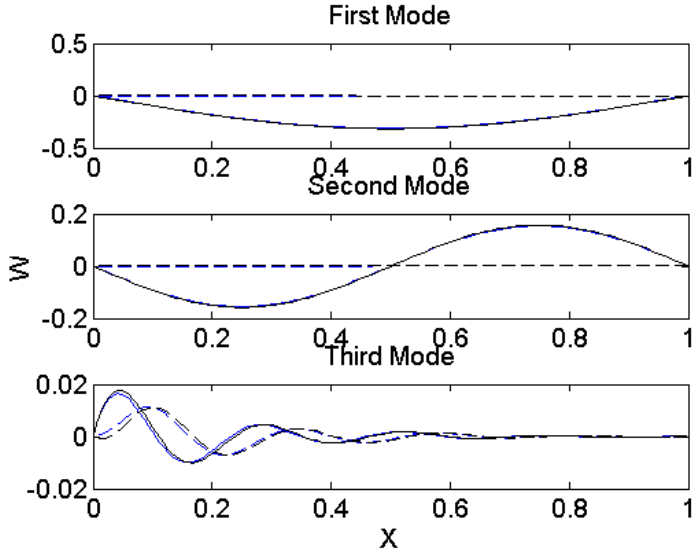

(b)

Figure 4-6 First 3 mode shapes of magnetic recording tape ($\bar{T} = 0.4070$, $\bar{V} = 0.0461$) for semi-discretization (blue) and full-discretization (black). Dash line: imaginary part, Solid line: real part. *N = 150*, *Δτ = 1e-7*. (a) $\bar{\eta} = 0$, (b) $\bar{\eta} = 0.0212$

Table 4-1 Typical values for tape, web and bandsaw systems

Dimensional Variables	**Tape (LTO-5)**	**Web[150]**	**Bandsaw [151]**
Tension, T (N)	0.5	12.25	2.5×10^{4}
Length, L (m)	4.0×10^{-2}	1.0	1.0
Thickness, h (m)	6.4×10^{-6}	0.27×10^{-3}	1.0×10^{-3}
Width, b (m)	12.7×10^{-3}	0.7	0.25
Speed, V_x (m/s)	7.5	2	50
Elastic modulus, E (GPa)	4.42	4.14	200
Loss modulus, η (Nm/s^2)	23000	—	—
Density, ρ (kg/m^3)	1400	1108	7800
Material (substrate)	PET	PE coated paper	Steel
Dimensionless Variables ($t_c=\sqrt{\left(\rho L^4\right)/\left(EI\right)}$, $A=bh$, $I=\left(b^3h\right)/12$)			
$\bar{T}=\sqrt{\left(Tt_c^{\,2}\right)/\left(\rho AL^2\right)}$	0.4070	0.0195	0.3098
$\bar{V}=V_xt_c/L$	0.0461	0.0051	0.1368
$\bar{\eta}=\left(\eta It_c\right)/\left(\rho AL^4\right)$	0.0212	0	0
$\bar{V}_c$ (critical speed)	3.1568	3.1432	3.1591

Table 4-2 First ten critical frequencies of magnetic recording tape ($\bar{T} = 0.4070$, $\bar{V} = 0.0461, \bar{\eta} = 0$) for different mesh schemes obtained by semi- and full- discretization with $\Delta\tau = 1\times10^{-6}$

Semi-discretization (Equation (4.37) , $\Delta\tau = 1\times10^{-6}$)				
	N = 20	**N = 50**	**N = 100**	**N = 150**
Ω_1	0.000 + 9.951i	-0.000 + 9.952i	0.000 + 9.948i	-0.000 + 9.957i
Ω_2	-0.000 + 39.560i	0.000 + 39.558i	-0.000 + 39.565i	0.000 + 39.563i
Ω_3	0.000 + 88.910i	-0.000 + 88.909i	0.000 + 88.906i	-0.000 + 88.913i
Ω_4	-0.000 + 158.012i	0.000 + 157.991i	0.000 + 157.990i	0.000 + 157.992i
Ω_5	-0.000 + 246.887i	-0.000 + 246.825i	0.000 + 246.821i	-0.000 + 246.821i
Ω_6	-0.000 + 355.579i	-0.000 + 355.392i	-0.000 + 355.391i	0.000 + 355.382i
Ω_7	0.000 + 484.163i	0.000 + 483.695i	-0.000 + 483.695i	-0.000 + 483.695i
Ω_8	-0.000 + 632.789i	-0.000 + 631.769i	0.000 + 631.738i	0.000 + 631.732i
Ω_9	0.000 + 801.612i	-0.000 + 799.578i	0.000 + 799.521i	-0.000 + 799.520i
Ω_{10}	-0.000 + 990.939i	-0.000 + 987.156i	-0.000 + 987.050i	-0.000 + 987.043i
Full-discretization (Equation (4.40), $\Delta\tau = 1\times10^{-6}$)				
Ω_1	0.000 + 9.951i	0.000 + 9.951i	0.000 + 9.951i	-0.000 + 9.951i
Ω_2	0.000 + 39.561i	-0.000 + 39.560i	-0.000 + 39.560i	0.000 + 39.560i
Ω_3	-0.000 + 88.912i	0.000 + 88.909i	0.000 + 88.908i	-0.000 + 88.908i
Ω_4	0.000 + 158.013i	-0.000 + 157.996i	-0.000 + 157.996i	-0.000 + 157.994i
Ω_5	-0.000 + 246.886i	0.000 + 246.824i	0.000 + 246.822i	0.000 + 246.817i
Ω_6	-0.000 + 355.578i	0.000 + 355.393i	0.000 + 355.387i	-0.000 + 355.408i
Ω_7	-0.000 + 484.167i	-0.000 + 483.705i	-0.000 + 483.695i	0.000 + 483.691i
Ω_8	0.000 + 632.783i	0.000 + 631.765i	0.000 + 631.738i	0.000 + 631.733i
Ω_9	-0.000 + 801.617i	-0.000 + 799.576i	-0.000 + 799.528i	-0.000 + 799.528i
Ω_{10}	0.000 + 990.938i	0.000 + 987.148i	0.000 + 987.040i	0.001 + 986.981i

Table 4-3 First ten critical frequencies of magnetic recording tape ($\bar{T} = 0.4070$, $\bar{V} = 0.0461, \bar{\eta} = 0$) for different mesh schemes obtained by semi- and full- discretization with $\Delta\tau = 1\times10^{-7}$.

Semi-discretization (Equation (4.37))				
	N = 20	**N = 50**	**N = 100**	**N = 150**
Ω_1	1.032 + 9.898i	1.032 + 9.889i	1.032 + 9.898i	1.032 + 9.866i
Ω_2	16.511 + 35.951i	16.511 + 35.951i	16.511 + 35.950i	16.510 + 35.976i
Ω_3	47.023 + 0.360i	47.008 + 0.373i	47.007 + 0.376i	47.004 + 0.380i
Ω_4	47.025 + 0.432i	47.012 + 0.442i	47.011 + 0.444i	47.008 + 0.307i
Ω_5	47.033 + 0.289i	47.015 + 0.306i	47.013 + 0.309i	47.011 + 0.448i
Ω_6	47.035 + 0.488i	47.022 + 0.498i	47.020 + 0.497i	47.020 + 0.495i
Ω_7	47.049 + 0.229i	47.028 + 0.249i	47.025 + 0.252i	47.022 + 0.249i
Ω_8	47.070 + 0.179i	47.044 + 0.202i	47.041 + 0.206i	47.040 + 0.203i
Ω_9	47.093 + 0.138i	47.061 + 0.168i	47.057 + 0.171i	47.056 + 0.169i
Ω_{10}	47.117 + 0.101i	47.076 + 0.139i	47.072 + 0.145i	47.075 + 0.143i
Full-discretization (Equation (4.40), $\Delta\tau = 1\times10^{-6}$)				
Ω_1	1.032 + 9.897i	1.032 + 9.897i	1.032 + 9.897i	1.032 + 9.897i
Ω_2	16.511 + 35.951i	16.511 + 35.951i	16.511 + 35.951i	16.511 + 35.951i
Ω_3	47.023 + 0.360i	47.008 + 0.373i	47.006 + 0.375i	47.005 + 0.375i
Ω_4	47.025 + 0.432i	47.011 + 0.443i	47.009 + 0.444i	47.009 + 0.444i
Ω_5	47.033 + 0.289i	47.015 + 0.305i	47.012 + 0.307i	47.012 + 0.308i
Ω_6	47.035 + 0.488i	47.022 + 0.497i	47.020 + 0.499i	47.019 + 0.499i
Ω_7	47.049 + 0.229i	47.028 + 0.248i	47.026 + 0.250i	47.025 + 0.251i
Ω_8	47.070 + 0.179i	47.045 + 0.202i	47.042 + 0.205i	47.041 + 0.205i
Ω_9	47.093 + 0.138i	47.062 + 0.167i	47.058 + 0.170i	47.058 + 0.171i
Ω_{10}	47.117 + 0.102i	47.077 + 0.140i	47.073 + 0.143i	47.072 + 0.144i

Table 4-4 First ten critical frequencies of magnetic recording tape ($\bar{T} = 0.4070$, $\bar{V} = 0.0461, \bar{\eta} = 0.0212$) for different time-steps obtained by full- discretization with *N=100*

Full-discretization (Equation (4.40), *N=100*)				
	$\Delta\tau = 1\times10^{-4}$	**$\Delta\tau = 1\times10^{-5}$**	**$\Delta\tau = 1\times10^{-6}$**	**$\Delta\tau = 1\times10^{-7}$**
Ω_1	1.032 + 9.897i	1.032 + 9.897i	1.032 + 9.897i	1.032 + 9.897i
Ω_2	16.511 + 35.951i	16.511 + 35.951i	16.511 + 35.951i	16.511 + 35.951i
Ω_3	47.005 + 0.375i	47.005 + 0.375i	47.005 + 0.375i	47.005 + 0.375i
Ω_4	47.009 + 0.444i	47.009 + 0.444i	47.009 + 0.444i	47.009 + 0.444i
Ω_5	47.012 + 0.308i	47.012 + 0.308i	47.012 + 0.308i	47.012 + 0.308i
Ω_6	47.019 + 0.499i	47.019 + 0.499i	47.019 + 0.499i	47.019 + 0.499i
Ω_7	47.025 + 0.251i	47.025 + 0.251i	47.025 + 0.251i	47.025 + 0.251i
Ω_8	47.041 + 0.205i	47.041 + 0.205i	47.041 + 0.205i	47.041 + 0.205i
Ω_9	47.058 + 0.171i	47.058 + 0.171i	47.058 + 0.171i	47.058 + 0.171i
Ω_{10}	47.072 + 0.144i	47.072 + 0.144i	47.072 + 0.144i	47.072 + 0.144i

Table 4-5 First ten critical frequencies of magnetic recording tape ($\bar{T} = 0.4070$, $\bar{V} = 0.0461, \bar{\eta} = 0.0212$) for different mesh schemes obtained by semi- and full-discretization with $\Delta\tau = 1\times10^{-7}$.

Semi-discretization (Equation (4.37))				
	N = 20	**N = 50**	**N = 100**	**N = 150**
Ω_1	0.000 + 9.951i	-0.000 + 9.952i	0.000 + 9.948i	-0.000 + 9.957i
Ω_2	-0.000 + 39.560i	0.000 + 39.558i	-0.000 + 39.565i	0.000 + 39.563i
Ω_3	0.000 + 88.910i	-0.000 + 88.909i	0.000 + 88.906i	-0.000 + 88.913i
Ω_4	-0.000 + 158.012i	0.000 + 157.991i	0.000 + 157.990i	0.000 + 157.992i
Ω_5	-0.000 + 246.887i	-0.000 + 246.825i	0.000 + 246.821i	-0.000 + 246.821i
Ω_6	-0.000 + 355.579i	-0.000 + 355.392i	-0.000 + 355.391i	0.000 + 355.382i
Ω_7	0.000 + 484.163i	0.000 + 483.695i	-0.000 + 483.695i	-0.000 + 483.695i
Ω_8	-0.000 + 632.789i	-0.000 + 631.769i	0.000 + 631.738i	0.000 + 631.732i
Ω_9	0.000 + 801.612i	-0.000 + 799.578i	0.000 + 799.521i	-0.000 + 799.520i
Ω_{10}	-0.000 + 990.939i	-0.000 + 987.156i	-0.000 + 987.050i	-0.000 + 987.043i
Full-discretization (Equation (4.40), $\Delta\tau = 1\times10^{-7}$)				
Ω_1	0.000 + 9.951i	0.000 + 9.951i	0.000 + 9.951i	-0.000 + 9.951i
Ω_2	0.000 + 39.561i	-0.000 + 39.560i	-0.000 + 39.560i	0.000 + 39.560i
Ω_3	-0.000 + 88.912i	0.000 + 88.909i	0.000 + 88.908i	-0.000 + 88.908i
Ω_4	0.000 + 158.013i	-0.000 + 157.996i	-0.000 + 157.996i	-0.000 + 157.994i
Ω_5	-0.000 + 246.886i	0.000 + 246.824i	0.000 + 246.822i	0.000 + 246.817i
Ω_6	-0.000 + 355.578i	0.000 + 355.393i	0.000 + 355.387i	-0.000 + 355.408i
Ω_7	-0.000 + 484.167i	-0.000 + 483.705i	-0.000 + 483.695i	0.000 + 483.691i
Ω_8	0.000 + 632.783i	0.000 + 631.765i	0.000 + 631.738i	0.000 + 631.733i
Ω_9	-0.000 + 801.617i	-0.000 + 799.576i	-0.000 + 799.528i	-0.000 + 799.528i
Ω_{10}	0.000 + 990.938i	0.000 + 987.148i	0.000 + 987.040i	0.001 + 986.981i

Table 4-6 First ten critical LTM frequencies of magnetic recording tape (Table 4-1) in roller-to-roller span (4 cm) for different time-steps obtained by full- discretization with *N=150*.

Full-discretization (Equation (4.40), *N=150*)				
	$\Delta t = 1\times10^{-5}$ s	$\Delta t = 1\times10^{-6}$ s	$\Delta t = 1\times10^{-7}$ s	$\Delta t = 1\times10^{-8}$ s
ω_1	$6.4272\times10^{2}+6.3311\times10^{3}i$	$6.6846\times10^{2}+6.4123\times10^{3}i$	$6.6873\times10^{2}+6.4132\times10^{3}i$	$6.6873\times10^{2}+6.4132\times10^{3}i$
ω_2	$6.8900\times10^{3}+2.1249\times10^{4}i$	$1.0645\times10^{4}+2.3280\times10^{4}i$	$1.0698\times10^{4}+2.3295\times10^{4}i$	$1.0699\times10^{4}+2.3296\times10^{4}i$
ω_3	$1.7301\times10^{4}+ 4.2090\times10^{4}i$	$3.0552\times10^{4}+2.4518\times10^{2}i$	$3.0459\times10^{4}+2.4295\times10^{2}i$	$3.0458\times10^{4}+2.4293\times10^{2}i$
ω_4	$6.0392\times10^{4}+ 3.7872\times10^{3}i$	$3.0554\times10^{4}+2.9056\times10^{2}i$	$3.0461\times10^{4}+2.8793\times10^{2}i$	$3.0461\times10^{4}+2.8790\times10^{2}i$
ω_5	$6.0401\times10^{4}+ 3.3691\times10^{3}i$	$3.0556\times10^{4}+2.0115\times10^{2}i$	$3.0464\times10^{4}+1.9933\times10^{2}i$	$3.0463\times10^{4}+1.9931\times10^{2}i$
ω_6	$6.0472\times10^{4}+ 2.8498\times10^{3}i$	$3.0561\times10^{4}+3.2623\times10^{2}i$	$3.0468\times10^{4}+3.2327\times10^{2}i$	$3.0467\times10^{4}+3.2324\times10^{2}i$
ω_7	$6.0601\times10^{4}+ 2.3528\times10^{3}i$	$3.0565\times10^{4}+1.6386\times10^{2}i$	$3.0472\times10^{4}+1.6237\times10^{2}i$	$3.0471\times10^{4}+1.3308\times10^{2}i$
ω_8	$6.0759\times10^{4}+ 1.9329\times10^{3}i$	$3.0575\times10^{4}+1.3431\times10^{2}i$	$3.0483\times10^{4}+1.3309\times10^{2}i$	$3.0482\times10^{4}+1.3308\times10^{2}i$
ω_9	$6.0921\times10^{4}+ 1.5987\times10^{3}i$	$3.0586\times10^{4}+1.1158\times10^{2}i$	$3.0493\times10^{4}+1.1057\times10^{2}i$	$3.0492\times10^{4}+1.1056\times10^{2}i$
ω_{10}	$6.1070\times10^{4}+ 1.3396\times10^{3}i$	$3.0596\times10^{4}+9.4236\times10^{1}i$	$3.0503\times10^{4}+9.3379\times10^{1}i$	$3.0502\times10^{4}+9.3374\times10^{1}i$

Table 4-7 First ten critical LTM frequencies of magnetic recording tape (Table 4-1) in roller-to-roller span (4 cm) for different mesh schemes obtained by semi- and full-discretization with $\Delta t = 1\times10^{-7}$.

Semi-discretization (Equation (4.37))				
	N = 20	**N = 50**	**N = 100**	**N = 150**
ω_1	$6.6873\times10^{2} + 6.4132\times10^{3}i$	$6.6873\times10^{2} + 6.4132\times10^{3}i$	$6.6873\times10^{2} + 6.4132\times10^{3}i$	$6.6873\times10^{2} + 6.4132\times10^{3}i$
ω_2	$1.0699\times10^{4} + 2.3296\times10^{4}i$	$1.0699\times10^{4} + 2.3296\times10^{4}i$	$1.0699\times10^{4} + 2.3296\times10^{4}i$	$1.0699\times10^{4} + 2.3296\times10^{4}i$
ω_3	$3.0470\times10^{4} + 2.3333\times10^{2}i$	$3.0460\times10^{4} + 2.4156\times10^{2}i$	$3.0459\times10^{4} + 2.4272\times10^{2}i$	$3.0458\times10^{4} + 2.4293\times10^{2}i$
ω_4	$3.0471\times10^{4} + 2.7999\times10^{2}i$	$3.0462\times10^{4} + 2.8676\times10^{2}i$	$3.0461\times10^{4} + 2.8772\times10^{2}i$	$3.0461\times10^{4} + 2.8790\times10^{2}i$
ω_5	$3.0476\times10^{4} + 1.8757\times10^{2}i$	$3.0464\times10^{4} + 1.9766\times10^{2}i$	$3.0463\times10^{4} + 1.9905\times10^{2}i$	$3.0463\times10^{4} + 1.9931\times10^{2}i$
ω_6	$3.0478\times10^{4} + 3.1641\times10^{2}i$	$3.0469\times10^{4} + 3.2225\times10^{2}i$	$3.0468\times10^{4} + 3.2308\times10^{2}i$	$3.0467\times10^{4} + 3.2324\times10^{2}i$
ω_7	$3.0487\times10^{4} + 1.4807\times10^{2}i$	$3.0473\times10^{4} + 1.6041\times10^{2}i$	$3.0472\times10^{4} + 1.6205\times10^{2}i$	$3.0471\times10^{4} + 1.6236\times10^{2}i$
ω_8	$3.0501\times10^{4} + 1.1573\times10^{2}i$	$3.0484\times10^{4} + 1.3082\times10^{2}i$	$3.0482\times10^{4} + 1.3273\times10^{2}i$	$3.0482\times10^{4} + 1.3308\times10^{2}i$
ω_9	$3.0515\times10^{4} + 8.9191\times10^{1}i$	$3.0495\times10^{4} + 1.0800\times10^{2}i$	$3.0493\times10^{4} + 1.1016\times10^{2}i$	$3.0492\times10^{4} + 1.1056\times10^{2}i$
ω_{10}	$3.0531\times10^{4} + 6.5957\times10^{1}i$	$3.0505\times10^{4} + 9.0504\times10^{1}i$	$3.0502\times10^{4} + 9.2930\times10^{1}i$	$3.0502\times10^{4} + 9.3371\times10^{1}i$
Full-discretization (Equation (4.40), $\Delta t = 1\times10^{-7}$ s)				
ω_1	$6.6873\times10^{2} + 6.4132\times10^{3}i$	$6.6873\times10^{2} + 6.4132\times10^{3}i$	$6.6873\times10^{2} + 6.4132\times10^{3}i$	$6.6873\times10^{2} + 6.4132\times10^{2}i$
ω_2	$1.0698\times10^{4} + 2.3296\times10^{4}i$	$1.0698\times10^{4} + 2.3295\times10^{4}i$	$1.0698\times10^{4} + 2.3295\times10^{4}i$	$1.0698\times10^{4} + 2.3295\times10^{4}i$
ω_3	$3.0471\times10^{4} + 2.3336\times10^{2}i$	$3.0461\times10^{4} + 2.4159\times10^{2}i$	$3.0459\times10^{4} + 2.4274\times10^{2}i$	$3.0459\times10^{4} + 2.4295\times10^{2}i$
ω_4	$3.0472\times10^{4} + 2.8001\times10^{2}i$	$3.0463\times10^{4} + 2.8679\times10^{2}i$	$3.0462\times10^{4} + 2.8775\times10^{2}i$	$3.0461\times10^{4} + 2.8793\times10^{2}i$
ω_5	$3.0477\times10^{4} + 1.8758\times10^{2}i$	$3.0465\times10^{4} + 1.9768\times10^{2}i$	$3.0464\times10^{4} + 1.9907\times10^{2}i$	$3.0464\times10^{4} + 1.9933\times10^{2}i$
ω_6	$3.0479\times10^{4} + 3.1644\times10^{2}i$	$3.0470\times10^{4} + 3.2228\times10^{2}i$	$3.0469\times10^{4} + 3.2311\times10^{2}i$	$3.0468\times10^{4} + 3.2327\times10^{2}i$
ω_7	$3.0488\times10^{4} + 1.4808\times10^{2}i$	$3.0474\times10^{4} + 1.6042\times10^{2}i$	$3.0473\times10^{4} + 1.6207\times10^{2}i$	$3.0472\times10^{4} + 1.6237\times10^{2}i$
ω_8	$3.0501\times10^{4} + 1.1574\times10^{2}i$	$3.0485\times10^{4} + 1.3083\times10^{2}i$	$3.0483\times10^{4} + 1.3274\times10^{2}i$	$3.0483\times10^{4} + 1.3309\times10^{2}i$
ω_9	$3.0516\times10^{4} + 8.9199\times10^{1}i$	$3.0496\times10^{4} + 1.0801\times10^{2}i$	$3.0494\times10^{4} + 1.1017\times10^{2}i$	$3.0493\times10^{4} + 1.1057\times10^{2}i$
ω_{10}	$3.0532\times10^{4} + 6.5963\times10^{1}i$	$3.0506\times10^{4} + 9.0513\times10^{1}i$	$3.0503\times10^{4} + 9.2939\times10^{1}i$	$3.0503\times10^{4} + 9.3379\times10^{1}i$

Table 4-8 First ten critical out-of-planl frequencies of magnetic recording tape (Table 4-1) in roller-to-roller span (4 cm) for different time-steps obtained by full- discretization with *N=150*.

Full-discretization (Equation (4.40), *N=150*)				
	$\Delta t = 1\times10^{-4}$ s	**$\Delta t = 1\times10^{-5}$** s	**$\Delta t = 1\times10^{-6}$** s	**$\Delta t = 1\times10^{-7}$** s
ω_1	1.7968e-04 + 8.0066×10^{2}i	$1.9142\times10^{-4} + 8.1781\times10^{2}$i	$1.9154\times10^{-4} + 8.1799\times10^{2}$i	$1.9126\times10^{-4} + 8.1799\times10^{2}$i
ω_2	2.4242e-03 + 1.5112×10^{3}i	$3.0566\times10^{-3} + 1.6346\times10^{3}$i	$3.0646\times10^{-3} + 1.6360\times10^{3}$i	$3.0653\times10^{-3} + 1.6360\times10^{3}$i
ω_3	9.7303e-03 + 2.0907×10^{3}i	$1.5422\times10^{-2} + 2.4493\times10^{3}$i	$1.5513\times10^{-2} + 2.4541\times10^{3}$i	$1.5514\times10^{-2} + 2.4541\times10^{3}$i
ω_4	2.3837e-02 + 2.5440×10^{3}i	$4.8517\times10^{-2} + 3.2609\times10^{3}$i	$4.9025\times10^{-2} + 3.2722\times10^{3}$i	$4.9029\times10^{-2} + 3.2724\times10^{3}$i
ω_5	4.5141e-02 + 2.8952×10^{3}i	$1.1775\times10^{-2} + 4.0685\times10^{3}$i	$1.1968\times10^{-1} + 4.0905\times10^{3}$i	$1.1970\times10^{-1} + 4.0907\times10^{3}$i
ω_6	7.3454e-02 + 3.1690×10^{3}i	$2.4242\times10^{-1} + 4.8710\times10^{3}$i	$2.4812\times10^{-1} + 4.9090\times10^{3}$i	$2.4818\times10^{-1} + 4.9093\times10^{3}$i
ω_7	1.0847e-01 + 3.3855×10^{3}i	$4.4533\times10^{-1} + 5.6675\times10^{3}$i	$4.5960\times10^{-1} + 5.7276\times10^{3}$i	$4.5974\times10^{-1} + 5.7282\times10^{3}$i
ω_8	1.4992e-01 + 3.5596×10^{3}i	$7.5240\times10^{-1} + 6.4572\times10^{3}$i	$7.8390\times10^{-1} + 6.5464\times10^{3}$i	$7.8423\times10^{-1} + 6.5473\times10^{3}$i
ω_9	1.9761e-01 + 3.7017×10^{3}i	1.1922 + 7.2393×10^{3}i	1.2554 + 7.3654×10^{3}i	1.2560 + 7.3667×10^{3}i
ω_{10}	2.5138e-01 + 3.8196×10^{3}i	1.7954 + 8.0129×10^{3}i	1.9129 + 8.1848×10^{3}i	1.9141 + 8.1865×10^{3}i

Table 4-9 First ten critical out-of-plan frequencies of magnetic recording tape (Table 4-1) in roller-to-roller span (4 cm) for different mesh schemes obtained by semi- and full-discretization with $\Delta t = 1\times10^{-6}$.

Semi-discretization (Equation (4.37))				
	N = 20	**N = 50**	**N = 100**	**N = 150**
ω_1	$1.9145\times10^{-4} + 8.1799\times10^{2}$i	$1.8245\times10^{-4} + 8.1799\times10^{2}$i	$1.7984\times10^{-4} + 8.1799\times10^{2}$i	$1.9268\times10^{-4} + 8.1799\times10^{2}$i
ω_2	$3.0563\times10^{-3} + 1.6360\times10^{3}$i	$2.0261\times10^{-3} + 1.6360\times10^{3}$i	$3.1729\times10^{-3} + 1.6360\times10^{3}$i	$3.0494\times10^{-3} + 1.6360\times10^{3}$i
ω_3	$1.5485\times10^{-2} + 2.4541\times10^{3}$i	$2.3687\times10^{-2} + 2.4541\times10^{3}$i	$1.5381\times10^{-2} + 2.4541\times10^{3}$i	$1.5539\times10^{-2} + 2.4541\times10^{3}$i
ω_4	$4.9182\times10^{-2} + 3.2724\times10^{3}$i	$2.4467\times10^{-2} + 3.2724\times10^{3}$i	$4.8875\times10^{-2} + 3.2724\times10^{3}$i	$4.9024\times10^{-2} + 3.2724\times10^{3}$i
ω_5	$1.1827\times10^{-1} + 4.0908\times10^{3}$i	$1.6702\times10^{-1} + 4.0908\times10^{3}$i	$1.1992\times10^{-1} + 4.0908\times10^{3}$i	$1.1975\times10^{-1} + 4.0908\times10^{3}$i
ω_6	$2.4726\times10^{-1} + 4.9094\times10^{3}$i	$1.8004\times10^{-1} + 4.9093\times10^{3}$i	$2.4873\times10^{-1} + 4.9093\times10^{3}$i	$2.4819\times10^{-1} + 4.9093\times10^{3}$i
ω_7	$4.5803\times10^{-1} + 5.7283\times10^{3}$i	$5.2225\times10^{-1} + 5.7282\times10^{3}$i	$4.5756\times10^{-1} + 5.7282\times10^{3}$i	$4.5948\times10^{-1} + 5.7282\times10^{3}$i
ω_8	$7.7993\times10^{-1} + 6.5477\times10^{3}$i	$7.5947\times10^{-1} + 6.5473\times10^{3}$i	$7.8614\times10^{-1} + 6.5473\times10^{3}$i	$7.8433\times10^{-1} + 6.5473\times10^{3}$i
ω_9	$1.2457 + 7.3675\times10^{3}$i	$1.2297 + 7.3668\times10^{3}$i	$1.2545 + 7.3668\times10^{3}$i	$1.2562 + 7.3667\times10^{3}$i
ω_{10}	$1.9123 + 8.1880\times10^{3}$i	$1.9450 + 8.1866\times10^{3}$i	$1.9122 + 8.1866\times10^{3}$i	$1.9143 + 8.1866\times10^{3}$i
Full-discretization (Equation (4.40), $\Delta t = 1\times10^{-6}$ s)				
ω_1	$1.9157\times10^{-4} + 8.1799\times10^{2}$i	$1.9157\times10^{-4} + 8.1799\times10^{2}$i	$1.9154\times10^{-4} + 8.1799\times10^{2}$i	$1.9154\times10^{-4} + 8.1799\times10^{2}$i
ω_2	$3.0626\times10^{-3} + 1.6360\times10^{3}$i	$3.0645\times10^{-3} + 1.6360\times10^{3}$i	$3.0645\times10^{-3} + 1.6360\times10^{3}$i	$3.0646\times10^{-3} + 1.6360\times10^{3}$i
ω_3	$1.5485\times10^{-2} + 2.4541\times10^{3}$i	$1.5510\times10^{-2} + 2.4541\times10^{3}$i	$1.5512\times10^{-2} + 2.4541\times10^{3}$i	$1.5513\times10^{-2} + 2.4541\times10^{3}$i
ω_4	$4.8871\times10^{-2} + 3.2722\times10^{3}$i	$4.9000\times10^{-2} + 3.2722\times10^{3}$i	$4.9020\times10^{-2} + 3.2722\times10^{3}$i	$4.9025\times10^{-2} + 3.2722\times10^{3}$i
ω_5	$1.1914\times10^{-1} + 4.0905\times10^{3}$i	$1.1957\times10^{-1} + 4.0905\times10^{3}$i	$1.1965\times10^{-1} + 4.0905\times10^{3}$i	$1.1968\times10^{-1} + 4.0905\times10^{3}$i
ω_6	$2.4676\times10^{-1} + 4.9090\times10^{3}$i	$2.4781\times10^{-1} + 4.9090\times10^{3}$i	$2.4806\times10^{-1} + 4.9090\times10^{3}$i	$2.4812\times10^{-1} + 4.9090\times10^{3}$i
ω_7	$4.5684\times10^{-1} + 5.7277\times10^{3}$i	$4.5879\times10^{-1} + 5.7276\times10^{3}$i	$4.5944\times10^{-1} + 5.7276\times10^{3}$i	$4.5960\times10^{-1} + 5.7276\times10^{3}$i
ω_8	$7.7932\times10^{-1} + 6.5467\times10^{3}$i	$7.8213\times10^{-1} + 6.5464\times10^{3}$i	$7.8354\times10^{-1} + 6.5464\times10^{3}$i	$7.8390\times10^{-1} + 6.5464\times10^{3}$i
ω_9	$1.2493 + 7.3662\times10^{3}$i	$1.2519 + 7.3654\times10^{3}$i	$1.2546 + 7.3654\times10^{3}$i	$1.2554 + 7.3654\times10^{3}$i
ω_{10}	$1.9076 + 8.1862\times10^{3}$i	$1.9065 + 8.1848\times10^{3}$i	$1.9115 + 8.1848\times10^{3}$i	$1.9129 + 8.1848\times10^{3}$i

Table 4-10 First then critical LTM frequencies of magnetic recording tape (Table 4-1) in reel-to-reel span (24 cm) for different time-steps obtained by full- discretization with *N=150*.

Full-discretization (Equation (4.40), *N=150*)				
	$\Delta t = 1\times10^{-5}$ s	**$\Delta t = 1\times10^{-6}$** s	**$\Delta t = 1\times10^{-7}$** s	**$\Delta t = 1\times10^{-8}$** s
ω_1	$5.1906\times10^{-1}+ 2.2431\times10^{2}i$	$5.1908\times10^{-1}+ 2.2432\times10^{2}i$	$5.1908\times10^{-1}+ 2.2432\times10^{2}i$	$5.1915\times10^{-1}+ 2.2431\times10^{2}i$
ω_2	$8.2686 + 7.6164\times10^{2}i$	$8.2733 + 7.6178\times10^{2}i$	$8.2734 + 7.6178\times10^{2}i$	$8.2732 + 7.6178\times10^{2}i$
ω_3	$4.1722\times10^{1}+ 1.6491\times10^{3}i$	$4.1834\times10^{1}+ 1.6506\times10^{3}i$	$4.1835\times10^{1}+ 1.6506\times10^{3}i$	$4.1835\times10^{1}+ 1.6506\times10^{3}i$
ω_4	$1.3108\times10^{2}+ 2.8842\times10^{3}i$	$1.3215\times10^{2}+ 2.8920\times10^{3}i$	$1.3216\times10^{2}+ 2.8921\times10^{3}i$	$1.3216\times10^{2}+ 2.8921\times10^{3}i$
ω_5	$3.1632\times10^{2}+ 4.4537\times10^{3}i$	$3.2251\times10^{2}+ 4.4822\times10^{3}i$	$3.2258\times10^{2}+ 4.4825\times10^{3}i$	$3.2258\times10^{2}+ 4.4825\times10^{3}i$
ω_6	$6.4280\times10^{2}+ 6.3315\times10^{3}i$	$6.6854\times10^{2}+ 6.4127\times10^{3}i$	$6.6881\times10^{2}+ 6.4136\times10^{3}i$	$6.6881\times10^{2}+ 6.4136\times10^{3}i$
ω_7	$1.1538\times10^{3}+ 8.4759\times10^{3}i$	$1.2381\times10^{3}+ 8.6678\times10^{3}i$	$1.2390\times10^{3}+ 8.6698\times10^{3}i$	$1.2390\times10^{3}+ 8.6698\times10^{3}i$
ω_8	$1.8811\times10^{3}+ 1.0831\times10^{4}i$	$2.1109\times10^{3}+ 1.1221\times10^{4}i$	$2.1135\times10^{3}+ 1.1225\times10^{4}i$	$2.1135\times10^{3}+ 1.1225\times10^{4}i$
ω_9	$2.8370\times10^{3}+ 1.3335\times10^{4}i$	$3.3789\times10^{3}+ 1.4033\times10^{4}i$	$3.3853\times10^{3}+ 1.4040\times10^{4}i$	$3.3853\times10^{3}+ 1.4040\times10^{4}i$
ω_{10}	$4.0115\times10^{3}+ 1.5930\times10^{4}i$	$5.1453\times10^{3}+ 1.7043\times10^{4}i$	$5.1595\times10^{3}+ 1.7055\times10^{4}i$	$5.1597\times10^{3}+ 1.7055\times10^{4}i$

Table 4-11 First ten critical LTM frequencies of magnetic recording tape (Table 4-1) in reel-to-reel span (24 cm) for different mesh schemes obtained by semi- and full-discretization with $\Delta t = 1\times10^{-7}$.

Semi-discretization (Equation (4.37))				
	N = 20	**N = 50**	**N = 100**	**N = 150**
ω_1	$5.1907\times10^{-1}+2.2432\times10^{2}i$	$5.1908\times10^{-1}+2.2432\times10^{2}i$	$5.1909\times10^{-1}+2.2432\times10^{2}i$	$5.1909\times10^{-1}+2.2432\times10^{2}i$
ω_2	$8.2732+7.6179\times10^{2}i$	$8.2733+7.6178\times10^{2}i$	$8.2734+7.6178\times10^{2}i$	$8.2734+7.6178\times10^{2}i$
ω_3	$4.1836\times10^{1}+1.6507\times10^{3}i$	$4.1835\times10^{1}+1.6506\times10^{3}i$	$4.1835\times10^{1}+1.6506\times10^{3}i$	$4.1835\times10^{1}+1.6506\times10^{3}i$
ω_4	$1.3218\times10^{2}+2.8924\times10^{3}i$	$1.3216\times10^{2}+2.8921\times10^{3}i$	$1.3216\times10^{2}+2.8921\times10^{3}i$	$1.3216\times10^{2}+2.8921\times10^{3}i$
ω_5	$3.2274\times10^{2}+4.4837\times10^{3}i$	$3.2258\times10^{2}+4.4826\times10^{3}i$	$3.2258\times10^{2}+4.4825\times10^{3}i$	$3.2258\times10^{2}+4.4825\times10^{3}i$
ω_6	$6.6951\times10^{2}+6.4169\times10^{3}i$	$6.6883\times10^{2}+6.4137\times10^{3}i$	$6.6882\times10^{2}+6.4136\times10^{3}i$	$6.6882\times10^{2}+6.4136\times10^{3}i$
ω_7	$1.2414\times10^{3}+8.6780\times10^{3}i$	$1.2390\times10^{3}+8.6700\times10^{3}i$	$1.2390\times10^{3}+8.6698\times10^{3}i$	$1.2390\times10^{3}+8.6698\times10^{3}i$
ω_8	$2.1205\times10^{3}+1.1243\times10^{4}i$	$2.1137\times10^{3}+1.1226\times10^{3}i$	$2.1135\times10^{3}+1.1225\times10^{4}i$	$2.1135\times10^{3}+1.1225\times10^{4}i$
ω_9	$3.4030\times10^{3}+1.4075\times10^{4}i$	$3.3858\times10^{3}+1.4041\times10^{3}i$	$3.3854\times10^{3}+1.4040\times10^{4}i$	$3.3853\times10^{3}+1.4040\times10^{4}i$
ω_{10}	$5.2003\times10^{3}+1.7115\times10^{4}i$	$5.1607\times10^{3}+1.7056\times10^{3}i$	$5.1597\times10^{3}+1.7055\times10^{4}i$	$5.1597\times10^{3}+1.7055\times10^{4}i$
Full-discretization (Equation (4.40), $\Delta t = 1\times10^{-7}$ s)				
ω_1	$5.1907\times10^{-1}+2.2432\times10^{2}i$	$5.1908\times10^{-1}+2.2432\times10^{2}i$	$5.1908\times10^{-1}+2.2432\times10^{2}i$	$5.1908\times10^{-1}+2.2432\times10^{2}i$
ω_2	$8.2732+7.6179\times10^{2}i$	$8.2733+7.6178\times10^{2}i$	$8.2734+7.6178\times10^{2}i$	$8.2734+7.6178\times10^{2}i$
ω_3	$4.1836\times10^{1}+1.6507\times10^{3}i$	$4.1835\times10^{1}+1.6506\times10^{3}i$	$4.1835\times10^{1}+1.6506\times10^{3}i$	$4.1835\times10^{-1}+1.6506\times10^{3}i$
ω_4	$1.3218\times10^{2}+2.8924\times10^{3}i$	$1.3216\times10^{2}+2.8921\times10^{3}i$	$1.3216\times10^{2}+2.8921\times10^{3}i$	$1.3216\times10^{2}+2.8921\times10^{3}i$
ω_5	$3.2274\times10^{2}+4.4837\times10^{3}i$	$3.2258\times10^{2}+4.4826\times10^{3}i$	$3.2258\times10^{2}+4.4825\times10^{3}i$	$3.2258\times10^{2}+4.4825\times10^{3}i$
ω_6	$6.6951\times10^{2}+6.4169\times10^{3}i$	$6.6883\times10^{2}+6.4137\times10^{3}i$	$6.6881\times10^{2}+6.4136\times10^{3}i$	$6.6881\times10^{2}+6.4136\times10^{3}i$
ω_7	$1.2414\times10^{3}+8.6780\times10^{3}i$	$1.2390\times10^{2}+8.6700\times10^{3}i$	$1.2390\times10^{3}+8.6698\times10^{3}i$	$1.2390\times10^{3}+8.6698\times10^{3}i$
ω_8	$2.1204\times10^{3}+1.1243\times10^{4}i$	$2.1137\times10^{2}+1.1226\times10^{4}i$	$2.1135\times10^{3}+1.1225\times10^{4}i$	$2.1135\times10^{3}+1.1225\times10^{4}i$
ω_9	$3.4029\times10^{3}+1.4075\times10^{4}i$	$3.3857\times10^{2}+1.4041\times10^{4}i$	$3.3853\times10^{3}+1.4040\times10^{4}i$	$3.3853\times10^{3}+1.4040\times10^{4}i$
ω_{10}	$5.2002\times10^{3}+1.7115\times10^{4}i$	$5.1606\times10^{2}+1.7056\times10^{4}i$	$5.1596\times10^{3}+1.7055\times10^{4}i$	$5.1595\times10^{3}+1.7055\times10^{4}i$

Table 4-12 First ten critical out-of-plane frequencies of magnetic recording tape (Table 4-1) in reel-to-reel span (24 cm) for different time-steps obtained by full- discretization with *N=150*.

Full-discretization (Equation (4.40), *N=150*)				
	$\Delta t = 1\times10^{-4}$ s	**$\Delta t = 1\times10^{-5}$** s	**$\Delta t = 1\times10^{-6}$** s	**$\Delta t = 1\times10^{-7}$** s
ω_1	$1.4763\times10^{-7}+ 1.3625\times10^{2}i$	$1.4770\times10^{-7}+ 1.3633\times10^{2}i$	$1.5251\times10^{-7}+ 1.3633\times10^{2}i$	$2.1958\times10^{-6}+ 1.3633\times10^{2}i$
ω_2	$2.3489\times10^{-6}+ 2.7200\times10^{2}i$	$2.3663\times10^{-6}+ 2.7265\times10^{2}i$	$2.3655\times10^{-6}+ 2.7266\times10^{2}i$	$5.8156\times10^{-6}+ 2.7266\times10^{2}i$
ω_3	$1.1783\times10^{-5}+ 4.0676\times10^{2}i$	$1.1975\times10^{-5}+ 4.0897\times10^{2}i$	$1.2007\times10^{-5}+ 4.0899\times10^{2}i$	$-8.2564\times10^{-6}+ 4.0899\times10^{2}i$
ω_4	$3.6773\times10^{-5}+ 5.4008\times10^{2}i$	$3.7842\times10^{-5}+ 5.4527\times10^{2}i$	$3.7840\times10^{-5}+ 5.4532\times10^{2}i$	$4.7903\times10^{-5}+ 6.8166\times10^{2}i$
ω_5	$8.8352\times10^{-5}+ 6.7151\times10^{2}i$	$9.2361\times10^{-5}+ 6.8155\times10^{2}i$	$9.2390\times10^{-5}+ 6.8165\times10^{2}i$	$6.6798\times10^{-5}+ 5.4532\times10^{2}i$
ω_6	$1.7971\times10^{-4}+ 8.0066\times10^{2}i$	$1.9145\times10^{-4}+ 8.1781\times10^{2}i$	$1.9169\times10^{-4}+ 8.1799\times10^{2}i$	$2.4941\times10^{-4}+ 8.1799\times10^{2}i$
ω_7	$3.2561\times10^{-4}+ 9.2718\times10^{2}i$	$3.5456\times10^{-4}+ 9.5404\times10^{2}i$	$3.5491\times10^{-4}+ 9.5432\times10^{2}i$	$3.3332\times10^{-4}+ 9.5432\times10^{2}i$
ω_8	$5.4170\times10^{-4}+ 1.0508\times10^{3}i$	$6.0458\times10^{-4}+ 1.0902\times10^{3}i$	$6.0493\times10^{-4}+ 1.0907\times10^{3}i$	$6.2017\times10^{-4}+ 1.0907\times10^{3}i$
ω_9	$8.4398\times10^{-4}+ 1.1711\times10^{3}i$	$9.6795\times10^{-4}+ 1.2264\times10^{3}i$	$9.6920\times10^{-4}+ 1.2270\times10^{3}i$	$9.6484\times10^{-4}+ 1.2270\times10^{3}i$
ω_{10}	$1.2482\times10^{-3}+ 1.2881\times10^{3}i$	$1.4745\times10^{-3}+ 1.3625\times10^{2}i$	$1.4772\times10^{-3}+ 1.3633\times10^{3}i$	$1.4710\times10^{-3}+ 1.3633\times10^{3}i$

Table 4-13 First ten critical out-of-plane frequencies of magnetic recording tape (Table 4-1) in reel-to-reel span (24 cm) for different mesh schemes obtained by semi- and full-discretization with $\Delta t = 1\times10^{-6}$.

Semi-discretization (Equation (4.37))				
	N = 20	**N = 50**	**N = 100**	**N = 150**
ω_1	$-1.7400\times10^{-5}+1.3633\times10^{2}i$	$-3.1438\times10^{-4}+1.3633\times10^{2}i$	$-1.7679\times10^{-3}+1.3634\times10^{2}i$	$-1.0621\times10^{-3}+1.3633\times10^{2}i$
ω_2	$5.4694\times10^{-5}+2.7266\times10^{2}i$	$6.5116\times10^{-3}+2.7265\times10^{2}i$	$1.9425\times10^{-2}+2.7261\times10^{2}i$	$1.3445\times10^{-2}+2.7267\times10^{2}i$
ω_3	$4.7930\times10^{-4}+4.0899\times10^{2}i$	$-2.0410\times10^{-2}+4.0901\times10^{2}i$	$1.1218\times10^{-2}+4.0902\times10^{2}i$	$-1.6577\times10^{-1}+4.0897\times10^{2}i$
ω_4	$-1.3987\times10^{-3}+5.4532\times10^{2}i$	$1.6204\times10^{-2}+5.4533\times10^{2}i$	$-3.3355\times10^{-1}+5.4563\times10^{2}i$	$1.1418+5.4454\times10^{2}i$
ω_5	$4.6901\times10^{-4}+6.8166\times10^{2}i$	$8.7638\times10^{-4}+6.8165\times10^{2}i$	$6.4016\times10^{-1}+6.8106\times10^{2}i$	$-2.5990+6.8292\times10^{2}i$
ω_6	$3.3374\times10^{-3}+8.1800\times10^{2}i$	$-3.2202\times10^{-2}+8.1797\times10^{2}i$	$1.6506\times10^{-1}+8.1855\times10^{2}i$	$2.5713+8.1854\times10^{2}i$
ω_7	$-3.6158\times10^{-3}+9.5435\times10^{2}i$	$1.2242\times10^{-1}+9.5436\times10^{2}i$	$-1.9169+9.5370\times10^{2}i$	$-2.8145+9.5451\times10^{2}i$
ω_8	$1.7636\times10^{-3}+1.0907\times10^{3}i$	$-2.1001\times10^{-1}+1.0906\times10^{3}i$	$2.2255+1.0914\times10^{3}i$	$2.9312\times10^{-2}+1.0876\times10^{3}i$
ω_9	$8.9512\times10^{-4}+1.2271\times10^{3}i$	$2.0878\times10^{-1}+1.2270\times10^{3}i$	$6.7641\times10^{-3}+1.2267\times10^{3}i$	$9.7032+1.2333\times10^{3}i$
ω_{10}	$9.2976\times10^{-4}+1.3636\times10^{3}i$	$-1.1332\times10^{-1}+1.3638\times10^{3}i$	$-1.0649+1.3623\times10^{3}i$	$-8.6444+1.3533\times10^{3}i$
Full-discretization (Equation (4.40), $\Delta t = 1\times10^{-6}$ s)				
ω_1	$1.5484\times10^{-7}+1.3633\times10^{2}i$	$1.5465\times10^{-7}+1.3633\times10^{2}i$	$1.5251\times10^{-7}+1.3633\times10^{2}i$	$1.7212\times10^{-7}+1.3633\times10^{2}i$
ω_2	$2.4247\times10^{-6}+2.7266\times10^{2}i$	$2.2726\times10^{-6}+2.7266\times10^{2}i$	$2.3655\times10^{-6}+2.7266\times10^{2}i$	$2.3119\times10^{-6}+2.7266\times10^{2}i$
ω_3	$1.1870\times10^{-5}+4.0899\times10^{2}i$	$1.1991\times10^{-5}+4.0899\times10^{2}i$	$1.2007\times10^{-5}+4.0899\times10^{2}i$	$1.2078\times10^{-5}+4.0899\times10^{2}i$
ω_4	$3.7648\times10^{-5}+5.4532\times10^{2}i$	$3.7931\times10^{-5}+5.4532\times10^{2}i$	$3.7840\times10^{-5}+5.4532\times10^{2}i$	$3.7510\times10^{-5}+5.4532\times10^{2}i$
ω_5	$9.2357\times10^{-5}+6.8166\times10^{2}i$	$9.2538\times10^{-5}+6.8165\times10^{2}i$	$9.2390\times10^{-5}+6.8165\times10^{2}i$	$9.2317\times10^{-5}+6.8165\times10^{2}i$
ω_6	$1.9046\times10^{-4}+8.1800\times10^{2}i$	$1.9140\times10^{-4}+8.1799\times10^{2}i$	$1.9169\times10^{-4}+8.1799\times10^{2}i$	$1.9206\times10^{-4}+8.1799\times10^{2}i$
ω_7	$3.5238\times10^{-4}+9.5434\times10^{2}i$	$3.5360\times10^{-4}+9.5432\times10^{2}i$	$3.5491\times10^{-4}+9.5432\times10^{2}i$	$3.5504\times10^{-4}+9.5432\times10^{2}i$
ω_8	$6.0136\times10^{-4}+1.0907\times10^{3}i$	$6.0436\times10^{-4}+1.0907\times10^{3}i$	$6.0493\times10^{-4}+1.0907\times10^{3}i$	$6.0458\times10^{-4}+1.0907\times10^{3}i$
ω_9	$9.6557\times10^{-4}+1.2271\times10^{3}i$	$9.6802\times10^{-4}+1.2270\times10^{3}i$	$9.6920\times10^{-4}+1.2270\times10^{3}i$	$9.6997\times10^{-4}+1.2270\times10^{3}i$
ω_{10}	$1.4751\times10^{-3}+1.3635\times10^{3}i$	$1.4721\times10^{-3}+1.3633\times10^{3}i$	$1.4772\times10^{-3}+1.3633\times10^{3}i$	$1.4784\times10^{-3}+1.3633\times10^{3}i$

Chapter 5 Mechanics of Lateral Positioning of a Translating Tape due to Tilted Rollers: Theory and Experiments

A mechanics based model to describe the lateral positioning of a thin, tensioned, translating tape over a tilted roller is introduced, based on the assumption that the transport velocity of the tape should match the surface velocity of the roller when there is sufficient traction. It is shown that this condition requires the slope of the neutral axis of the tape and the slope of the centerline of the tilted roller to be the same over the wrapped segment. An extension of this model is discussed including the possibility of circumferential and lateral sliding, depending on the velocity difference between the tape and the roller. The new model is incorporated into a generalized model of a tape path that consists of numerous rollers as well as the appropriate boundary conditions for the take-up and supply reel dynamics. The nonlinear equation of motion is solved numerically, and the steady state solution is found by an implicit time stepping algorithm. An experimental setup with one tilting roller, two or three nearly ideally oriented rollers and two reels is used for verification of the model. The effects of roller tilt angle, tape wrap

angle, and the lengths of the free-tape spans upstream and downstream of the tilted roller on the steady state lateral tape position are investigated experimentally and by simulations. The experiments show that the circumferential position of the wrap on the upstream side of a tilted roller has the strongest effect on pushing the tape in the lateral direction. The total wrap angle around the roller has a smaller effect. It was also shown that the tape segments upstream and downstream of the tilted roller interact, and the combined effect results in a different overall lateral tape response in steady state.

In this chapter, we introduce a mathematical model of a rolling guide. A comprehensive description of the coordinate system associated with the drives, rollers and tape are also provided. The motivation for developing a roller model and a comprehensive literature review are provided in Section 5.1. The mathematical model, experiment setups and results are described in detail in Section 5.2, 5.3, and 5.4 respectivley. Section 5.5 summarizes this chapter.

5.1 Introduction

Lateral tape motion is generally not acceptable in a tape drive. Nevertheless, it is also generally unavoidable. Various strategies have been developed to deal with LTM. LTM can be suppressed to a certain extent by using flanged rollers, which could damage the edge of the tape, and introduce high frequency low amplitude lateral tape vibrations. On the other hand, use of flangeless rollers could eliminate these issues, but they can also amplify the low frequency LTM [152]. One of the key factors in understanding the effects of imperfections on lateral tape/web dynamics has been mechanistic modeling of the tape transport process. In particular, mechanics of a translating tape/web interacting with a roller has been the subject of several critical works. Shelton and Reid (SR) showed that the lateral web deflections can be modeled by using the beam theory, and they described the mechanics of the web as it comes into contact with a cylindrical roller [61]. Their work, which describes the web dynamics in the free span between two rollers, was the first to identify the boundary conditions between the web and the downstream roller. Sievers extended this work to a system with multiple rollers and used the Timoshenko beam theory [116]. Benson obtained the downstream boundary conditions by using the minimum total potential energy principle, and described the mechanics of a spliced web

by using the Timoshenko beam theory [115]. In the limit when Euler-Bernoulli and Timoshenko beam models are identical the boundary conditions described by SR and Benson models are identical. The aforementioned works do not directly model the interaction of a web with a roller. Mechanics of a string travelling over a cylindrical roller was described by Ono [67] and Moustafa [57], and over a general axisymmetric roller by Yang [58]. Raeymaekers et al. extended Ono's model by adding the effects of bending stiffness [28]. However, these models have not considered systems with multiple rollers, and they do not take into account the roller misalignment. In Shelton's work the effect of roller misalignment on the free-span web dynamics can be introduced by using the boundary conditions. Eaton described the geometry of the tape over a roller that has an arbitrary tilt with respect to the drive base, but did not consider the tape's flexure over the roller. He described the reel-to-reel dynamics of the tape by using the tape geometry over the rollers as boundary conditions of multiply connected tape segments [59]. Brake and Wickert [20, 21] introduced a framework where various types of guides on a tape path can be modeled by applying concentrated forces and moments. Brake and Wickert [9] added tape flexure to Eaton's description of the tape geometry over a tilted roller. The present work introduces a general model for modeling the lateral dynamics of a web travelling between two reels, supported by multiple rollers. In this proposal, we make two contributions. The first one of these is the introduction of a mathematical formulation that incorporates the velocity matching rule of Shelton and Reid [61, 63] at the location of the rollers. This condition is imposed by matching tape slope to the slope of the centerline of the tilted roller, by using a penalty formulation. This allows the system to find the steady state deflected shape of the tape along the tape path. Note that we impose this condition as a continuous constraint applied on the entire segment of tape wrapped over a roller, rather than a concentrated force/moment. The second contribution allows modeling of the dynamic interactions between a roller and a tape, and involves the possibility of slip over the roller.

5.2 Model

The tape mechanics is described with respect to a *tape-based coordinate* system (x, z) that coincides with the neutral axis of the idealized tape as shown in Figure 5-1. The

origin of the tape-coordinate system is located at the tape tangency point on the supply reel. Figure 5-1 shows the tape in a configuration that is unwrapped onto a plane.

Each roller is assumed to have a set of *roller coordinate axes* (Figure 5-2) designated as (x_1^r, x_2^r, x_3^r). In case the roller is exactly perpendicular to the drive base (x_1^r, x_2^r, x_3^r) are coincident with the *ground* (*or drive-base*) *coordinate system* (x_1, x_2, x_3). Otherwise, the orientation of the roller coordinate axes is described with respect to the ground system by using the *tilt angle* δ and the *orientation angle* α as shown in Figure 5-2. Note that the tilt angle δ represents a rotation about the x_2 axis. The orientation angle α, which is a measure of the location of the x_1^r axis with respect to x_1 axis, on the (x_1, x_2) plane as shown in Figure 5-2, also represents a rotation about the x_3 axis. This notation was first used by [59] and then by [9, 59].

It is generally assumed that tape sticks on to the roller if there is sufficient traction in the tape-roller interface [61]. Therefore, it is critical to describe the position of a tilted roller with respect to the tape. Note that the circumferential centerline of the roller develops a height variation $w_g(\theta)$ with respect to the (x_1, x_2) plane in case the roller axis is tilted [59],

$$w_g(\theta) = -R\sin\delta\cos\theta \tag{5.1}$$

where R is the radius of the roller as shown in Figure 5-2c. Note that in this case the circumferential position θ is referred to the x_1^r axis as shown in Figure 5-2b. Also note that the x-axis of the tape-based coordinate system and the circumferential position are in general related as $dx = Rd\theta$. As a result, the slope of the centerline of the tilted roller can be expressed in the tape based coordinate system as follows [59],

$$\theta_g(x) = \frac{dw_g}{dx} = \sin\delta\sin\theta \tag{5.2}$$

Equations. (5.1) and (5.2) enable the position and slope of an imperfectly oriented roller to be described with respect to the tape-based coordinate system.

Shelton's normal entry law [60] states that the tape transport velocity and the roller velocity match in the absence of slipping. Therefore, when the tape encounters a tilted roller, its slope $\partial w/\partial x$ will follow the slope of the roller θ_g, but it will settle at a shifted equilibrium position. This assertion follows, directly and naturally from Shelton's law [60], and Benson's [115] description of tape motion over a roller. In this work the slope condition is imposed by using a penalty formulation. Lateral slip is also considered as a perturbation around the deflected, steady-state tape path.

The equation of lateral tape motion first introduced in the theory section in this chapter is modified as follows [27],

$$\rho A\frac{D^2w}{Dt^2}+\frac{\partial^2}{\partial x^2}\left[EI\frac{\partial^2 w}{\partial x^2}+\eta I\frac{D}{Dt}\left(\frac{\partial^2 w}{\partial x^2}\right)\right]-\frac{\partial}{\partial x}\left(T\frac{\partial w}{\partial x}\right)+\sum_{i=1}^{N_g}H_i\left[k\left(\frac{\partial w}{\partial x}-\theta_{g_i}\right)+q_{f_i}-\frac{\partial m_{f_i}}{\partial x}\right]$$
$$=f(x,t)+\sum_{i=1}^{N_g}H_i\left[\frac{T}{R_i}\cos\theta_{g_i}(x)\sin\delta_i\right] \tag{5.3}$$

where, w is the lateral tape deflection, x is the longitudinal coordinate axis, t is time, ρ is the mass density of tape, A is the cross section area of tape. V_x is the tape translating velocity, E is the elastic modulus, η is the loss modulus, I is the second moment of area of the tape cross-section, T is the tape tension, the subscript i refers to the roller number, $w(x, t)$ is the lateral deflection of the tape, t represents time, H_i is a windowing function that is equal to 1 over a roller and 0 elsewhere, k is the penalty stiffness used to impose the slope matching condition, θ_g is the guide slope given by Eqn. (5.3), q_{f_i} and m_{f_i} are the frictional forces and moments acting on the tape over the rollers. Note that the rollers considered in this paper do not have any flanges, as a result no flange force are included in Equation(5.3).

The effects of the rollers on the tape are represented by the fourth term in Equation (5.3). The first term of this square bracket represents a corrective distributed moment of magnitude $k\left(\partial w/\partial x-\theta_{g_i}\right)$, applied in case the tape slope deviates from the slope of the

guide. This term becomes zero at steady state. The frictional forces and moments that act on the roller in a distributed manner are derived in the Figure 5-10. These terms are expressed as follows,

$$q_{f_i} = -\mu_{z_i} \frac{T}{R_i} \operatorname{sgn}\left(\frac{\partial w}{\partial t} + V\left(\frac{\partial w}{\partial x} + \theta_{g_i} \right) \right) \text{ (a) ; } m_{f_i} = \mu_{x_i} \frac{Tb}{12R_i} \operatorname{sgn} \frac{D}{Dt}\left(\frac{\partial w}{\partial x} \right) \text{ (b)} \qquad (5.4)$$

where, μ_x and μ_z are the dynamic friction coefficients in the longitudinal and lateral directions, respectively, and *b* is the width of the tape. The last term of Equation (5.3) represents the lateral component of the distributed contact force which develops due to the guide tilt [59]. The boundary conditions as stated in the Section 3.1.

5.3 Experiments

An experimental, reconfigurable tape-path was used to assess the effects of a tilted guide on the lateral tape deflections. The tape-path was composed of two reels and several grooved-rollers. One of the rollers was designed so that its spin axis can be tilted as described by [152]. This roller was positioned on the drive-base in such a way that only the tilt angle δ was non-zero. The other rollers were manufactured with sufficiently high tolerances that they could be considered normal to the drive base.

Four edge sensors were used to measure the lateral tape deflection as also described by [152]. The standard deviation of the noise floor of the sensors was ~50 nm in a 10 kHz bandwidth. Two sensors were placed on each side of the tilting guide, and numbered from upstream to downstream as S_1 to S_4 (Figure 5-3(a)). Sensors-S_2 and -S_3 were placed as close as possible to the tangency points of the tape over the roller. Moreover, Sensors-S_1 and -S_2 are located as close as possible to S_3 and S_4, respectively. The S_1-S_2 and S_3-S_4 distances were measured carefully to enable assessment of the tape slope in addition to tape deflection. Tape slopes at the upstream and downstream points of the roller were found by using a finite difference approximation, as follows,

$$\theta_{upstream}^{meas} \cong \frac{w_2^{meas} - w_1^{meas}}{d_{upstream}} \text{ and } \theta_{downstream}^{meas} \cong \frac{w_4^{meas} - w_3^{meas}}{d_{downstream}} \qquad (5.5)$$

where, $d_{\text{up/downstream}}$ represent the S_1–S_2 and S_3–S_4 spacings, respectively, and the w_i^{meas} represent the measured LTM values on the sensors.

In this work, the effects of the *tilt-angle* δ, the *tape-wrap angle* θ_w, and the upstream and downstream *free span lengths* on the steady state lateral tape position were investigated experimentally and through simulations. The values of these three variables are reported in Table 5-2 and Table 5-1and in the respective figure captions. Tape properties and roller dimensions are listed in Table 5-1.

5.4 Results

The tape path used in the experiments is shown in Figure 5-3. Note that the tilting roller is located at position i = 2. The effect of roller-tilt on the lateral tape position was tested for different wrap angle values for this configuration. The wrap angle was changed by changing the position of the roller-1 (i = 1). The roller-tilt δ is imposed on roller-2 (i = 2) while keeping the orientation angle α zero. Tape runs from the supply-reel (pack-1) to the take-up reel (pack-2). The tape lengths upstream and downstream of the roller-2 remain constant during these tests at $L_2 = L_3 = 8\times10^{-2}$ m. Four different wrap angle values (θ_{w2}) were considered: 30, 45, 60 to 90 degrees. In Figure 3, the tape wraps around the tiling-roller by θ_{w2} = 90 degrees. The drive base coordinate system (x_1, x_2) is presented on Figure 5-4. Note that in order to provide sufficient traction and to prevent excessive slipping [62], the wrap angles on the rollers-1 and -3 (i = 1, 3) had to be kept larger than 15 degrees. Therefore, one extra roller was added to the system for the case of θ_{w2} = 60 degrees. As a result the tilting roller is located at position i = 4, for this case. Four guide tilt-angle values were applied to each wrap as reported in Table 5-2. Due to the construction of the setup it was not possible to apply the exact same δ values. The radii of the supply pack and the take-up pack during the tests are also reported in Table 5-2. Different pack radii are reported as measurements are done on different part of tape and damaged tape was removed from tape path.

Computed steady-state tape profiles, spanning the range between the two reels, is shown in Figure 5-5. The tilted roller is predicted to cause significant lateral displacement of the

tape. The lateral displacement is clearly more significant on the downstream side of the tilted roller. However, some lateral displacement spills over to the upstream side as well. Rollers, located upstream and downstream from the tilted roller, are perfectly aligned. Therefore, the tape slope is nearly zero on these rollers. In other words, these two rollers are able to "correct" the slope change caused by the tilted roller. Nevertheless, a residual shift remains in the tape path. The shift on the downstream side, which is on the order of 50 – 250 μm depending on the case, is dictated by the take-up reel and is much larger than the shift on the upstream side. The velocity matching boundary conditions given by Equation (3.11) allows for this lateral shift to be simulated.

The steady-state lateral tape deflections measured at the sensor positions S_1–S_4 are plotted in Figure 5-6 along with the simulated results. The span of the tilted roller, located between sensors S_2 and S_3, is also marked. The slopes of the tape at the up-stream and down-stream locations are computed from the measured positions, and compared to the computed values in Figure 5-7. Note that the average and the standard deviation of the test data are computed based on 5 different measurements.

Figure 5-6 and Figure 5-7 show that both of the lateral tape deflection, and the tape-slope simulation results agree well with experimental measurements. With this said, it is interesting to note (Figure 5-6) that the lateral shift of the tape decreases with wrap-angle, θ_w. In fact, this lateral shift is actually due to the location of the upstream tangency point $\theta_2^{upstream}$ with respect to the reference position of θ (x_1-axis in these examples) where the $w_g(\theta)$ has its maximum. Therefore, changing $\theta_2^{upstream}$ from –180 degrees (Figure 5-6a) to –120 degrees in (Figure 5-6d) forces the tape to make initial contact with the roller at a higher position, eventually resulting in a larger lateral shift.

The length of the tape upstream and downstream of a roller contributes to its stiffness, and therefore has an effect on the lateral position/slope of the tape over the roller at steady state. In order to investigate this effect, four different configurations of the upstream and downstream span lengths were tested, for a fixed wrap angle (θ_{w3} = 60 deg.) over the tilted roller. The computed tape deflection profiles at steady state are shown in Figure 5-8, for upstream and downstream free span length (L_3, L_4) combinations of (8, 8),

(8, 4) (4, 8) and (4, 4) cm. As expected the longer tape span is more compliant and displays a larger lateral deflection (Figure 5-8a, d). Moreover, for a given upstream span length (e.g. L_3 = 8 mm) the lateral shift w_L (Figure 5-8e) is reduced with decreasing downstream span length, as expected. Figure 5-9 shows that the measured and computed lateral tape deflections at steady state compare well.

The tilted-roller causes an accumulated lateral-shift w_L at the tangency point of the tape ($x = L$) with the take-up reel as shown in Figure 5-5 and Figure 5-8. The effects of the tilt-angle δ, wrap-angle θ_{wi} and upstream and downstream free span lengths L_i and L_{i+1} on the total lateral shift w_L are assessed by simulation and presented in Figure 5-5e and Figure 5-8e. It is interesting to note that w_L is linearly proportional to the tilt-angle δ. As indicated before, the total tape shift is affected by the initial position at which the tape is making contact, which is governed by $\theta_i^{upstream}$. Thus in this tape path-configuration the larger wrap angle makes the initial contact position between the tape and the roller at a lower position and results in a smaller amount of lateral shift. Also, as indicated, the length of the free span on the downstream side L_{i+1} has significant effect on the total lateral shift. Shorter L_{i+1} is stiffer and therefore causes lower lateral shift.

5.5 Summary

A model for the interactions of a thin, tensioned, travelling tape with a flangeless cylindrical-roller is introduced. The model is based on the expectation that the tape speed and the roller speed match for tilted rollers, and thus obeys Shelton and Reid's normal entry law [61]. This tape-roller interaction model is integrated into a system level tape transport model which accommodates simulating the dynamics of tape supported by multiple rollers, between two reels [21]. The steady state tape deflections are found by using solving the non-linear governing equations transiently with a numerical approach. Lateral tape deflection and slope are measured upstream and downstream of a tilted-roller on an experimental, configurable tape-path as a function of roller tilt-angle, tape's wrap angle over the roller and the lengths of free tape span upstream and downstream of the tilted-roller. Model predictions compare very favorably with experimental measurements.

This work showed that the most significant parameter that affects the lateral shift of the tape over a tilted roller is the point of contact of the tape with the roller. This point is determined by the tape position on the upstream side of the tilted-roller. This work also demonstrated that the length of the free span of the tape upstream and downstream of the tilted roller has a strong influence. For a fixed upstream span increasing downstream span length causes more lateral shift under similar conditions.

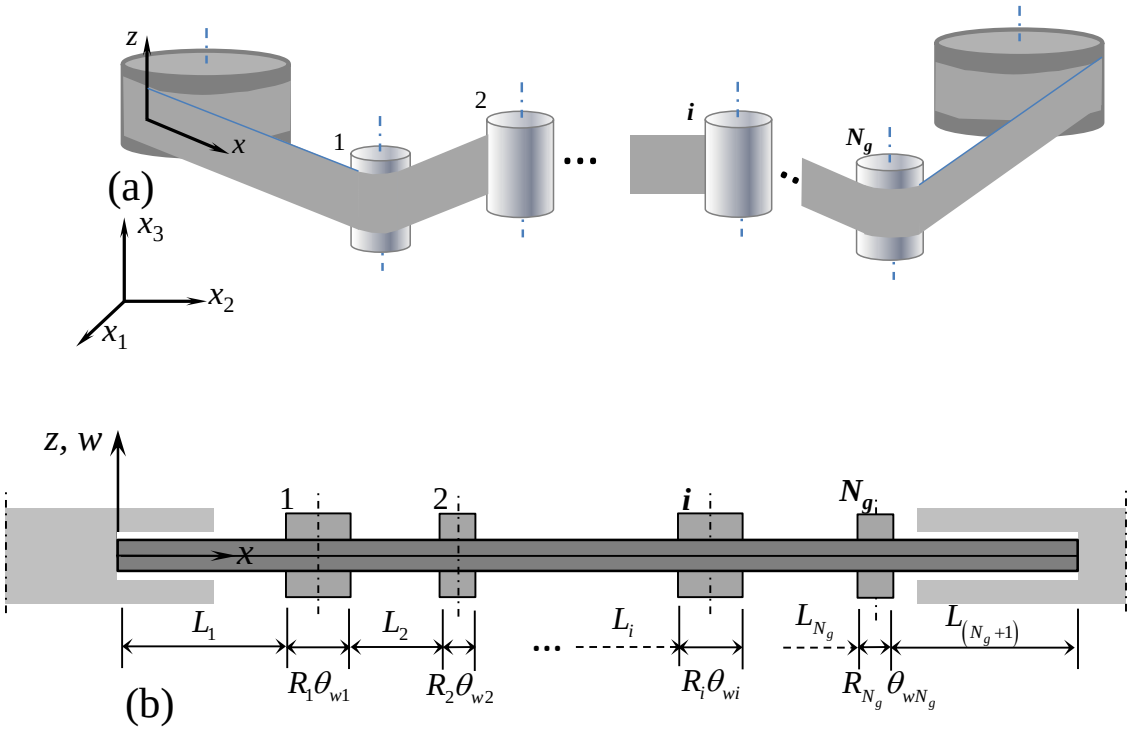

Figure 5-1 Tape path coordinate system

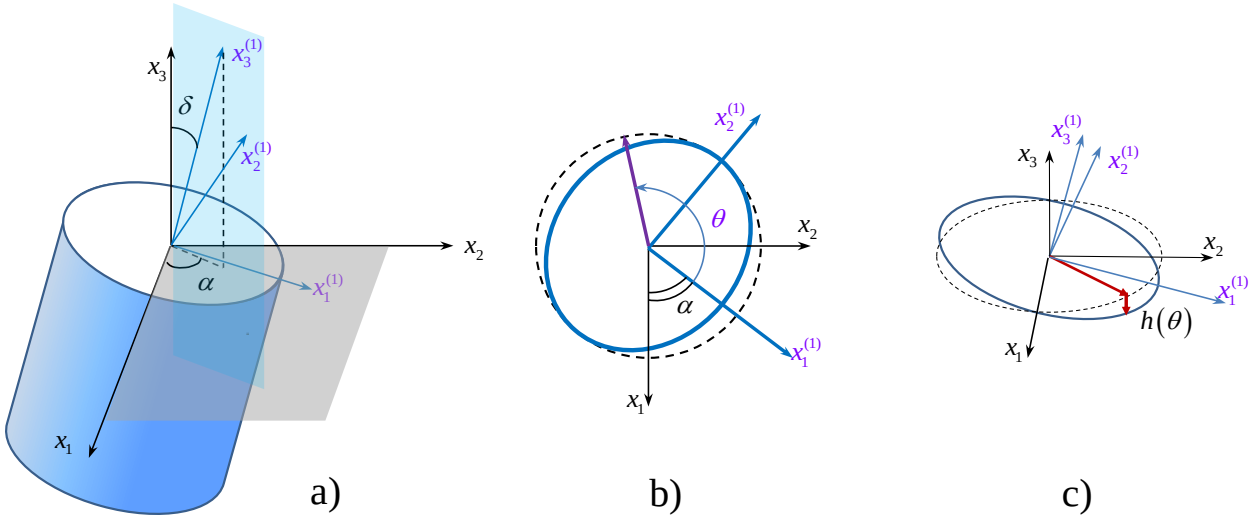

Figure 5-2 Roller coordinate axes

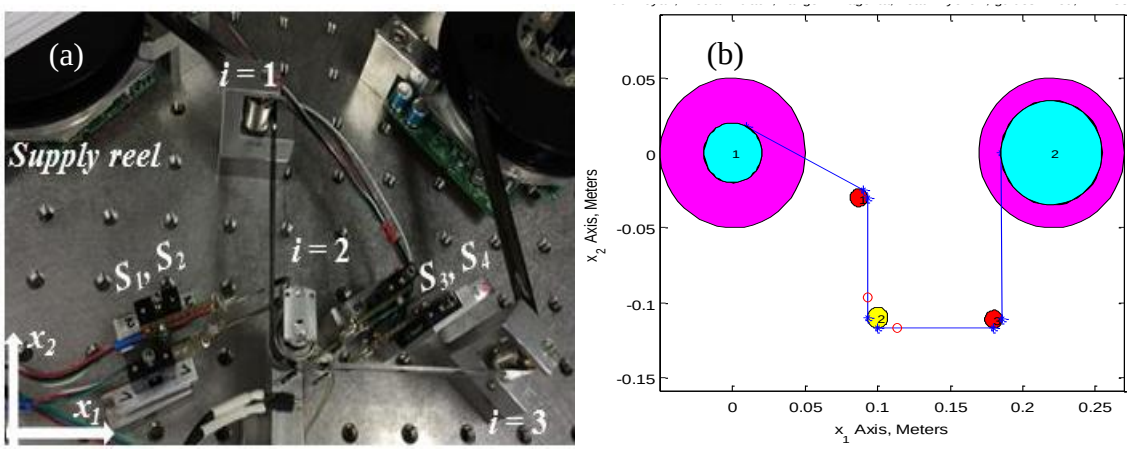

Figure 5-3 Experimental and corresponding simulation tape path

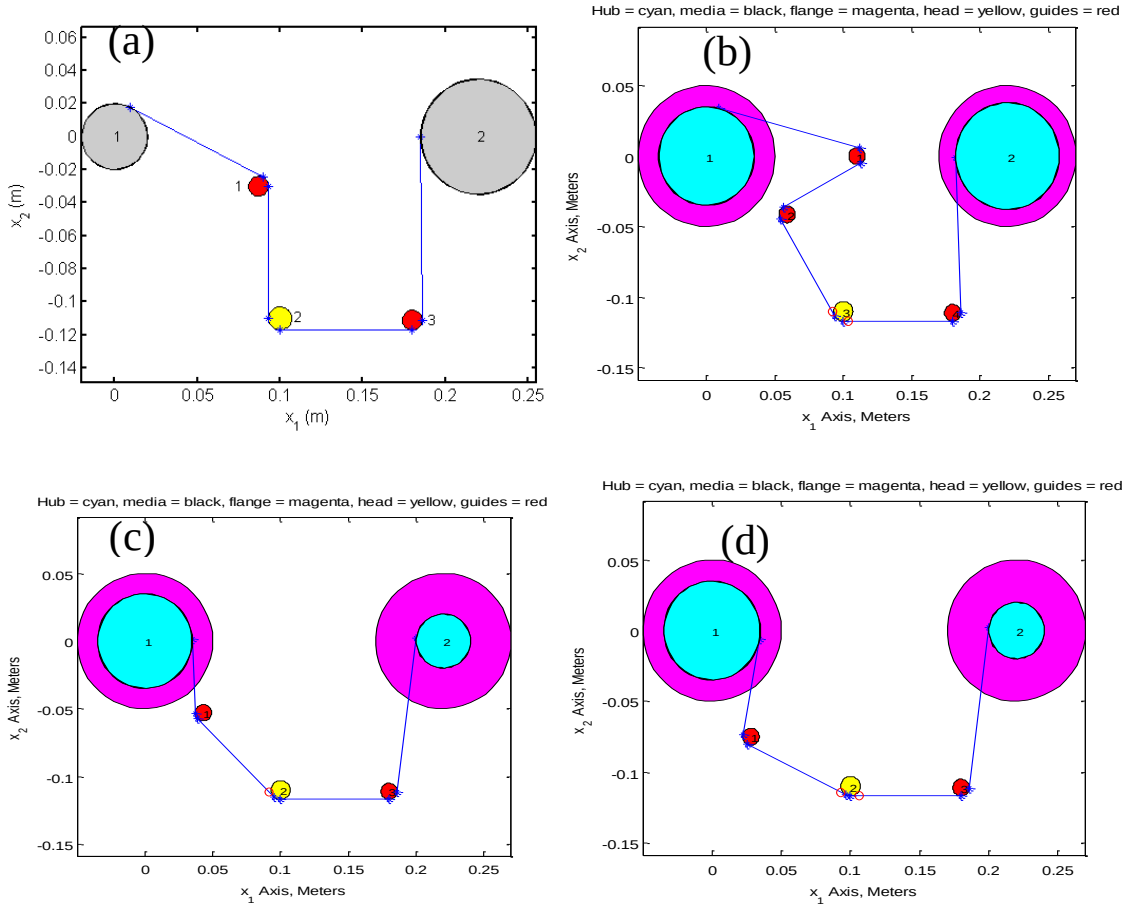

Figure 5-4 Four different entering angle layouts

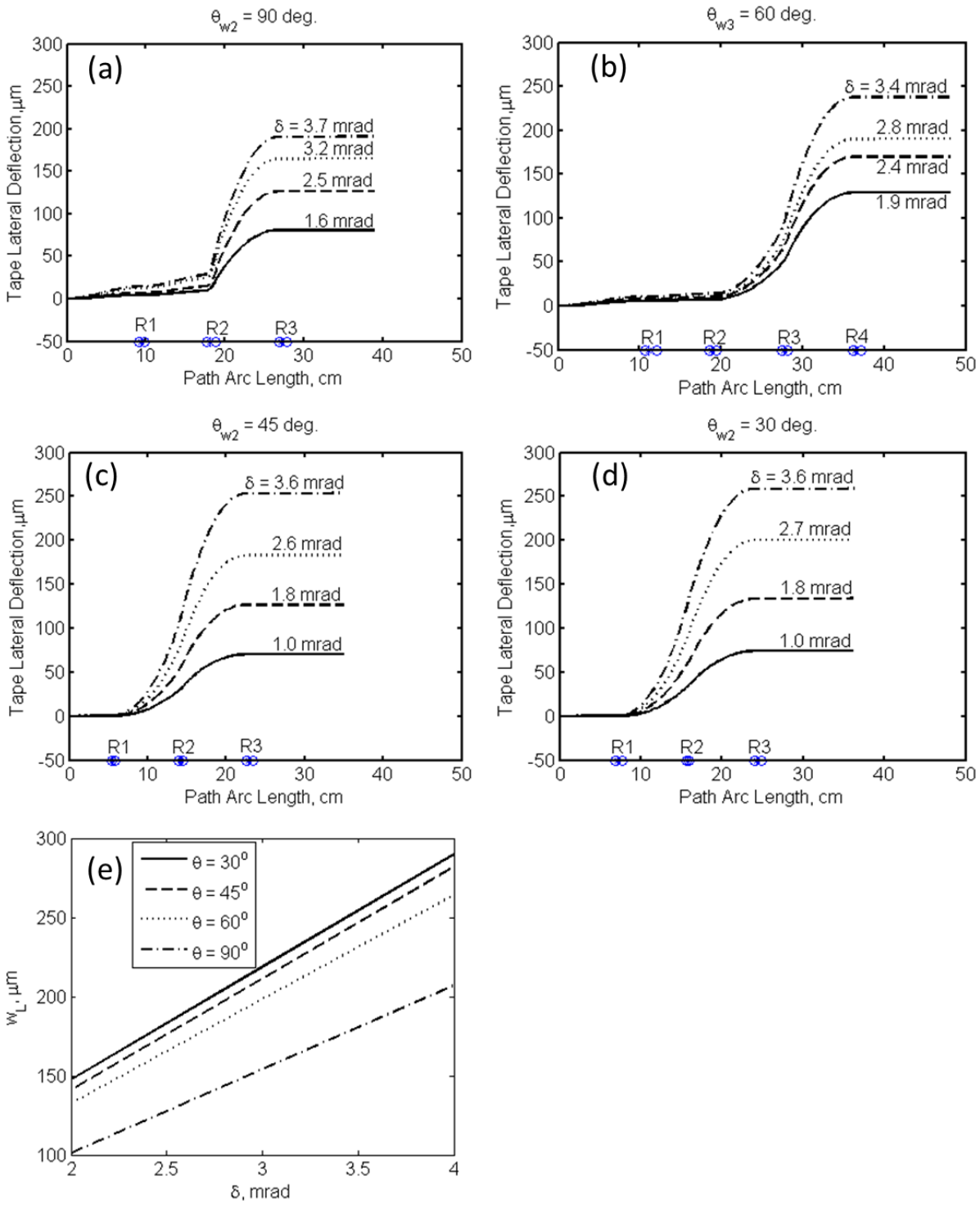

Figure 5-5 Tape steady-state shape of four different entering angles

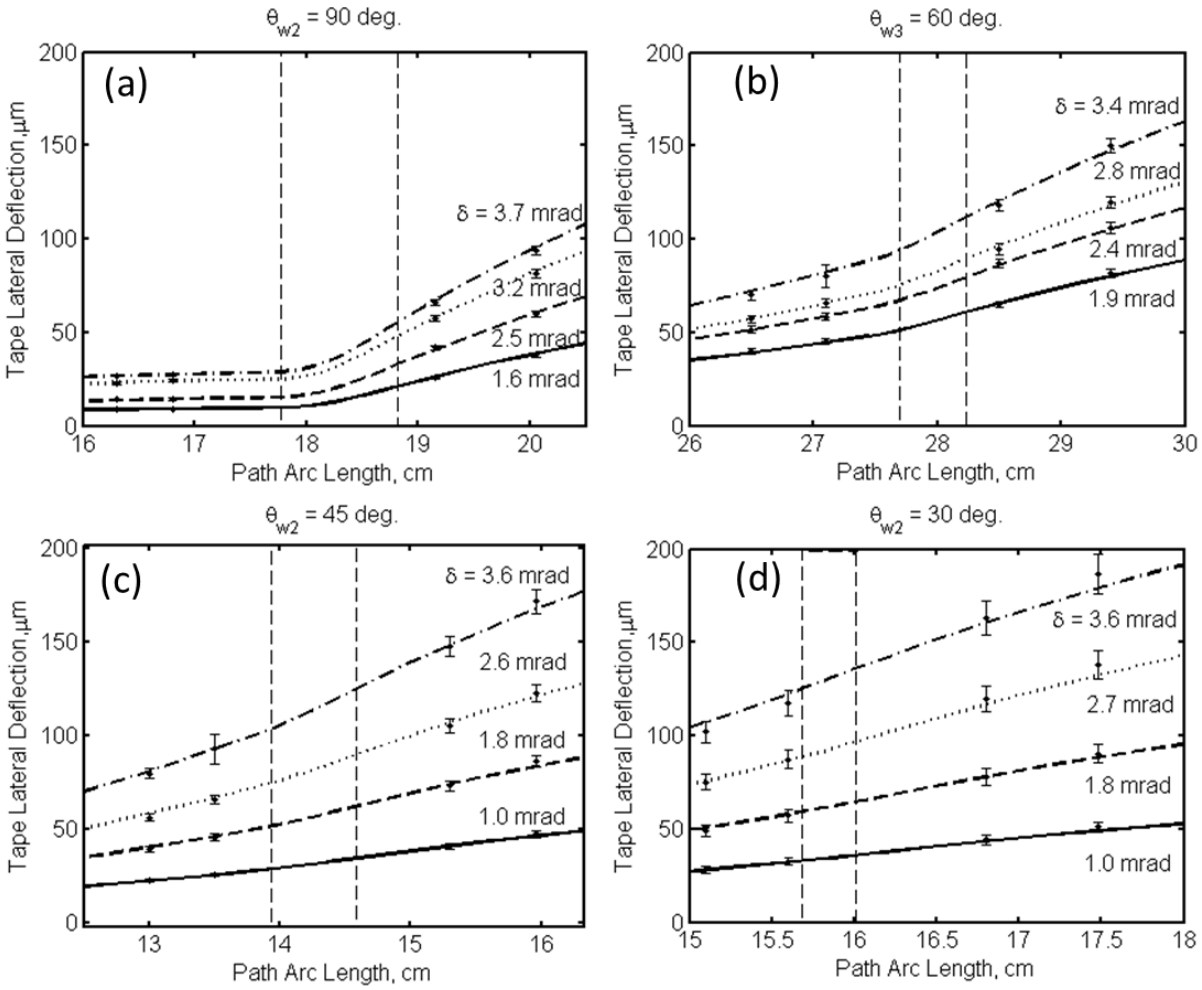

Figure 5-6 LTM at sensor locations and simulated tape deflections of four different entering angles.

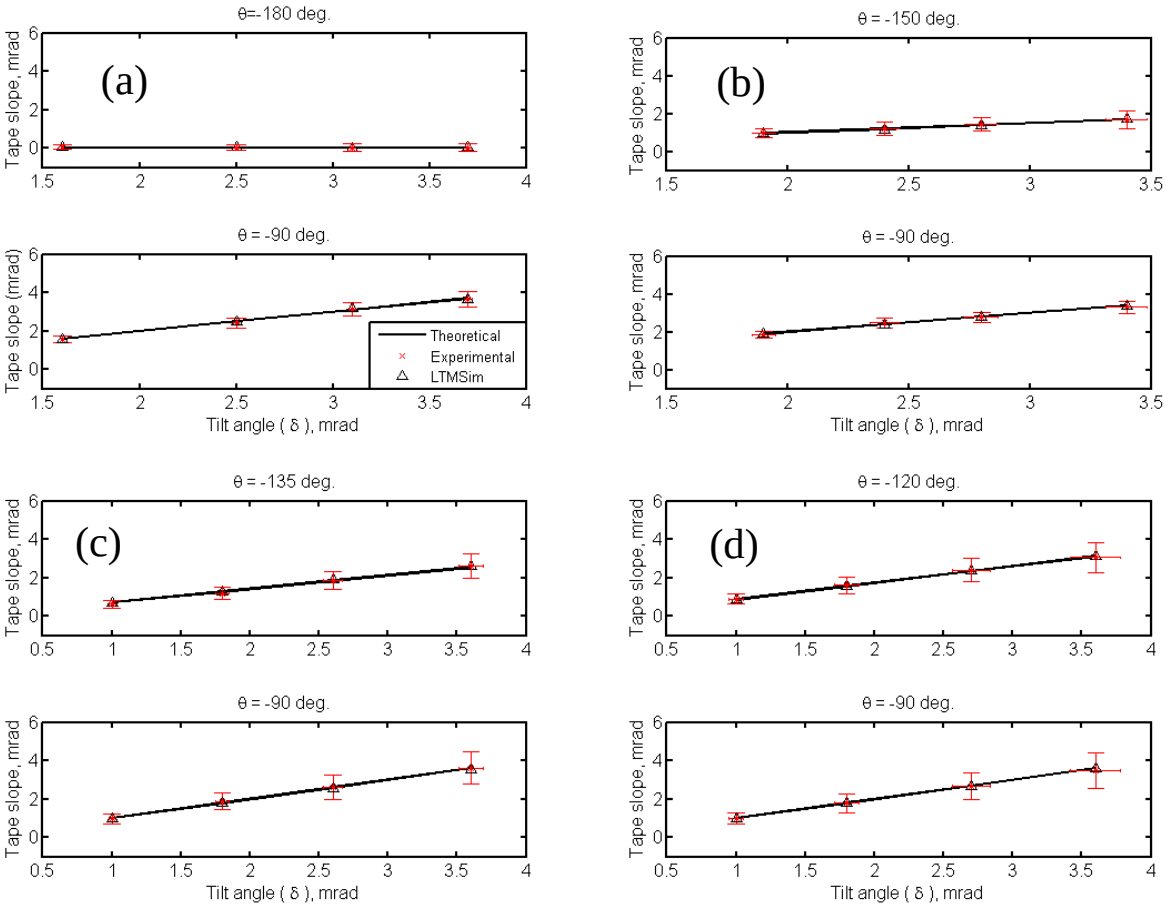

Figure 5-7 Entering and leaving slopes of four different entering angles

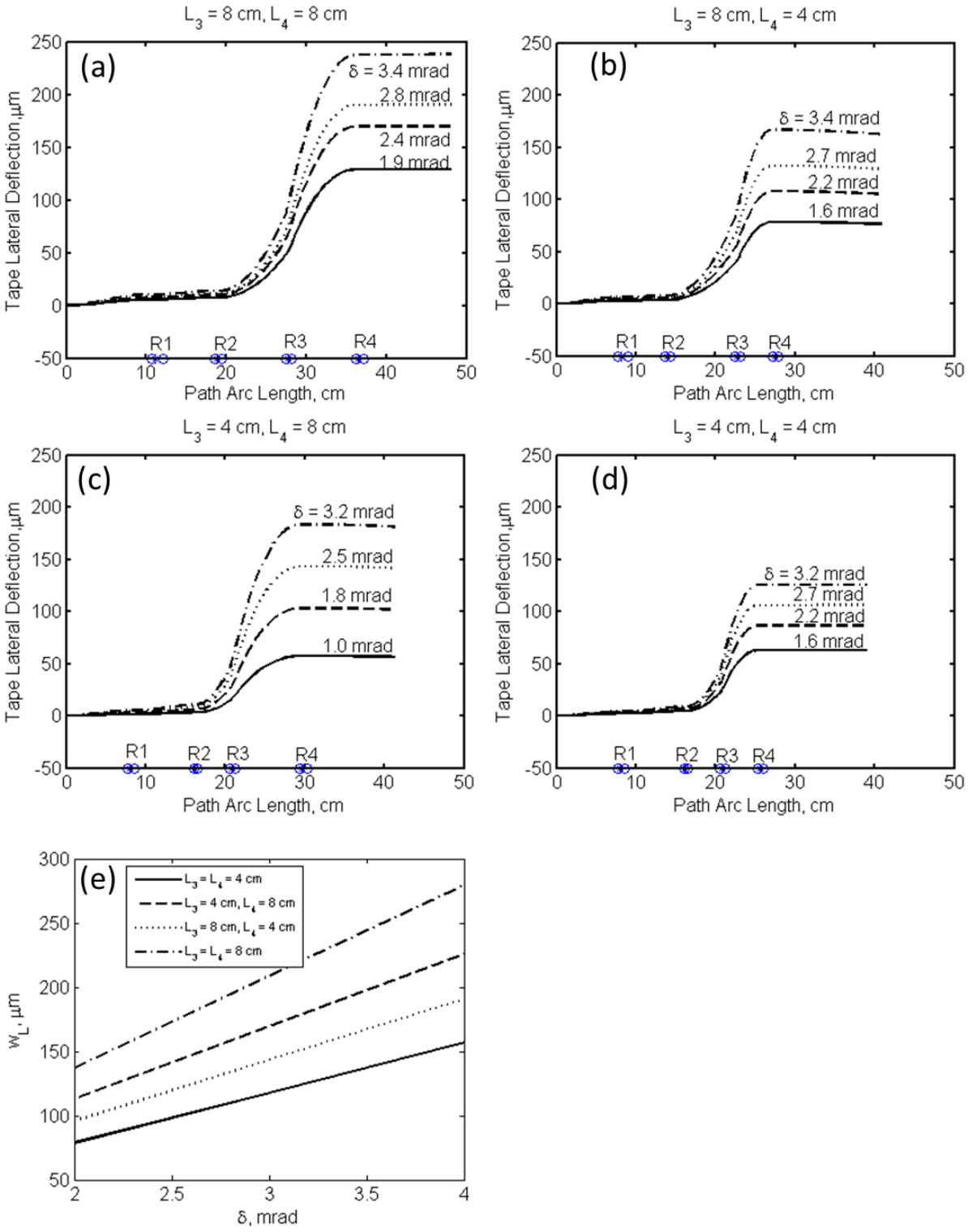

Figure 5-8 Tape steady-state shape of 4 different span length combinations

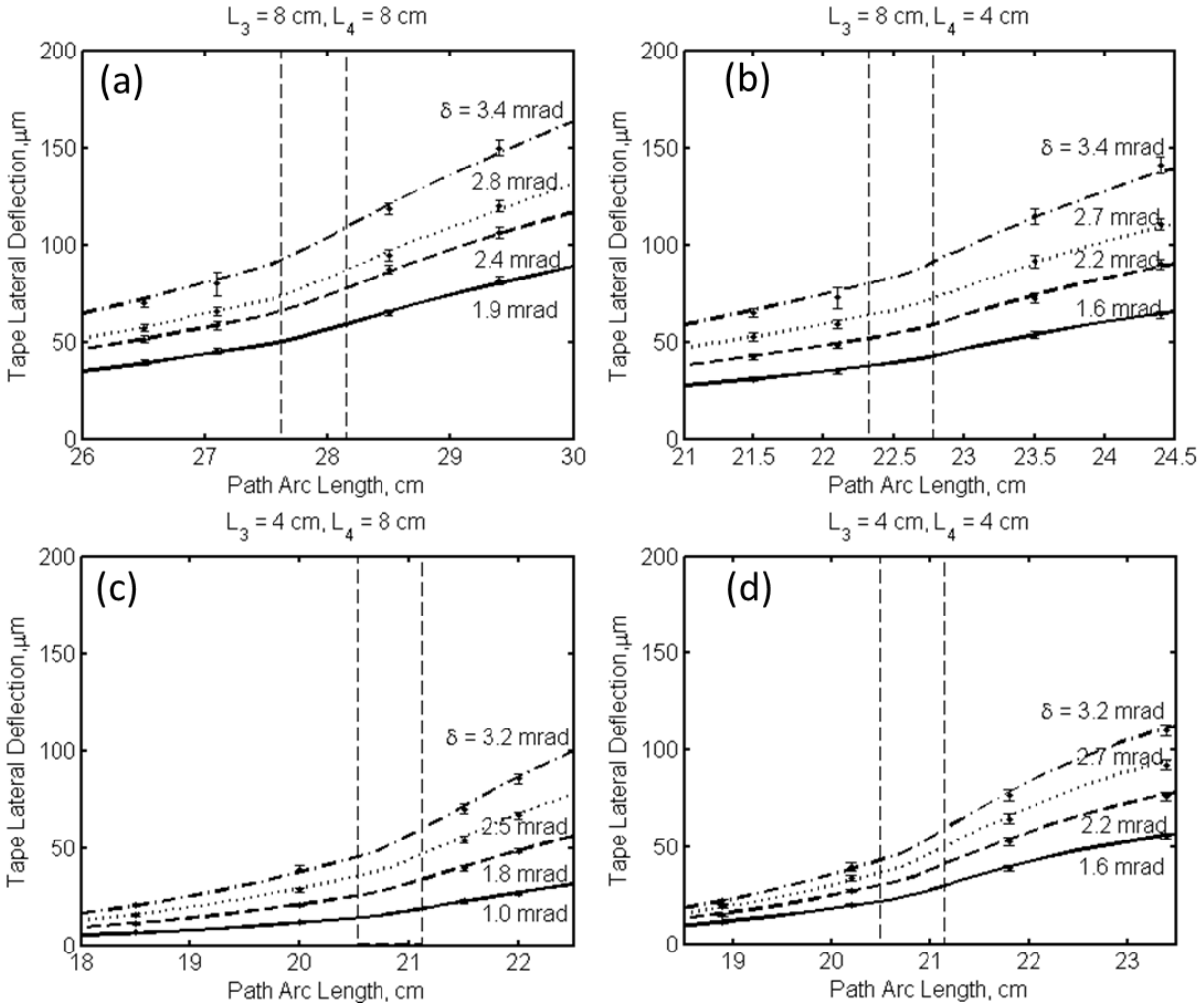

Figure 5-9 LTM at sensor locations and simulated tape deflections of four different span length combinations

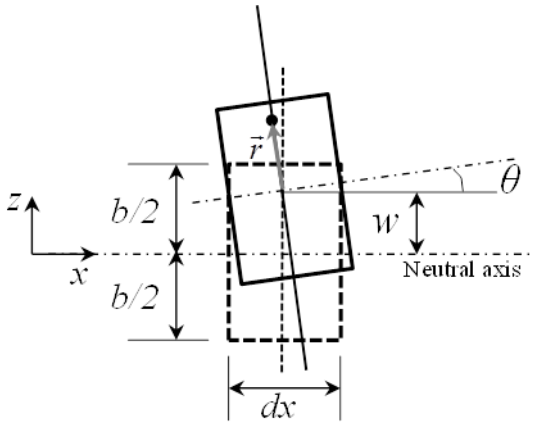

Figure 5-10 Schematic plots of tape lateral motion over roller surface.

Table 5-1 Tape properties and roller radii

Tape properties	
Substrate material	Polyethylene Naphthalate (PEN)
Total tape thickness	6.4 μm
Composite Young's modulus	5.6 GPa
Tape width	12.7×10^{-3} m
Bending rigidity (EI)	5.2×10^{-3} Nm^2
Rollers	
R_1, R_3 (guiding rollers)	6×10^{-2} m
R_2 (tilting roller)	7×10^{-2} m

Table 5-2 Testing parameters used in experiments

Wrap angle θ_{w2} (deg.)	**Tangency points** $\theta_2^{upstream}, \theta_2^{downstream}$	**Tilt-angle** δ (mrad)	**Radii of pack-1 and-2** (m)
90	-180, -90	1.6, 2.5, 3.2, 3.7	2.0×10^{-2}, 3.5×10^{-2}
60	-150, -90	1.9, 2.4, 2.8, 3.4	3.5×10^{-2}, 3.8×10^{-2}
45	-135, -90	1.0, 1.8, 2.6, 3.6	3.5×10^{-2}, 2.0×10^{-2}
30	-120, -90	1.0, 1.8, 2.7, 3.6	2.0×10^{-2}, 3.8×10^{-2}

Table 5-3 Tape span lengths

	Upstream Length, L_1 (cm)	Downstream Length, L_3 (cm)
(a)	8	8
(b)	8	4
(c)	4	8
(d)	4	4

Chapter 6 Stick and Slip Dynamics of a Stationary Tape Interacting with a Laterally Actuated Grooved-Roller: Experiments and Theory

In this chapter the effects of friction forces on the lateral dynamics of a magnetic recording tape, wrapped around a grooved roller are studied experimentally and theoretically. Including the effects of stick and slip and velocity dependence of the friction force render the tape's equation of motion non-linear. In the experiments, tape was wrapped around a grooved roller in a customized tape path, and tensioned. The tape running speed along the axial direction was set to zero, thus only the lateral effects were studied. The grooved roller was attached to an actuator, which moved across the tape. The test was performed in slow and fast actuation modes. Slow mode was used to identify the static, or breakaway friction coefficient. In the fast mode, the roller was actuated and a periodic 'stick-slip' phenomenon was observed. The stick-to-slip and slip-to-stick transitions occurred when the tape vibration speed matched the roller actuation speed. The breakaway forces in the slow and fast actuation modes were similar one another. Both experiments and theory show that upon slip, tape vibrates primarily at its

natural frequency, and vibrations are attenuated relatively fast due to frictional and internal damping.

Literature survey is provided in Section 6.1. Experiments and theory are described in Section 6.2. A discussion of the results is given in Section 6.3.

6.1 Introduction

In modern tape drive systems, rollers with circumferential grooves are often preferred in order to reduce slip between the tape and the roller. Resistance to lateral tape motion (LTM) has been proven to be considerably higher with grooved rollers. In general, two effects are thought to be responsible for this. First, by using a grooved surface the effects of air lubrication in the roller-tape interface are substantially reduced [62, 84]. This provides an adequate amount of contact force, and eventually the Coulomb friction between the tape and the roller provides resistance to LTM. Second, as the tape bends into the grooves, a natural corrugated shape develops which further increases the lateral friction and resistance to LTM.

Ono [19, 67] studied the mechanics of LTM over a frictional guiding-post by using a translating string model. He pointed out that the friction coefficient in the tape-to-guide interface could have different values in the lateral and longitudinal directions. Raeymaekers and Talke [28, 68] extended Ono's work by using a beam model. Raeymaekers and his colleagues also investigated the effect of surface roughness, sliding speed, tape tension, material properties and guide geometry on the tape-to-post coefficient of friction [86] and proposed laser surface texturing to enhance the traction between tape and guide [87]. Their conclusions match well with their experimental results. Yang [58] extended Ono's analysis to accommodate generalized 'cylindrical' rollers. Shelton and Reid [61, 63] modelled lateral tape dynamics over a roller. Three stages of interactions between a tape and a roller, namely stick, circumferential slippage and lateral slippage, were identified by Young, Shelton and Fang [62, 64]. Friction was found to be helpful to reduce the high-frequency lateral tape vibration by Wickert and Kartick [153]. Eaton [59] described mechanics of a string over a post. Brake and Wickert [20] improved Eaton's model and developed a model for the friction induced vibration, in

the case of a laterally actuated cylindrical guide. Moustafa [57] proposed a thread model over a rotating roller surface. Yang *et al*. [154] studied the lateral tape deflection over an imperfect roller. McClelland and Imaino [69] presented a model for tape to roller interaction by using the Timoshenko model. Jape *et al*. [72] experimentally investigated frictional interactions between a roller and a tape and identified regions of predominant-stick or -slip for different operation parameters. Kartik and Eleftheriou [41] proposed a friction-induced model representing actively-positioned read/write head. Engelen and Lantz [155] described the tape-head friction by including contributions from head edges and surface.

As also observed in our experiments, within a dynamic system it is often possible to observe the bodies transition between stick and slip states [156]. The nature of static and dynamic friction forces contribute to stick-slip phenomenon [157-159]. Various analytical approaches have been formulated for modeling stick-slip in single degree of freedom systems. Cameron and Singh investigated the critical value of the driven surface velocity [160, 161]. Shaw showed the effects of viscous damping on stability of the system [162]. Armstrong-Helouvry reported on stick-slip in lubricated metal contacts [163].

In this chapter we describe an experimental method to measure the friction force between the tape and a grooved roller. An experimental setup where one of the rollers can be actuated in the lateral direction is built. This setup was used to measure tape deflections and friction force as a result of the motion of the actuated roller. Resulting friction induced vibration, stick and slip motion between the tape and the actuated roller is measured in dynamic test conditions. A mathematical model of stick and slip in the tape to roller interface is also introduced.

6.2 Experimental Materials and Methods

Tape transport speed was set to be zero for this study. Two sets of experiments were conducted by using the configurable tape path shown in Figure 6-1. Five grooved, flangeless rollers were used in these tests (Figure 6-3). Upstream and the downstream rollers, denoted as supporting rollers, were used to set the wrap angle around the test

roller. Two additional rollers were placed such that the wrap angle of the supporting rollers is sufficiently large. This is aimed to establish a system between two supporting rollers isolated from the other tape path components such as the reels. Tape was tensioned by applying appropriate level of torques to the two reels. The tension fluctuation for running tape is 50 mN (std. dev.) and the stationary tape has tension measured error of ±30mN. In the first (slow mode) test (Figure 6-2a) the lateral traction capacity of the tape-roller interface was tested by moving the testing roller relative to the tape with a micrometer until slip is detected. In the second (fast mode) test (Figure 6-2b)), the central roller was attached to an actuator, and tape dynamics was investigated as the roller was actuated in the lateral direction. Figure 6-1d shows the top view of experiment setup. In this work the tape transport speed was set to zero in order to isolate to the basic frictional interaction characteristics between the tape and the roller. The experimental parameters and the mechanical properties of the tape used in these tests are given in Table 6-1.Note that the reported elastic modulus value E = 4.42 ± 0.122 GPa was measured by using a CETR-UMT (Bruker, Campbel, CA). The loss modulus η value of 23,000 Pa.s was obtained by using our model and fitting to the experimental results. The thickness h = 6.4 μm and width b = 12.7 mm of the tape are standard for the LTO-5 tape [1]. The mass density of the tape is 1,400 kg/m^3 [21].

6.2.1 Experimental characterization of static friction behavior

The tractive capacity of the tape-roller interface in the lateral direction, with zero tape transport velocity, was measured by using the test configuration shown in Figure 6-2a. The test roller was attached to a hand operated micrometer moving in the lateral direction. The total lateral force acting on this roller was measured using a Honigmann RFS 150 XY strain gauge sensor (10N range) connected to a Tensiotron TS 621 HD amplifier. The lateral roller displacement d and the lateral tape displacement w are measured by two photogate position sensors (custom built). The relationship between the tape deflection and the lateral force acting on the roller due to a tensioned stationary tape was measured by manually displacing the roller with the micrometer. An example measurement is shown in Figure 6-4 with tape tension T = 0.25 N, and wrap angle θ_w = 15 degrees. This

measured force versus displacement relationship is used to calibrate the effective stiffness of the tape. The details of these measurements are explained in Section 6.3.1.

6.2.2 Experimental characterization of dynamic friction behavior

The dynamic slip characteristics of the tape-roller interface in the lateral direction, without tape transport, were investigated using the test configuration shown in Figure 6-2b. The test roller was mounted on an actuator that can move the roller in the axial direction. Four custom-built photogate position sensors were placed on the tape path to measure LTM. Sensor-2 measures the LTM near the actuated roller. Sensor-3 measures the roller displacement. Sensors-1 and -4 are located at the entry side of roller-2 and exit side of roller-4, respectively. Typical LTM signals obtained from sensors-1 and -4 are shown in Figure 6-5a; the tape displacements at sensor-1 and sensor-4 are much smaller O(± 0.2 μm) than the LTM imposed by the actuator at roller-3. This implies that the imposed LTM does not pass through rollers-2 and -3. LTM signals from sensor-2 for two different roller actuation amplitudes are shown in Figure 6-5b and 4c. The balance between the interface friction and tape restoring forces is maintained such that the tape moves synchronously with the roller in Figure 6-5b, in which case the maximum roller amplitude is about 55 μm. On the other hand when the roller amplitude is increased to 150 μm the tape can follow the roller only for 80 μm beyond which it slips (Figure 6-5c). The corresponding tape and roller velocities (Figure 6-5d) reveal that following the slip event, the tape velocity oscillates around 0 m/s with gradually decreasing amplitude. At the same time the roller velocity decreases and changes direction due to sinusoidal excitation. At the point when the tape and roller velocities match, at approximately 0 m/s, the tape starts moving with the roller in the opposite direction. The static friction force is calculated from the measured displacement at which slip occurs and the measured effective tape stiffness.

6.2.3 Theory

The tape mechanics between the upstream and downstream support rollers is modeled as a tensioned, Euler-Bernoulli beam, with internal dissipation (Figure 6-6). The tape deflections on the upstream and downstream rollers are negligible as mentioned above.

Based on Shelton's law [61, 63] and a recent study by the authors [154] it is reasonable to assume that the tape on the two supporting rollers can be modeled to have clamped boundaries for which tape deflection and slope are zero (Figure 6-6). The test roller is located at the center of the span, with equal free span lengths L_1 and L_2. The test roller is wrapped by the tape at angle θ_w. The total length of the tape between the supports is $L = L_1 + L_2 + R\theta_w$. The test roller interacts with the tape by contact and shear stresses, which are due to belt-wrap pressure and friction. The equation of motion of the tape as described in Chapter 3 and Chapter 6 is,

$$\rho A\left(\frac{\partial^2 w}{\partial t^2}+2V_x\frac{\partial^2 w}{\partial t\partial x}+V_x^2\frac{\partial^2 w}{\partial x^2}\right)+EI\frac{\partial^4 w}{\partial x^4}-\frac{\partial}{\partial x}\left(T\frac{\partial w}{\partial x}\right)+\eta I\frac{\partial^5 w}{\partial t\partial x^4}++\eta IV_x\frac{\partial^5 w}{\partial x^5}=-H(x)q_f \tag{6.1}$$

where w is the lateral tape deflection, x is the longitudinal coordinate axis, t is time, ρ is the mass density of tape, A is the cross section area of tape. V_x is the tape translating velocity, E is the elastic modulus, η is the loss modulus, I is the second moment of area of the tape cross-section, T is the tape tension, and q_f is the magnitude of the friction force acting in the lateral direction. H is a window function with value 1 when the tape is over a guide ($L_1 \le x \le L_1 + R\theta_w$) and 0 otherwise. In this work, the tape translation velocity V_x is zero. The friction force per length q_f acting between the tape and the roller is assumed to be due to Coulomb friction,

$$q_f = -\mu F_c \operatorname{sgn}\left(v_{rel}\right) \tag{6.2}$$

where the magnitude of contact force per length is F_c and relative lateral velocity between the roller and the tape is,

$$v_{rel} = \frac{\partial w}{\partial t} - v_{roller} \tag{6.3}$$

with $v_{roller} = \frac{d}{dt}d_r$ as the roller velocity and d_r as the roller displacement. In this work, the contact force per length F_c is assumed to be equal to T/R.

While friction force is proportional to normal force, it can also be speed dependent [164]. Dependence of the friction force on speed can be conveniently represented in terms of the coefficient of friction μ. In the simplest model, static (break-away) friction force can be greater than the dynamic friction force. In lubricated contacts, the Stribeck effect could cause a relatively smooth but physically complex transition between static and dynamic friction coefficients. These possibilities are depicted in Figure 6-7. Speed dependence of the friction force (Figure 6-7b) can be represented in terms of the coefficient of friction μ as follows,

$$\mu(v_{rel}) = (\mu_s - \mu_d)e^{-a|v_{rel}|} + \mu_d \tag{6.4}$$

where the parameter *a* controls the rate of decay of the coefficient of friction with increasing velocity from static friction coefficient μ_s to an asymptotically reached dynamic friction coefficient μ_d. The parameter *a* is set to be zero in this study.

In general, two bodies that are in contact exchange tangential (friction) and normal tractions on the contact plane. Due to the nature of the friction force, and depending on *i*) the relative velocity between the two surfaces, and *ii*) the balance of friction $\vec{F}_f$, external $\vec{F}_e$ and restoring $\vec{F}_r$ forces, the two bodies continue their relative motion, albeit affected by frictional loading, or they become stuck, and move synchronously. If the relative velocity between the surfaces is zero, despite the fact that an external force is applied on the system, the two bodies are said to be in a stick state. In this case, the friction force is smaller than the limiting, static friction (or break-away) force. On the other hand, if the relative velocity between the surfaces is greater than zero, the friction force is equal to the dynamic friction force. In general, the friction force vector is expressed as follows,

$$\vec{F}_f = \begin{cases} -\left(\vec{F}_e + \vec{F}_r\right) & \text{if } \vec{v}_{rel} = 0, \text{ with } \left|\vec{F}_e + \vec{F}_r\right| < \left|\vec{F}_{fs}\right| \\ -\mu F_c \dfrac{\vec{v}_{rel}}{\left|\vec{v}_{rel}\right|} & \text{if } \left|\vec{v}_{rel}\right| \neq 0 \end{cases} \tag{6.5}$$

where $\vec{F}_{fs}$ is the breakaway friction force and μ is given by Equation (6.4). The restoring force $\vec{F}_r$ includes inertial, damping and structural stiffness effects and $\vec{F}_e$ represents all external effects, except for friction forces. Based on this discussion, the friction force per unit length q_f acting on the tape can be obtained from Equation (6.5) as follows,

$$q_f = \begin{cases} -\left(F_{et} + F_{rt}\right) & \text{if } v_{rel} = 0 \\ -\mu \dfrac{T}{R} \operatorname{sgn}\left(v_{rel}\right) & \text{if } v_{rel} \neq 0 \end{cases} \tag{6.6}$$

We have dropped the vector notation because all forces and velocities are along the lateral direction. The subscript $_t$ indicates that the external and restoring forces are specific to Equation (6.1). The restoring force F_{rt} is represented by the left hand side of Equation (6.1) and external force F_{et} is zero in this study.

The friction force in this vibrating tape system depends on the lateral sliding direction of the tape. This renders the equation of motion non-linear. Additional system nonlinearity is due to the nature of the friction force. In particular, the discontinuity at $\vec{v}_{rel} = 0$ is of concern. Regularization of this discontinuity in the friction force was proposed by Karnopp [165]. Haessig and Friedland suggested two improved models based on Karnopp's model [166]. Their models removed the discontinuity in friction force in Karnopp's model, but this model did not balance the external force [167]. Quinn [168] proposed a new regularization method which can both remove the discontinuity and maintain the consistency. Quinn's model described the friction as a function of relative velocity if slip occurs, and a function of external force if stick occurs. A fixed-step friction model was designed by Kikuuwe *et., al* [167] aiming to obtain absolute zero relative velocity at the sticking phase. However, their method only works for the case of a stationary base.

In a numerical solution, an exact value of zero relative velocity is rarely reached; therefore, a narrow range of relative velocity $\left|\vec{v}_{rel}\right| < \varepsilon$ is defined to represent the stick

region. The slip state occurs when the net force $\left|\vec{F}_e + \vec{F}_r\right|$ is greater than the static friction force, and the relative velocity lies outside the stick-range. While this description is often applied to stick and slip of single degree of freedom systems, here it is generalized to one dimensional continuous systems. For any tape material point on the roller, Quinn's model is used to regularize Equation (6.6) in stick phase by ε as function of relative velocity, but also as function of net force [168] as follows,

$$q_f(x) = \frac{T}{R}\begin{cases} -\mu_s \dfrac{\bar{v}_{rel}(x)}{\varepsilon} & \text{if } \left|\bar{v}_{rel}(x)\right| \le \varepsilon \\ -\mu \operatorname{sgn}\left(\bar{v}_{rel}(x)\right) & \text{if } \left|\bar{v}_{rel}(x)\right| > \varepsilon \end{cases} \tag{6.7}$$

where

$$\bar{v}_{rel}(x) = \begin{cases} v_{rel}(x) + \varepsilon \dfrac{F_{rt}(x) + F_{et}(x)}{\mu_s \dfrac{T}{R}} & \text{if } \left|F_{rt}(x) + F_{et}(x)\right| \le \mu_s \dfrac{T}{R} \\ v_{rel}(x) + \varepsilon \operatorname{sgn}\left(F_{rt}(x) + F_{et}(x)\right) & \text{if } \left|F_{rt}(x) + F_{et}(x)\right| > \mu_s \dfrac{T}{R} \end{cases} \tag{6.8}$$

μ_s and μ_d are determined according to Equation (6.4). This model is also visualized in Figure 6-7c. Note that the dynamic friction force can generated by Figure 6-7a or using Equation (6.4). A transient solution to the system of equations (6.1), (6.3), (6.4), (6.7) and (6.8) is obtained numerically as outlined in Chapter 3.

6.3 Results

6.3.1 Static friction test

Figure 6-4 shows the force acting on the roller and the lateral displacement of the tape edge as function of time, as the roller is moved by the micrometer as described in Section 6.2.1. The micrometer motion starts at time t_1. Between t_1 and t_2, the friction in the tape-roller interface is sufficient to keep the tape motion in phase with the roller. The static friction force is greater than or equal to the tape restoring force during this interval. The maximum static friction force that the interface can bear is reached at t_2, after which the force balance at the interface is broken and slip occurs. The tape displacement at this

breakaway point w_b and the corresponding force acting on the roller are recorded. A jump in signal is observed at time t_2 as a consequence of the slip event. After t_2 the tape and the force signal stay constant, while the roller displacement sensor signal keeps increasing until t_3 when the micrometer motion is stopped. The slipping portion of this curve is not of interest in this part of the experiments.

The force acting on the roller as a function of roller displacement d_r, is shown for three different tensions and wrap angles in Figure 6-8. This shows that the force-displacement relationship is nonlinear. While the curves for different wrap angles are approximately coincident, the end point of each curve, which represents the breakaway point w_b, becomes larger with increasing wrap angle. Up to the point where the tape slips, the measured friction force F_f is equal to the restoring force F_r exerted by the tensioned tape on the roller for a tape deflection equal to w,

$$F_r = F_f = g(w) \tag{6.9}$$

where $g(w)$ represents a polynomial fit to the curves in Figure 6-8 (see Table 6-2). The maximum friction force F_{fs} that the interface can sustain is found at the breakaway point. The static coefficient of friction (COF) μ_s can then be determined by assuming Coulomb friction in the interface as follows,

$$F_{fs} = \mu_s p_c A_c = \mu_s T \theta_w \tag{6.10}$$

where μ is coefficient of friction (COF), p_c (= T/Rb) is contact pressure, and A_c (= $R\theta_w b$) is contact area, where b, R and θ_w indicate the tape width, roller radius, and wrap angle, respectively.

The non-linearity of $g(w)$ is attributed to wrinkle formation in the tape, which reduces the tension and thus the lateral stiffness of the tape [123]. Beisel [169] describes the critical shear stress (F_{cr}/hb) that causes wrinkling in a tensioned, orthotropic plate due to a lateral force applied by a roller. For isotropic materials the critical lateral force is given as follows,

$$F_{cr} = hb\left[\frac{\pi}{L}\left(\frac{\pi}{L}\frac{E^*}{3}\frac{hT}{b} + \sqrt{\frac{E^*}{3}\frac{T^3}{hb^3}}\right)\right]^{1/2} \tag{6.11}$$

where $E^* = E/(1-\nu^2)$, E is elastic modulus, ν is Poisson's ratio, and h is thickness of the tape. For small values of tape deflection, the load-deflection response can be calculated by using the equation of equilibrium of the tensioned Euler-Bernoulli beam, with clamped-clamped boundaries. The load on the tape due to frictional forces is assumed to be concentrated mid-span (L/2), resulting in the following shape for the tape,

$$w(x) = \frac{-F_f}{2EI\lambda^3}\left(\tanh\frac{\lambda L}{4}\left[\cosh\lambda x - 1\right] + \sinh\lambda x - \lambda x\right) \tag{6.12}$$

where $\lambda = (T/EI)^{1/2}$. Before the breakaway happens, the mid-span tape deflection w(L/2) is equal to the roller displacement d_r,

$$w\left(\frac{L}{2}\right) = d = -\frac{F_f}{EI\lambda^3}\left(\tanh\frac{\lambda L}{4} - \frac{\lambda L}{4}\right) \tag{6.13}$$

Thus, we can define an *effective tape stiffness* k_{eff}^t as follow,

$$k_{eff}^t = -\frac{EI\lambda^3}{\tanh\frac{\lambda L}{4} + \frac{\lambda L}{4}} \tag{6.14}$$

We calculate that experimental tape stiffness k_{eff}^e values in the regime where the friction force is subcritical ($F < F_{cr}$), as predicted by Equation (6.11). The tape stiffness values calculated from Equation (6.14) deviate less than 3% from the experimental tape stiffness values (see Table 6-3).

The breakaway position w_b is in the non-linear region of the experiments. Figure 6-9 shows the results of the dynamic tests. The results in Figure 6-9 will be further discussed in Section 6.3.2. Figure 6-9a and Figure 6-9b show all breakaway displacements measured and the corresponding friction force values $g(w_b)$, as a function of tape tension and wrap angle. The static coefficient of friction μ_s in the lateral direction, which

determines the lateral tractive capacity for the tape-roller interface, can be found as follows,

$$\mu_s = \frac{g\left(w_b\right)}{T\theta_w} \tag{6.15}$$

and shown in Figure 6-9c.

6.3.2 Dynamic friction test

The dynamic friction characteristics of the tape-roller interface were investigated by the actuated roller set-up described in Section 6.2 and Figure 6-1c, with the parameters listed in Table 6-1. The tape deflection on the support rollers was negligibly small compared to the roller displacement (Figure 6-5a). Sensors-2 and -3 measure the tape deflection $w(x^*)$ and roller displacement d_r, respectively, where x^* indicates the location of sensor-3 adjacent to the actuated roller (Figure 6-1b). A typical output (Figure 6-5b,c) of these sensors shows that as the roller is actuated, the tape is driven laterally by the surface friction force. Depending on the actuator motion amplitude, the tape can move synchronously with the roller (Figure 6-5b), or can break away (Figure 6-5c). In case the tape breaks away, it vibrates around a fixed position with decreasing (damped) amplitude until the roller's lateral speed and the tape speed match. The tape then re-synchronizes with the roller when their speeds are equal. This happens when the tape vibration velocity is near zero. The tape then moves synchronously with the roller, until breakaway occurs on the opposite side of the sinusoidal roller displacement. This stick and slip behavior continues with the period of roller motion. The phase shift between the roller and tape signals stems from the fact that after breakaway, the roller moves continuously in the lateral direction, while tape vibrates around the breakaway point.

The breakaway friction forces in the lateral direction as measured through dynamic experiments are given in Figure 6-9a. The corresponding coefficient of friction μ_s values are calculated using Equation (6.15). Each experiment has duration of 5 seconds and was repeated three times. The actuator frequency was 50 Hz. The friction force and COF results that are reported represent the average of 750 cycles. Table 6-4 lists the average

COF values (μ_{mean}) and corresponding standard deviation (μ_{std}) for the 9 cases. The overall COF measured is $\mu_s = 0.40 \pm 0.035$.

The interactions between the tape and the roller were simulated by using the theoretical model presented in Section 6.2.3. The model was solved numerically as described in the Appendix. Note that the grooved nature of the rollers is not modelled, and instead a constant COF is used for the tape-roller contact area. The measured roller displacement was used as an input to the model. For each tension and wrap angle the measured breakaway friction coefficient values reported in Figure 6-9c and Table 6-4 were used. For example, for the case where the tension is 0.5 N and the wrap angle is 15 degrees, a breakaway coefficient of friction in the range of $\mu_s = 0.41 \pm 0.041$ was used. The simulation results and the experimental measurements are compared in Figure 6-10. As expected, the breakaway predicted by the model depends on the COF value. The model predicts the breakaway displacement reasonably well (Figure 6-10a). Both the experiments and the model show that, following the slip event, the tape vibrates with a considerably higher frequency than the roller actuation frequency. The vibration amplitude is damped until the tape and roller "stick" again, as explained above. The model accounts for frictional and internal damping (loss modulus is reported in Table 6-1), but does not account for the grooved nature of the roller surface. Under tension, the tape bends into the grooves, leading to additional internal damping. A recent study [170] showed that the contact pressure along the edges of the lands is higher than the belt wrap pressure (T/Rb). We therefore expect higher frictional damping in the experiments as observed.

The COF value that results in the experimentally measured breakaway position was found by numerical experimentation. Figure 6-9b demonstrates that $\mu_s = 0.4$ gives the best match for this case. For all tension and wrap angle combinations, the μ_s value that closely simulates the experimental breakaway position was found to be very close to the average of the measured COF value reported in Figure 6-9c. Table 6-4 shows the COF values used in the theoretical calculations that give the best match to the experimentally measured breakaway position.

Figure 6-11 shows a comparison of the computed and measured tape deflection and tape vibration velocity traces for the case of T = 0.25 N and θ_w = 10 degrees with the best fit COF value. The stick and slip behavior is captured well in the model, with good predications for the breakaway displacement, sticking velocity, and phase plane behavior of the system. The model predicts a slightly lower onset velocity than the measurements. Note that breakaway occurs at displacements where the tape is likely to have buckled as described in Section 6.3.1. As the model does not take this effect into account, the simulated force-displacement response is stiffer than the measurements.

It is also interesting to note that roller trajectory is not symmetrical, which is clearly seen in the phase-plane (Figure 6-11c). The root cause of this behavior is due to the coupling of the roller dynamics to the tape and presence of gravity. These effects are not modeled in this work.

Finally, the frequency content of the vibration after the slip event is investigated. Figure 6-12 shows a typical plot of the tape velocity vibration frequency versus vibration amplitude obtained by using the fast Fourier transform (FFT) for the case of T = 0.25 N and θ_w = 10 degrees. The vibration is dominated by the roller frequency and its higher harmonics, as expected. Measured and simulated results agree well. The frequency analysis also shows that the first resonance of the tape is excited. In Figure 6-12 this occurs at ~2450 Hz. Incidentally, tape vibrates with this frequency in the sliding phase as shown in detail in Figure 6-10b. This indicates that the stick-to-slip transition creates an impulse-like load which excites a wide band response in the tape. This high frequency tape motion is of particular interest and concern as it is very challenging for the track follow control system of a tape drive to follow such high frequency motion. The slip phase event in time and frequency domain as plotted in Figure 6-13 for the case of T = 0.25 N and θ_w = 10 degrees within 17~25 ms. Simulation accurately catches the tape velocity response at the beginning of sliding phase. The FFT plot shows a clearer frequency signal that that model predicts the natural frequency close to the test.

Theoretical natural frequencies of the tape are computed by two different approaches. First, an eigenvalue analysis of the tape vibration is performed as described in Chapter 4. Second, the natural frequency is obtained from the FFT plot of the computed tape

response (e.g. Figure 6-11). These two computed frequencies are compared with the measured values for all parameters used in this work in Table 6-5

The natural frequency decreases with increasing wrap angle. This is due to an increase of the total length of tape, as a results of which the system become more compliant. The effect of tension on natural frequency is not significant in this range of tension values. The natural frequency obtained by eigenvalue analysis represents the free vibration of a clamped, tensioned beam. The natural frequency of the numerical simulations represents the vibration characteristics of a non-linear system, rendered so by the velocity dependence of the friction force. The differences between the eigenvalue analysis and computed results are within 10%. Note that the measured natural frequencies are closer to the values found from numerically simulated tape response described in Section 2.3, indicating the influence of friction induced non-linearity in the system.

6.4 Conclusion

In this chapter, the lateral traction characteristics of a grooved roller and a magnetic recording tape are investigated experimentally and theoretically. The tape is modeled as a viscoelastic, tensioned beam subjected to belt wrap pressure and friction forces. The inclusion of stick and slip and velocity dependence of the friction force renders the tape's equation of motion non-linear. In the experiments, the tape is tensioned (0.25 – 0.75 N) and wrapped (10 – 20 degrees) around a grooved roller in a customized tape path. The tape running speed is set to zero. A grooved roller is attached to an actuator that moves the roller laterally across the tape. The test was performed in static (slow) and dynamic (fast) actuation modes. The static mode was used to measure the tape restoring force in the lateral direction (tape stiffness) and to identify the tractive capacity and the static/breakaway friction coefficient. We found COF values in the range of 0.40± 0.035. In dynamic mode, the roller was actuated with 50 Hz frequency and more than 200 μm amplitude. A periodic stick and slip phenomenon was observed. Stick-to-slip and slip-to-stick transitions occur when the tape lateral speed matches the roller lateral speed. This occurred near zero tape and roller velocity. The fast actuation mode, which exhibited stick and slip phenomena, shows that the tractive behavior of the tape is similar to the results of the slow actuation mode for all tested parameters. Both experiment and theory

show that upon slip, tape vibrates primarily at its natural frequency, and vibrations are attenuated relatively fast due to frictional and internal damping. This work also indicates that the friction resulting from the complex interaction and bending of a tape tensioned over a grooved roller can be well described by an effective coefficient of friction for a range of wrap angle and tension values. Moreover, within the experimental uncertainty the results can be captured with a single coefficient of friction for the range of tensions and wrap angles studied. For the tape type and roller design studied here we find a COF value of 0.42 ± 0.02 fits the experimental results well. This indicates that by making a single experimental measurement of friction for a given roller design and tape type, our model can be used to predict the behavior over a wide range of wrap angles and tape tensions. The effects of tape streaming velocity and the coupling between roller and tape dynamics are interesting topics for future studies.

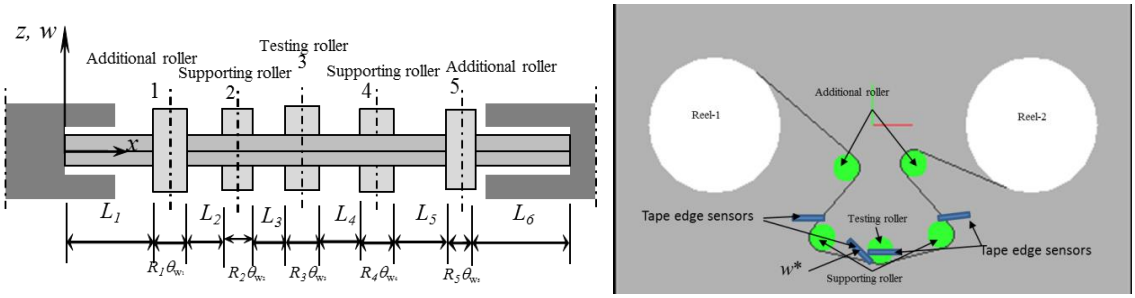

(a) (b)

Figure 6-1 (a) Schematic depiction of the configurable tape path. (b) Topview of the test setup.

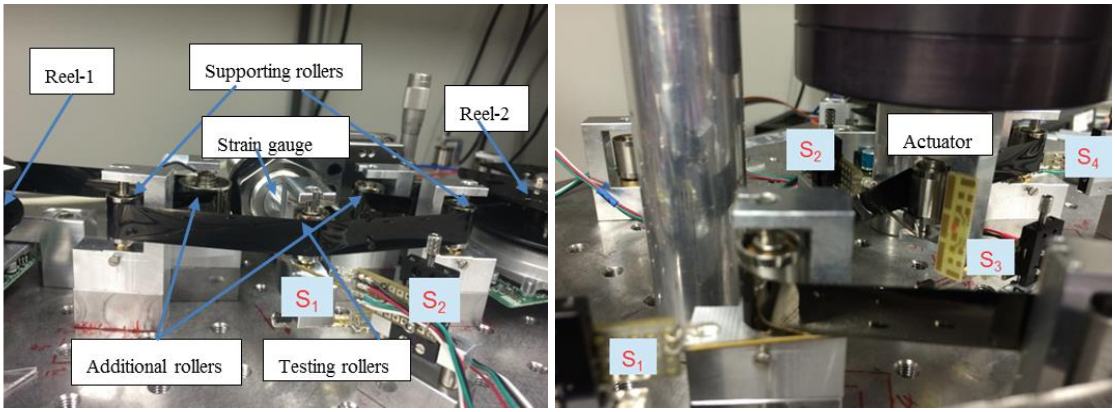

(a) (b)

Figure 6-2 (a) The setup used for studying the stick and slip behavior between the tape and the actuated roller, (b) The setup used for studying the stick and slip behavior between the tape and the actuated roller

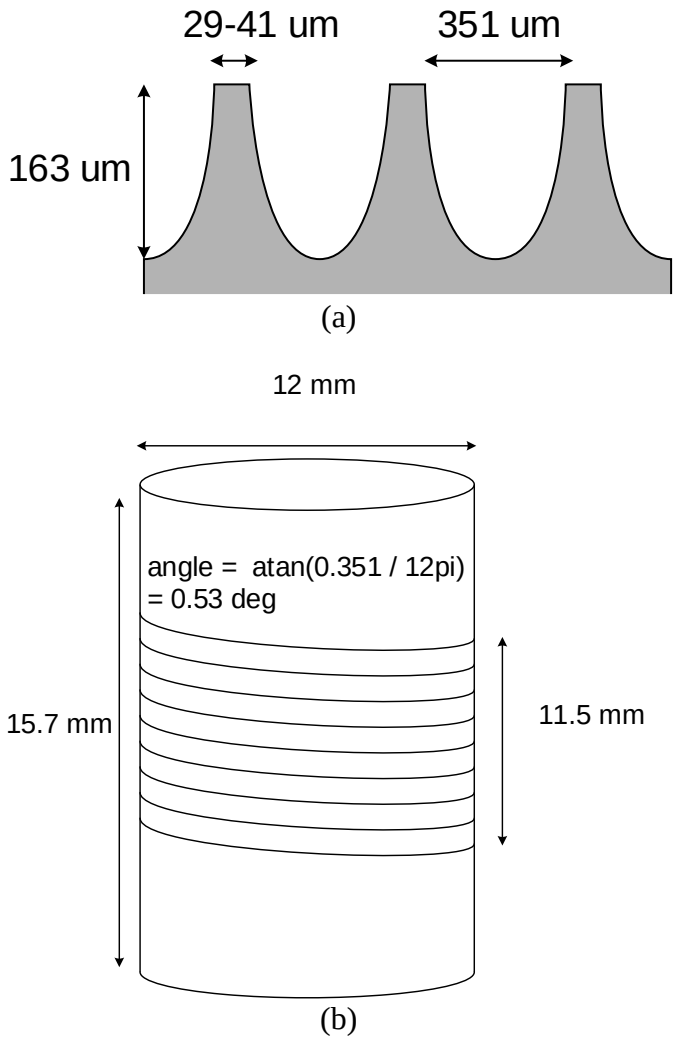

Figure 6-3 Dimensions of grooved roller. (a) Groove profile. (b) Roller.

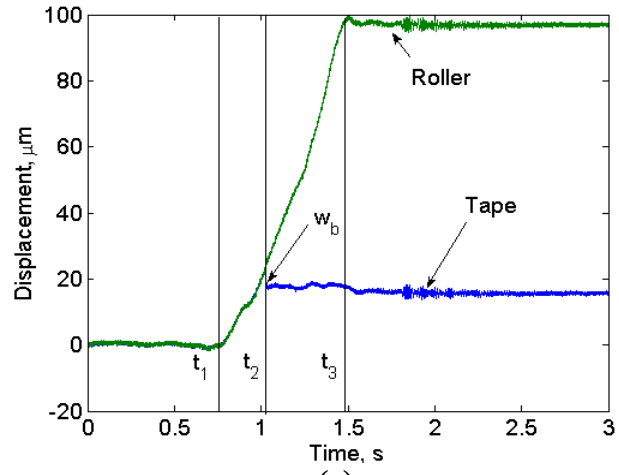

(a)

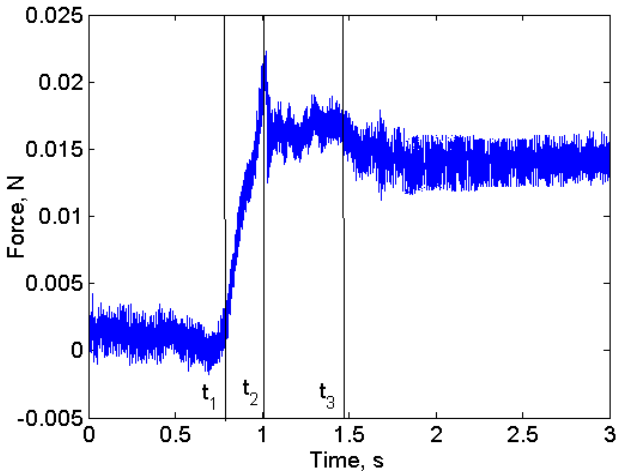

(b)

Figure 6-4 Results of a typical static friction test (T = 0.25 N, R = 6 mm and θ_w = 15 deg). (a) Lateral tape displacement near the roller at sensor-2 (Figure 6-1b) and the roller displacement. (b) Force acting on the roller representing the friction force.

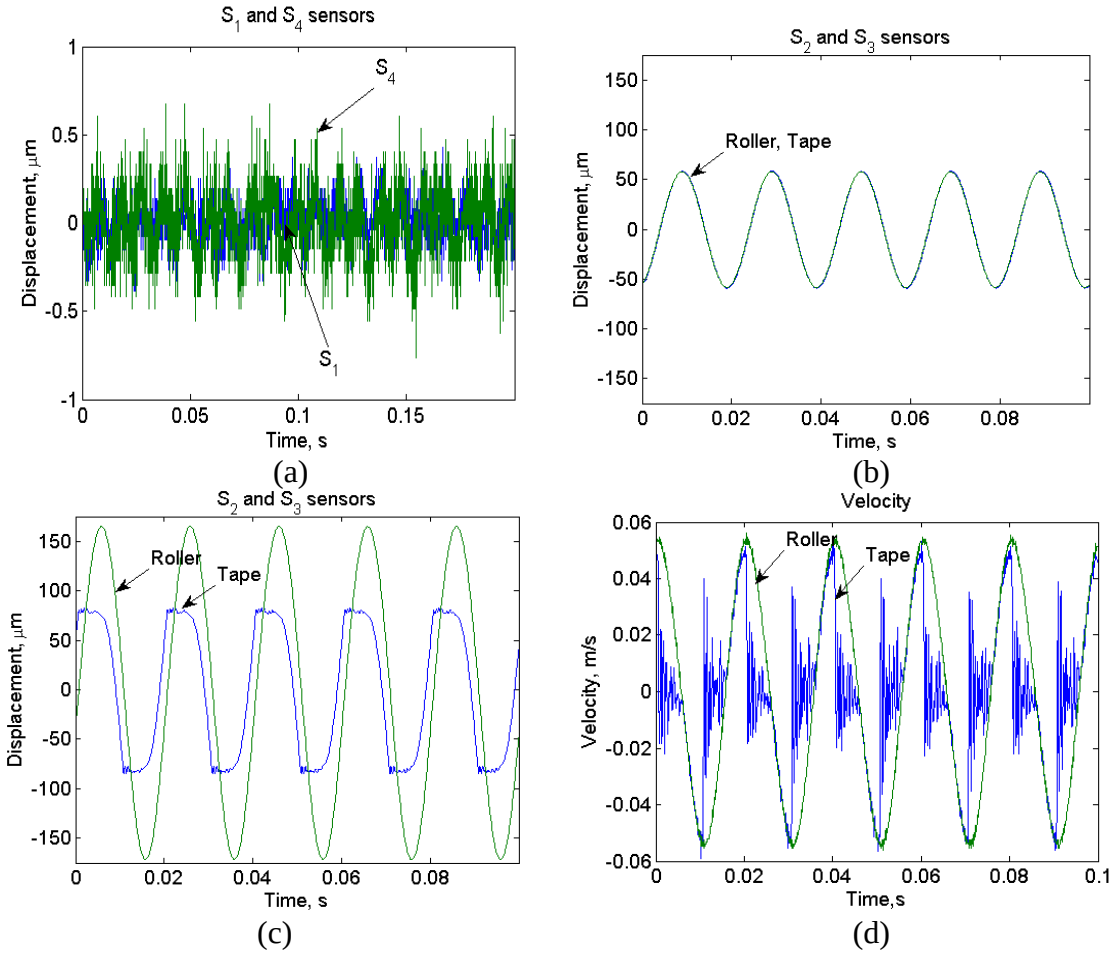

Figure 6-5 (a) Lateral tape displacement measured by sensors S1 and S4, located near the upstream and downstream rollers for a tension of 0.5 N and a wrap angle of 20 degrees; (b) Sensors S2 and S3 measure the actuator and tape deflection, when tape sticks on roller; (c) Displacement of out-of-phase motion between tape and roller, when stick-to-slip transitions occur; (d) Tape vibration velocity (c).

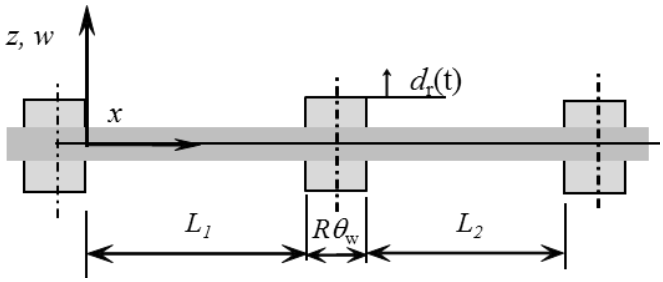

Figure 6-6 Schematic depiction of the tape mechanics model, with the support rollers on both ends and the actuated roller in the middle.

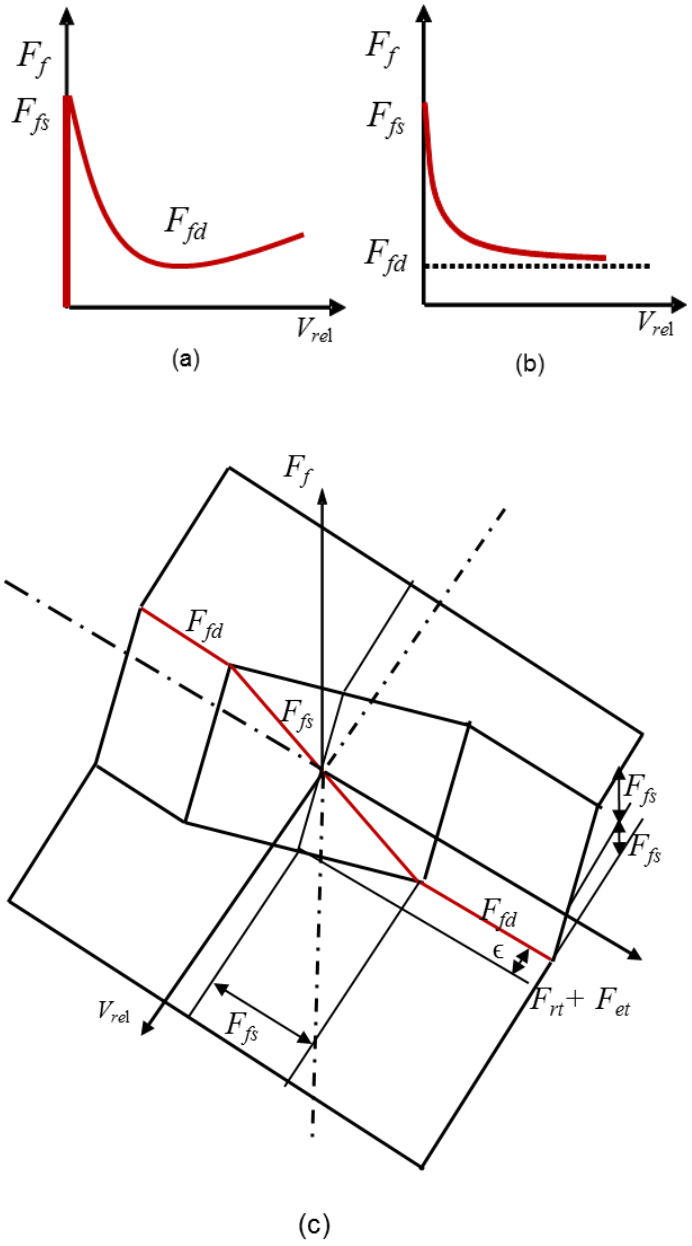

Figure 6-7 (a) tape and roller displacement signal (upper) and force measured by strain gauge (lower), (b) plotted by tape displacement vs force measured

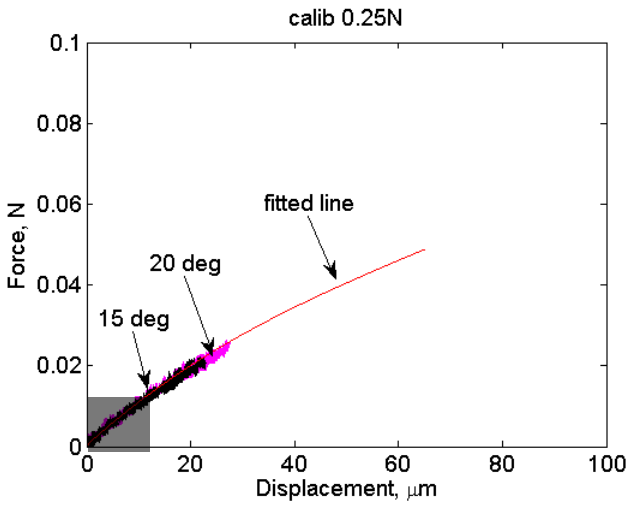

(a)

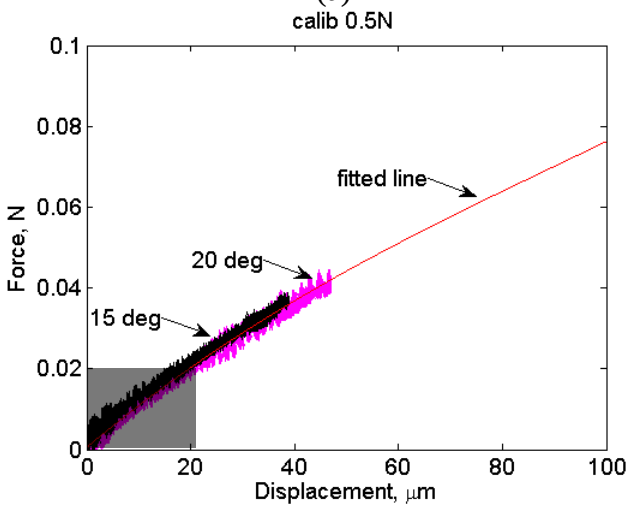

(b)

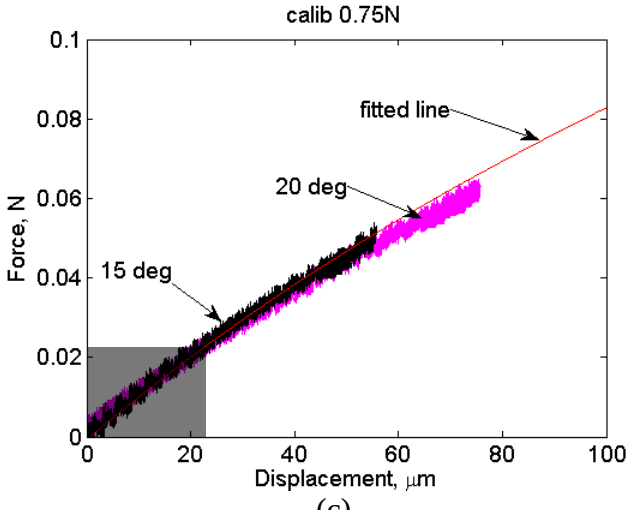

(c)

Figure 6-8 Results of slow mode tests for tension values of (a) 0.25, (b) 0.50 and (c) 0.75 N for 15, and 20 degrees.

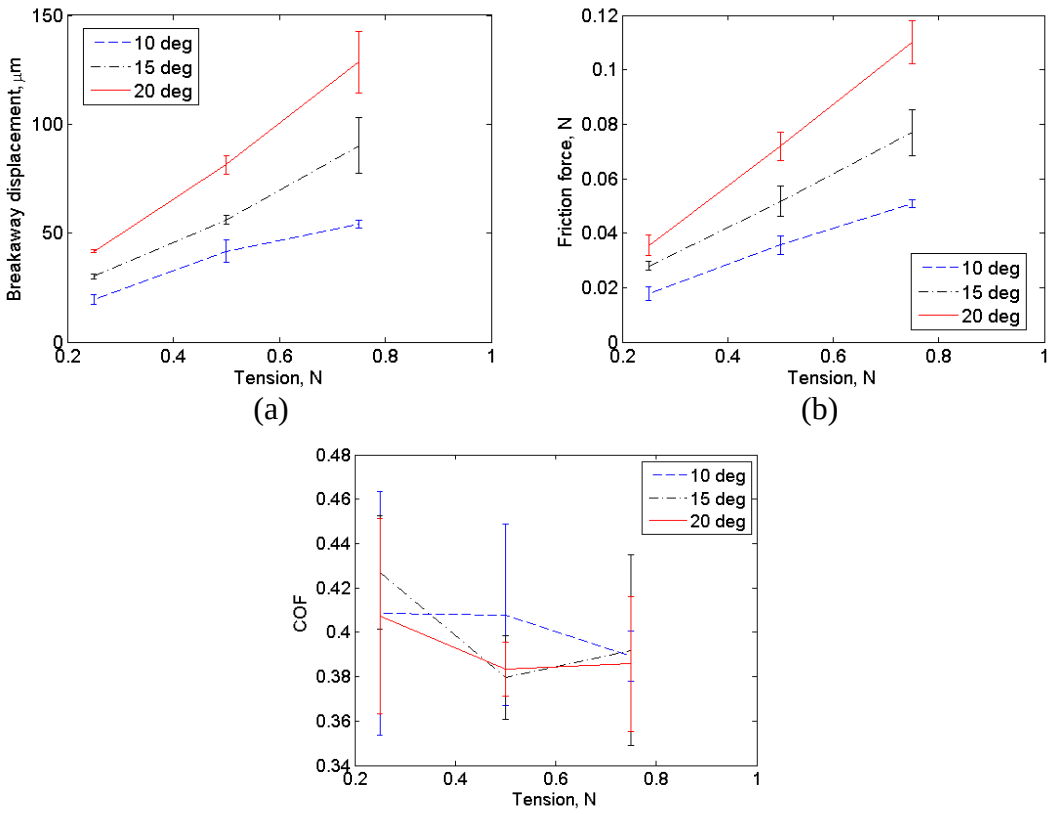

Figure 6-9 (a) The breakaway displacements and (b) friction force for the slow mode tests. (c) Calculated coefficient of friction. Each case was 3 repeated tests and each test has a duration of of 5 sec with 50 Hz frequency.

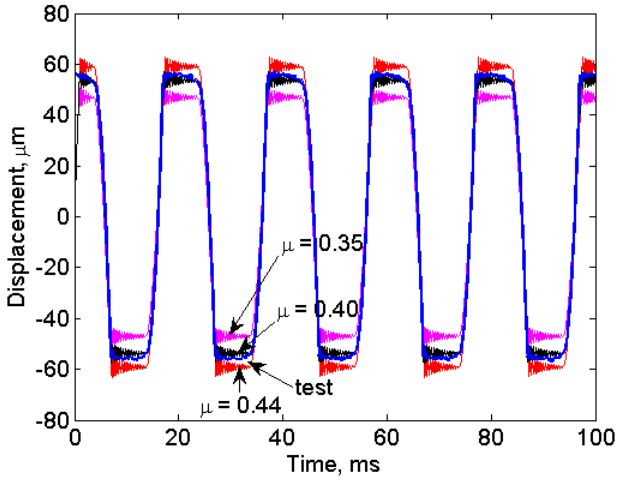

(a)

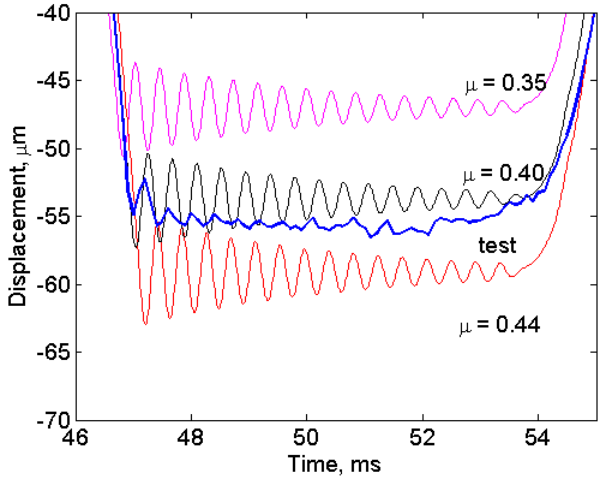

(b)

Figure 6-10 Comparison of simulation results with the fast mode experiments by using the range of COF values found in the static COF measurements. T = 0.5 N, θ_w = 15 degrees. Simulation results: best match (black), upper limit (red) and lower limit (magenta) and measurements (blue). (a) 0.1 s simulation period, (b) magnification into the simulation span of 46-55 ms.

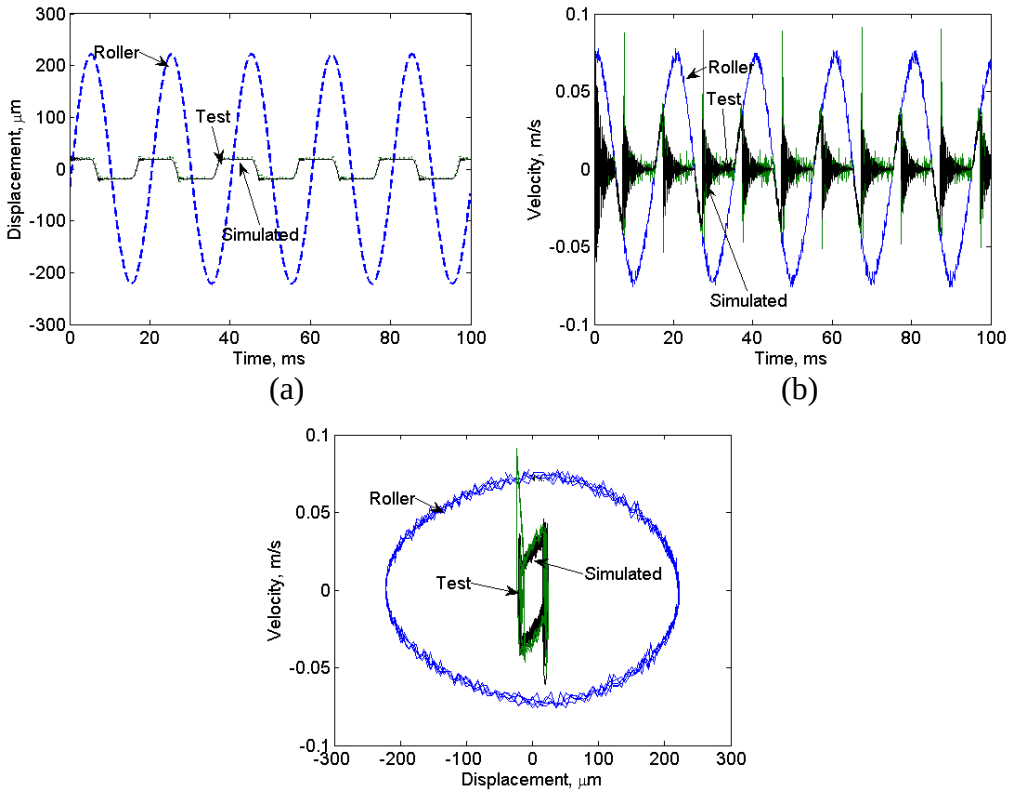

Figure 6-11 (a) Simulated (black) and measured displacement (green), (b) velocity, (c) phase plane histories of the lateral tape deflection for the case of 0.25 N tension and 10 degrees of wrap. The blue curve indicates the roller motion

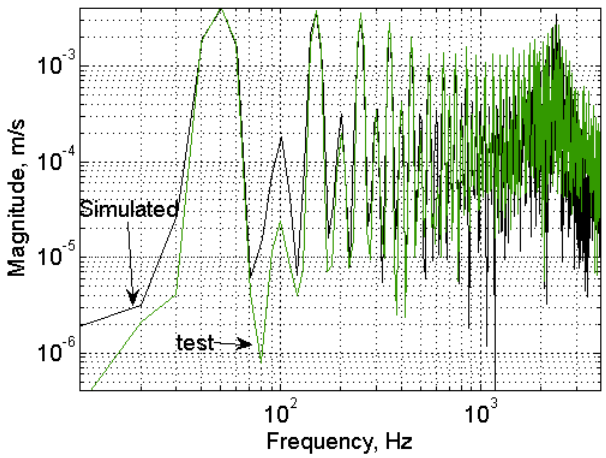

Figure 6-12 Frequency spectrum of tape deflection (Figure 6-11b) obtained by the fast Fourier transform algorithm for both simulated and measured signals.

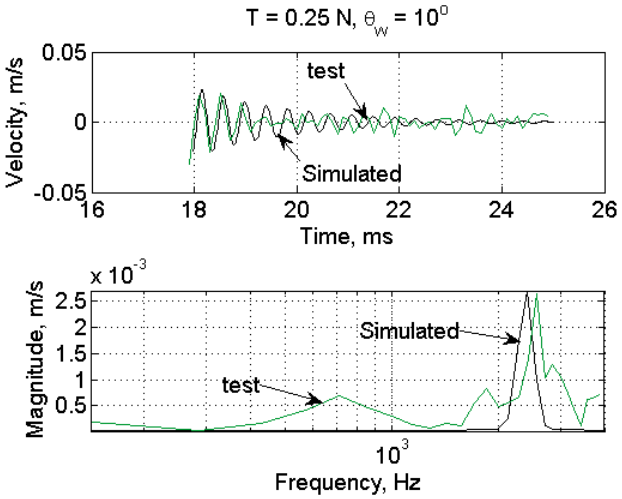

Figure 6-13 Slip phase velocity and frequency spectrum of tape deflection (Figure 6-11b) obtained by the fast Fourier transform algorithm for both simulated and measured signals.

Table 6-1 Parameters used in this work.

Test parameters	
Tension, T (N)	0.25, 0.5, 0.75
Up/down-stream span lengths, L_1, L_2 (cm)	5
Wrap angle, θ_w (degrees)	10, 15, 20
Roller radius, R (mm)	6
Testing side of the tape	Front (recording)
Roller surface	Grooved (Figure 6-3 shows roller dimensions)
Roller Frequency(Hz) for dynamic test	50
LTO-5 tape properties	
Width, b (mm)	12.7
Thickness, h (μm)	6.4
Elastic modulus, E (GPa)	4.42
Loss Modulus, η (kPa.s)	23
Poisson Ratio, ν	0.3
Density, ρ (kg/m^3)	1400

Table 6-2 Polynomial coefficients of the curve fitting in Figure 6-8: $g(w) = \sum_{i=0}^{3} p_i w_i$

T (N)	p_0 (N)	p_1 (N/μm)	p_2 (N/μm^2)	p_3 (N/μm^3)
0.25	4.9795×10^{-8}	-9.5441×10^{-6}	1.1559×10^{-3}	2.7828×10^{-4}
0.50	8.6883×10^{-9}	-5.6928×10^{-6}	2.0509×10^{-3}	-1.8964×10^{-4}
0.75	2.1448×10^{-8}	-6.5235×10^{-6}	2.0491×10^{-3}	-1.48689×10^{-3}

Table 6-3 Critical shear force F_{cr} that causes wrinkling according to Equation, tape stiffness k_{eff}^{t} according to Equation, and experimental values k_{eff}^{e} in the linear range defined by F_{cr}. Note that F_{cr} from Equation is divided by 2, due to symmetry of the test setup.

T (N)	F_{cr} (mN)	k_{eff}^{t} (N/m)	k_{eff}^{e} (N/m)
0.25	12.2	939	962
0.50	20.5	951	979
0.75	27.7	963	985

Table 6-4 Mean (μ_{mean}) and standard deviation (μ_{std}) bound of measured breakaway coefficients of friction values and the best fitting value obtained through simulation (μ_{best}).

	θ_w = 10 deg		θ_w = 15 deg		θ_w = 20 deg	
T (N)	$\mu_{mean}\pm\mu_{std}$	μ_{best}	$\mu_{mean}\pm\mu_{std}$	μ_{best}	$\mu_{mean}\pm\mu_{std}$	μ_{best}
0.25	0.41±0.055	0.44	0.43±0.026	0.42	0.41±0.045	0.4
0.50	0.41±0.042	0.4	0.41±0.041	0.4	0.41±0.041	0.4
0.75	0.39±0.012	0.4	0.39±0.031	0.42	0.39±0.035	0.42

Table 6-5 Natural frequency of the tested configuration from eigenvalue, simulation and test.

Tension (N)	Wrap angle (degrees)	Eigenvalue analysis (Hz)	FFT of simulation (Hz)	FFT of experiments (Hz)
0.25	10	2271	2368	2452
	15	2230	2280	2302
	20	2225	2250	2102
0.5	10	2272	2400	2455
	15	2231	2300	2320
	20	2227	2257	2202
0.75	10	2274	2426	2460
	15	2233	2361	2364
	20	2228	2350	2252

Chapter 7 Effects of Tape Contact with Roller Flanges on Lateral Tape Dynamics

In the previous sections we discussed LTM due to friction and roller stiffness on guiding elements. Despite of induced vibration from head, most the passive elements with friction and stiffness contribute to reduction of LTM. There is one more common structure in tape drive has significant constraint on LTM, flange. We will investigate this type of constrain in this Chapter.

The investigation aims to uncover the sources of high frequency of LTM by introducing the linear or nonlinear guide stiffness and COF (coefficient of friction) one at a time including. Linear stiffness does not change the frequency motion by considering characteristic length reduction. Increasing the nonlinearity of support stiffness, edge stiffness, makes the response of tape more intensive. The response due to nonlinearity gets regularized by introducing COF.

7.1 Introduction

As tape moves laterally, it experiences roller surface friction and stiffness simultaneously and then flange engagement happens. The complete model would have to include all these effects. LTM over fixed guides has been modeled by Ono [67], Brake and Wickert [21] and Raeymakers and Talke[68], and LTM over rollers has been investigated by Shelton [61, 63], Sievers *et al*. [65, 116], Eaton [59], Benson [115], and Müftü [171].

7.2 Model

LTM between the supply ($x = 0$) and take-up ($x = L$) reels is (Figure 7-1) modeled by the equation of motion of a travelling, tensioned Euler-Bernoulli beam [9, 20] as follows,

$$\rho \frac{D^2 w}{Dt^2} + \frac{\partial^2}{\partial x^2}\left(\eta I \frac{D}{Dt} \frac{\partial^2 w}{\partial x^2} + EI \frac{\partial^2 w}{\partial x^2} \right) - \frac{\partial}{\partial x}\left(T \frac{\partial w}{\partial x} \right) = \sum_{i=1}^{NG} H_i \left[q_{f_i} + f_{g_i} + f_i \right] \tag{7.1}$$

where w is the lateral tape deflection, x is the longitudinal coordinate axis, t is time, ρ is the mass density of tape, A is the cross section area of tape. E is the elastic modulus, η is the loss modulus, I is the second moment of area of the tape cross-section, T is the tape tension. The first term represents the inertial forces including effects of tape transport on gyroscopic acceleration. Effects of material damping, bending, and tension are modeled by the second, third and fourth terms, respectively. H_i is a window function equal to 1 over a guide or head and 0 otherwise, NG is the number of guides on the tape path, q_{f_i} is the friction force over the fixed guide or head, f_{g_i} represents the tape to guide interaction, f_i is the impulse force due to sudden impact of tape to guide edges. The fixed guides and write/read heads in this study are modeled as concentrated forces acting at center position ($R_{w_i}\theta_{w_i}/2$) where the guide/head are located. The interaction of the tape with a fixed guide (Figure 7-1) is modeled as a nonlinear spring force,

$$f_{g_i}(x_{g_i}, t) = \begin{cases} -k_{g_f} c_r - k_{e_r}\left(w - c_r \right) & \text{if} \quad w \geq c_r \\ -k_{g_f} w & \text{if} \quad -c_l < w < c_r \\ -k_{g_f} c_l - k_{e_l}\left(w + c_l \right) & \text{if} \quad w \leq -c_l \end{cases} \tag{7.2}$$

where c_r and c_l are clearances between the tape and the guide flanges (Figure 7-1b), k_{e_r}, k_{e_l} are the corresponding edge stiffnesses, k_{g_f} is the guide stiffness, representing tape's resistance to LTM over the guide. Note that the interaction force (f_{g_i}) only applies to fixed guide. It also causes a damping force in the lateral direction as follows,

$$q_{f_i} = -\int_0^{\theta_{w_i}} \mu_{z_i} \left(\frac{T(\theta)}{R_i} \right) \frac{\left(w_{,t} + V_x w_{,x} \right)}{\sqrt{\left(w_{,t} + V_x w_{,x} \right)^2}} R_i d\theta \tag{7.3}$$

where θ_{w_i}, R_i, and μ_{z_i} are the tape wrap angle, radius and coefficient of friction in lateral direction of the i^{th} guide/head respectively, V_x is the tape translating velocity. In this work the supply reel is assumed to feed the tape perfectly along the intended path, whereas the Shelton boundary condition is used on the supply reel as follows,

$$\begin{gathered} w = 0 \text{ and } \quad w_{,x} = 0 \text{ at } x = 0 \\ w_{,t} + V_x w_{,x} = 0 \text{ and } w_{,xt} + V_x w_{,xx} = 0 \text{ at } x = L \end{gathered} \tag{7.4}$$

The dynamics is energized by applying periodically varying impulses (f_i) at different locations, which represent the axial run out of a roller, or tape impacting the flanges of a reel,

$$f_i = \begin{cases} F_0 & \text{if } t_{ib} \le t \le t_{ib} + \Delta t_i \\ 0 & \text{otherwise} \end{cases} \tag{7.5}$$

where, F_0 is impulse force magnitude (N), t_{ib} is time impulse begins (s), Δt_i represents the impulse duration (s). The capstan formula is applied to modify the tension increase due to friction in the running direction as follows,

$$T = T_0 \prod_{i=1}^{NG} e^{\mu_{x_i} \theta_{w_i}} \tag{7.6}$$

where, T_0 is the applied tension, μ_{x_i} is the coefficient of friction of i-th guide in the tape running direction. Solution to the governing equations is obtained numerically as described in Sections 3.2 and 3.3.

7.3 Materials and Methods

The schematic plot of tape path is shown in Figure 7-1a. Two fixed (non-rotating) guides with radii R_1 and R_2, are located at L_1 and L_3 The head is positioned at L_2, and has radius R_2. Figure 7-3 describes the top view of tape path. The tape runs from left to right with

supply and take-up reels numbered by 1, 2, respectively. The three guiding elements are fixed guide-1, the head 2 and the fixed guide-3.

Transient response of the tape, to periodic impulses generated at the second fixed-guide is computed numerically with $\Delta t = 0.2\ \mu s$. This guide is denoted as guide-3 in Figure 7-2. The results are saved and reported with a rate of 40 MHz. In this chapter we report the tape's transient response at the head location for different tape-to-guide clearance values and friction conditions. Table 7-1 lists the baseline parameters used in this study.

7.4 Results

In Figure 7-3, a case where the clearance between the tape and the flanges is 10 μm, is presented. Based on the phase-plane (w-vs-$w_{,t}$) plot, it is seen that the tape settles into a "periodic" response, and that it is displaced by about +6 μm due to the impulse events. In fact in this case the tape never engages the flanges. The frequency spectrum of the tape response, also shown in this figure, is primarily dominated by that of the input impulse events.

A case with a narrow tape-to-guide clearance, $c_l = c_r = c = 0.1$ μm, with and without friction is presented in Figure 7-4. In the case without friction, the regular periodic tape response is entirely lost due to the non-linear forces imparted on the tape by the guides. Such transient contacts are known as flange-hits. When guide friction is added to the system, $\mu_x = \mu_z = 0.1$, it is seen that some regularity to the system is recovered, in Figure 7-4. Tape dynamics involves more frequencies on the lower frequency range and more energy is sent to higher frequencies. A similar case with a slightly wider tape-to-guide clearance, $c_l = c_r = c = 0.5$ μm, is shown in Figure 7-5. In both cases it is shown that friction helps regularize the dynamic response of the system. But, the non-linear guides can cause extremely irregular tape response. This includes widening of the frequency response as well.

7.5 Summary and Conclusions

In general, periodic impulses can act on the tape due to unwinding of irregularly wrapped tape at the reels and axial run-out of a roller. In this work the tape response due to flange

hits is investigated by a mathematical model of the tape path. It is shown that flange hits can cause a wide-band frequency response in the tape, and the tape can have very non-periodic motion. Friction in the system helps reduce some of the complexity of the response.

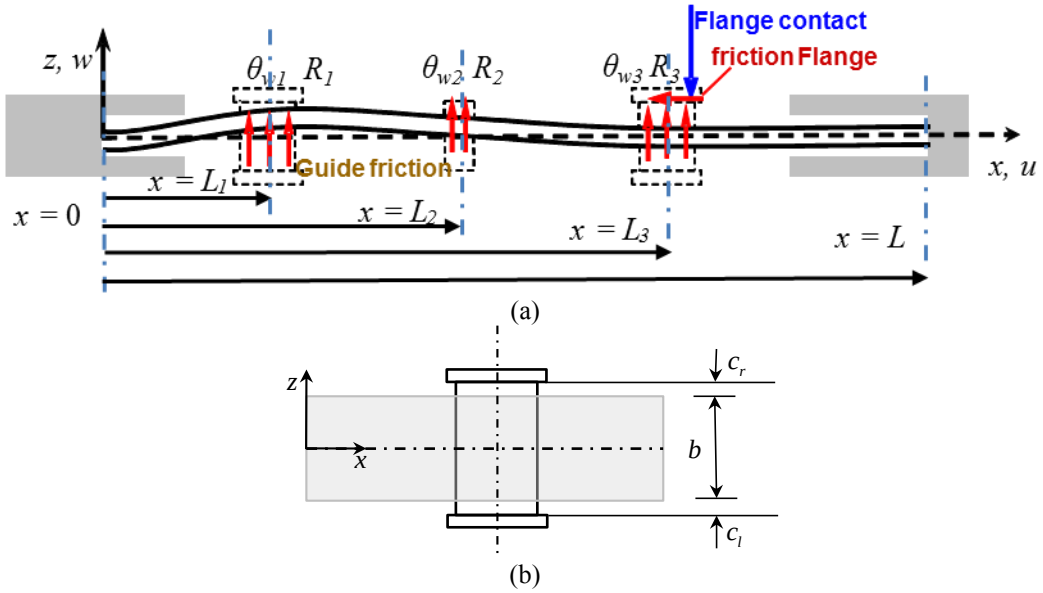

Figure 7-1(a) Schematic depictions of the tape path and (b) the guide-to-tape clearances, c_r and c_l.

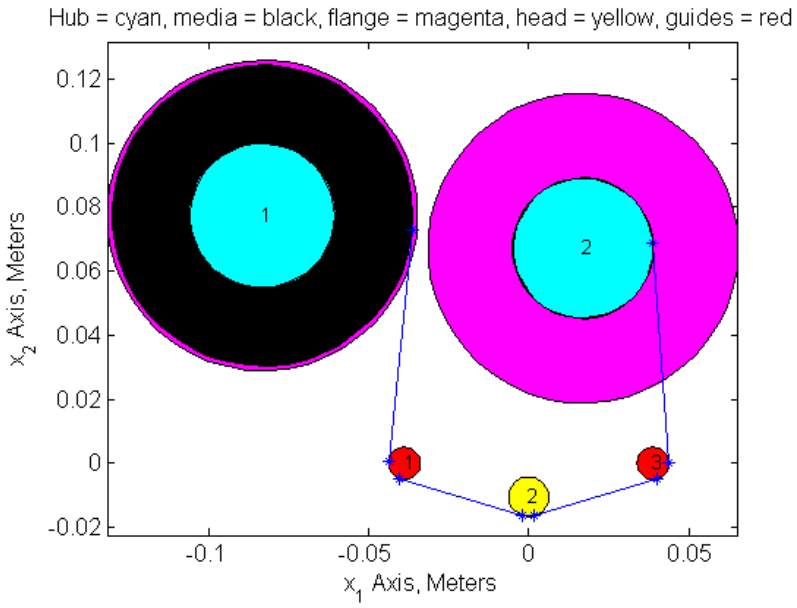

Figure 7-2 Top view of the tested tape path

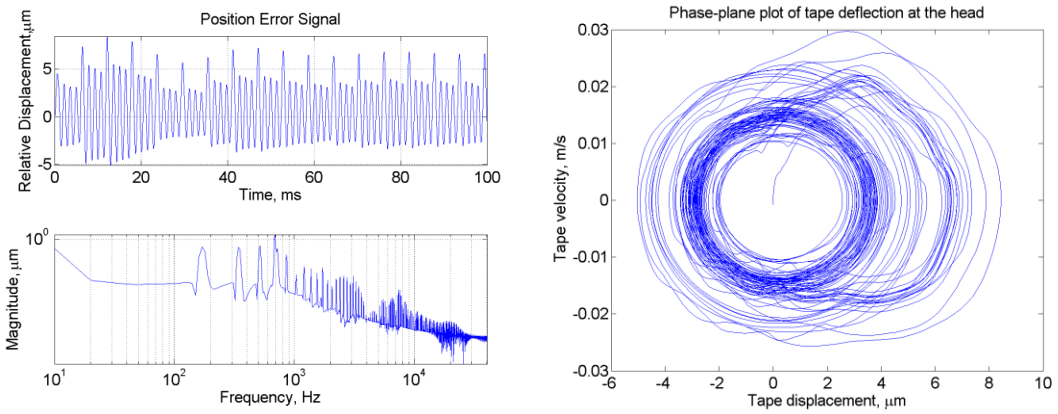

Figure 7-3 Effects of clearance $c_l = c_r = 10$ μm on tape transients at the head without friction.

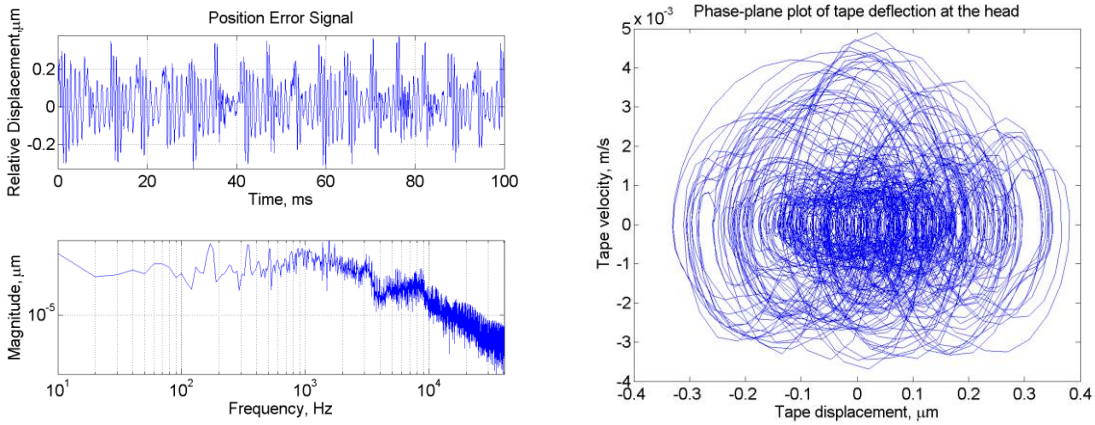

(a)

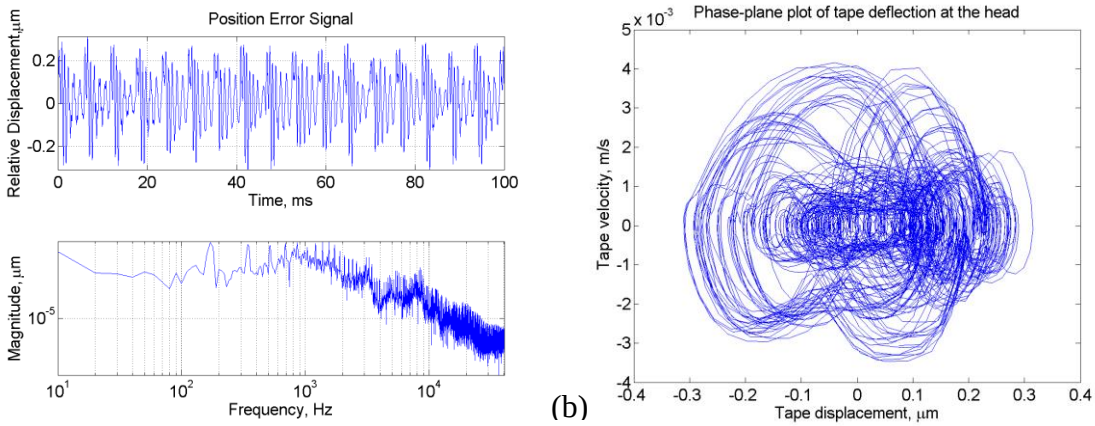

(b)

Figure 7-4 Effects of tape-to-guide clearance and friction on the transient response as at the head. (a) $c_l = c_r = 0.1$ μm and no friction**,** (b) $c_l = c_r = 0.1$ μm and $\mu_x = \mu_z = 0.1$.

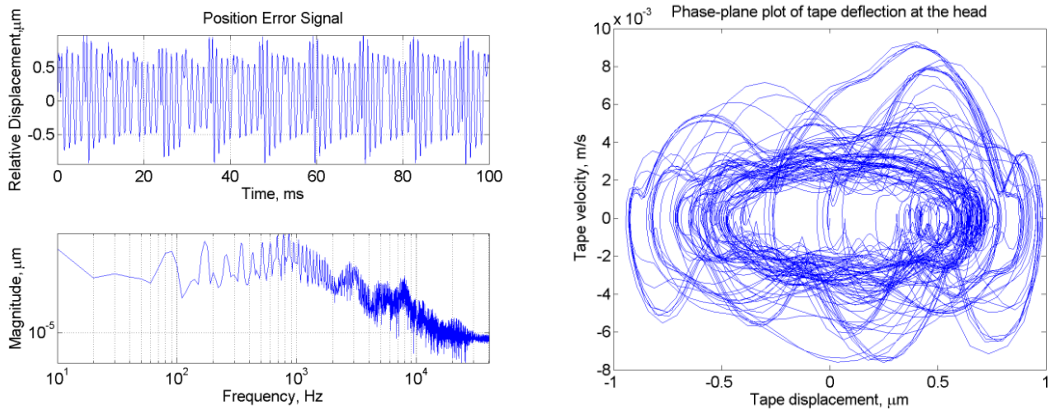

(a)

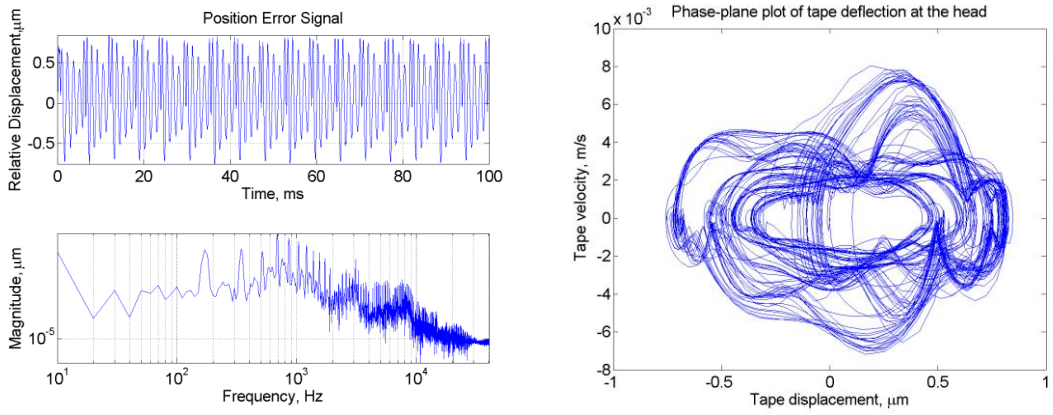

(b)

Figure 7-5 Effects of tape-to-guide clearance and friction on the transient response as at the head (a) $c_l = c_r = 0.5\ \mu$m and $\mu_x = \mu_z = 0$, (b) $c_l = c_r = 0.5\ \mu$m and $\mu_x = \mu_z = 0.1$.

Table 7-1 Baseline parameters

Tape properties		
Tape thickness	h (μm)	9
Tape width	b (mm)	12.7
Bending rigidity	EI (N·m^2)	0.0128
Tape tension	T (N)	1
Loss modulus	η (Pa·s)	13,000
Linear density	ρ (kg/m)	1.6002×10^{-4}
Tape velocity	V_x (m/s)	5.4
Tape length	L_1, L_2, L_3, and L(cm)	7.60, 12.15, 16.69, and 23.88
Fixed guides/head properties		
Radius	R_1, R_2, and R_3 (mm)	5, 6.2, and 5
Guide stiffness	k_g (N/m)	10^2
Guide edge stiffness	k_e (N/m)	10^4
Wrap angle	θ_{w1}, θ_{w2} and θ_{w3} (º)	67.3, 33.8, 77.2
Coefficient of friction	μ_x ,μ_z	0, 0.1
Edge Clearance	$c_l = c_r$ (μm)	10, 0.1, 0.5
Impulse (2nd guide)		
Impulse force magnitude	F_0 (N)	1×10^{-3}
Duration	Δt_i (s)	1×10^{-3}
Impulse begins	t_{ib} (s)	0

Chapter 8 Coupling Between Longitudinal and Lateral Tape Vibrations

The effects of tape, roller, guide or reel imperfections on the LTM are reasonably well understood. Yet, the effects of disturbances in the longitudinal (in-plane) direction, which can couple into LTM, have not been well described. Longitudinal tape vibrations can be due to, but not limited to a) tension dynamics due to servo control of the tape reels, b) and/or tension impulses due to the unwinding of tape layers that experience sticking. The problem is further complicated because of the uncertainty of the tape length on the downstream side, as a result of the "floating layers" in the take-up reel. In this work, the equations of motion of the longitudinal and lateral tape motion are derived from first principles. The coupling caused by non-linear longitudinal strain is considered. The equations of motion are solved by using the finite element method, and an explicit time integration algorithm. The entire tape path is modeled directly, where the interaction of the tape with the recording head and the guides are represented as concentrated forces, and moments. The effects of disturbances, typical for a tape transport system, on the coupling or lack there off are investigated.

The derivation of equation of motion and solution method is presented in Section 8.2. Convergence study and verification are in Section 8.3. The longitudinal disturbances coupled into LTM are discussed in Section 8.4.1 and 8.4.2. COF and guide positioning effect on resonance tuning can be found in Section 8.4.3.

8.1 Introduction

The effects of imperfections, such as the alignment of the rollers, fixed guides, read-write (RW) heads, and tape reels, as well as some the small and random variations have been modeled extensively with linear steady state model [28, 68, 73, 86], linear transient model [42, 97]. In practice, LTM can be handled by moving the read-write (RW) head laterally, with a servo-control strategy that is designed to follow magnetic servo-tracks pre-written on the tape [97]. On the other hand, the effects of the events that cause sudden or random changes in tape tension have not been well understood [1]. In general, longitudinal tape vibrations can be caused by various effects. For example, micro-slip between a smooth tape and a RW-head can cause scrape flutter. During start-up, the tape that has been stuck on a head, a guide, or a pack layer can suddenly release a tension wave, which will propagate through the tape path with unknown consequences. These types of tension or transport speed fluctuations may cause parametric resonance in tape drive system. Several efforts have been made to understand such nonlinear, parametrically excited systems [12, 34, 35, 45, 46, 51]. However, these works were restricted to very simple tape drive layouts. Tension and transport speed control were also studied related to lateral tape motion [60, 73, 116, 118, 119] and simple stretch in longitudinal direction [101, 102]. The coupling between longitudinal and lateral deflection components has not been reported. In this paper a comprehensive mathematical model that is capable of predicting the longitudinal tape dynamics and its coupling to LTM with a variety of disturbances is introduced.

8.2 Model

Figure 3-1shows schematic depictions of a typical tape path and the definitions of the deflection components *u, v, w* with respect to a fixed Cartesian coordinate system (*x, y, z*), where *x*-, *y*- and *z*- axes represent the longitudinal, lateral and out-of plane directions,

respectively. The tape is assumed to be translating in the longitudinal direction with transport velocity V_x. Each one of the deflection components is a function of (x, t). The strain free configuration of the tape follows an idealized path between the two reels with perfectly aligned components. Tape mechanics is analyzed in an unwrapped, straight configuration, and the effects of the various guides and the reels are imposed with appropriate external forces and boundary conditions, respectively [97]. In this chapter, we focus on the coupling between the longitudinal $u(x,t)$ and the lateral tape deflection $v(x,t)$. The tape is modeled as a translating beam that can stretch in the longitudinal direction. The longitudinal strain ε_{xx} in the tape is represented as follows [43, 172, 173],

$$\varepsilon_{xx} = \varepsilon_m + \varepsilon_b \tag{8.1}$$

where the membrane and bending strains are defined as follows,

$$\varepsilon_m = \frac{\partial u}{\partial x} + \frac{1}{2}\left(\frac{\partial v}{\partial x}\right)^2 \quad \text{(a)}$$

$$\varepsilon_b = -y\left(\frac{\partial^2 v}{\partial x^2}\right) \quad \text{(b)} \tag{8.2}$$

Because of the nonlinearity of this system, the minimum energy form as expressed in Equation (3.1) is not valid, and the principle of virtual work is used,

$$\int_{t_1}^{t_2} \left(\delta K - \delta U + \delta W\right) dt = 0 \tag{8.3}$$

where δK, δU and δW represent the variations of the kinetic energy, the strain energy, and the work done on the system, defined in the usual sense of the variational calculus, respectively [173]. The details of the derivation are omitted here for the sake of brevity. However, it should be mentioned that the viscoelastic nature of the polymeric tape material is considered. The constitutive behaviour for a translating viscoelastic string is given as follows [12],

$$\sigma_{xx} = E\varepsilon_{xx} + \eta \frac{D\varepsilon_{xx}}{Dt} \tag{8.4}$$

where σ_{xx} is the longitudinal stress in the tape, and E and η are the elastic and loss moduli, respectively. With these provided, the kinetic energy is given as follows,

$$\delta K = \int_{V_0} \rho V \delta V dV_0 \tag{8.5}$$

where, V_0 is the control volume in the Eulerian reference frame, and V is tape material velocity. By the knowing that variation is only in the spatial variables,

$$\delta\left(\frac{Du}{Dt}+V_x\right)=\delta\left(\frac{\partial u}{\partial t}\right)+V_x\delta\left(\frac{\partial u}{\partial x}\right) \text{ and } \delta\left(\frac{Dv}{Dt}\right)=\delta\left(\frac{\partial v}{\partial t}\right)+V_x\delta\left(\frac{\partial v}{\partial x}\right) \tag{8.6}$$

expanding Equation (8.5) gives

$$\delta K=\int_0^L \rho A\left(\frac{\partial u}{\partial t}+V_x\frac{\partial u}{\partial x}+V_x\right)\left(\delta\frac{\partial u}{\partial t}+V_x\delta\frac{\partial u}{\partial x}\right)dx+\int_0^L \rho A\left(\frac{\partial v}{\partial t}+V_x\frac{\partial v}{\partial x}\right)\left(\delta\frac{\partial v}{\partial t}+V_x\delta\frac{\partial v}{\partial x}\right)dx \tag{8.7}$$

The longitudinal and lateral kinetic energy are independent. Stress and strain tensors reduce to one single scalar quantity due to the assumptions of the beam theory. Therefore, the strain energy term becomes,

$$\delta U = \int_{V_0} \left(\sigma_{xx}+\sigma_0\right)\delta\varepsilon_{xx} dV_0 \tag{8.8}$$

where, σ_0 is pre-stress due to pretension. The variation on strain is found as follows,

$$\begin{aligned}\delta\varepsilon_{xx} &= \delta\varepsilon_m+\delta\varepsilon_b \\ &= \delta\left(\frac{\partial u}{\partial x}\right)+\frac{\partial v}{\partial x}\delta\left(\frac{\partial v}{\partial x}\right)-y\delta\left(\frac{\partial^2 v}{\partial x^2}\right)\end{aligned} \tag{8.9}$$

Thus, substitution Equation (8.9) into Equation (8.8) and setting,

$$\varepsilon_m=\frac{\partial u}{\partial x}+\frac{1}{2}\left(\frac{\partial v}{\partial x}\right)^2,\ \delta\varepsilon_m=\delta\left(\frac{\partial u}{\partial x}\right)+\frac{\partial v}{\partial x}\delta\left(\frac{\partial v}{\partial x}\right) \text{ and } \kappa=\frac{\partial^2 v}{\partial x^2} \tag{8.10}$$

we find,

$$\delta U = \int_0^L \left[\left(\int_A \sigma_{xx} dA \right) \delta\varepsilon_m + \left(\int_A \sigma_0 dA \right) \delta\varepsilon_m + \left(-\int_A \sigma_{xx} y dA \right) \delta\left(\frac{\partial^2 v}{\partial x^2} \right) + \left(-\int_A \sigma_0 y dA \right) \delta\left(\frac{\partial^2 v}{\partial x^2} \right) \right] dx \tag{8.11}$$

The four integrations over the cross-section area represent normal force, pretension, bending moment and moment due to pretension respectively,

$$N = \int_A \sigma_{xx} dA,\ T = \int_A \sigma_0 dA,\ M = -\int_A \sigma_{xx} y dA,\ -\int_A \sigma_0 y dA = 0 \tag{8.12}$$

Moment due to pretension is zero because pre-stress is assumed to be uniform over the cross-section. By using constitutive relation given by Equation (8.4) the membrane stress resultant is found as follows,

$$N = \int_A E\varepsilon_m dA + \int_A \eta \frac{D\varepsilon_m}{Dt} dA - \int_A E\left(y \frac{\partial^2 v}{\partial x^2} \right) dA - \int_A \eta \left(y \frac{D}{Dt}\left(\frac{\partial^2 v}{\partial x^2} \right) \right) dA \tag{8.13}$$

Because integration of odd functions over a symmetric area, the last two terms are zero. Consistent with Mockensturm's string model [33], the membrane stress resultant becomes,

$$N = A\left(E\varepsilon_m + \eta \frac{D\varepsilon_m}{Dt} \right) \tag{8.14}$$

Bending moment is expressed as,

$$M = -\int_A Ey\varepsilon_m dA - \int_A \eta y \frac{D\varepsilon_m}{Dt} dA + \int_A Ey^2 \frac{\partial^2 v}{\partial x^2} dA + \int_A \eta y^2 \frac{D}{Dt}\left(\frac{\partial^2 v}{\partial x^2} \right) dA \tag{8.15}$$

Same reason as the membrane force derivation procedure makes the first two terms of this expression be equal to zero. Furthermore, second moment of area, is by definition

$$I = \int_A y^2 dA \tag{8.16}$$

The moment formula, obtained here is the same as Brake's linear beam model [21].

$$M = EI\frac{\partial^2 v}{\partial x^2} + \eta I\frac{D}{Dt}\left(\frac{\partial^2 v}{\partial x^2}\right) \tag{8.17}$$

Substitution Equation (8.14) and (8.17) back into Equation (8.11), the strain energy can be found as follows,

$$\delta U = \int_0^L N\delta\varepsilon dx + \int_0^L T\delta\varepsilon dx + \int_0^L M\delta\kappa dx \tag{8.18}$$

By combining Equation (8.3), (8.7) and (8.18), equations of motion in the x and y direction for a translating tensioned beam is found as follows,

$$\rho A\frac{D^2 u}{Dt^2} - \frac{\partial}{\partial x}\left(T + EA\varepsilon_m + \eta A\frac{D\varepsilon_m}{Dt}\right) = \sum_{i=1}^{N^g} f_{x_i}^g \delta\left(x - L_{g_i}\right) \tag{8.19}$$

$$\begin{aligned}&\rho A\frac{D^2 v}{Dt^2} - \frac{\partial}{\partial x}\left[T + A\left(E\varepsilon_{xx} + \eta\frac{D\varepsilon_{xx}}{Dt}\right)\frac{\partial v}{\partial x}\right] + \frac{\partial^2}{\partial x^2}\left[I\left(E\frac{\partial^2 v}{\partial x^2} + \eta\frac{D}{Dt}\left(\frac{\partial^2 v}{\partial x^2}\right)\right)\right] \\ &= \sum_{i=1}^{N^g} f_{y_i}^g \delta\left(x - L_{g_i}\right)\end{aligned} \tag{8.20}$$

where $f_{x_i}^g$, $f_{y_i}^g$ (i = 1, N^g) represents the forces acting on the tape due to guides, each located at $x = L_{g_i}$ shown in Figure 8-1, N^g is the total number of guides, and $\delta(x)$ is the Dirac delta function, not to be confused with the variational symbol in Equation (8.3) and (8.21). The detail derivation can be found in Section 8.2.1. The following boundary conditions are found from the principle of virtual work,

$$\left[\rho AV_x\left(\frac{Du}{Dt} + V_x\right) - \left(EA\varepsilon_m + T + \eta A\frac{D\varepsilon_m}{Dt}\right)\right]\delta u\Big|_0^L = 0 \quad \text{(a)}$$

$$\left\{\rho AV_x\frac{Dv}{Dt} - \left(EA\varepsilon_m + T + \eta A\frac{D\varepsilon_m}{Dt}\right)\frac{\partial v}{\partial x} + \frac{\partial}{\partial x}\left[EI\frac{\partial^2 v}{\partial x^2} + \eta I\frac{D}{Dt}\left(\frac{\partial^2 v}{\partial x^2}\right)\right]\right\}\delta w\Big|_0^L = 0 \quad \text{(b)} \tag{8.21}$$

$$\left[EI\frac{\partial^2 v}{\partial x^2} + \eta I\frac{D}{Dt}\left(\frac{\partial^2 v}{\partial x^2}\right)\right]\delta\left(\frac{\partial w}{\partial x}\right)\Big|_0^L = 0 \quad \text{(c)}$$

We assume the tape tension is applied at the both ends as external force. Therefore, the tension term T can be dropped from Equation (8.19), (8.20) and (8.21), The governing equations are modified as follows,

$$\rho A\frac{D^2u}{Dt^2}-\frac{\partial}{\partial x}\left(EA\varepsilon_m+\eta A\frac{D\varepsilon_m}{Dt}\right)=\sum_{i=1}^{N^g}f_{x_i}^{g}\delta\left(x-L_{g_i}\right) \quad \text{(a)}$$

$$\rho A\frac{D^2v}{Dt^2}-\frac{\partial}{\partial x}\left[A\left(E\varepsilon_{xx}+\eta\frac{D\varepsilon_{xx}}{Dt}\right)\frac{\partial v}{\partial x}\right]+\frac{\partial^2}{\partial x^2}\left[I\left(E\frac{\partial^2 v}{\partial x^2}+\eta\frac{D}{Dt}\left(\frac{\partial^2 v}{\partial x^2}\right)\right)\right] \quad \text{(b)} \quad (8.22)$$

$$=\sum_{i=1}^{N^g}f_{y_i}^{g}\delta\left(x-L_{g_i}\right)$$

8.2.1 External force due to fixed guide

In this work the guides are modelled as non-rotating, cylindrical supports. Therefore, the external forces acting on the tape contain contributions due to sliding friction. The frictional force acting on guide is integrated over the wrap region and applied to the middle point of wrap length (shown in Figure 8-2) as a concentrated force, namely,

$$\vec{f}_{fric_i}=-\int\tau\frac{\vec{v}_{rel}}{\left|\vec{v}_{rel}\right|}dA=-\int_0^{\theta_{wi}}\boldsymbol{\mu}_i\frac{T(\theta)}{R_i}\frac{\vec{v}_{rel}}{\left|\vec{v}_{rel}\right|}Rd\theta \quad (8.23)$$

where, $\frac{T(\theta)}{R_i}$ is wrap pressure along the wrap angle. Because of existence of friction, belt wrap tension formula is applied, $T(\theta)=T_{0_i}e^{\mu_x\theta}$ and $\boldsymbol{\mu}_i=\left\{\mu_{x_i}\quad \mu_{y_i}\right\}^T$. T_{0_i} represents the tension value before increasing due to the belt wrap. In spite of $\vec{v}_{rel}$ being a function of location, explicit time integration allows us to treat the value of $\vec{v}_{rel}$ as constant obtained from the previous time step. Thus, it is valid to take the term $\vec{v}_{rel}/\left|\vec{v}_{rel}\right|$ outside of the integral. Distributed friction force acting over a guide then becomes,

$$\vec{f}_{fric_i}=-T_{0_i}\frac{\vec{v}_{rel}}{\left|\vec{v}_{rel}\right|}\int_0^{\theta_{wi}}\boldsymbol{\mu}e^{\mu_x\theta}d\theta=-T_{0_i}\frac{\boldsymbol{\mu}}{\mu_x}\frac{\vec{v}_{rel}}{\left|\vec{v}_{rel}\right|}\left(e^{\mu_x\theta_{wi}}-1\right) \quad (8.24)$$

In addition, the aggregate effect of the tape's resistance to lateral motion over a guide is represented as a linear spring force [9, 78]. This gives the following force vector components,

$$f_{x_i}^{\,g} = -T_{0_i} \frac{Du/Dt + V_x}{\sqrt{\left(Du/Dt + V_x\right)^2 + \left(Dw/Dt\right)^2}} \left(e^{\mu_x \theta_{wi}} - 1\right) \tag{8.25}$$

$$f_{y_i}^{\,g} = -T_{0_i} \frac{\mu_{y_i}}{\mu_{x_i}} \frac{Dw/Dt}{\sqrt{\left(Du/Dt + V_x\right)^2 + \left(Dw/Dt\right)^2}} \left(e^{\mu_x \theta_{w_i}} - 1\right) + f_{g_i} \tag{8.26}$$

where the subscript–*i* indicates the guide number, T_{0_i} is the tape tension upstream of the guide, μ_{x_i} and μ_{y_i} are the friction coefficients, θ_{w_i} is the wrap angle, and f_{g_i} is defined in Equation (7.2).

8.2.2 Spatial discretization

Longitudinal and lateral components of beam deflection are approximated over an element of length *L* as follows,

$$\begin{Bmatrix} u \\ v \end{Bmatrix} = \boldsymbol{Nd} = \begin{bmatrix} N_1^u & 0 & 0 & N_2^u & 0 & 0 \\ 0 & N_1^v & N_2^v & 0 & N_3^v & N_4^v \end{bmatrix} \begin{Bmatrix} u_1 \\ v_1 \\ \theta_1 \\ u_2 \\ v_2 \\ \theta_2 \end{Bmatrix} \tag{8.27}$$

where N_i^v (*i*=1-4) are the C^1 continuous, Hermite shape functions given in Equation (3.14). N_i^u (*i*=1-2) are the following linear shape functions,

$$\begin{aligned} N_1^u &= 1 - \frac{x}{L} \quad (a) \\ N_2^u &= \frac{x}{L} \quad (b) \end{aligned} \tag{8.28}$$

u_i, v_i and θ_i are the nodal values of deflection components and slope respectively at the ends (1, 2)of the element. The shape functions that interoperate displacements in x and y direction of the beam model can be generated as follows,

$$\boldsymbol{N}^v = \begin{bmatrix} N_1^v & N_2^v & N_3^v & N_4^v \end{bmatrix} \text{ and } \boldsymbol{N}^u = \begin{bmatrix} N_1^u & N_2^u \end{bmatrix} \tag{8.29}$$

The corresponding displacement vectors are defined as,

$$\boldsymbol{v} = \begin{Bmatrix} v_1 & \theta_1 & v_1 & \theta_2 \end{Bmatrix}^T, \text{ and } \boldsymbol{u} = \begin{Bmatrix} u_1 & u_2 \end{Bmatrix}^T \tag{8.30}$$

The element matrix presentation of governing equation in this case is different and it is as follows,

$$\boldsymbol{m}\ddot{\boldsymbol{d}} + (\boldsymbol{g} + \boldsymbol{c})\dot{\boldsymbol{d}} + (\boldsymbol{k} - \boldsymbol{s} + \boldsymbol{d})\boldsymbol{d} = \boldsymbol{F} \tag{8.31}$$

where, mass matrix is in lumped form for explicit time integration. In addition the element mass, nonlinear stiffness and damping matrices are [173],

$$\boldsymbol{m} = \rho AL\begin{bmatrix} 1/2 & 1/2 & L^2/24 & 1/2 & 1/2 & L^2/24 \end{bmatrix} \tag{8.32}$$

$$\boldsymbol{g} = 2\rho AV_x \int_0^L \boldsymbol{N}^T \frac{d}{dx}\boldsymbol{N}dx \tag{8.33}$$

$$\boldsymbol{s} = \rho AV_x^2 \int_0^L \frac{d}{dx}\boldsymbol{N}^T \frac{d}{dx}\boldsymbol{N}dx \tag{8.34}$$

$$\boldsymbol{k}^{11}{}_{2\times 2} = \int_0^L EA\frac{d}{dx}\left(\boldsymbol{N}^u\right)^T \frac{d}{dx}\boldsymbol{N}^u dx \tag{8.35}$$

$$\boldsymbol{k}^{12}{}_{2\times 4} = \frac{1}{2}\int_0^L EA\frac{dv^0}{dx}\frac{d}{dx}\left(\boldsymbol{N}^u\right)^T \frac{d}{dx}\boldsymbol{N}^v dx \tag{8.36}$$

$$\boldsymbol{k}^{21}{}_{4\times 2} = \frac{1}{2}\int_0^L EA\frac{dv^0}{dx}\frac{d}{dx}\left(\boldsymbol{N}^v\right)^T \frac{d}{dx}\boldsymbol{N}^u dx \tag{8.37}$$

$$\boldsymbol{k}^{22}{}_{4\times4} = \frac{1}{2}\int_0^L EA\left(\frac{du^0}{dx} + \left(\frac{dv^0}{dx}\right)^2\right)\frac{d}{dx}\left(\boldsymbol{N}^v\right)^T \frac{d}{dx}\boldsymbol{N}^v dx + \int_0^L EI\,\frac{d^2}{dx^2}\left(\boldsymbol{N}^v\right)^T \frac{d^2}{dx^2}\boldsymbol{N}^v dx \tag{8.38}$$

u^0, v^0 are the element displacements obtained from previous step,

$$u^0 = \boldsymbol{N}^u\boldsymbol{u}^{n-1}, \text{ and } v^0 = \boldsymbol{N}^v\boldsymbol{v}^{n-1} \tag{8.39}$$

where, n represents the current time step. Then nonlinear stiffness matrix is,

$$\boldsymbol{k} = \begin{bmatrix} \boldsymbol{k}^{11} & \boldsymbol{k}^{12} \\ \boldsymbol{k}^{21} & \boldsymbol{k}^{22} \end{bmatrix}_{6\times6} \tag{8.40}$$

Similarly, the damping matrix due to viscoelasticity,

$$\boldsymbol{c}^{11}{}_{2\times2} = \int_0^L \eta A\frac{d}{dx}\left(\boldsymbol{N}^u\right)^T \frac{d}{dx}\boldsymbol{N}^u dx \tag{8.41}$$

$$\boldsymbol{c}^{12}{}_{2\times4} = \int_0^L \eta A\frac{dv^0}{dx}\frac{d}{dx}\left(\boldsymbol{N}^u\right)^T \frac{d}{dx}\boldsymbol{N}^v dx \tag{8.42}$$

$$\boldsymbol{c}^{21}{}_{4\times2} = \int_0^L \eta A\frac{dv}{dx}\frac{d}{dx}\left(\boldsymbol{N}^v\right)^T \frac{d}{dx}\boldsymbol{N}^u dx \tag{8.43}$$

$$\boldsymbol{c}^{22}{}_{4\times4} = \int_0^L \eta A\left(\frac{dv^0}{dx}\right)^2 \frac{d}{dx}\left(\boldsymbol{N}^v\right)^T \frac{d}{dx}\boldsymbol{N}^v dx + \int_0^L \eta I\,\frac{d^2}{dx^2}\left(\boldsymbol{N}^v\right)^T \frac{d^2}{dx^2}\boldsymbol{N}^v dx \tag{8.44}$$

$$\boldsymbol{c} = \begin{bmatrix} \boldsymbol{c}^{11} & \boldsymbol{c}^{12} \\ \boldsymbol{c}^{21} & \boldsymbol{c}^{22} \end{bmatrix}_{6\times6} \tag{8.45}$$

And stiffness matrix due to internal damping and gyroscopic effect,

$$\boldsymbol{h}^{11}{}_{2\times2} = \int_0^L \eta A V_x\,\frac{d}{dx}\left(\boldsymbol{N}^u\right)^T \frac{d^2}{dx^2}\boldsymbol{N}^u dx = 0 \tag{8.46}$$

$$\boldsymbol{h}^{12}{}_{2\times4} = \frac{1}{2}\int_0^L \eta A V_x \frac{dv^0}{dx}\frac{d}{dx}\left(\boldsymbol{N}^u\right)^T \frac{d^2}{dx^2}\boldsymbol{N}^v dx \tag{8.47}$$

$$\boldsymbol{h}^{21}{}_{4\times2} = \frac{1}{2}\int_0^L \eta A V_x \frac{dv^0}{dx}\frac{d^2}{dx^2}\left(\boldsymbol{N}^v\right)^T \frac{d}{dx}\boldsymbol{N}^u dx \tag{8.48}$$

$$\boldsymbol{h}^{22}{}_{4\times4} = \int_0^L \eta A V_x \left(\frac{dv^0}{dx}\right)^2 \frac{d^2}{dx^2}\left(\boldsymbol{N}^v\right)^T \frac{d}{dx}\boldsymbol{N}^v dx + \int_0^L \eta I V_x \frac{d^3}{dx^3}\left(\boldsymbol{N}^v\right)^T \frac{d^2}{dx^2}\boldsymbol{N}^v dx \tag{8.49}$$

$$\boldsymbol{h} = \begin{bmatrix} \boldsymbol{h}^{11} & \boldsymbol{h}^{12} \\ \boldsymbol{h}^{21} & \boldsymbol{h}^{22} \end{bmatrix}_{6\times6} \tag{8.50}$$

where, $dv^0/dx = \left(d\boldsymbol{N}^v/dx\right)\boldsymbol{v}^{n-1}$. Numerical method, finite element, discretizes the external force acting at *i*-th fixed guide into nodes (*j*-th for example) shown in Figure 8-2,

$$f^j_{fric\_y_i} = -T_{0_i}\frac{\mu_{y_i}}{\mu_{x_i}}\frac{Dv_j/Dt}{\sqrt{\left(Du_j/Dt + V_x\right)^2 + \left(Dv_j/Dt\right)^2}}\left(e^{\mu_{x_i}\theta_{w_i}} - 1\right) \tag{8.51}$$

$$f^j_{fric\_x_i} = -T_{0_i}\frac{Du_j/Dt + V_x}{\sqrt{\left(Du_j/Dt + V_x\right)^2 + \left(Dv_j/Dt\right)^2}}\left(e^{\mu_{x_i}\theta_{w_i}} - 1\right) \tag{8.52}$$

The material derivative terms in Equation (8.51) and (8.52) are interpolated as follows,

$$Dv_j/Dt = \frac{dv_j}{dt} + V_x\frac{dv_j}{dx} \text{ and } Du_j/Dt = \frac{du_j}{dt} + V_x\frac{du_j}{dx} \tag{8.53}$$

They are obtained from previous time step. The time integration solution is outlined in Section 8.2.3. $dv_j/dx = \theta_j$ due the assumption of beam model and $du_j/dx = \left(u_{j+1} - u_j\right)/L$.

To accurately represent the tension varying from node-(*j-1*) to node-*j*, to node-(*j+1*) due to friction, the integration in Equation (8.52) is divided down to two parts, i.e., from 0 to $\theta_{w_i}/2$ and $\theta_{w_i}/2$ to θ_{w_i}, which implies,

$$f_{fric\_x_i}^{j-1} = -T_{0_i} \tag{8.54}$$

$$f_{fric\_x_i}^{j} = -T_{0_i} \frac{Du/Dt + V_x}{\sqrt{\left(Du/Dt + V_x\right)^2 + \left(Dv/Dt\right)^2}} \left(e^{\mu_{x_i} \frac{\theta_{w_i}}{2}} - 1 \right) \tag{8.55}$$

$$f_{fric\_x_i}^{j+1} = -T_{0_i} \frac{Du/Dt + V_x}{\sqrt{\left(Du/Dt + V_x\right)^2 + \left(Dv/Dt\right)^2}} \left(e^{\mu_{x_i}\theta_{w_i}} - e^{\mu_{x_i} \frac{\theta_{w_i}}{2}} \right) \tag{8.56}$$

The external force vector on *i*-th fixed-guide is as follows,

$$\boldsymbol{f} = \begin{cases} \left\{ \frac{f_{fric\_x_i}^{j-1}}{2} \quad 0 \quad 0 \quad \frac{f_{fric\_x_i}^{j}}{2} \quad \frac{f_{fric\_y_i}^{j}}{2} \quad 0 \right\}^T & \text{element } j-1 \\ \left\{ \frac{f_{fric\_x_i}^{j}}{2} \quad \frac{f_{fric\_y_i}^{j}}{2} \quad 0 \quad \frac{f_{fric\_x_i}^{j+1}}{2} \quad 0 \quad 0 \right\}^T & \text{element } j \\ \left\{ 0 \quad 0 \quad 0 \quad 0 \quad 0 \quad 0 \right\}^T & \text{else} \end{cases} \tag{8.57}$$

The /2 terms in Equation (8.57) is due global nodal force is the sum of two adjacent elements' nodal force. Using the higher case to donate the global matrices and vectors, the global matrices representation of governing equation is as follows,

$$\boldsymbol{M}\ddot{\boldsymbol{D}} + \left(\boldsymbol{G} + \boldsymbol{C}\right)\dot{\boldsymbol{D}} + \left(\boldsymbol{K} - \boldsymbol{S} + \boldsymbol{H}\right)\boldsymbol{D} = \boldsymbol{F} \tag{8.58}$$

8.2.3 Time integration

Consider the natural of this coupled physics, the implicit method requires nonlinear solver, like Newton-Raphson method, in each time step. This puts lots difficulties on coding. As a first attempt of tackling this problem, explicit method is implemented. Since explicit method requires much smaller time step, the nonlinearity can be well taken care within each time step.

Newmark method is a widely use algorithm, but here we introduce the improvement of Newmark method, α-method as predictor and corrector. The explicit time integration scheme is as follows [26]:

1. Predict displacement and velocities using $\tilde{\boldsymbol{D}}^{n+1}$ and $\tilde{\dot{\boldsymbol{D}}}^{n+1}$ by

$$\tilde{\boldsymbol{D}}^{n+1} = \boldsymbol{D}^{n} + \Delta t\dot{\boldsymbol{D}}^{n} + \frac{\Delta t^{2}}{2}\left(1-2\beta\right)\ddot{\boldsymbol{D}}^{n} \tag{8.59}$$

$$\tilde{\dot{\boldsymbol{D}}}^{n+1} = \dot{\boldsymbol{D}}^{n} + \Delta t\left(1-\gamma\right)\ddot{\boldsymbol{D}}^{n} \tag{8.60}$$

2. Update the nonlinear matrices $\boldsymbol{K}$, $\boldsymbol{C}$ and $\boldsymbol{H}$ by $\boldsymbol{D}^{n}$ at time step n,
3. Solve for acceleration at time step $n + 1$ using,

$$\begin{aligned}\boldsymbol{M}\ddot{\boldsymbol{D}}^{n+1} = {} & \left(1+\alpha\right)\boldsymbol{F}^{n+1} - \alpha\boldsymbol{F}^{n} - \left(1+\alpha\right)\left(\left(\boldsymbol{G}+\boldsymbol{C}\right)\tilde{\dot{\boldsymbol{D}}}^{n+1} + \left(\boldsymbol{K}-\boldsymbol{S}+\boldsymbol{H}\right)\tilde{\boldsymbol{D}}^{n+1}\right) \\ & +\alpha\left(\left(\boldsymbol{G}+\boldsymbol{C}\right)\dot{\boldsymbol{D}}^{n} + \left(\boldsymbol{K}-\boldsymbol{S}+\boldsymbol{H}\right)\boldsymbol{D}^{n}\right)\end{aligned} \tag{8.61}$$

4. Calculate the correctors $\boldsymbol{D}^{n+1}$ and $\dot{\boldsymbol{D}}^{n+1}$ by

$$\boldsymbol{D}^{n+1} = \tilde{\boldsymbol{D}}^{n+1} + \Delta t^{2}\beta\ddot{\boldsymbol{D}}^{n+1} \tag{8.62}$$

$$\dot{\boldsymbol{D}}^{n+1} = \tilde{\dot{\boldsymbol{D}}}^{n+1} + \gamma\Delta t\ddot{\boldsymbol{D}}^{n+1} \tag{8.63}$$

5. Increment time by Δt, let $n + 1 \rightarrow n$, and go to Step 1 until $n\Delta t = t_{\text{final}}$.

The stability condition requirements as follows [126],

$$\gamma = \frac{1}{2}\left(1-2\alpha\right), \text{ and } \beta = \frac{1}{4}\left(1-\alpha\right)^{2} \tag{8.64}$$

$$\alpha \in \left[-\frac{1}{3}, 0\right] \tag{8.65}$$

8.3 Convergence Study and Verification

Mesh convergence is carried out for the geometry described as top view in Figure 3-1b and side view in Figure 7-1a, without any guides. We model the effect of such sudden changes in tension by applying a square tension impulse at the supply reel (x = 0) as follows,

$$T_b(0,t)=\begin{cases} T_0 & \text{for} \quad 0\le t\le t^* \\ (1+r)T_0 & \text{for} \quad t^*\le t\le t^*+\tau^* \\ T_0 & \text{for} \quad t>t^*+\tau^* \end{cases} \tag{8.66}$$

where r is the tension amplitude ratio ($r > -1$) and the duration of impulse is τ^*. The other boundary conditions of the system are prescribed as follows,

$$\begin{aligned} v(0,t)=v_0,\ \frac{\partial v}{\partial x}(0,t)=\psi_0 \quad &\text{(a)} \\ u(L,t)=0,\ v(L,t)=V_x\psi_L,\ \frac{\partial v}{\partial x}(L,t)=\dot{\psi}_L \quad &\text{(b)} \end{aligned} \tag{8.67}$$

where v_0 and Ψ_0 represent a static tilt at the supply reel ($x = 0$), represents the Shelton boundary condition at the take-up reel ($x = L$).

For this investigation the supply pack is tilted by $\psi_0 = 0.1$ mrad, and an impulse is applied in the tensile direction at the supply pack. The boundary conditions of Equation (8.67) modified as follows,

$$\begin{aligned} v(0,t)=0,\ \frac{\partial v}{\partial x}(0,t)=1\times10^{-4} \quad &\text{(a)} \\ u(L,t)=0,\ v(L,t)=0,\ \frac{\partial v}{\partial x}(L,t)=0 \quad &\text{(b)} \end{aligned} \tag{8.68}$$

The amplitude of the impulse is $1.2T_0$ with duration of 15 ms. The mean tension is 0.25 N, and the tape velocity is 7.5 m/s. The other parameters can be found in Table 8-1.

Dynamics of the mid-point of the tape span is monitored for different number of elements (20, 30, 40, 50 and 60) and time step sizes (5, 10, 50 *ns*). Results are compared in Figure 8-3. The change in the predicted response by increasing the number of elements from 20 (blue solid line) to 30 (blue dash-dot line) is significant. The change is much less from 40 elements to 60. The difference between the 50 (blue dashed line) and 60 (blue dashed line) elements is within 1 nm. In this study, 50 elements, with corresponding length of Δx = 4.77 μm, is used. The temporal convergence study shows (Figure 8-3(b)) that the results

are virtually identical for all three time step sizes. In the rest of this study Δt = 10 *ns* is used.

The same numerical approach outlined above is used for a tape translating between two supports. Equation (8.22) are subjected to following boundary conditions,

$$\begin{aligned} &v(0,t) = v_0 \sin\left(2\pi\Omega_T t\right),\ \frac{\partial v}{\partial x}(0,t) = 0 && \text{(a)} \\ &u(L,t) = 0,\ v(L,t) = 0,\ \frac{\partial v}{\partial x}(L,t) = 0 && \text{(b)} \end{aligned} \tag{8.69}$$

A frequency sweep in the range $0 \le \Omega_T \le 3$ kHz is conducted for v_0 = 1 μm, for different tape transport speeds. Figure 8-4 demonstrates the effects of velocity on the natural frequencies. Figure 8-4 also shows that the natural frequencies decrease by increasing velocity for all the modes in the range investigated. This trend is consistent with Wickert [23].

8.4 Results and Discussion

In this work we accommodate for the floating tape layers in the take-up reel [121] by extending the length of the tape between the guide-3 and reel-2 by integer multiples of $2\pi R_{R2}$, where R_{R2} is the current radius of the take-up pack (Figure 8-5).

8.4.1 LTM due to an impulsive change in tension

There are several facts that can cause a sudden change in tape tension. For example, as the tape is unwound at the supply reel, the wound-in stress in the circumferential direction of the pack needs to adjust to tensile the tape. The tension impulse is described in Section 8.3.

The effects of these two variables are investigated in the following ranges: $-0.5 \le r \le 0.5$ and τ^* = 5, 10, and 15 ms. Boundary conditions are as stated in Equation (8.68) .

Figure 8-6 shows the longitudinal and lateral tape deflection histories monitored at the head (guide-2) position, for r = 0.5 and τ^* =15 *ms*. Figure 8-6 (upper) shows that the in

plane displacement component experiences two sudden changes at the onset and end of the square wave impulse, which causes high frequency (2066 Hz), in plane vibration with maximum amplitude of ~35 and 20 μm, respectively. As a consequence of this in plane action, vibration in the lateral direction is excited as shown in Figure 8-6 (lower). This vibration shifts the tape by ~25 nm in the lateral direction, at the location of the head. The primary frequency of the vibration shown in Figure 8-6 (lower) is 666 Hz.

In the course of this investigation it was found that, for a fixed *r* value, the maximum tape deflection is independent of the duration of the impulse, τ^*. Therefore, in Figure 8-7 we only present the effect of *r* on the maximum tape deflection for τ^* = 15 ms. This figure shows that the maximum tape deflection is a linear function of *r*. The static tilt angle at supply reel is responsible for the unequal slopes in Figure 8-7(b) for the positive and negative *r*-values. This linear behavior in this nonlinear system is due to the definition of longitudinal strain in Equation(8.2), which in this case is dominated by $\partial u / \partial x$, due to the nature of the input. This in turn ends up dominating the longitudinal and lateral responses. It is also important to notice that when a lateral deflection is the source of energy input into the system, a linear relationship of the kind described above is not expected. In that case, a larger lateral motion is expected to enhance the nonlinearity. But, this is beyond the scope of the current investigation.

8.4.2 LTM due to tension dynamics

In a typical tape drive, the tape speed servo action causes tension fluctuations, even at steady state operating conditions [119, 174]. In order to investigate the effects of the in plane tension fluctuations on the LTM, the system of equations are solved with a simple harmonic tension variation, $T_{b0}(t)$. The following boundary conditions are used,

$$\begin{aligned} &T_b(0,t) = T_0\left(1 + r\sin\left(2\pi\Omega_T t\right)\right), v(0,t) = v_0, \frac{\partial v}{\partial x}(0,t) = \psi_0 && \text{(a)} \\ &u(L,t) = 0, \quad v(L,t) = V_x\psi_L, \quad \frac{\partial v}{\partial x}(L,t) = \dot{\psi}_L && \text{(b)} \end{aligned} \tag{8.70}$$

where Ω_T is the frequency of tension fluctuation applied at the supply reel (x = 0).

The tension fluctuation frequency is swept in the range $0 \leq \Omega_T \leq 5$ kHz, with relatively coarse increments of 100 Hz. Near the peaks the increments are reduced to 10 Hz. Simulations are carried out with parameter values that are relevant for the technological application: $T_0 = 0.25$, 0.5, and 0.75 N; $V_x = 2.5$, 5.0, and 7.5 m/s [1]; and, with 0, 1 and 2 floating layers.

Figure 8-8 shows the frequency response of the longitudinal and lateral tape motions for three different tape transport velocities. In this frequency range, the tape has a single resonant frequency in its longitudinal dynamics, around 2100 Hz as shown in Figure 8-8(a). This is close to 2250 Hz, obtained from $(E/\rho)^{1/2}/4L_b$, which is found for a non-travelling string with fixed-free boundary conditions. In response to tension fluctuations, three resonant peaks are excited in the lateral direction. These peaks are located around 700, 2100 and 3000 Hz. Transport velocity affects not only the damping in the system, but also the stiffness due to the inherent nature of the gyroscopic behavior as expressed in the material time derivative of Equation (8.4). In fact, increasing tape velocity raises the Coriollis acceleration, and eventually decreases damping and stiffness of the tape. The natural frequency and amplitudes of the lateral component of tape deflection increase, as a result of increasing the tape velocity from 2.5 m/s to 7.5 m/s. No significant frequency shift is observed at the second resonant frequency, but the response amplitude increases. A vibration mode in the lateral motion is excited around 2950 Hz. This mode absorbs increasingly more energy with increasing tape velocity. Also note that only one resonant frequency is coincident in both longitudinal and lateral directions.

The effect of mean tension, T_0, on the resonant frequencies of the system is shown in Figure 8-9. This result shows a clear coupling between the two vibration directions. Magnitude of the mean tension does not change the natural frequency of vibration in the longitudinal direction as shown in Figure 8-10(a). However, energy is absorbed into the longitudinal vibrations by increasing mean tension. Increasing tension stiffens the tape in the lateral direction, and results in increasing resonant frequencies of the lateral vibration modes. This increase is small at the natural frequency, but it can be seen more clearly at around 2,800 Hz (fourth resonant frequency). Also note that a resonant frequency around

1,600 Hz appears at the T_0 = 0.25 N. This frequency is merged with the third natural frequency for higher tension values.

The effect of the floating layers in the take-up pack is analysed for 0, 1 and 2 layers. Floating layers increase the tape span. In order to stay consistent in numerical analysis, the element size is kept constant, but the number of elements is increased. Figure 8-10 shows that the increasing number of floating layers dramatically reduces the resonant frequencies of the longitudinal and lateral tape dynamics. Both lateral and longitudinal vibration resonant frequencies move to lower values with increasing number of layers. In spite of using a sampling rate of 10 Hz in the 100 – 1000 Hz range, the frequency spectrum of the case of 2 layers shows sharp variations in Figure 8-10(b). Increasing the number of layers adds more resonant frequency values into the scoped window (5 kHz range). This result is attributed to the fact that longitudinal and lateral tape vibrations have natural frequencies somewhat proportional to the reciprocal of total tape length.

8.4.3 Resonance tuning due to coefficients of friction (COF) and guide position

The effects friction introduced by stationary a cylindrical guide on the system is investigated in this section. Figure 8-11 depicts a tensioned tape travelling between two supports located at x = 0, L which represent the positions of the reels. The guide stiff nesses are set to be zero.

For the case of N_g = 0, the effects of tape transport velocity on the first three resonant frequencies are plotted (Figure 8-12a) for T_0 = 0.5, 1, and 2 N. In general, the resonant frequencies and the critical velocities increase by increasing tension. The critical velocities were found to be 118.5, 143.7, and 171.8 m/s for the three tensions, respectively.

Friction effects were investigated by placing a head/guide at $x = d_{g2}$ (Figure 8-11). There is no friction applied at the other two guides' locations. Coefficient of friction (COF) values in the longitudinal and lateral directions (μ_x, μ_y) were varied in a relatively wide range (0 – 2.5). Note that some large COF values can be obtained by using a sub-ambient foil bearing or laterally oriented grooves.Figure 8-12(b) shows the first three resonant frequencies as a function of tape velocity for an upstream tension value of T_0 = 0.25 N,

and COF values of μ_x = 1 and μ_y = 1.3. This analysis shows that by introducing a frictional support at $d_g = L/2$ the critical velocity increased to 122.1 m/s from 118.5 m/s with no-frictional guiding. This effect is attributed to increase in tape tension over the guide due to the longitudinal component of friction force. Figure 8-12 (b) also demonstrates that the natural frequencies of the tape are significantly reduced at low tape velocities, in the range of 0 – 8 m/s. This prediction is attributed to the over-damping introduced into the system by the lateral component of the friction force. At faster speeds, over-damping effect is surpassed by inertial forces due to Coriollis acceleration. The range of tape velocity in which there is significant over-damping is wider for mode-1 than mode-3, indicating that the lower modes can absorb more energy. Also note that mode-2 remains unaffected from damping. This is attributed to the location of the guide which is placed at the nodal point of mode-2.

The effect of frictional damping on the natural frequency (mode-1) is plotted for different longitudinal (μ_y) and lateral (μ_x) COF values in Figure 8-13, in a moderate tape velocity range of 2.5 – 10 m/s. This group of figure denotes the coupling between the longitudinal and lateral frictions. In the case of that system is dominated by the longitudinal friction (low$-\mu_y$) the natural frequency increases with increasing longitudinal friction because of tension increased. Alternatively, in the cases of that the lateral friction dominates the tape drive (high$-\mu_y$) the natural frequency can be reduced substantially even at moderate tape speeds, as shown in this figure. The transition state of these two studies occurs at the intersection of these curves, and the value increases with increasing tape speed.

The effect of guide position (d) on the first three resonant frequencies was investigated for T_0 = 0.25 N, V_x = 6 m/s and $\mu_x = \mu_y$ = 1.0. Figure 8-14 gives the frequency spectra of the tape for a single guide of different positioning. The optimal guide position is located at the center of tape path as all the modes have substantially reduced amplitudes. A group study results of 3-guide positioning is demonstrated in Figure 8-15. The schematic plot is shown in Figure 8-11 and study is performed by fixing the guide-2 at the center of tape and moving guide-1 and guide-3 along the upstream and downstream of tape path respectively. There is no significant frequency shift observed of 2nd and 3rd mode. When a guide is placed at downstream side, 2nd mode becomes entirely anti-resonant. Moreover,

by tuning the positions of guide-1 and guide-3, the amplitude of 2^{nd} and 3^{rd} mode are not simply monotonic. These phenomena could due to mode shapes. Consistence with single guide investigation, positioning the guides toward the center efficiently over-damped the first mode.

8.5 Summary and Conclusions

Equation of motion of a tensioned tape, translating between two reels, and supported by friction guides is presented. In particular the non-linear coupling between the longitudinal and lateral tape deflection components is modelled. The coupling is investigated for two scenarios that are common in current tape drive systems: a) tension impulse due to mismatch of longitudinal stresses in the reel and the tension on the tape-path; and b) tension fluctuations due to tape–speed servo control.

It was shown that the tension impulse can cause a high frequency high amplitude wave in the longitudinal direction, and also excites lateral motion. The effect of the longitudinal wave can potentially cause local stretching of the bits.

The amplitude of the longitudinal and lateral deflections due to tension impulse varies linearly with the impulse strength. It was also shown that the tension fluctuation, which primarily affects the longitudinal tape deflection, can excite resonances in the lateral tape motion. Tape velocity and tension have relatively small effects on the resonant frequencies in the range considered, but deflection amplitudes increase with increasing values of T_0 and V_x, as expected. On the other hand, the increasing numbers of floating layers on the take-up pack lower the natural frequencies and "invite" more resonances into the $0 - 5$ kHz range. The tape drive designers must be aware of parametric resonant frequency and try to avoid the engine speed from these frequencies.

A nonlinear coupling between the longitudinal friction, lateral friction and tape velocity was described which could result in sufficient energy dissipation to lower the natural frequencies of the high mode-numbers. The position of the frictional guide was found to have a significant effect on the damping and frequency reduction. The first three modes were found to be optimally damped when a single guide is positioned at middle of tape span.

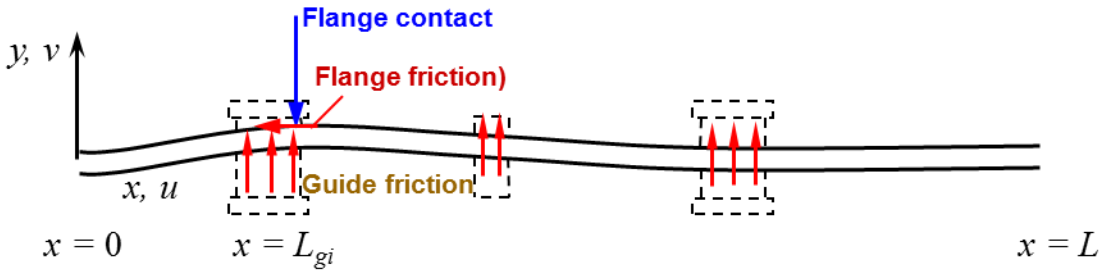

Figure 8-1 Schematic plot of tape path with fixed guides

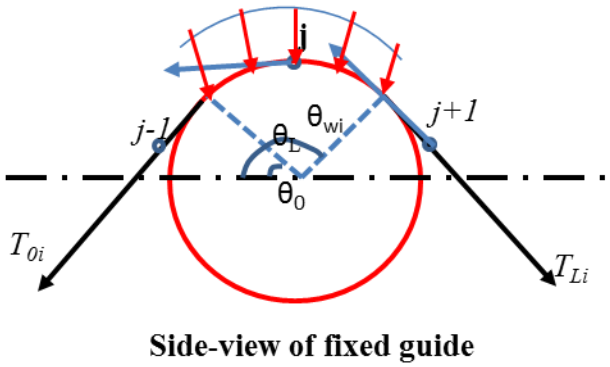

Figure 8-2 Side view of discretized tape over a fixed guide

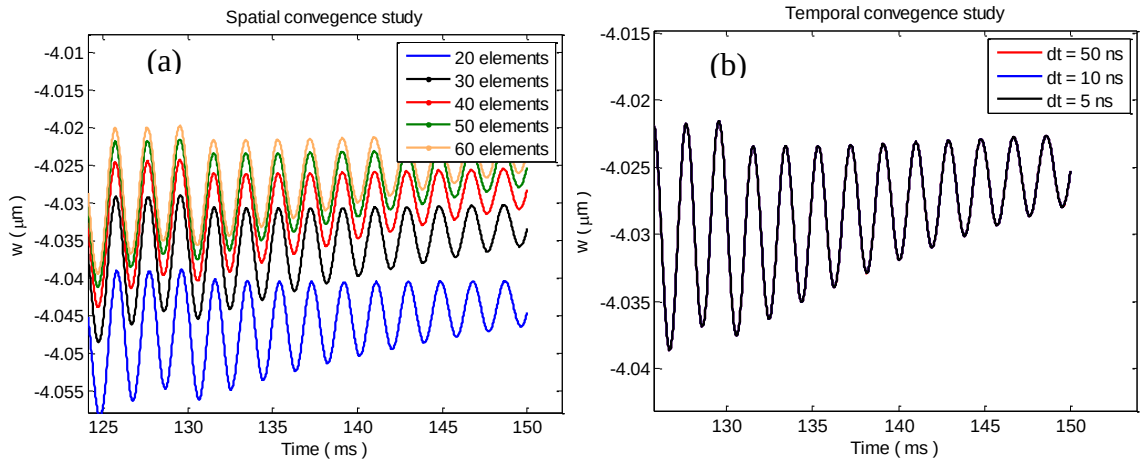

Figure 8-3 Convergence study for testing the effects of (a) the mesh size, Δx, and (b) the time increment, Δt.

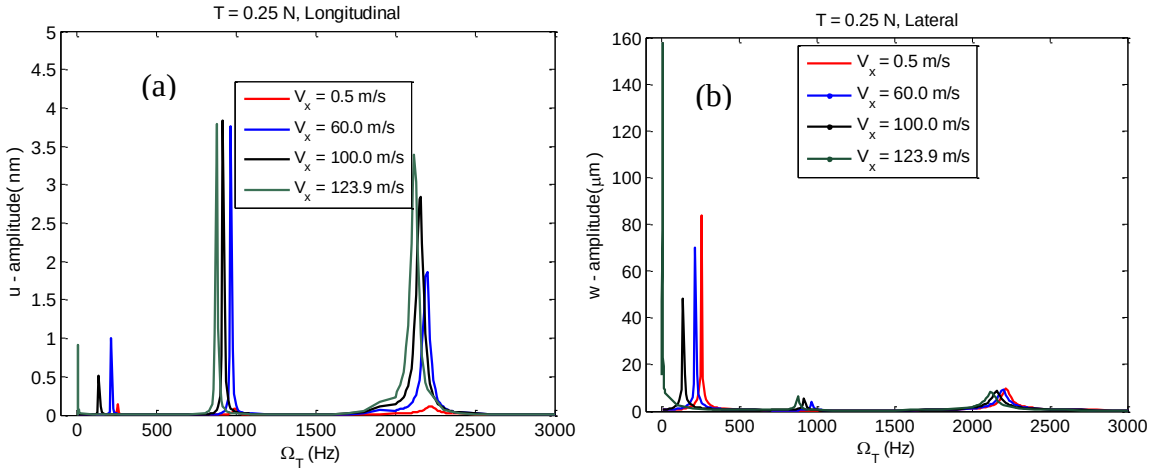

Figure 8-4 Frequency response of the tape traveling between two supports for different tape transport speeds (a) longitudinal and (b) lateral.

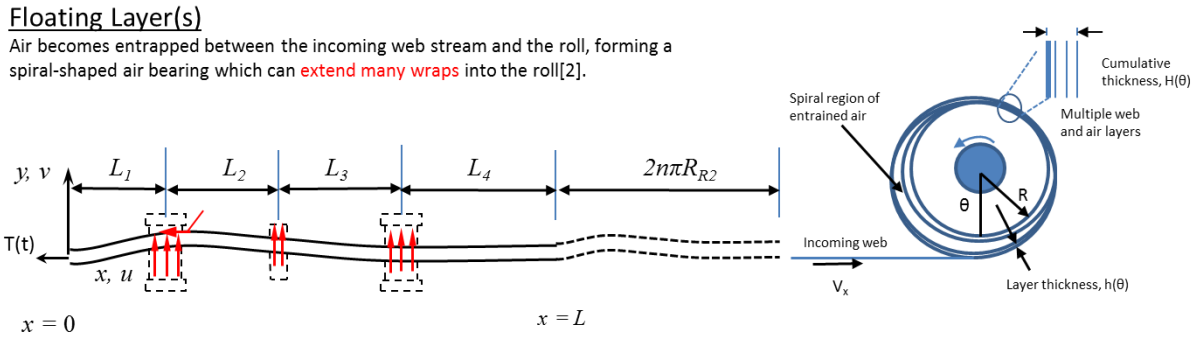

Figure 8-5 Schematic plot of floating layer

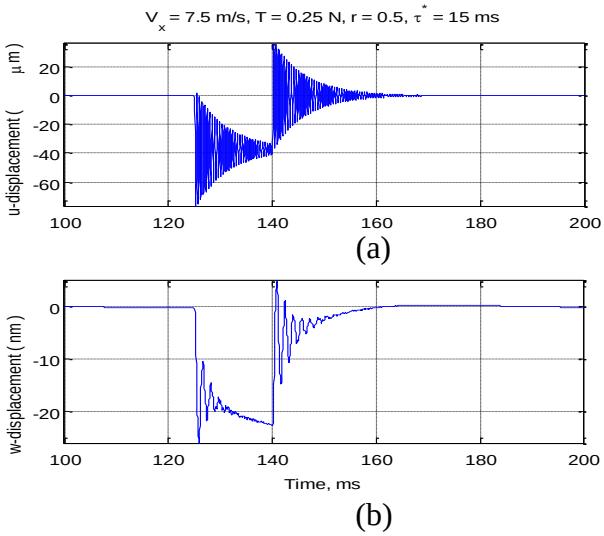

Figure 8-6 Tape's longitudinal (top) and lateral (bottom) dynamics in response to a tension impulse T_0 = 0.25 N, r = 0.5, t* = 125 ms, and τ* = 15 ms, at V_x = 7.5 m/s.

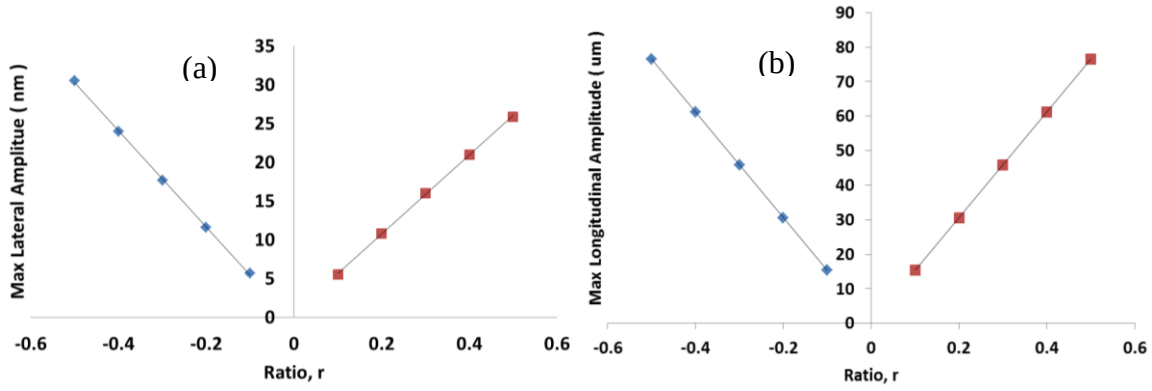

Figure 8-7 Maximum tape deflection in (a) lateral and (b) longitudinal directions, in response to a tension impulse T_0 = 0.25 N, r = -0.5 - 0.5, t* = 135 ms, τ* = 15 ms, V_x = 7.5 m/s.

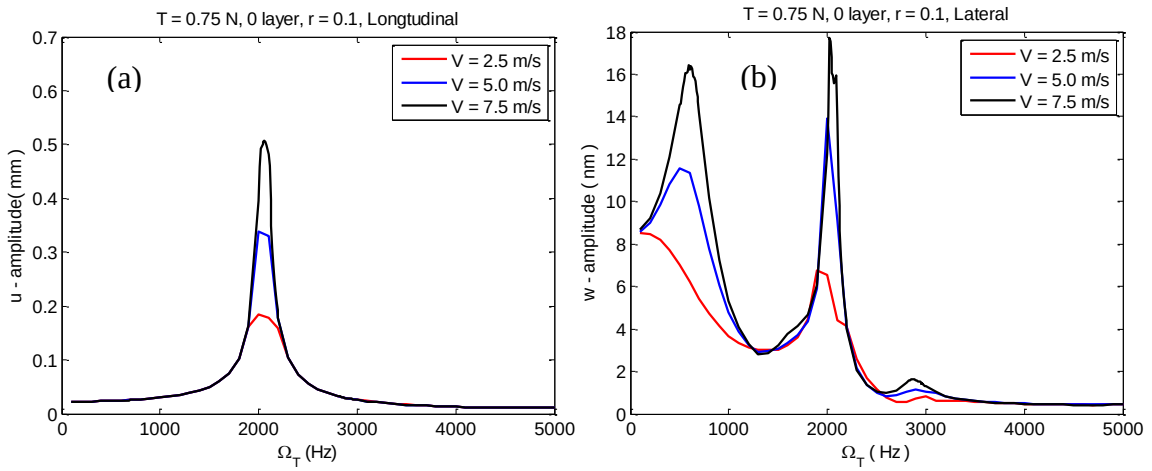

Figure 8-8 Frequency spectra in (a) lateral and (b) longitudinal directions, for tape at different tape transport velocitys, V_x = 2.5, 5.0, and 7.5 m/s with T = 0.75 N, r = 0.1, and zero floating layers.

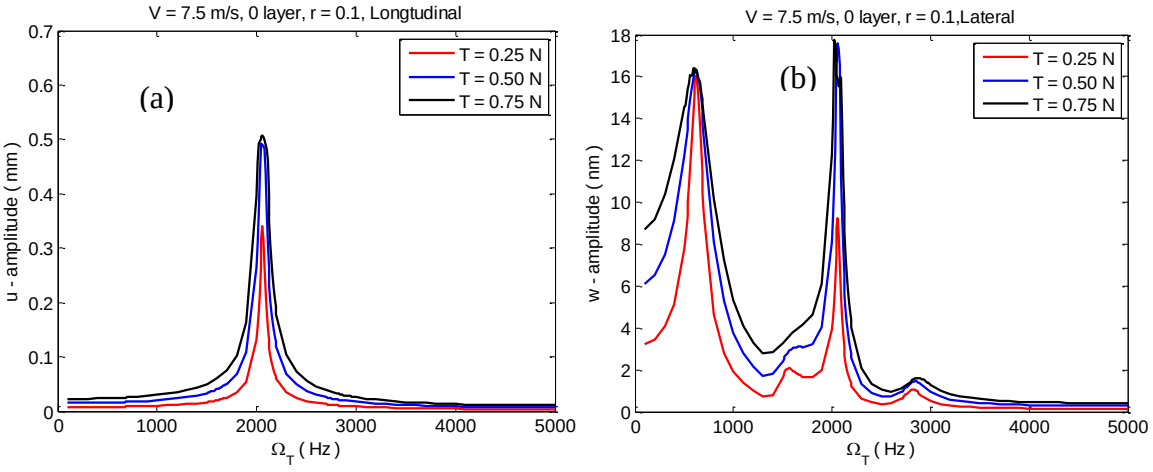

Figure 8-9 Frequency spectra in (a) lateral and (b) longitudinal directions, for tape at under T = 0.25, 0.5, and 0.75N tension with, V_x = 7.5 m/s r = 0.1, and zero floating layers.

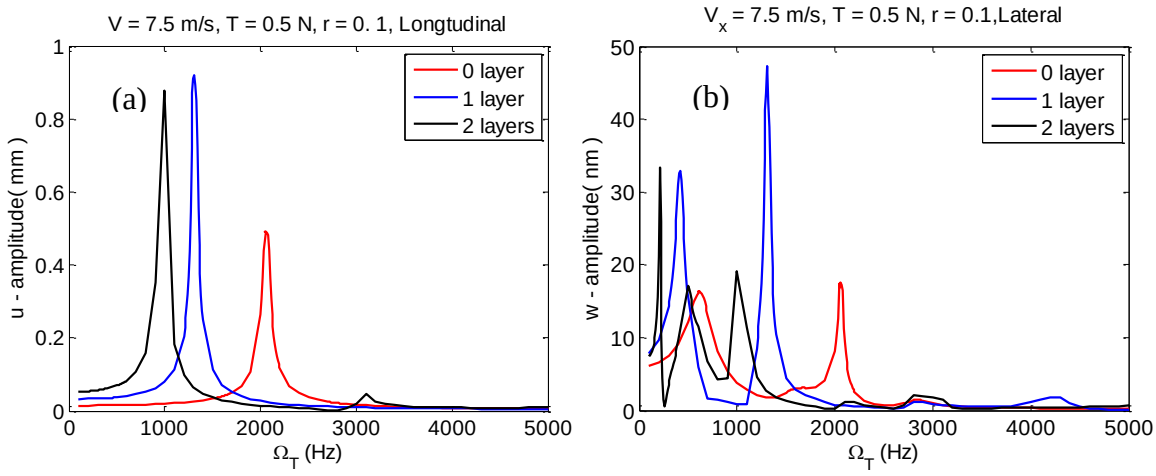

Figure 8-10 Frequency spectra in (a) longitudinal and (b) lateral directions for tape with 0, 1 and 2 floating layers at the take-up pack, with V_x = 7.5 m/s, T = 0.5 N, and r = 0.1.

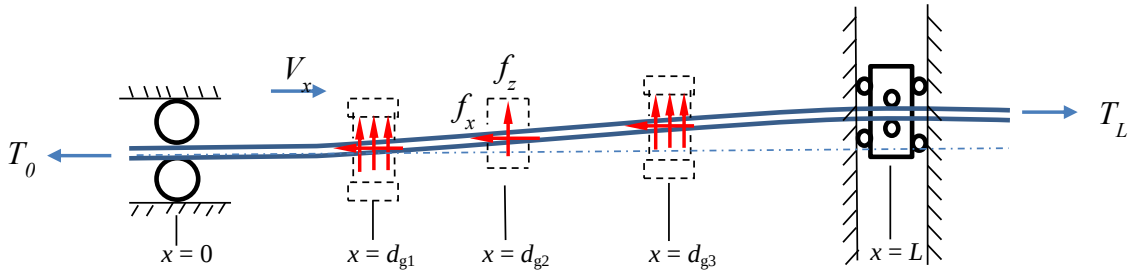

Figure 8-11 Schematic depiction of tensioned, translating tape with three (Ng = 3) intermediate guides.

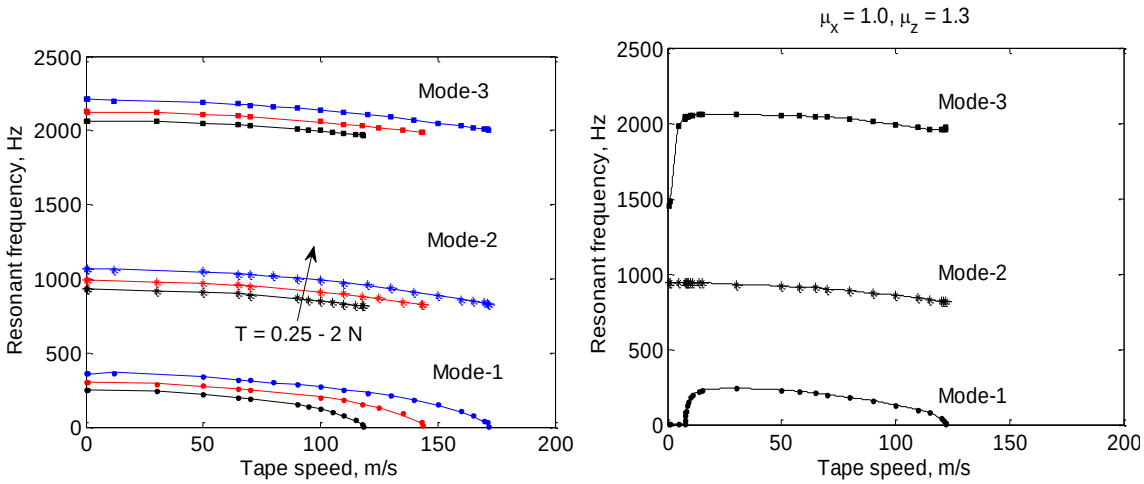

Figure 8-12 Effect of tape transport velocity on the resonant frequencies: (a) for N_g = 0 and T_0 = 0.25, 1, and 2 N; and, (b) for N_g = 1, d_g/L = 0.5, and T_0 = 0.25 N.

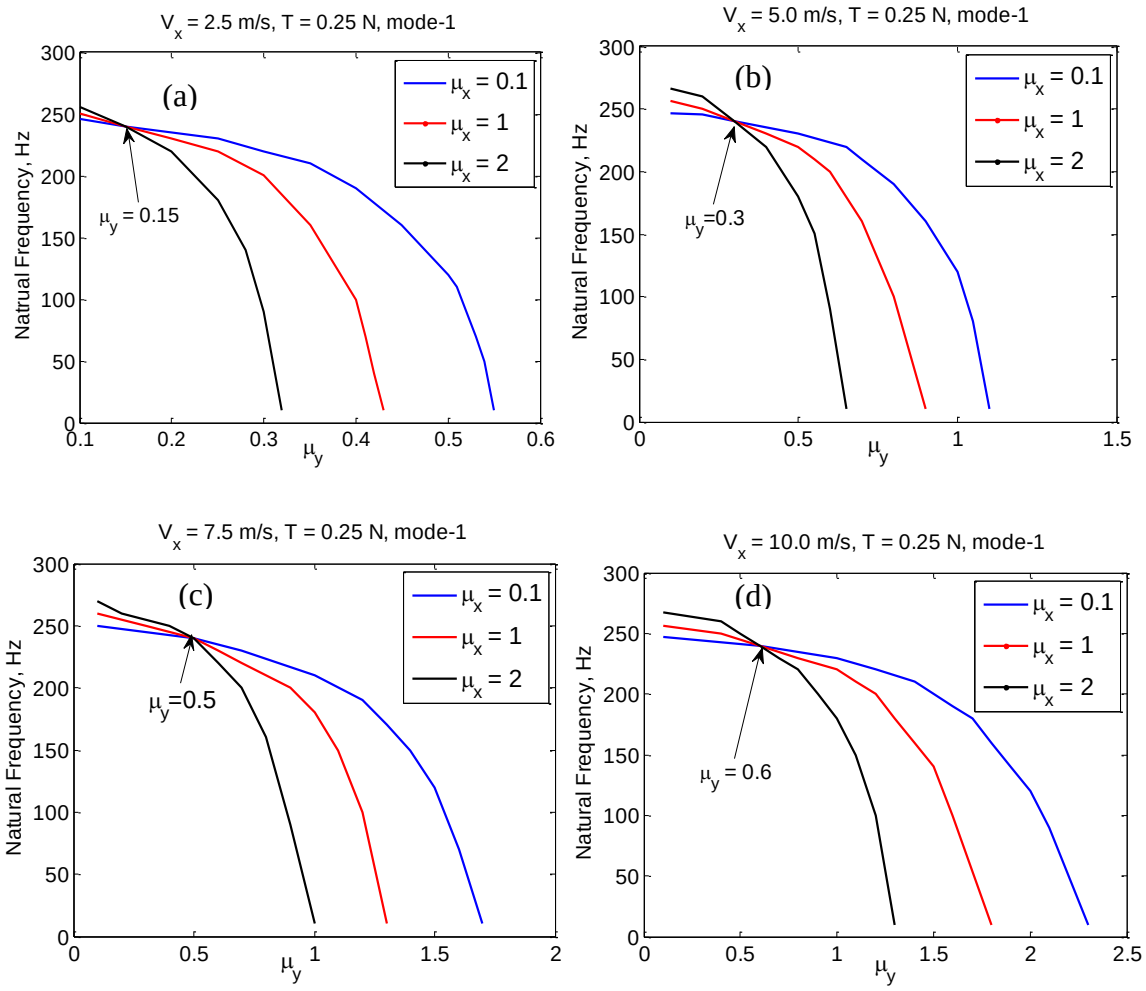

Figure 8-13 Natural frequency variation with different lateral (μ_y) and longitudinal (μ_x) COF values, for (a) 2.5 m/s, (b) 5.0 m/s, (c) 7.5 m/s, (d) 10.0 m/s

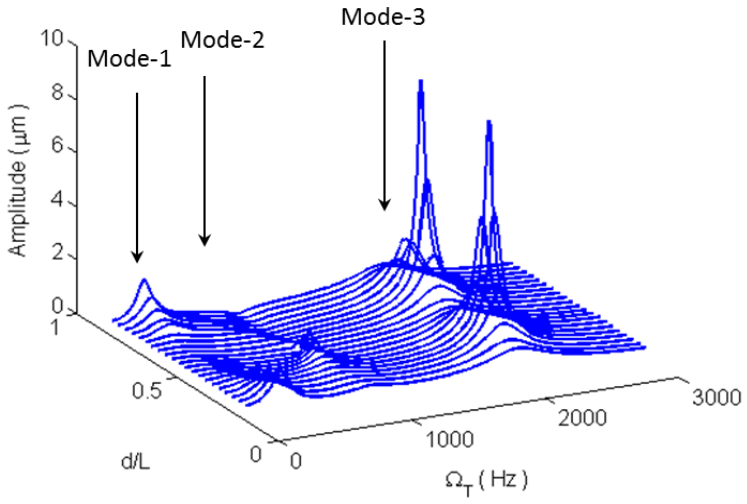

Figure 8-14 The effect of guide position (d/L) on frequency spectrum the tape for V_x = 6 m/s and $\mu_x = \mu_y = 1.0$, $T_0 = 0.25$ N.

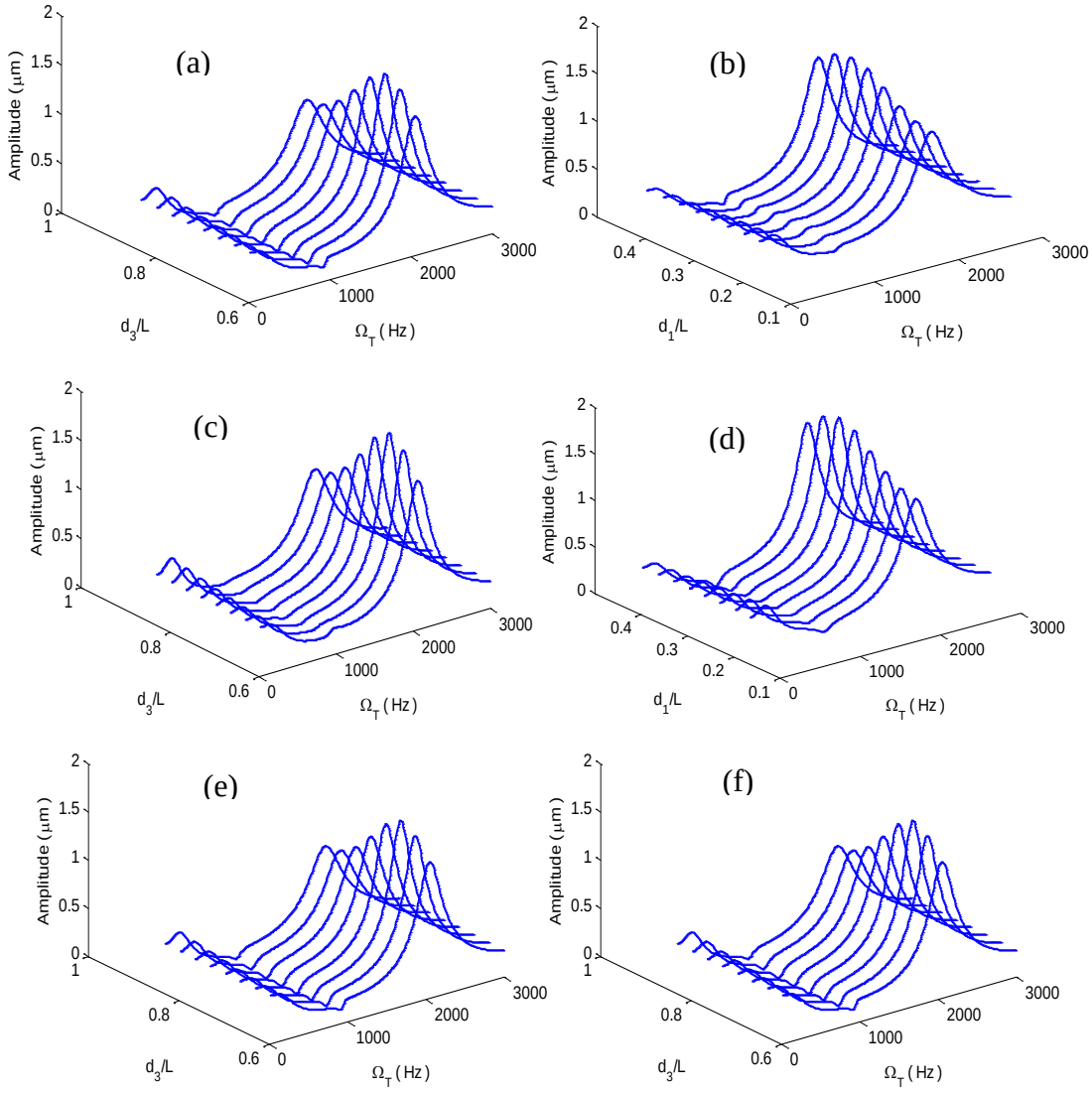

Figure 8-15 Effect of three guides positioning ($d_2/L=0.5$) on frequency spectrum the tape for V_x = 6 m/s and $\mu_x^{g1} = \mu_x^{g3} = 0.2$, $\mu_y^{g1} = \mu_y^{g3} = 0.15$, $\mu_x^{g2} = \mu_y^{g2} = 0.5$ T_0 = 0.25 N. (a) $d_1/L=0.2$, (b) $d_3/L=0.6$, (c) $d_1/L=0.3$, (d) $d_3/L=0.7$, (e) $d_1/L=0.4$, (f) $d_3/L=0.8$.

Table 8-1 Baseline Parameters in Figure 3-1b for this study.

Tape properties		
Tape thickness	h (μm)	6.4
Tape width	b (mm)	12.7
Bending rigidity	EI (N·m^2)	7.792×10^{-3}
	EA	5.797×10^{-2}
Tape tension	T (N)	vary
Loss modulus	η (Pa·s)	13,000
Density	ρ (kg/m^3)	1400
Tape velocity	V (m/s)	vary
Tape length	L_1, L_2, L_3, and L(cm)	7.60, 12.15, 16.69, and 23.88
Fixed guides/head properties		
Radius	R_1, R_2, and R_3 (mm)	5, 6.2, and 5
Guide stiffness	k_g (N/m)	10, 0, 100
Guide edge stiffness	k_e (N/m)	0
Wrap angle	θ_{w1}, θ_{w2} and θ_{w3} (º)	78.9, 33.8, 77.2
Coefficient of friction	μ_x ,μ_z	vary
Edge Clearance	$c_l = c_r$ (μm)	Large enough to avoid contact
Packs		
Radii (supply, take-up)	R_{R1} , R_{R2} (cm)	4.7, 2.2

Chapter 9 Summary and Conclusion

A comprehensive literature review of axially moving media is provided in Chapter 2. This chapter covers experimental work related to axially moving media, and the theoretical work related to string, beam and plate models for simulation and analysis of dynamics of axially moving media, mechanics of different types of guiding elements and mechanics of support/take-up reels.

The equation of motion of a linear viscoelastic, axially moving material is derived by using the beam theory and solved by the finite element method as described in Chapter 3. This equation can be used to simulate web handling and magnetic tape recording applications. The accuracy of the numerical solution is investigated in the frequency domain in Chapter 4. Effects of rollers and recording heads on the tape dynamics are modeled as external loads, as presented in Chapters 5 – 7. Chapter 8 discusses the nonlinear coupling between lateral and longitudinal tape deflections.

9.1 Investigation of the Accuracy of Numerical Solution

The wave response of the translating, tensioned, viscoelastic beam is investigated in a non-dimensional analysis. Waveguide finite element (WFE) and finite difference (FD) methods are used to investigate the accuracy of numerical modeling in the frequency domain. State-space form of seeking eigenvalues of gyroscopic systems is applied to the fully-discretized system. The numerical results are compared with the analytical solution.

9.1.1 Conclusions

Good agreement is found between the numerical and analytical solution. In particular, the WFE method shows better accuracy than the FD approach at high frequencies. The WFE method can be used to find the critical frequencies of a translating beam system with internal damping.

9.2 Tilted Roller

A tilted roller model based on the expectation that the tape speed and the roller speed match [60] at steady state for tilted rollers is introduced and validated experimentally in Chapter 5. This model includes the effects of lateral friction force, frictional-moment and lateral component of the wrap pressure due to roller tilt. The slope of the centerline of the tilted roller can be expressed in the tape based coordinate system [59]. Lateral tape deflection and slope are measured at upstream and downstream of a tilted-roller on an experimental, configurable tape-path as a function of roller tilt-angle, tape's wrap angle over the roller and the lengths of free tape span upstream and downstream of the tilted-roller. This tape-roller interaction model is integrated into a system level tape transport model which accommodates simulating the dynamics of tape supported by multiple rollers, between two reels [21].

9.2.1 Conclusions

Model predictions compare very favorably with experimental measurements. This work shows that the tape position on the upstream side of the tilted-roller most significantly affects the lateral shift of the tape over the roller. A strong influence of the length of the free span of the tape upstream and downstream on LTM is also demonstrated. The length of the tape upstream and downstream of a roller contributes to its stiffness, and therefore has an effect on the lateral position/slope of the tape over the roller at steady state. The longer tape span is more compliant and displays a larger lateral deflection. For a fixed upstream span increasing downstream span length causes more lateral shift under similar conditions.

9.3 Roller Friction

A model for the effective lateral friction coefficient between a magnetic recording tape (LTO-5) and a grooved roller is developed and examined experimentally in Chapter 6. In these tests the tape transport velocity was set to zero, but the roller was actuated laterally. The experiments were performed in static (slow) and dynamic (fast) actuation modes. Both methods gave a breakaway coefficient of friction value close to 0.40.

A periodic stick and slip phenomenon was observed in the fast-actuation mode tests. The stick-to-slip and slip-to-stick transitions occur when the tape lateral speed matches the roller lateral speed, which happens near zero tape and roller velocities. The inclusion of stick and slip, and velocity dependence of the friction force renders the tape's equation of motion non-linear. Both the experiments and the theory show that upon slip, the tape vibrates primarily at its natural frequency, and vibrations are attenuated relatively fast due to frictional and internal damping.

9.3.1 Conclusions

This work shows that the friction resulting from the complex interaction and bending of a tape tensioned over a grooved roller can be well described by an effective coefficient of friction for a range of wrap angle and tension values. This work also shows that the sudden lateral slip could excite the tape into high frequency vibrations.

9.4 Flange Contact

Tape response due to flange hits is investigated by a mathematical model of the tape path in Chapter 7. It is shown that flange hits can cause a wide-band frequency response in the tape, and the tape can have very non-periodic motion. Friction in the system helps reduce some of the complexity of the response.

9.5 LTM and Longitudinal Coupling

The non-linear coupling between the longitudinal and lateral tape deflection components is modelled in Chapter 8. The coupling is investigated for two scenarios that are common in current tape drive systems: a) tension impulse due to mismatch of longitudinal stresses

in the reel and the tension on the tape-path; and b) tension fluctuations due to tape–speed servo control.

Also in Chapter 8 coupling between the longitudinal friction, lateral friction and tape velocity were described which could result in sufficient energy dissipation to lower the natural frequencies of the high mode-numbers.

9.5.1 Conclusions

It was shown that the tension impulse can cause a high frequency high amplitude wave in the longitudinal direction, and also excites lateral motion. The effect of the longitudinal wave can potentially cause local stretching of the bits. The amplitude of the longitudinal and lateral deflections due to tension impulse varies linearly with the impulse strength.

It was also shown that the tension fluctuation, which primarily affects the longitudinal tape deflection, can excite resonances in the lateral tape motion. Tape velocity and tension have relatively small effects on the resonant frequencies in the range considered, but deflection amplitudes increase with increasing values of T_0 and V_x, as expected. On the other hand, the increasing numbers of floating layers on the take-up pack lower the natural frequencies and "invite" more resonances into the $0 - 5$ kHz range. The tape drive designers must be aware of parametric resonant frequency and try to avoid exciting these frequencies.

In contrast to the lateral COF damping the natural frequencies, the longitudinal COF increases frequencies for low values, but becomes a negative factor after a critical value. This critical value increases with the tape transport velocity. The position of the frictional guide was found to have a significant effect on the damping and frequency reduction. The first three modes were found to be optimally damped when a single guide is positioned at middle of tape span.

Chapter 10 Future Work

Tape industry anticipates thinner, smoother media and faster translating speed. Along with this development, some new guiding elements are introduced to reduce the LTM and improve the system behavior. However dynamic response of some existing guiding components is still not clear to the community. In addition the appropriate simulation method of axially moving media is still an open issue especially for nonlinear problems. Moreover, these changes and uncertainties lay challenges for our system level simulation tool (LTMSim). In this chapter, we will discuss the future work mainly in three aspects: new/existing guiding elements (Section 0), higher order modeling (Section 0) and analysis of LTM (Section 0).

10.1 Guiding Elements

Active guiding roller is the type of roller that can pivot along its axis as introduced in Chapter 5. This concept is used to optimize web guiding control [119]. The detailed mechanics is described by Kartik and Wickert [153] and Kartik and Eleftheriou [41]. The control method is also investigated extensively in both web [61-64] and tape [152] industries. Although Chapter 5 has examined the static behavior of the interaction between the active roller and media, the dynamic response of model needs validation by

experiments. To achieve this goal, understanding the friction force acting between roller and running tape/web is essential. The measured effective lateral friction force and the stick and slip model introduced in Chapter 6 have good agreement. Future work could focus on the coupling between roller dynamics and tape dynamics. Effects of surface roughness of the tape and the roller on friction are should also be investigated.

Hashimoto [175] analyzed and tested porous foil bearing guides and concluded that it behaviors better when controlling web (tape) to guide spacing. The pressurized air bearing guides exhibits significant lower LTM than rollers [73]. IBM group used a special tape drive with pressured air bearing guides which was used in the record breaking areal recording density demonstrations [176, 177] . Simulation of pressurized roller could provide a guidance of using it in real tape drive product.

Flat read/write head is the only active component current in tape drive system [178]. The flat contour is designed for keeping tape to head in contact and enables higher recording densities [179]. The spacing [180], tape deflection [181] on head and friction [155] are studied independently. A possible research topic in this area could be building a numerical model that simulate the tape to head interaction and integrated into system level tool (LTMSim).

10.2 Modelling

Chapter 8 presents a nonlinear beam model for axially moving materials. This model can be verified by using tension fluctuation in real tape drive. Figure A-4 in the Appendix has demonstrated that as the number of point loads increases the Timoshenko beam theory (TBT) would predict different results than those predicted by the Euler-Bernoulli theory (EBT). In commercial tape drives, there are more than three guiding elements over the entire tape span, and the distance between the guides are about 4 cm. To accurately predict the short tape span on guiding elements, Timoshenko beam is more favorable than Euler-Bernoulli beam. The out of plane tape deflection can be modelled by 3D beam, plate, or even more accurately by shell models. The higher order model is also useful to simulate wrinkling behavior. The air-entrainment at reels is another modeling topic that can help control design minimize the misalignment between different layers.

The computational complexity would increase exponentially by applying these models. In order to maintain the efficiency, LTMSim could have different modules for different prediction tasks.

10.3 Analysis of LTM Signal

Models, especially system level simulation, need be validated by measurements. Often, the disturbance signals obtained in experiments are not fully understood. Kartik [40] provided a methodology of identifying spinning frequencies of guiding elements as well as two reels. A series of band-stop filters may be carefully designed to filter out these known disturbances. However, the high frequency contents, due to friction, edge engagement, grooved contact and other effects are tangled with each other. This problem could be tackled by using experiment setup described in Section 6.2 that isolates one disturbance from others.

APPENDIX

Timoshenko Beam Theory

Timoshenko beam model considers the effects of shear deformation in bending of beams. The shear deformation becomes important for beams with relatively high depth-to-length ratio (short beams). The governing equations of the Timoshenko beam theory are as follows,

$$\frac{\partial}{\partial x}\left[\kappa GA\left(\frac{\partial w}{\partial x}-\beta\right)\right]+q(x)=0 \quad \text{(a)}$$
$$\kappa GA\left(\frac{\partial w}{\partial x}-\beta\right)+\frac{\partial}{\partial x}\left(EI\frac{\partial \beta}{\partial x}\right)=0 \quad \text{(b)} \qquad \text{(A.1)}$$

where, κ is the shear correction coefficient, which depends on the geometry ($\kappa=\frac{10(1+\nu)}{12+11\nu}$ for rectangular cross-section), G is the shear modulus ($G=\frac{E}{2(1+\nu)}$ for homogeneous isotropic linear elastic material), and β is the bending rotation of the normal to the neutral axis of the beam. Other variables are stated in Chapter 3.

Finite Element Solution

The derivation of element stiffness matrix for Timoshenko beam element is not presented here, may be found in reference [182] as follows,

$$\boldsymbol{k}=\frac{EI}{(1+\phi)L^3}\begin{bmatrix} 12 & 6L & -12 & 6L \\ 6L & L^2(\phi+4) & -6L & -L^2(\phi-2) \\ -12 & -6L & 12 & -6L \\ 6L & -L^2(\phi-2) & -6L & L^2(\phi+4) \end{bmatrix} \qquad \text{(A.2)}$$

where, $\phi=\frac{12EI}{\kappa GAL^2}$. Note that for $\phi\to 0$ (or $G\to\infty$), Equation (A.2) reduces to the element stiffness matrix derived for the Euler-Bernoulli beam. The nodal displacement

and force vectors are defined in the same way as in Chapter 3, $\boldsymbol{d} = \begin{bmatrix} w_1 & \theta_1 & w_2 & \theta_2 \end{bmatrix}^T$ and $\boldsymbol{r} = \begin{bmatrix} F_1 & M_1 & F_2 & M_2 \end{bmatrix}^T$.

The convergence study is shown in Figure A-1 for clamped-clamped beam with point load acting at the middle. Tape parameters are listed in Table A-1. 32 elements are able to capture the tape deflection curve as demonstrated in Figure A-1b.

The comparison between Euler-Bernoulli and Timoshenko beam theories are depicted in Figure A-2 for a tape with clamped-clamped boundary conditions, subjected to point load at the middle of its span. No appreciable difference can be visually detected. The ratio of Euler-Bernoulli beam deflection over Timoshenko beam deflection at the middle point (maximum deflection) is defined as, $error = \left| w_{TBT} - w_{EBT} / w_{EBT} \right| \times 100\%$. This shows that the maximum error is ~3.4%.

The comparison for the case with with three point loads for the deflection of a beam with clamped-clamped boundaries is shown in Figure A-3. Although the ratio at the maximum deflection is still $error \approx 3.43\%$, the TBT has overall deflection profile starts to deviate from EBT. Figure A-4 plots the error along the tape arc length for both loading cases. The error grows to large values (~30-40%) near the clamped-boundaries. The error drops to ~3.43% at the middle. Note that the case with three points loads, has overall larger error than the case with single point load.

As the boundary conditions at the ends of a tape system, over the supply and take-up reels, are not necessarily represented by clamped boundary conditions, we also considered the effects of using simple-support conditions on the overall error in the solution. For the model with simple-simple boundary conditions (shown in Figure A-5 and Figure A-6), the EBT and TBT theories predict deflection profiles that are very similar in Figure A-5b and Figure A-6b. The corresponding error is about 0.8% as shown in Figure A-5c and Figure A-6c, respectively.

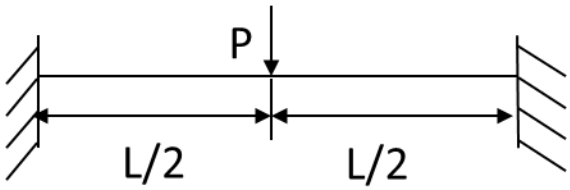

(a)

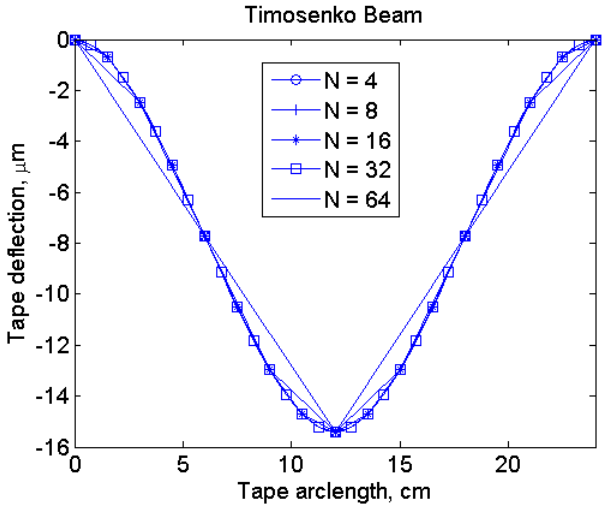

(b)

Figure A-1 (a) Clamped-clamped beam with a point load acting at the middle, (b) Convergence study of Timoshenko beam element for the geometry in (a)

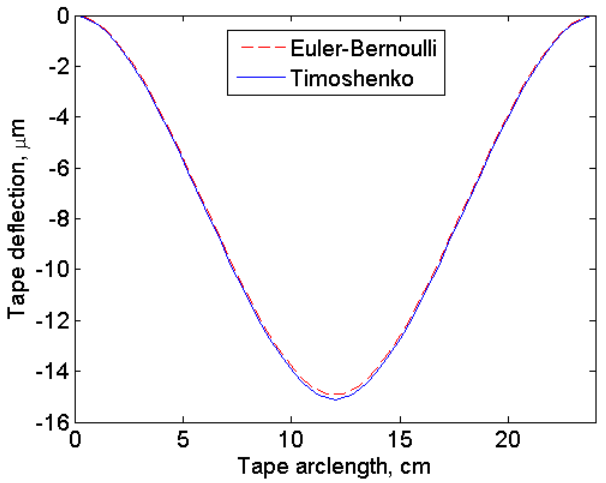

Figure A-2 Comparison of the tape deflection profiles computed by using the EBT and TBT for the geometry defined in Figure A-1a

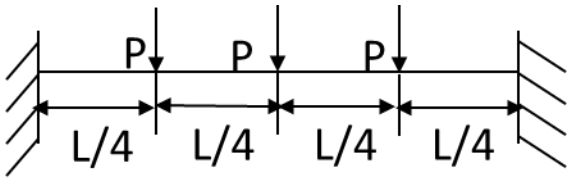

(a)

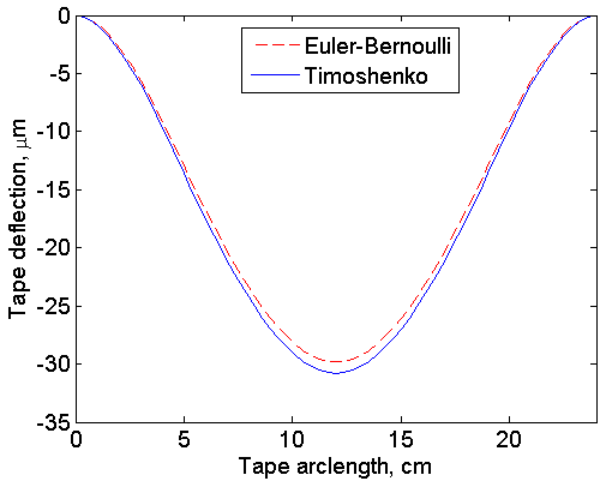

(b)

Figure A-3 (a) Clamped-clamped beam with three point loads acting at quarters of the total length, (b) Comparison of the tape deflection profiles computed by using the Euler-Bernoulli and Timoshenko beam theories for the problem defined in Figure A-3a.

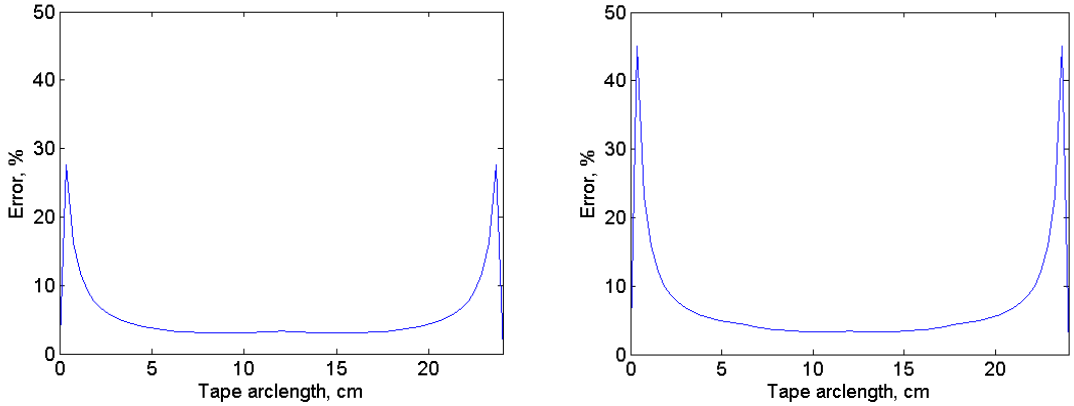

Figure A-4 Error plots of (a) one point load, (b) three point loads presented in Figures A-2 and A-3.

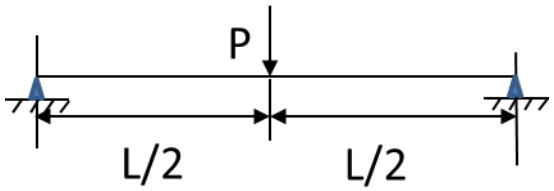

(a)

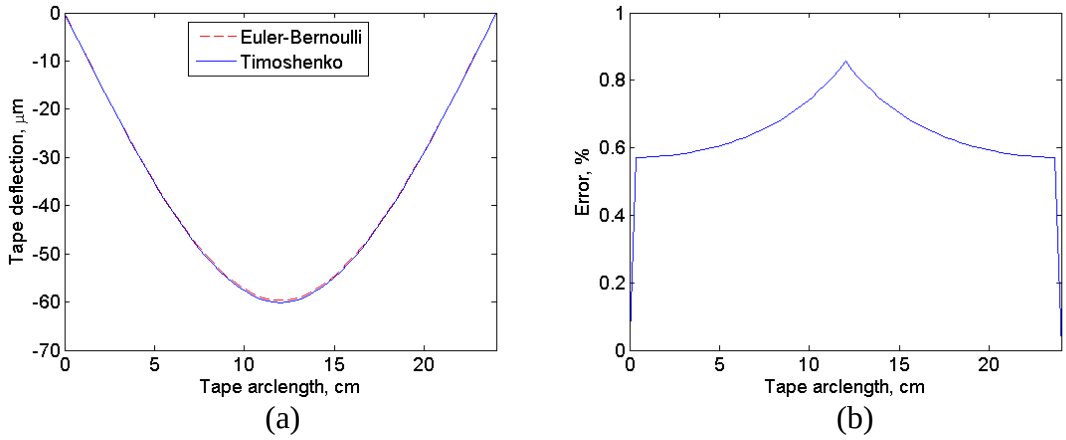

Figure A-5 (a) Simple-simple beam with point load acting at the middle (b) Comparison of the tape deflection profiles computed by using the EBT and TBT for the geometry defined in Figure A-5a and (c) the corresponding error.

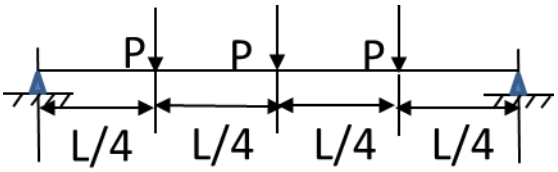

(a)

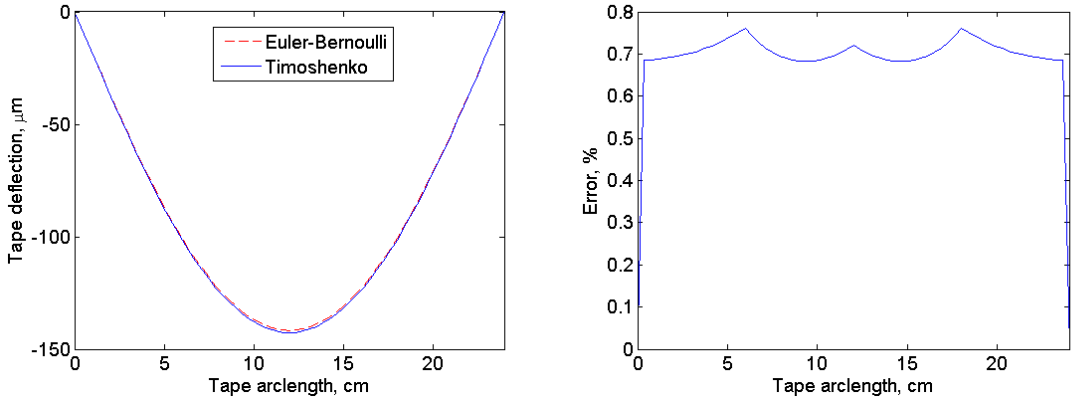

(a) (b)

Figure A-6 (a) Simple-simple beam with point loads acting at quarters of the total length (b) Comparison of the tape deflection profiles computed by using the EBT and TBT for the geometry defined in Figure A-6a and (c) the corresponding error plot.

Table A-1 Tape parameters used in this study

Dimensional Variables	**Tape**
Length, L (m)	24.0×10^{-2}
Thickness, h (m)	6.4×10^{-6}
Width, b (m)	12.7×10^{-3}
Elastic modulus, E (GPa)	4.42
Shear modulus, G (GPa)	$\frac{E}{2(1+\nu)}$
Poisson's ratio, ν	0.3
Shear coefficient, κ	$\frac{10(1+\nu)}{12+11\nu}$
Point load, P (N)	1×10^{-3}

REFERENCES

1. Anonymous, *International Magnetic Tape Storage Technology Roadmap, 2012-2022*. 2012.
2. McLellan, C. *Storage in 2014: An overview*. 2014 January 8 [cited 2015 2/12]; Available from: http://www.zdnet.com/article/storage-in-2014-an-overview/.
3. Gantz, J. and D. Reinsel, *THE DIGITAL UNIVERSE IN 2020: Big Data, Bigger Digital Shadow s, and Biggest Grow th in the Far East*. 2012, IDC.
4. Anonymous. *Data Protection & Archiving*. in *Tape summit*. 2012. London.
5. Hilbert, M. and P. Lopez, *The World's Technological Installed Capacity to Store Information.* Science, 2011. **332**(60).
6. Council, T.S., *2012 Tape Market State of the Union Memo.* 2012.
7. Council, T.S., *Tape Storage Meets Long-Term Data Retention Challenges*. 2013.
8. Council, T.S., *Data Growth and Technology Innovations Fuel Tape's Future.* 2014.
9. Brake, M.R. and J.A. Wickert, *Tilted Guides with Friction in Web Conveyance Systems.* International Journal of Solids and Structures, 2010. **47**: p. 2952-2957.
10. Renshaw, A.A., C.D. Rahn, J.A. Wickert, and C.D. Mote JR, *Energy and Conserved Functionals for Axially Moving Materials.* Transactions of the ASME, 1998. **120**: p. 634-636.
11. Ghayesh, M.H., *Stability Charateristics of an Axially Accelerating String Supported by an Elastic Foundation.* Mechanism and Machine Theory, 2009. **44**: p. 1964-1979.
12. Mockensturm, E.M. and J. Guo, *Nonlinear Vibration of Parametrially Excited, Viscoelastic, Axially Moving Strings.* Journal of Applied Mechanics, 2005. **72**: p. 374-380.
13. Lin, C.C., *Stability and Vibration Characteristics of Axially Moving Plates.* International Journal of Solids and Structures, 1997. **34**(24): p. 3179-3190.
14. Roisum, D.R.X., *The Mechanics of Web Handling*. 1998: Tappi Press.
15. Mote JR, C.D., *A Study of Band Saw Vibrations.* Journal of Tthe Franklin Institute, 1965. **279**(6): p. 430-444.

16. Zhu, W.D. and J. Ni, *Energetics and Stability of Translating Media with an Aribtrarily Varying Length.* Journal of Vibration and Acoustics, 2000. **122**: p. 295-304.
17. Zhu, W.D. and N.A. Zheng, *Exact Response of a Translating String with Arbitrarily Varying Length Under General Excitation.* Transactions of the ASME, 2008. **75**: p. 031003-(2-14).
18. Zhu, W.D., H. Ren, and C. Xiao, *A Nonlinear Model of a Slack Cable With Bending Stiffness and Moving Ends with Application to Elevator Traveling and Compensation Cables.* Journal of Applied Mechanics, 2011. **78**: p. 041017-1-13.
19. Ono, K., *Lateral Motion Transfer Characteristics of Axially Moving Tape over Guide Post with Coulomb Friction.* Toraiborojisuto (Journal of Japanese Society of Tribologists), 1997. **42**(5): p. 363-368.
20. Brake, M.R. and J.A. Wickert, *Frictional vibration transmission from a laterally moving surface to a traveling beam.* Journal of Sound and Vibration, 2008. **310**(3): p. 663-675.
21. Brake, M.R.W., *Lateral Vibration of Moving Media with Frictional Contact and Nonlinear Guides*, in *Department of Mechanical Engineering*. 2007, Carnegie Mellon University: Pittsburgh, PA 15213.
22. Zhu, W.D., J. Ni, and J. Huang, *Active Control of Translating Media With Arbitrarily Varying Length.* Journal of Vibration and Acoustics, 2001. **123**: p. 347-358.
23. Wickert, J.A. and C.D. Mote JR, *Classical vibration analysis of axially moving continua.* Journal of Applied Mechanics, 1990. **57**: p. 738-744.
24. Jha, R.K. and R.G. Parker, *Spatial Discretization of Axially Moving Media VIbration Problems.* Transactions of the ASME, 2000. **122**: p. 290-294.
25. Brake, M.R. and D.J. Segalman. *A New Approach to Modeling Discrete Nonlinear Constraints in Continuous System: The Method of Discontinuous Basis Funcstions*. in *ASME 2011 International Design Engineering Technical Conference & Computers and Information in Engineering Conference*. 2011. Washington, DC, USA.

26. Muftu., S., *The Transient Foil Bearing Problem in Magnetic Recording*, in *Department of Mechanical Engineering*. 1994, University of Rochester: Rochester, New York.
27. Yang., H. and S. Muftu. *A General Model of Lateral Web Dynamics between Two Reel*. in *Proceedings of the 13th International Web Handling Conference (IWEB)*. 2013. Oklahoma State University, Stillwater, OK.
28. Raeymaekers, B. and F.E. Talke, *Lateral Motion of an Axially Moving Tape on a Cylindrical Guide Surface.* Journal of Applied Mechanics, 2007. **74**(5): p. 1053.
29. Parker, R.G., *Supercritical Speed Stability of the Trivial Equilibrium of an Axially-Moving String on an Elastic Foundation.* Journal of Sound and Vibration, 1998. **221**(2): p. 205-219.
30. Chen, J.-S., *Natural Frequencies and Stability of an Axially-Traveling String in Contact with a Stationary Load System.* Transactions of the ASME, 1997. **119**: p. 152-157.
31. Cheng, S.-P. and N.C. Perkins, *The Vibration and Stability of a Friction-Guided, Translating String.* Journal of Sound and Vibration, 1991. **144**(2): p. 291-291.
32. Zen, G. and S. Muftu., *Stability of an accelerating string subjected to frictional guiding forces.* Journal of Sound and Vibration, 2006. **289**: p. 551-576.
33. Mockensturm, E.M., N.C. Perkins, and G.A. Ulsoy, *Stability and Limit Cycles of Parametrically Excited, Axially Moving Strings.* Journal of Vibration and Acoustics, 1996. **118**(3): p. 346-351.
34. Zhang, L. and J.W. Zhu, *Nonlinear Vibration of Parametericlly Excited Moving Belts, Part I: Dynamic Response.* Transactions of the ASME, 1999. **66**: p. 396-402.
35. Zhang, L. and J.W. Zhu, *Nonlinear Vibration of Parametrically Excited Viscoelastic Moving Belts, Part II: Stability Analysis.* Journal of Applied Mechanics, 1999. **66**: p. 403-409.
36. Chen, L.-Q., Y.-Q. Tang, and J.W. ZHu, *Nonlinear Transverse Vibration of Axially Accelerating Strings with Exact Internal Resonances and Longitudinally Varying Tensions.* Nonlinear Dynamics, 2014.

37. Taylor, R.J., M. Chung, and F.E. Talke, *Dynamic Simulation of In-plane Transverse Displacament of Tape.* Microsystem Technologies, 2006. **12**: p. 1117-1124.
38. Bokaian, A., *Natural Frequencies of beam under tensile axial loads.* Journal of Sound and Vibration, 1990. **142**(3): p. 481-498.
39. Gaith, M. and S. Muftu., *Lateral Vibration of Two Axially Translating Beams Interconnected by a Winkler Foundation.* Journal of Vibration and Acoustics, 2007. **129**: p. 380-385.
40. Kartik, V., *In-Plane and Transverse Vibration of Axially-Moving Media with Advanced Guiding and Actuation Elements*, in *Department of Mechanical Engineering*. 2006, Carnegie Mellon University: Pittsburgh, PA 15213.
41. Kartik, V. and E. Eleftheriou. *Friction-induced dynamics of axially-moving media in contact with an actively-positioned surface*. in *ASME 2008 International Mechanical Engineering Congress and Exposition*. 2008. Boston, Massachusetts, USA.
42. Kartik, V. and J.A. Wickert, *Surface Friction Guiding for Reduced High-Frequency Lateral Vibration of Moving Media.* Journal of Vibration and Acoustics, 2008. **129**: p. 371-379.
43. Wickert, J.A., *Non-Linear Vibration of a Traveling Tensioned Beam.* International Journal of Non-Linear Mechanics, 1992. **27**(3): p. 503-517.
44. Chakraborty, G. and A.K. Mallik, *Non-Linear Vibration of a Traveling Beam Having an Intermediat Guide.* Nonlinear Dynamics, 1999. **20**: p. 247-265.
45. Parker, R.G. and Y. Lin, *Parametric Instability of Axially Moving Meida Subjected to Multifrequency Tension and Speed Fluctuations.* Journal of Applied Mechanics, 2001. **68**: p. 49-57.
46. Chen, L.-Q., Y.-Q. Tang, and C.W. Lim, *Dynamic Stability in Parametric Resonance of Axially Accelerating Viscoelastic Timoshenko Beams.* Journal of Sound and Vibration, 2010. **329**: p. 547-565.
47. Orloske, K., M.J. Leamy, and R.G. Parker, *Flexural-Torsional Buckling of Misaligned Axially Moving Beams. I. Three-Dimensional Modeling, Equilibria,*

and Bifurcations. International Journal of Solids and Structures, 2006. **43**: p. 4297-4322.

48. Orloske, K. and R.G. Parker, *Flexural-Torsional Buckling of Misaligned Axially Moving Beams II. Vibration and Stability Analysis.* International Journal of Solids and Structures, 2006. **43**: p. 4323-4341.
49. Muftu., S. and R.C. Benson, *A Study of Cross-Width Variations in the Two-Dimensional Foil Bearing Problem.* Journal of Tribology, 1996. **118**: p. 407-414.
50. Muftu., S. and R.C. Benson, *A Numerical Solution for the Transient Displacement of a Circumferentially Moving Cylindrical Shell.* Journal of Vibration and Acoustics, 1994. **116**: p. 567-572.
51. Kartik, V. and J.A. Wickert, *Parametric Instability of a Traveling Plate Partially Supported by a Laterally Moving Elastic Foundation.* Journal of Vibration and Acoustics, 2008. **130**(5): p. 051006.
52. Banichuk, N., J. Jeronen, P. Neittaanmaki, and T. Tuovinen, *On the instability of an axially moving elastic plate.* International Journal of Solids and Structures, 2010. **47**: p. 91-99.
53. Lin, C.C. and C.D. Mote JR, *The Wrinkling of Thin, Flat, Rectangular Webs.* Journal of Applied Mechanics, 1996. **63**(3): p. 774-779.
54. Lin, C.C. and C.D. Mote JR, *The Wrinkling of Rectangular Webs Under Nonlinearly Distributed Edge Loading.* Journal of Applied Mechanics, 1996. **63**(3): p. 655-659.
55. Mockensturm, E.M. and C.D. Mote JR, *Steady Motions of Translating, Twisted Webs.* International Journal of Non-Linear Mechanics, 1998. **34**: p. 247-257.
56. Mockensturm, E.M. and C.D. Mote JR, *Free Response of Twisted Plates with Fixed Support sparation.* Journal of Vibration and Acoustics, 2001. **123**: p. 175-180.
57. Moustafa, M., *The Bahvior of Threads over Rotating Rolls.* Journal of Engineering Sciences, 1975. **1**(2): p. 37-43.
58. Yang, R.-J., *Steady Motion of a Thread over a Rotating Roller.* Journal of Applied Mechanics, 1994. **61**: p. 16-22.

59. Eaton, J.H., *Behavior of a tape path with imperfect components.* Advances in Information Storage Systems, 1998. **8**: p. 77-92.
60. Shelton, J.J., *Lateral Dynamics of A Moving Web*. 1968, Oklahoma State University.
61. Shelton, J.J. and K.N. Reid, *Lateral Dynamics of an Idealized Moving Web.* Journal of Dynamic Systems, Measurement, and Control, 1971. **93**(3): p. 187-192.
62. Young, G.E., J.J. Shelton, and B. Fang, *Interaction of Web Spans: Part I - Statics.* Journal of Dynamic Systems, Measurement, and Control, 1989. **111**: p. 490-496.
63. Shelton, J.J. and K.N. Reid, *Lateral Dynamics of a Real Moving Web.* Journal of Dynamic Systems, Measurement, and Control, 1971. **93**(3): p. 180-186.
64. Young, G.E., J.J. Shelton, and B. Fang, *Interaction of Web Spans: Part II—Dynamics.* Journal of Dynamic Systems, Measurement, and Control, 1989. **111**(3): p. 497-504.
65. Sievers, L.A., M.J. Balas, and A.H. Von Flotow, *Modeling of Web Conveyance Systems for Multivariable Control.* IEEE Transactions on Automatic Control, 1988. **33**(6): p. 524-531.
66. Brake, M.R. and J.A. Wickert, *Lateral Vibration and Read/Write Head Servo Dynamics in Magnetic Tape Transport.* Journal of Dynamic Systems, Measurement, and Control, 2010. **132**(011012-1).
67. Ono, K., *Lateral Motion of an Axially Moving String on a Cylindrical Guide Surface.* Journal of Applied Mechanics, 1979. **46**: p. 905-912.
68. Raeymaekers, B. and F.E. Talke, *Attenuation of LTM due to frictional inteaction with a cylindrical guide.* Tribology International, 2009. **42**(5): p. 609-614.
69. Lee, D.E., G.M. McClelland, and W. Imaino. *Simulation and Experimental Measurements of Lateral Tape Motion Proximate to a Flangeless Grooved Roller*. in *ASME Information Storage and Processing Systems Conference* 2011. Santa Clara, CA, USA.
70. Yu, L., Z. Zhao, and G. Ren, *Mutibody Dynamic Model of Web Guiding System With Moving Web.* Journal of Dynamic Systems, Measurement, and Control, 2010. **132**: p. 051004-1-051004-9.

71. Taylor, R.J. and F.E. Talke, *Investigation of roller interactions with flexible tape medium.* Tribology International, 2005. **38**(6-7): p. 599-605.
72. Jape, S.S., B. Ganapathysubramanian, and J.A. Wickert, *Exploring the Effect of Stick-Slip Friction Transition Across Tape-Roller Interface on the Transmission of Lateral Vibration.* IEEE Transactions on Magnetics, 2012. **48**(3): p. 1189-1199.
73. Raeymaekers, B. and F.E. Talke, *Measurement and Sources of Lateral Tape Motion: A Review.* Journal of Tribology, 2009. **131**(1): p. 011903.
74. Yang., H. and S. Muftu. *Frictional Induced Vibration Effects on A Tape in Contact with A Slewing Head*. in *Proceeding of the ASME 2013 Conference on Information Storage and Processing Systems*. 2013. Santa Clara, California, USA.
75. Jose, J., R.J. Taylor, R.A. de Callafon, and F.E. Talke, *Characterization of lateral tape motion and disturbances in the servo position error signal of a linear tape drive.* Tribology International, 2005. **38**(6-7): p. 625-632.
76. Raeymaekers, B., M.R. Graham, R.A. de Callafon, and F.E. Talke, *Design of a dual stage actuator tape head with high-bandwidth track following capability.* Microsystem Technologies, 2009. **15**(10-11): p. 1525-1529.
77. Taylor, R.J. and F.E. Talke, *High Frequency Lateral Tape Motion and the Dynamics of Tape Edge Contact.* Microsystem Technologies, 2005. **11**: p. 1166-1170.
78. Yang., H. and S. Muftu., *Lateral Tape Dynamics over Non-Linear Guides*, in *2012 ASME-ISPS /JSME-IIP Joint International Conference on Micromechatronics for Information and Precision Equipment, MIPE2012*. 2012: Santa Clara, California, USA.
79. Wang, J.H. and F.E. Talke, *Tape Edge Wear and its Relationship to Lateral Tape Motion.* Microsystem Technologies, 2005. **11**(8-10): p. 1158-1165.
80. Wang, J.H. and F.E. Talke, *Measurement and prediction of tape edge wear using accelerated wear testing.* Wear, 2005. **259**(7-12): p. 1362-1366.
81. Wang, J.H. and F.E. Talke, *Simulation of tape edge wear of magnetic tapes.* Wear, 2007. **262**(5-6): p. 499-504.
82. Lakshmikumaran, A.V. and D.J. Wickert, *Edge Buckling of Imperfectly Guided Webs.* Transactions of the ASME, 1998. **120**: p. 346-352.

83. Kartik, V. and J.A. Wickert, *Vibration and Guiding of Moving Media with Edge Weave Imperfections.* Journal of Sound and Vibration, 2006. **291**(419-436).

84. Ducotey, K.S. and J.K. Good, *The Importance of Traction in Web Handling.* Journal of Tribology, 1995. **117**: p. 676-684.

85. Wickert, J.A., *Free Linear Vibration of Self-Pressurized Foil Bearings.* Journal of Vibration and Acoustics, 1993. **115**: p. 145-151.

86. Raeymaekers, B., I. Etsion, and F.E. Talke, *Influence of operating and design parameters on the magnetic tape-guide friction coefficient.* Tribology Letters, 2007. **25**(1): p. 161-171.

87. Raeymaekers, B., I. Etsion, and F.E. Talke, *Enhancing tribological performance of the magnetic tape-guide interface by laser surface texturing.* Tribology Letters, 2007. **27**(1): p. 89-95.

88. Nagao, R. and J.-Y.J. Chang, *Experimental Investigation of Air-Bearing Mechanism to Enhance Proximity bewteen Traveling Tape and a Guider.* Journal of Advanced Mechanical Design, System, and Manufacturing, 2010. **4**(1): p. 290-300.

89. Keshavan, M.B. and J.A. Wickert, *Air Enterainment During Steady-State Web Winding.* Journal of Applied Mechanics, 1997. **64**: p. 916-922.

90. Keshavan, M.B. and D.J. Wickert, *Transient Dischange of Entrained Air From a Wound Roll.* Journal of Applied Mechanics, 1998. **65**(4): p. 804-810.

91. Bhushan, B. and K. Tonder, *Roughness Induced Shear and Squeeze Film Effects in Magnetic Recording —Part I: Analysis.* Journal of Tribology, 1989. **111**: p. 220-227.

92. Bhushan, B. and K. Tonder, *Roughness Induced Shear and Squeez Film Effects in Magnetic Recoarding-Part II: Applictation.* Journal of Tribology, 1989. **111**: p. 228-237.

93. Acton, K. and B. Weick, *Orthotropic Viscoelastic Behavior of Polymer Tape in a Wound Roll.* Mechanics of Advanced Materials and Structures, 2014. **21**(1): p. 53-66.

94. Baumgart, M.D. and L.Y. Pao., *Robust Control of Nonlinear Tape Transport Systems With and Without Tension Sensors.* Journal of Dynamic Systems, Measurement, and Control, 2007. **129**: p. 41-55.

95. Baumgart, M.D. and L.Y. Pao. *Robust Lyapunov-Based Feedback Control of Nonlinear Web-Winding Systems*. in *Proceedings of the 42nd IEEE Conference on Decision and Control*. 2003. Maui, Hawaii USA.

96. Lu, Y. and W.C. Messner. *Disturbance Observer Design for Tape Transport Control*. in *Proceedings of the American Control Conference*. 2001. Arlington, VA.

97. Lu, Y. and W.C. Messner. *Robust Servo Design for Tape Transport*. in *Proceedings of the 2001 IEEE International Conference on Control Applications*. 2001. Mexico City, Mexico.

98. Mathur, P.D. and W.C. Messner, *Controller Development for a Prototype High-Speed Low-Tension Tape Transport.* IEEE Transactions on Control Systems Technology, 1997. **6**(4): p. 534-542.

99. Zhong., H. and L.Y. Pao., *Regulating Web Tension In Tape Systems with Time-varying Radii*, in *2009 American Control Conference*. 2009: Hyatt Regency Riverfron, St. Louis, MO, USA.

100. Whitworth, D.P.D. and M.C. Harrison, *Tension variations in pliable material in production machinery.* Appl. Math. Modelling, 1983. **7**: p. 189-196.

101. Branca, C., P.R. Pagilla, and K.N. Reid, *Governing Equations for Web Tension and Web Velocity in the Presence of Nonideal Rollers.* Journal of Dynamic Systems, Measurement, and Control, 2013. **135**: p. 011018-1-011018-10.

102. Lee, G.T., J.M. Shin, H.M. Kim, and J.S. Kim, *A Web Tension Control Strategy for Multi-span Web Transport Systems in Annealing Furnace.* ISIJ International, 2010. **50**(6): p. 854-863.

103. Lee, W.S. and M.V.C. Rao, *Modeling and design of tape transport mechanism.* Mathematics and Computers in Simulation, 2006. **72**: p. 26-37.

104. Lin, K.C., *Observer-Based Tension Feedback Control With Friction and Inertia Compensation.* IEEE Transactions on Control Systems Technology, 2003. **11**(1): p. 109-118.

105. Lin, K.C., T. Ming-Ching, and C. Kung-Yi, *Web Tension Control of a Start-up Process using Observer Techniques with Friction and Inertia Compensation*, in *IECON'01: The 27th Annual Conference of the IEEE Industrial Electronics Society*. 2001. p. 529-534.

106. Imaino, W., *Photoacoustic determination of tension in magnetic tape.* Microsystem Technologies, 2004. **10**: p. 334-337.

107. Raeymaekers, B., T.R. J., and T.F. E., *Non-contact tape tension measurement and correlation of LTM and tape tension transients.* Microsystem Technologies, 2006. **12**: p. 814-821.

108. Altman, H.C., *Formulas for Computing the Stresses in Center Wound Rolls.* TAPPI Journal, 1968. **51**: p. 176-179.

109. Pfeiffer, J.D., *Prediction of roll defects from roll structure formulas.* Tappi J., 1979. **62**(10): p. 83-85.

110. Hakiel, Z., *Nonlinear model for wound roll stresses.* Tappi J., 1987. **70**(5): p. 113-117.

111. Benson, R.C., *A Nonlinear Wound Roll Model Allowing for Large Deformation.* Journal of Applied Mechanics, 1995. **62**: p. 853-859.

112. Yagoda, H.P., *Resolution of a Core Problem in Wound Rolls.* Journal of Applied Mechanics, 1980. **47**(4): p. 847-854.

113. Lee, Y.M. and J.A. Wickert, *Stress Field in Finite Width Axisymmetric Wound Rolls.* Journal of Applied Mechanics, 2002. **69**: p. 130-138.

114. Lee, C., H. Kang, H. Kim, and K. Shin, *Effect of taper tension profile on the telescoping in a winding process of high speed roll to roll printing system.* Journal of Mechanical Science and Technology, 2009. **23**: p. 2036-3048.

115. Benson, R.C., *Lateral Dynamics of a Moving Web With Geometrical Imperfection.* Journal of Dynamic Systems, Measurement, and Control, 2002. **124**(1): p. 25.

116. Sievers, L.A., *Modeling and Control of Web Conveyance Systems*, in *Department of Electrical and Computer Systems Engineering*. 1987, Rensselaer Polytechnic Institute: Troy, New York.

117. Sievers, L.A., M.J. Balas, and A.H. von Flotow, *Modeling of Web-Roller Interactions and Lateral Web Dynamics*, in *28th Structures, Structural Dynamics and Materials Conference*. 1987: Monterey, CA, USA.

118. Young, G.E., J.J. Shelton, and C. Kardamilas, *Modeling and Control of Mutiple Web Spans Using State Estimation.* Journal of Dynamic Systems, Measurement, and Control, 1989. **111**: p. 505-510.

119. Aravind, S. and P.R. Pagilla, *Optimal Web Guiding.* Journal of Dynamic Systems, Measurement, and Control, 2010. **132**: p. 011006-1-011006-10.

120. Han, F., F. Xiong, P. Yi, and T. Shi. *Axial Motion of Flat Belt Induced by Angular Misalignment of Rollers*. in *Proceedings of the 2009 IEEE, International Conference on Mechatronics and Automation*. 2009. Chengchun, China.

121. Pagilla, P.R. and Y. Diao, *Resonant Frequencies in Web Process Lines Due to Idle Rollers and Spans.* Journal of Dynamic Systems, Measurement, and Control, 2011. **133**: p. 061018(1)-061018(10).

122. Good, J.K., D.M. Kedl, and J.J. Shelton. *Shear Wrinkles in Isolated Spans*. in *Proceedings of the Fourth International Conference on Web Handling*. 1997. Web Handling Research Center, Oklahoma State University, Stillwater, Oklahoma.

123. Good, J.K. and P. Straughan. *Wrinkling of Webs Due to Twist*. in *Proceedings of the Fifth International Conference on Web Handling*. 1999. Web Handling Research Center, Oklahoma State University, Stillwater, Oklahoma.

124. Bower, A.F., *Applied Mechanics of Solids*. 2009: CRC press.

125. Cook, R.D., D.S. Malkus, M.E. Plesha, and R.J. Witt, *Concepts and applications of finite element analysis*. 2002, Hoboken, NJ 07030, USA John Wiley & Sons. Inc.

126. Hughes, T.J.R., *The finite element method: linear static and dynamic finite element analysis*. 2000, Mineola, New York, USA: Dover Publications Inc.,.

127. Meirovitch, L., *A Modal Analysis for the Response of Linear Gyroscopic Systems.* Journal of Applied Mechanics, 1975. **42**(2): p. 446-450.

128. Meirovitch, L., *A new method of solution of the eigenvalue problem for gyroscopic systems.* AIAA Journal, 1974. **12**(10): p. 1337-1342.

129. Tonoli, A., E. Zenerino, and N. Amati, *Modeling the Flexural Dynamic Behavior of Axially Moving Continua by Using the Finite Element Method.* Journal of Vibration and Acoustics, 2014. **136**(1): p. 011012.
130. Graff, K.F., *wave motion in elastic solids*. 1975, New York: Dover Publication Inc.
131. Doyle, J.F., *Wave propagation in structures: an FFT-based spectral analysis*. 1989, USA: Springer-Verlag New York.
132. Banerjee, J.R., *Dynamic Stiffness Formulation for Structural Elements: A General Approach.* Computer and Structures, 1997. **63**(1): p. 101-103.
133. Lee, U. and H. Oh, *Dynamics of an axially moving viscoelstic beam subject to axial tension.* International Journal of Solids and Structures, 2005. **42**: p. 2381-2398.
134. Chakraborty, G. and A.K. Mallik, *Wave propagation in and vibration of a travelling beam with and without non-linear effects, part I: free vibration.* Journal of Sound and Vibration, 2000. **236**(2): p. 277-290.
135. Chakraborty, G. and A.K. Mallik, *Wave propagation in and vibration of a travelling beam with and without non-linear effects, Part II: forced vibraton.* Journal of Sound and Vibration, 2000. **236**(2): p. 291-305.
136. Banerjee, J.R. and W.D. Gunawardana, *Dynamic stiffness matrix development and free vibration analysis of a moving beam.* Journal of Sound and Vibration, 2007. **303**: p. 135-143.
137. Mace, B.R., D. Duhamel, M.J. Brennan, and L. Hinke, *Finite element prediction of wave motion in structural waveguides.* Journal of Acoustical Society of America, 2005. **117**(5): p. 2835-2840.
138. Duhamel, D., B.R. Mace, and M.J. Brennan, *Finite Element Analysis of the Vibrations of Waveguides and Periodic Structures*, in *ISVR Technical Memorandum*. 2003.
139. Hinke, L., B.R. Mace, and M.J. Brennan, *Finite Element Analysis of Waveguides*, in *ISVR Technical Memorandum*. 2004.

140. Mace, B.R. and E. Manconi, *Modelling wave propagation in two-dimensional structures using finite element analysis.* Journal of Sound and Vibration, 2008. **318**: p. 884-902.
141. Manconi, E. and B.R. Mace, *Wave characterization of cylindrical and curved panels using a finite element method.* Journal of Acoustical Society of America, 2009. **125**(1): p. 154-163.
142. Manconi, E. and R. Garziera, *Modelling moving one-dimensional waveguides using waves and finite elmenet analysis*, in *ECCOMAS Thematic Conference on Computational Methods in Structural Dynamics and Earthquake Engineering*, M. Papadrakakis, M. Fragiadakis, and V. Plevris, Editors. 2011: Corfu. Greece.
143. Rogers, K.S., N.S. Ferguson, A.A. Perryman, and B.R. Mace, *Modelling Axially Moving Beams of Varying Length using the Finite Element Method*, in *7th EROMECH Solid Mechanics Conference*, J.e.a. Ambrosio, Editor. 2009: Lisbon, Portugal.
144. Subbaraj, K. and M.A. Dokainish, *A survey of direct time-integration methods in computational structural dynamics—II. Implicit methods.* Computers & structures., 1989. **32**(6): p. 1387-1401.
145. Trefethen, L.N., *Finite difference and spectral methods for ordinary and partial differential equations*. 1996.
146. Waki, Y., B.R. Mace, and M.J. Brennan, *Numerical issues concerning the wave and finite element method for free and forced vibration of waveguides.* Journal of Sound and Vibration, 2009. **327**: p. 92-108.
147. D'Eleuterio, G.M.T. and P.C. Hughes, *Dynamics of Gyroelastic Continua.* Journal of Applied Mechanics, 1984. **51**(2): p. 415-422.
148. Hughes, P.C. and G.M.T. D'Eleuterio, *Model Parameter Analysis of Gyroelastic Continua.* Journal of Applied Mechanics, 1986. **53**(4): p. 918-924.
149. Zhong, W. and F. Williams, *On the direct solution of wave propagation for repetitive structures.* Journal of Sound and Vibration, 1995. **181**(3): p. 485-501.
150. Rice, B.S., *Reduction in Web-to-roller Traction as a Result of Air Lubrication*. 2003.

151. Ulsoy, A.G. and C.D. Mote, *Analysis of bandsaw vibration.* Wood Science, 1980. **13**(1): p. 1-10.

152. Pantazi, A., M. Lantz, W. Haberle, W. Imaino, J. Jelitto, and E. Eleftheriou. *Active tape guiding*. in *ASME Information Storage and Processing Systems Conference*. 2010. Santa Clara, CA, USA.

153. Kartik, V. and J.A. Wickert, *Surface Friction Guiding for Reduced High-Frequency Lateral Vibration of Moving Media.* Journal of Vibration and Acoustics, 2007. **129**(3): p. 371.

154. Yang, H., J.B.C. Engelen, A. Pantazi, W. Haberle, M.A. Lantz, and S. Muftu, *Mechanics of lateral positioning of a translating tape due to tilted rollers Theory and experiments.* International Journal of Solids and Structures, 2015. **66**: p. 88-97.

155. Engelen, J.B.C. and M.A. Lantz, *Asymmetrically Wrapped Flat-Profile Tape–Head Friction and Spacing.* Tribology Letters, 2015. **59**(1): p. 1-8.

156. Leine, R.I., D.H. van Campen, and A. de Kraker, *Stick-Slip Vibration Induced by Alternate Friction Models.* Nonlinear Dynamics, 1998. **16**: p. 41-54.

157. Byerlee, J.D., *The mechanics of stick-slip.* Tectonophysics, 1970. **9**(2): p. 475-486.

158. Ernest, R., *The Nature of the Static and Kinetic Coefficients of Friction.* Journal of Applied Physics, 1951. **22**(11): p. 1373-1379.

159. Block, H., *Fundamental Mechanical Aspects of Boundary Lubrication.* Journal of the Society of Automotive Engineers, 1940. **46**: p. 54-68.

160. Cameron, R., *Friction induced vibration by Roderick*, in *Mechanical Engineering*. 1959, The University of British Columbia: Glasgow.

161. Singh, B.R. and V. Push, *Stick-slip sliding under forced vibration.* Journal of Science and Engineering, 1957. **1**: p. 227-232.

162. Shaw, S.W., *On the dynamic response of a system with dry friction.* Journal of Sound and Vibration, 1986. **108**(2): p. 305-325.

163. Armstrong-Helouvry, B., *Stick Slip and Control in Low-Speed Motion.* Transactions on Automatic Control, 1993. **38**(10): p. 1483-1496.

164. Southward, S.C., C.J. Radcliffe, and C.R. MacCluer, *Robust Nonlinear Stick-Slip Friction Compensation.* Journal of Dynamic Systems, Measurement, and Control, 1991. **113**: p. 639-644.

165. Karnopp, D., *Computer simulation of stick-slip friction in mechanical dynamic system.* Journal of Dynamic Systems, Measurement, and Control, 1985. **107**: p. 100-103.

166. Haessig, D.A.J. and B. Friedland, *On the modeling and simulation of friction.* Journal of Dynamic Systems, Measurement, and Control, 1991. **113**: p. 354-362.

167. Kikuuwe, R., N. Takesue, A. Sano, H. Mochiyama, and H. Fujimoto. *Fixed-step friction simulation, from classical Coulomb model to modern continuous models*. in *Proc. IEEE/RSJ Int. Conf. Intell. Robots Syst.* 2005.

168. Quinn, D.D., *A new regularization of Coulomb friction.* Journal of vibration and acoustics, 2004. **126**(3): p. 391-397 0739-3717.

169. Beisel, J.A., *Single span web buckling due to roller imperfections in web process machinery,* in *Graduate College*. 2006, Oklahoma State University: Stillwater, OK.

170. Kasikci, T. and S. Müftü, *Wrap Pressure between a Flexible Web and a Circumferentially Grooved Cylindrical Guide.* Journal of Tribology, 2015.

171. Muftu., S., *Monthly Report for December 2011 for the INSIC Project: Tape Path Mechanics.* 2011.

172. Nayfeh, A.H. and D.T. Mook, *Nonlinear Oscillations*. 1979, New York, USA: Wiley.

173. Reddy, J.N., *An introdunction to nonlinear finite element analysis*. 2004, United State: OXFORD.

174. Mathur, P.D. and W.C. Messner, *Controller Development for a Prototype High-Speed Low-Tension Tape Transport.* IEEE Transactions on Control Ssytems Technology, 1998. **6**(4): p. 534-542.

175. Hashimoto, H., *Experimental study of porous foil bearings for web-handling.* Tribology international, 2000. **33**(3): p. 191-196 0301-679X.

176. Lantz, M., S. Furrer, J. Engelen, A. Pantazi, H. Rothuizen, R. Cideciyan, G. Cherubini, W. Haeberle, J. Jelitto, and E. Eleftheriou, *123 Gb/in^2 Recording Areal Density on Barium Ferrite Tape.*

177. Furrer, S., M. Lantz, J.B.C. Engelen, A. Pantazi, H.E. Rothuizen, R.D. Cideciyan, G. Cherubini, W. Haeberle, J. Jelitto, and E. Eleftheriou, *85.9 Gb/in^2 Recording Areal Density on Barium Ferrite Tape.* Magnetics, IEEE Transactions on, 2015. **51**(4): p. 1-7

178. Biskeborn, R.G. and J.H. Eaton, *Flat-profile tape recording head.* Magnetics, IEEE Transactions on, 2002. **38**(5): p. 1919-1921 0018-9464.

179. Hintereger, H. and S. Muftu, *Contact tape recording with a flat head contour*, in *1996 IEEE International Magnetics Conference (INTERMAG 96)*. 1996: Seattle, WA, USA. p. 3476-3478.

180. Müftü, S. and D.J. Kaiser, *Measurements and theoretical predictions of head/tape spacing over a flat-head.* Tribology international, 2000. **33**(5): p. 415-430 %@ 0301-679X.

181. Hinteregger, H.F. and S. Muftu, *Flat heads for contact tape recording: Performance measurements at different wrap angles, tape tensions, speeds, and stiffnesses.* Journal of Information Storage and Processing Systems, 2000. **2**(1-2): p. 75-82 %@ 1099-8047.

182. Bhatti, M.A., *Advanced topics in finite element analysis of structures: with Mathematica and MATLAB computations*. 2006: John Wiley & Sons, Inc.